The Proton Spin Structure Function g_2 at Low Q^2 and Applications of Polarized ^{3}He

Jie Liu

Shaoyang, Hunan, China

B.S., University of Science and Technology of China (2010)

A Dissertation Presented to the Graduate Faculty
of the University of Virginia in Candidacy for the Degree of
Doctor of Philosophy

Department of Physics

University of Virginia

May, 2017

Abstract

Since the Stern-Gerlach experiment in 1922, spin has had major implications on practically almost all areas of modern physics. Quantum chromodynamics (QCD) is the fundamental theory that describes strong interaction in terms of quark and gluon degrees of freedom. While QCD has been well tested in the high-energy regime, it is still unsolved in the low-energy, non-perturbative regime. With developments in polarized beam and polarized target technologies, spin offers a unique tool to probe the internal structure of nucleons and non-perturbative QCD dynamics. The polarization techniques developed for these fundamental nuclear physics study also bring new impulses to the idea of polarized fusion, in which spin-polarized deuterium and tritium (D-T) fuel in a tokamak reactor would provide a boost to the fusion rate.

This thesis consists of three topics based on spin physics. The first topic is the Jefferson Lab (JLab) Hall A E08-027 (g_2^p) experiment performed with the polarized electron beam scattering off a polarized ammonia target to obtain the proton spin-dependent structure function g_2 in the low momentum transfer region ($0.02 < Q^2 < 0.2$ GeV^2). The measured data will provide a benchmark test of Chiral Perturbation Theory (χPT) calculations in the non-perturbative region by extracting the generalized longitudinal-transverse polarizability δ_{LT}, and help test the Burkhardt-Cottingham Sum Rule at low Q^2. This thesis will discuss the physics motivation, data analysis, and preliminary results from the E08-027 experiment in Chapters 2−5. The second topic is focused on the JLab polarized ^{3}He target, which is essential for the neutron spin structure study. Progress on the upgrade of this target for the JLab 12 GeV program will be presented in Chapter 6. The final topic is an application of such polarization techniques in thermonuclear fusion. A direct test of spin-polarized fusion was proposed for the DIII-D tokamak in San Diego using the isospin mirror reaction D-^{3}He. Preliminary results on the polarized ^{3}He performance in inertial confinement fusion (ICF) polymer pellets will be presented in Chapter 7.

Acknowledgments

There are so many people who have supported, guided, and encouraged me during my Ph.D. study. I would like to take this opportunity to express my deepest appreciation to all of them who have always been with me and for me in this exciting journey.

First of all, I would like to thank my research advisor, Xiaochao Zheng, for her excellent advising and giving me the freedom to do the research I want. I clearly remember the weekly physics discussion every Tuesday afternoon when I just started to do research. During the physics discussion, she would become an audient and listen carefully to my lectures with free physics topics that I chose freely, which I presented with no note, no slide and only handwriting on the blackboard. She would ask me all kinds of questions I might never think myself, which greatly cultivated my critical thinking and problem solving abilities. I'm also thankful for her help in correcting the draft of this thesis and preparation for defense. Her passion and insights into her work set an excellent example for me and will always motivate me.

I would like to thank Nilanga Liyanage for being my co-advisor in the first three years and a committee member in my thesis defense. Our discussions were always productive and enjoyable, and he taught me how to build a big picture of the projects I worked on. I am also very grateful for the guidance I received from my annual review committee member, Louis Bloomfield, and my thesis committee members, Donal Day and Eric Murphy.

I would like to thank Jian-Ping Chen as my supervisor at JLab. During my four years stay at JLab, he not only supervised me closely in all steps of my research on E08-027 experiment data analysis and the polarized ^{3}He target upgrade, but also taught me to organize multi-works and be the master of my life.

I would like to thank the E08-027 co-spokespersons, Alexandre Camsonne, Jian-Ping Chen, Don Crabb and Karl Slifer for their scientific vision and leading roles to realize the experiment. I would also thank the Hall A collaboration and the JLab target group, without whose efforts the experiment could not have succeeded. Many thanks to the fellow graduate students, post-docs and colleagues: Kalyan Allada, Toby Badman, Melissa Cummings, Chao Gu, Min Huang, Ellie Long, James Maxwell, Vincent Sulkosky, Jixie Zhang, Pengjia Zhu, and Ryan Zielinski for their excellent work and wish the best of luck in their future pursuits.

I would like to thank the JLab polarized ^{3}He collaboration, Jian-Ping Chen, Kai Jin, Nguyen Ton, Zhiwen Zhao for making the target upgraded smoothly and full of fun. I am also very grateful for the kind help from Todd Averett, Gordon Cates, Chunhua Chen, Jin Huang, Yi Qiang, Mark Taylor, William Tobias, Yunxiao Wang, Yawei Zhang, Yi Zhang and Yuan Zheng.

I would like to thank the JLab-UVa spin-polarized fusion group, Alexandre Deur, Michael Lowry, Wilson Miller, Andrew Sandorfi, Kevin Wei, Xiangdong Wei, and Xiaochao Zheng. It was my honor to work with these awesome scientists, and the days and nights we spent together in the lab were unforgettable.

I would like to thank Bingbing Dong, Tianming Li, Dien Nguyen, Longwu Ou, Peng Peng, Pei Wang, Tianxiong Wang, Yang Wang, Wei Xu, Xiuchang Yang, Yuxiang Zhao, and other friends at University of Virginia and JLab for the joyful time we shared.

I would like to thank my parents for their unconditional love and endless encouragements for all decisions I made. Finally, I would like to thank Nguyen Ton for all her understanding and support for a happy and beautiful journey.

Dedicated to my parents, Guiqiu Liu and Fuchun Liu

Contents

List of Figures

List of Tables

Chapter 1

Introduction

The history of spin physics can be traced back to the Stern-Gerlach experiment[1] in 1922. In this experiment, a beam of silver particles was passed through an inhomogeneous magnetic field and was observed to follow a deflection either up or down at two highly-localized points. In 1925, Uhlenbeck and Goudsmit postulated that the electron possesses an intrinsic angular momentum[2], referred to as "spin", to explain the Stern-Gerlach experiment. This postulation had no solid theoretical framework until Dirac combine quantum mechanics and special relativity and published his famous relativistic wave equation[3], which required the electron to have such intrinsic angular momentum. In Dirac formulation, a structureless spin-1/2 particle has a magnetic momentum $\hat{\mu} = \frac{Q}{M}\hat{S}$ where Q is the charge, M is the mass, and $\hat{S}$ is the spin. When applied to electrons, the magnetic moment given by the Dirac equation agrees with the results of the Stern-Gerlach experiment. By the end of the 1920s, the role of electron spin to the atomic electronic structure is fundamentally understood.

In 1933, Estermann and Stern measured the magnetic moment of the proton[4] and discovered that the proton's magnetic moment has a marked deviation ($\sim 150\%$) from Dirac's prediction, which was the first indication that proton has internal structure. In the late 1930s, Rabi and his colleagues developed the technique to discern the magnetic moment and nuclear spin of atoms by using an extended version of the Stern-Gerlach apparatus[5, 6]. In their work, an oscillating magnetic field was showed to induce the magnetic moment transitions from one state to the other, which evolved into the techniques of modern Nuclear Magnetic Resonance (NMR) and Magnetic Resonance Imaging (MRI), now in use daily worldwide.

Since the 1950s, with the advancement of techniques to devise high density, high polarization targets, polarimeters and detectors capable of incredible sensitivity, and accelerators to accelerate, store and collide polarized particles, spin has become an important tool to understand the fundamental structure of matter and properties of the four interactions. In 1956, Wu and collaborators observed a clear violation of parity conservation in the beta decay of ^{60}Co nuclei with spin aligned in a magnetic field[8], which confirmed Lee and Yang's hypothesis[7] that parity is not conserved in weak interactions. Later on, spin offers an effective laboratory to study Quantum Chromodynamics (QCD) in both perturbative and non-perturbative region to understand how the nucleon is constructed from the fundamental quark and gluon degrees of freedom. It was originally expected that the quark spin carried all of the nucleon spin, but experiments at SLAC[9] and CERN[10] performed with polarized beams and polarized targets in the late 1980s contradicted this expectation. The experimental results suggested that only a small percentage of the nucleon spin is carried by spin of quarks. This disagreement astonished physicists at that time and is sometimes referred to as the "proton spin crisis". In the 30 years that followed, experimental research on these topics has been continued at SLAC, CERN, DESY, RHIC, Jefferson Lab (JLab) and other facilities[11]. Through decades of efforts in both theoretical and experimental approaches, the current understanding is that the quark spin contribution towards the nucleon spin is about 30% and the rest is carried either by the gluon spin, or by the orbital angular momentum of gluon and quark.

In parallel with the elementary particle physics study, the polarization techniques have been adopted and further developed for other applications in practically almost all other areas of physics and beyond: from atomic-molecular-optical physics, condensed matter physics, to chemistry, biology and medicine. The University of Virginia (UVa) is one of the world centers for research and application of spin physics. Besides the production of polarized NH_3[13], ND_3[13], and ^{3}He[14] targets for JLab QCD spin physics study, the polarized ^{3}He and ^{129}Xe applied in MRI in medicine enabled direct observation of inhaled gas in airways[15], such as in lungs or sinuses, organs that are poorly seen with standard MRI based on the detection of proton (water) spin in tissue. In addition, the UVa-JLab collaboration is developing the technique to apply polarized ^{3}He and polarized deuterium[17] for the first proof-of-principle, in-situ test of polarization survival and polarization dependence of D-^{3}He fusion in the DIII-D tokamak[18], which would pave the way for spin-polarized fusion[19].

This thesis is organized as follows: Chapters 2−5 gives a review of the physics motivation, experimental setup, data analysis, and preliminary results for the HALL A E08-027 experiment which measure the proton spin-dependent structure function g_2 in the low Q^2 region. Chapter 6 presents the upgrade progress of JLab polarized ^{3}He target for the 12 GeV program which is essential for neutron spin structure study. Chapter 7 gives a detailed discussion of spin-polarized fusion, and preliminary results on the polarized ^{3}He performance in inertial confinement fusion (ICF) polymer pellets using data acquired with a clinical 1.5-T MRI scanner. Chapter 8 presents conclusion of this thesis.

Chapter 2

Physics Motivation for the g_2^p Measurement

2.1 Introduction to the Nucleon Spin Structure Study

Understanding the nature of the atomic nucleus and its fundamental constituents, including precision tests of their interactions, is an on-going effort that has lead to many great discoveries along the way. The seeds of physics about the nucleus took root with the discovery of the nuclear atomic model by Rutherford in 1911[20]. In the famous gold foil scattering experiment, Rutherford demonstrated that the positive charge, and most of the mass of the atom is concentrated in a tiny nucleus. In the 1920s, Rutherford named the nucleus of the lightest atom (hydrogen) as proton and predicted the existence of an electrically neutral twin to the proton, the neutron[21], later discovered in 1932 by Chadwick[22]. However, the internal structure of the nucleon, proton and neutron, remained a mystery until the mid-1960s. In 1964, Gell-Mann and Zweig proposed that hadrons are in fact composed of quarks, which are point-like charged spin-1/2 fermions: a three quark composite particle is called a baryon, such as the proton and the neutron; and a quark-antiquark particle is called a meson like the pion and the kaon[23, 24]. The first confirmation of the existence of quarks was provided by inelastic electron-proton scattering experiments carried out at Stanford Linear Accelerator Center (SLAC) in the late 1960s and early

1970s[25]. Soon thereafter, QCD emerged as a fundamental theory to describe the strong interaction between quarks in the form of gluon exchange. In QCD, a nucleon consists of three quarks (valence quarks), a sea containing quark-antiquark pairs (sea quarks), and gluons.

QCD has two important features: asymptotic freedom that the strong coupling constant becomes asymptotically weak as energy increases and the distance between quarks decreases, and confinement that color charged particles cannot be isolated singularly but must form together as colorless hadrons. Although QCD is a complete theory, a full analytic QCD calculation of real physical process is mathematically impossible at the current stage and a perturbative QCD (pQCD) calculation is used whenever appropriate. In pQCD, the calculation of a physical process is expanded in terms of the strong coupling constant α_s. In the high energy and large momentum transfer region, where α_s is small and the quarks in the hadrons behave as quasi-free particles to some extent, predictions from perturbative QCD have been proven to describe experimental results very well. In the low energy (non-perturbative) region, where α_s becomes large (~ 1), perturbative calculation becomes inappropriate. The dynamical properties and the degrees of freedom of quarks and gluons are combined with some non-perturbative QCD aspects, such as confinement and dynamic chiral symmetry breaking, to provide predictions for measured physical quantities. These are commonly referred to as low-energy effective field theories such as the chiral perturbation theory (χPT).

Understanding how the nucleon is constructed from the underlying fundamental quarks and gluons is one of the most important and challenging questions in modern nuclear physics. Among all nucleon properties, understanding its spin constitution is particularly interesting. The nucleon spin structure is often described by various spin structure functions, which provide insights about how the nucleon spin is distributed among the nucleon's constituents (quarks and gluons) and the underlying dynamic mechanism. As mentioned in Chapter 1, a series of experiments determined the quark spin contribution to the nucleon spin to be $\approx 30\%$ using polarized beam and polarized target, but how the remaining 70% of the nucleon spin emerges from quarks and gluons is still not understood from QCD.

The detailed spin structure function of the nucleon can be studied by measuring precisely the spin structure function g_1 and g_2. The proton spin structure function g_1^p and the neutron spin structure functions g_1^n and g_2^n have been measured extensively over a very wide kinematic range[11, 26], however the proton spin structure function g_2^p remains largely unmeasured. The JLab Hall A Experiment E08-027 was a measurement of the proton g_2^p structure function at low momentum transfers using the polarized electron scattering off polarized NH_3 target. These proton g_2^p data will help study the quark-gluon interactions and provide tests of χPT predictions in the non-perturbative region.

The following sections will give an introduction about inclusive electron scattering first, then discuss the theoretical background and motivation (quark-parton model, Operator Product Expansions, sum rules and moments, χPT, proton hyperfine structure) for the proton spin structure function g_2^p measurement.

2.2 Inclusive Electron Scattering

Lepton scattering, particularly electron scattering, has been proven to be a powerful microscope to probe the nucleon structure. Here "inclusive" refer to scattering measurement where only the scattered electrons are detected. It is a clean probe with the electromagnetic interaction well understood in the framework of Quantum Electrodynamics (QED). With the development in polarized beam and polarized target technologies, doubly polarized inclusive electron scattering experiments have been used in the study of nucleon spin structure functions. In the following sections, the relevant kinematic variables, the differential cross-sections and the formulation of nucleon structure functions will be discussed.

2.2.1 Kinematic Variables

The general process of inclusive electron scattering is described by:

$$e(k) + N(P) \rightarrow e(k^{'}) + X(P^{'}), \tag{2.1}$$

with the one-photon exchange (Born approximation) shown in Fig. 2-1. Here the incident electron with four-momentum $k^\mu = (E, \vec{k})$ scatters off a target nucleon (or nucleus) with four-momentum $P^\mu = (E_p, \vec{P})$ via the exchange of a single virtual photon with four-momentum $q^\mu = (\nu, \vec{q})$. In this process, the energy ν and momentum $\vec{q}$ are transferred to the target. The virtual photon has $q^2 < 0$ and is called "off the mass shell", and the Lorentz-invariant four-momentum transfer squared $Q^2 \equiv -q^2$ is commonly used to describe the scattering process. The virtual photon can be viewed as the electromagnetic probe to the target nucleon (or nucleus) and the amplitude of Q^2 is associated with the scale (or resolution) that the probe is sensitive to. The scattered electron $e(k')$ is detected at an angle θ with four-momentum $k'^\mu = (E', \vec{k'})$, which defines the photon's $q^\mu = k^\mu - k'^\mu$, while the final hadronic state X(P') with four-momentum $P'^\mu = (E'_p, \vec{P'})$ goes undetected. The invariant mass of the undetected hadronic state is $W = \sqrt{(P+q)^2}$. Two additional dimensionless and relativistically invariant variables are sometimes used as well: the Bjorken scaling variable $x = Q^2/(2P \cdot q)$ and the fraction of electron energy loss $y = P \cdot q/(P \cdot k)$.

For a fixed-target experiment, the target has $P^\mu = (M, 0)$ in the lab-frame. It is useful to summarize kinematic relations as follows:

$$\begin{aligned}
\nu &\equiv E - E', && (2.2)\\
Q^2 &\equiv -q^2 = 4EE' \sin^2 \frac{\theta}{2}, && (2.3)\\
W^2 &\equiv (P+q)^2 = M^2 + 2M\nu - Q^2, && (2.4)\\
x &\equiv \frac{Q^2}{2P \cdot q} = \frac{Q^2}{2M\nu}, && (2.5)\\
y &\equiv \frac{P \cdot q}{P \cdot k} = \frac{\nu}{E}, && (2.6)\\
& && (2.7)
\end{aligned}$$

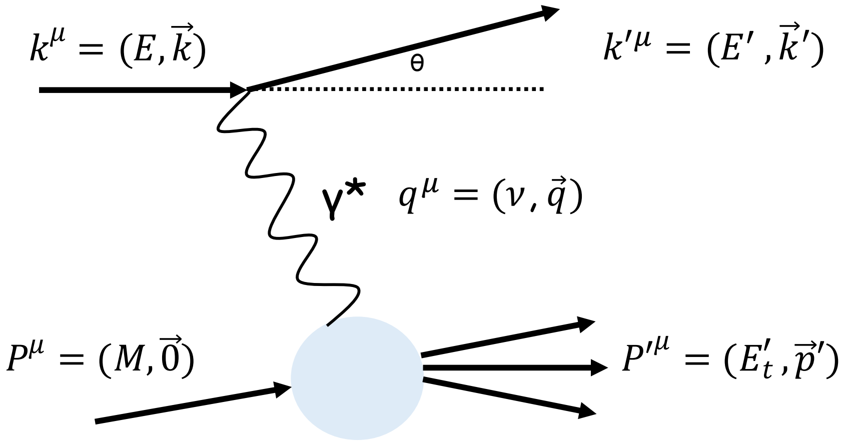

Figure 2-1: Lowest order diagram for inclusive electron scattering.

where the electron mass is neglected if $E \gg m_e c^2$ and $E' \gg m_e c^2$.

The cross section for electron scattering depends on the kinematics Q^2 and ν. As the increase of Q^2 and ν, nucleon electron scattering off light nuclei can be separated to different types: elastic, quasi-elastic, resonance, and deep inelastic regions. For the E08-027 experiment, inclusive electron-proton scattering was used, thus no quasi-elastic is present.

2.2.2 Electron-nucleon Differential Cross Sections

Consider the inclusive electron-nucleon scattering shown in Fig. 2-1, the invariant matrix T_{fi} is:

$$T_{fi} = [\bar{u}_{s'}(k')\ (-ie\gamma_\mu)\ u_s(k)] \frac{-i}{q^2} \langle X(P')|ieJ_\nu(\xi)|N_S(P)\rangle, \tag{2.8}$$

where u represents the lepton Dirac spinors, $s(s')$ is the covariant spin four-vector of the initial (final) lepton, S is the spin four-vector of the initial proton, γ_u is one of the Dirac matrices, ξ is the spatial four-vector, and $J_\nu(\xi)$ represents the unknown electromagnetic current operator of the hadron. In the laboratory frame, the scattering cross section reads[27, 28]:

$$d\sigma = \frac{|T_{fi}|^2}{\Im}\frac{d^3k'}{2E'(2\pi)^3}\frac{d^3P'}{2E'_p(2\pi)^3}(2\pi)^4\delta^4(k-k'+P-P'), \tag{2.9}$$

where $\Im = 4\sqrt{(P\cdot k)^2 - m_e^2M^2} \approx 4P\cdot k = 4EM$ is the flux factor, $\frac{d^3k'}{2E'(2\pi)^3}$ and $\frac{d^3P'}{2E'_p(2\pi)^3}$ are normalized phase space factors for the final particle states. $d\sigma$ must contain all the possible transitions of the nucleon from the ground state to any excited states, hence Eq. 2.9 becomes:

$$d\sigma = \frac{d^3k'}{4EE'}\int\frac{d^4P'}{2E'_p}\frac{1}{2M}\sum_{s',X}|T_{fi}|^2(2\pi)^{-2}\delta^4(k-k'+P-P'). \tag{2.10}$$

For detecting the final electron in the solid angle $d\Omega$ and in the final energy range $(E',\ E'+dE')$, one can employ

$$d^3k' = |\vec{k'}|^2 d|\vec{k'}|d\Omega \approx {E'}^2 dE' d\Omega, \tag{2.11}$$

and obtain the differential cross section

$$\frac{d^2\sigma}{d\Omega dE'} = \frac{E'}{E}\frac{1}{(2\pi)^2}\int\frac{d^4P'}{2E'_p}\frac{1}{2M}\sum_{s',X}|T_{fi}|^2\delta^4(k-k'+P-P'). \tag{2.12}$$

The integral part of Eq. 2.12 can be expressed as the form of leptonic tensor $L_{\mu\nu}$ and hadronic tensor $W^{\mu\nu}$ and then Eq. 2.12 can be written as[28]:

$$\begin{aligned}\frac{d^2\sigma}{d\Omega dE'} &= \frac{E'}{E}\frac{1}{(4\pi)^2}\times\frac{e^4}{Q^4}L_{\mu\nu}W^{\mu\nu}\\ &= \frac{\alpha^2}{Q^4}\frac{E'}{E}L_{\mu\nu}W^{\mu\nu},\end{aligned} \tag{2.13}$$

where $\alpha \equiv \frac{e^2}{4\pi} = \alpha_{em}$ is the electromagnetic fine structure constant. $L_{\mu\nu}$ and $W^{\mu\nu}$ tensors completely represent the electron and nucleon's states (momentum and spin), respectively, including both before and after the virtual photon exchange.

The leptonic tensor is well known and can be calculated in QED as the sum over unobserved final electron spin states:

$$L_{\mu\nu}(k,s;k') \;=\; \sum_{s'} [\bar{u}_{s'}(k')\;\gamma_\mu\;u_s(k)]^*\;[\bar{u}_{s'}(k')\;\gamma_\nu\;u_s(k)]. \tag{2.14}$$

It can be split into symmetric (S) and antisymmetric (A) parts under the μ, ν interchange:

$$L_{\mu\nu}(k,s;k') = 2\{L^{(S)}_{\mu\nu}\;(k;k') + iL^{(A)}_{\mu\nu}\;(k,s;k')\}, \tag{2.15}$$

with

$$L^{(S)}_{\mu\nu}\;(k;k') \;=\; k_\mu k'_\nu + k'_\mu k_\nu - g_{\mu\nu}\;(k\cdot k' - m^2), \tag{2.16}$$

$$L^{(A)}_{\mu\nu}\;(k,s;k') \;=\; m\;\varepsilon_{\mu\nu\alpha\beta}\;s^\alpha\;q^\beta, \tag{2.17}$$

where $g_{\mu\nu}$ is the space-time metric, spin four-vector $s_u = \bar{u}\;\gamma_\mu\gamma_5\;u$, and $\varepsilon_{\mu\nu\alpha\beta}$ is the totally antisymmetric Levi-Cevita tensor with convection $\varepsilon_{0123} = +1$. For an unpolarized incident lepton beam, $L^{(A)}_{\mu\nu}$ vanishes when averaged over the initial spin.

The hadronic tensor $W_{\mu\nu}$, however, depends on the internal structure of the nucleon. This tensor can be expressed in a compact form using the completeness of the state $|X\rangle$:

$$\begin{aligned} W_{\mu\nu}(q;P,S) &= \int \frac{d^4P'}{4ME'_p} \sum_X \langle N_S(P)|J_\mu(0)|X(P')\rangle\langle X(P')|J_\nu(0)|N_S(P)\rangle\delta^4(P'-P-q) \\ &= \frac{1}{4\pi M}\langle N_S(P)|J_\mu(0)J_\nu(0)|N_S(P)\rangle(2\pi)^4\delta^4(P'-P-q) \\ &= \frac{1}{4\pi M}\int d^4\xi e^{iq\cdot\xi}\langle N_S(P)|J_\mu(\xi)J_\nu(0)|N_S(P)\rangle, \end{aligned} \tag{2.18}$$

where the last step used the integral representation for the δ function:

$$\delta^4(P'-P-q) = \int \frac{d^4\xi}{(2\pi)^4} e^{-i(P'-P-q)\cdot\xi} \tag{2.19}$$

Analogous to Eq. (2.15), $W_{\mu\nu}(q;P,S)$ can be further decomposed into symmetric (S)

and antisymmetric (A) parts :

$$W_{\mu\nu}(q;P,S) = W^{(S)}_{\mu\nu}(q;P) + i\, W^{(A)}_{\mu\nu}(q;P,S). \tag{2.20}$$

Following the parity conservation and gauge invariance of the electromagnetic probe, the most general form of the $W_{\mu\nu}$ can be expressed as:

$$\begin{aligned} W^{(S)}_{\mu\nu}(q;P) &= W_1(\nu,Q^2)\left[\frac{q_\mu q_\nu}{q^2} - g_{\mu\nu}\right] \\ &+ \frac{W_2(\nu,Q^2)}{M^2}\left[P_\mu - \frac{P\cdot q}{q^2}q_\mu\right]\left[P_\nu - \frac{P\cdot q}{q^2}q_\nu\right], \end{aligned} \tag{2.21}$$

and

$$W^{(A)}_{\mu\nu}(q;P,s) = \varepsilon_{\mu\nu\alpha\beta}\, q^\alpha \left\{ G_1(\nu,Q^2)S^\beta + \frac{G_2(\nu,Q^2)}{M^2}\left[(P\cdot q)S^\beta - (S\cdot q)\, P^\beta\right] \right\}, \tag{2.22}$$

where $S^u = u(\bar{P})\ \gamma^\mu\gamma_5\ u(P)/2M$ is the hadron spin four-vector, $W_{1,2}(\nu,Q^2)$ and $G_{1,2}(\nu,Q^2)$ are four scalar structure functions describing the internal structure of the nucleon.

The structure functions can be experimentally extracted from inclusive electron-nucleon scattering by measuring cross-sections or differences between cross-sections with different polarization orientations of the initial electron and the target nucleon. The details will be discussed below.

2.2.3 Unpolarized Structure Functions

Spin-independent structure functions $W_{1,2}(\nu,Q^2)$, related to the symmetric components of the current tensor, $W^{(S)}_{\mu\nu}$(Eq. 2.21), can be extracted from the unpolarized cross-section:

$$\begin{aligned} \frac{d^2\sigma^{unpol}}{d\Omega\ dE'}(k,P;k') &= \frac{1}{4}\sum_{s,S}\frac{d^2\sigma}{d\Omega\ dE'}(k,s,P,S;k',s') \\ &= \frac{\alpha^2}{q^4}\,\frac{E'}{E}\,2L^{(S)}_{\mu\nu}\,W^{\mu\nu(S)}\,. \end{aligned} \tag{2.23}$$

Substitute Eq. 2.16 and Eq. 2.21 into Eq. 2.23, the unpolarized differential cross section is

$$\begin{aligned}\frac{d^2\sigma_{unpol}}{d\Omega\ dE'} &= \frac{4\alpha^2 E'^2}{q^4}\left[2W_1(\nu,Q^2)\sin^2\frac{\theta}{2} + W_2(\nu,Q^2)\cos^2\frac{\theta}{2}\right] \\ &= (\frac{d\sigma}{d\Omega})_{Mott}\left[2W_1(\nu,Q^2)\tan^2\frac{\theta}{2} + W_2(\nu,Q^2)\right],\end{aligned} \tag{2.24}$$

where $(\frac{d\sigma}{d\Omega})_{Mott} = \frac{4\alpha^2 E'^2\cos^2\frac{\theta}{2}}{q^4}$ is the cross section for scattering an electron off a point-like infinitely heavy target.

2.2.3.1 Structure Functions $F_{1,2}(\nu, Q^2)$

$W_{1,2}(\nu, Q^2)$ are often substituted by two dimensionless structure functions in terms of the Bjorken variable x and the squared four-momentum transfer Q^2:

$$F_1(x,Q^2) = MW_1(\nu,Q^2), \tag{2.25}$$

$$F_2(x,Q^2) = \nu W_2(\nu,Q^2). \tag{2.26}$$

$F_{1,2}(x,Q^2)$ can be projected from the hadronic tensor by operators $P^{\alpha\beta}_{1,2}[2MW_{\alpha\beta}] = F_{1,2}$ with [29]

$$P_1^{\alpha\beta} \equiv \frac{1}{4}\left[\frac{1}{a}P^\alpha P^\beta - g^{\alpha\beta}\right], \tag{2.27}$$

$$P_2^{\alpha\beta} \equiv \frac{3P\cdot q}{4a}\left[\frac{P^\alpha P^\beta}{a} - \frac{1}{3}g^{\alpha\beta}\right], \tag{2.28}$$

and

$$a = \frac{P\cdot q}{2x} + M^2, \tag{2.29}$$

in any reference frame and for arbitrary directions of the nucleon spin four-vector.

The unpolarized differential cross section Eq. 2.24 can then be expressed as

$$\frac{d^2\sigma_{unpol}}{d\Omega\ dE'} = (\frac{d\sigma}{d\Omega})_{Mott}\left[\frac{2}{M}F_1(x,Q^2)\tan^2\frac{\theta}{2} + \frac{1}{\nu}F_2(\nu,Q^2)\right]. \tag{2.30}$$

As mentioned in Sec. 2.1, the study of $F_{1,2}(\nu, Q^2)$ at SLAC provided the first experimental evidence that nucleons are made of point-like spin 1/2 quarks. In the deep inelastic scattering region (typically $W > 2GeV$ and $Q^2 > 1GeV^2$), the structure functions are observed to have weak dependence on Q^2 for a fixed value of x[9], in contrast to the elastic form factors (see Sec. 2.2.3.2) that decrease rapidly with Q^2. This phenomenon is known as Bjorken scaling. Any particle with finite size must have a form factor, so the scaling behavior implies that electrons are scattering off point-like constituents (quark) within the proton.

The limit of Bjorken scaling is defined in the deep inelastic scattering as [30]:

$$\begin{aligned} Q^2 &\rightarrow \infty, \\ \text{and} \ \nu &\rightarrow \infty, \\ \text{with} \ x &= \frac{Q^2}{2M\nu} \ \text{fixed.} \end{aligned} \tag{2.31}$$

In this limit, the Bjorken variable x can be interpreted as the fraction of the total nucleon momentum carried by the stuck quark and the structure functions only depends on x: $F_{1,2}(\nu, Q^2) \rightarrow F_{1,2}(x)$. In other words, the electron nucleon scattering can be viewed as the electron elastically scattering off an asymptotically free quark (parton) that carries a fraction x of the nucleon momentum. This is often referred to as the quark-parton model, to be discussed in more detail in Sec. 2.3.

2.2.3.2 Form Factors $G_{E,M}(Q^2)$

In the kinematic region of elastic scattering, the final nucleon state remains unchanged (in the ground state) but with a finite recoil to absorb the transfer energy and momentum. Hence the invariant mass is equal to the mass of proton. In this case, the scattered electron energy E' is determined by

$$E' = \frac{E}{1 + 2\frac{2E}{M}\sin^2\frac{\theta}{2}}, \tag{2.32}$$

and the energy loss of the electron is

$$\nu = \frac{Q^2}{2M}. \tag{2.33}$$

The structure functions $W_{1,2}(\nu, Q^2)$ are commonly written in the form of electromagnetic Sachs form factors[28]:

$$\begin{aligned} W_1(\nu, Q^2) &= \tau G_M^2(Q^2)\delta(\nu - \frac{Q^2}{2M}), & (2.34)\\ W_2(\nu, Q^2) &= \frac{G_E^2(Q^2) + \tau G_M^2(Q^2)}{1+\tau}\delta(\nu - \frac{Q^2}{2M}), & (2.35)\end{aligned}$$

where $\tau = \frac{Q^2}{4M^2}$. Now one can obtain the Rosenbluth formula[31] for unpolarized elastic scattering:

$$\frac{d^2\sigma_{el}}{d\Omega} = (\frac{d\sigma}{d\Omega})_{Mott}\frac{E'}{E}\left[\frac{G_E^2(Q^2)\cos^2(\frac{\theta}{2}) + \tau G_M^2(Q^2)}{1+\tau} + 2\tau G_M^2(Q^2)\sin^2(\frac{\theta}{2})\right], \tag{2.36}$$

where the factor $\frac{E'}{E}$ comes from the recoil with:

$$\begin{aligned} \delta(\nu - \frac{Q^2}{2M}) &= \delta\left(E - E' - \frac{4EE'\sin^2\frac{\theta}{2}}{2M}\right) \\ &= \frac{E'}{E}\delta\left(E' - \frac{E}{1+\frac{2E}{M}\sin^2\frac{\theta}{2}}\right). \end{aligned} \tag{2.37}$$

The Sachs form factors $G_E(Q^2)$ and $G_M(Q^2)$ must have specific values at $Q^2 = 0$ according to the static properties of the corresponding nucleon[28]:

$$\begin{aligned} G_{Ep}(0) &= 1, & (2.38)\\ G_{Mp}(0) &= \mu_p, & (2.39)\\ G_{En}(0) &= 0, & (2.40)\\ G_{Mn}(0) &= \mu_n, & (2.41)\end{aligned}$$

which means $G_E(0)$, $G_M(0)$ are equal to the electric charge and magnetic momentum with $p(n)$ refers to the proton (neutron), $\mu_p = 2.793$ and $\mu_n = -1.913$ are given in units of nuclear magneton $\mu_N = \frac{e\hbar}{2m_{\rm p}}$.

In the non-relativistic limit, $G_{E,M}(Q^2)$ can be interpreted as the Fourier transformation of charge distribution $\rho_{charge}(r)$ and magnetization distribution $\rho_{magnetic}(r)$. Therefore the elastic scattering cross section allows to map out the extended charge and current distributions inside the nucleon. From Eq. 2.36, one can extract separately the electric and magnetic form factors by measuring the elastic scattering cross sections at fixed Q^2 and different scattering angle.

2.2.4 Polarized Structure Functions

Spin-dependent structure functions $G_{1,2}(\nu, Q^2)$, related to the asymmetric components of the current tensor, $W^{(A)}_{\mu\nu}$(Eq. 2.22), can be measured from the differences of cross-sections with opposite target spins:

$$\begin{aligned}\frac{d^2\sigma^{s,S}}{d\Omega\, dE'} - \frac{d^2\sigma^{s,-S}}{d\Omega\, dE'} &= \frac{d^2\sigma}{d\Omega\, dE'}\,(k,s,P,-S;k') - \frac{d^2\sigma}{d\Omega\, dE'}\,(k,s,P,S;k') \\ &= \frac{\alpha^2}{q^4}\,\frac{E'}{E}\,4L^{(A)}_{\mu\nu}\,W^{\mu\nu(A)}\,.\end{aligned} \tag{2.42}$$

Substitute Eq. 2.17 and Eq. 2.22 into Eq. 2.42, the polarized differential cross section is

$$\begin{aligned}&\frac{d^2\sigma^{s,S}}{d\Omega\, dE'} - \frac{d^2\sigma^{s,-S}}{d\Omega\, dE'} = \frac{8\alpha^2 E'}{q^4 E}\times \\ &\left\{\big[(q\cdot S)(q\cdot s) + Q^2(s\cdot S)\big]\,MG_1(\nu,Q^2) + Q^2\Big[(s\cdot S)(P\cdot q) - (q\cdot S)(P\cdot s)\Big]\frac{G_2(\nu,Q^2)}{M}\right\}.\end{aligned} \tag{2.43}$$

Similar to the definitions of unpolarized structure functions in Eq. 2.25 and Eq. 2.26, $G_{1,2}(\nu, Q^2)$ are often written as dimensionless structure function of Bjorken x and Q^2:

$$g_1(x,Q^2) = M\nu G_1(\nu,Q^2), \tag{2.44}$$

$$g_1(x,Q^2) = \nu^2 G_2(\nu,Q^2). \tag{2.45}$$

The corresponding projection operators are $P_3^{\alpha\beta}[2MW_{\alpha\beta}] = g_1$ and $P_4^{\alpha\beta}[2MW_{\alpha\beta}] = g_1 + g_2$ with [29]

$$P_3^{\alpha\beta} \equiv \frac{(P\cdot q)^2}{bM^2(q\cdot S)}\left[(q\cdot S)S_\lambda + q_\lambda\right] P_\eta \varepsilon^{\alpha\beta\lambda\eta}, \tag{2.46}$$

$$P_4^{\alpha\beta} \equiv \frac{1}{b}\left\{\left[\frac{(P\cdot q)^2}{M^2} + 2(P\cdot q)x\right] S_\lambda + (q\cdot S)q_\lambda\right\} P_\eta \varepsilon^{\alpha\beta\lambda\eta}. \tag{2.47}$$

with

$$b = -4M\left[\frac{(P\cdot q)^2}{M^2} + 2(P\cdot q)x - (q\cdot S)^2\right]. \tag{2.48}$$

Similar to $F_{1,2}(x,Q^2)$, $g_1(x,Q^2)$ are also approximately scaled with Bjorken x at the Bjorken limit:

$$\lim_{Bj} g_1(x,Q^2) = g_1(x), \tag{2.49}$$

$$\lim_{Bj} g_2(x,Q^2) = g_2(x)\,. \tag{2.50}$$

To measure the spin-dependent structure functions $g_{1,2}(x,Q^2)$, one can consider the case where electrons are longitudinally polarized with spin along ($\rightarrow$) or opposite ($\leftarrow$) the direction of motion, while the target nucleons are polarized along (S) or opposite to ($-S$) an arbitrary direction, then Eq. 2.43 becomes:

$$\frac{d^2\sigma^{\rightarrow,S}}{d\Omega\, dE'} - \frac{d^2\sigma^{\rightarrow,-S}}{d\Omega\, dE'} = -\frac{4\alpha^2}{Q^2\nu M}\,\frac{E'}{E}$$
$$\times\left\{[E\cos\alpha + E'\cos\Theta]g_1(x,Q^2) + \frac{2EE'}{\nu}[\cos\Theta - \cos\alpha]\; g_2(x,Q^2)\right\}.$$

where α (Θ) is the angle between the nucleon spin direction $\hat{S}$ and the incident (outgoing) electron momentum $\hat{k}$ ($\hat{k}'$), and ϕ is the azimuthal angle between the $(\hat{k},\hat{k}')$ scattering plane and the $(\hat{k},\hat{S})$ polarization plane, as shown in Fig. 2-2. Then $\cos\Theta$ can be expressed as

$$\cos\Theta = \sin\theta\sin\alpha\cos\phi + \cos\theta\cos\alpha.$$

Hence one can measure the cross section with particular target spin directions to optimize the $g_{1,2}(x, Q^2)$ significance. There are two favorable target spin configurations: longitudinal and transverse, defined respect to the electron momentum.

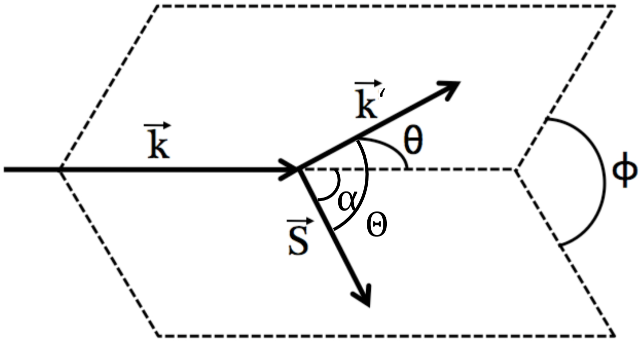

Figure 2-2: Angular Kinematics of polarized electron scattering. The $\vec{k}, \vec{k}'$ are the momentum of incident and outgoing electron, $\vec{S}$ is the target spin direction, θ is the scattering angle and α, ϕ and Θ define the nucleon spin direction.

For the longitudinal configuration, the target nucleon is longitudinally polarized parallel ($\overset{\Rightarrow}{\rightarrow}$ with $\alpha = 0$) or anti-parallel ($\overset{\Leftarrow}{\rightarrow}$ with $\alpha = \pi$) to the incoming electron spin, where $\Rightarrow$ ($\Leftarrow$) denotes the spin direction of target nucleon along (opposite to) the beam direction. In this case, $\Theta = \theta$ and the cross section difference is given by:

$$\begin{aligned}\Delta\sigma_{\parallel} &= \frac{d^2\sigma^{\overset{\Leftarrow}{\rightarrow}}}{d\Omega\, dE'} - \frac{d^2\sigma^{\overset{\Rightarrow}{\rightarrow}}}{d\Omega\, dE'} \\ &= \frac{4\alpha^2 E'}{Q^2 \nu M E} \times \left\{ [E + E' \cos\Theta] g_1(x, Q^2) + \frac{2EE'}{\nu}[\cos\Theta - 1]\ g_2(x, Q^2) \right\} \\ &= \frac{4\alpha^2 E'}{Q^2 \nu M E} \times \left\{ [E + E' \cos\theta] g_1(x, Q^2) - 2Mx\ g_2(x, Q^2) \right\}.\end{aligned} \tag{2.51}$$

It is obvious that the $g_1(x, Q^2)$ is much more accessible than the $g_2(x, Q^2)$ for longitudinal mode at energies of or above a few GeV and at small scattering angle θ.

For the transverse configuration, the polarized electrons scatter off the target nucleon transversely polarized with respect to the electron beam direction. In this case, $\alpha = \pi/2$, $\phi = 0$, and $\Theta = \arccos(\sin\theta)$. The cross section difference is given by:

$$
\begin{aligned}
\Delta\sigma_{\perp} &= \frac{d^2\sigma^{\rightarrow\Uparrow}}{d\Omega\ dE'} - \frac{d^2\sigma^{\rightarrow\Downarrow}}{d\Omega\ dE'} \\
&= \frac{4\alpha^2 E'}{Q^2 \nu M E} \times \left\{ [E' \sin\theta] g_1(x,Q^2) + \frac{2EE'}{\nu} \sin\theta\ g_2(x,Q^2) \right\} \qquad (2.52) \\
&= \frac{4\alpha^2 E'^2}{Q^2 \nu M E}\ \sin\theta \left[g_1(x,Q^2) + \frac{2E}{\nu} g_2(x,Q^2) \right],
\end{aligned}
$$

where $\Downarrow$ ($\Uparrow$) denotes a target spin in the scattering plane, perpendicular to the incident electron momentum and pointing toward (opposite to) the side of the beamline where scattered electrons are detected. One can see that the $g_2(x,Q^2)$ contribution is amplified by a factor of $2E/\nu$ compared with the $g_1(x,Q^2)$. Hence $g_2(x,Q^2)$ is more favorable in the transverse configuration measurement.

If the spin of the initial electron is flipped while keeping the same target spin direction, one can obtain the same results as Eq. 2.51 and Eq. 2.52 when ignoring the parity violation.

In principle, according to Eq. 2.51 and Eq. 2.52, performing two independent cross-section measurements, with longitudinal and transverse target configurations, allows measurements of both $g_1(x,Q^2)$ and $g_2(x,Q^2)$ as

$$
\begin{aligned}
g_1(x,Q^2) &= \frac{MQ^2}{4\alpha^2} \frac{y}{(1-y)(2-y)} \left[\Delta\sigma_{\parallel} + \tan^2\frac{\theta}{2} \Delta\sigma_{\perp} \right], \qquad (2.53) \\
g_2(x,Q^2) &= \frac{MQ^2}{4\alpha^2} \frac{y^2}{2(1-y)(2-y)} \left[-\Delta\sigma_{\parallel} + \frac{1+(1-y)\cos\theta}{(1-y)\sin\theta} \Delta\sigma_{\perp} \right], \qquad (2.54)
\end{aligned}
$$

where $y = \nu/E$.

In practice, rather than measuring the two cross section differences, $\Delta\sigma_{\parallel}$ and $\Delta\sigma_{\perp}$, which can be difficult to measure, one can form the structure functions by measuring asymmetries, in which many experimental limitations and sources of error cancel out. For a longitudinally polarized target, the longitudinal spin asymmetry $A_{\parallel}$ is defined as

$$
A_{\parallel} = \frac{d\sigma^{\stackrel{\leftarrow}{\Rightarrow}} - d\sigma^{\stackrel{\rightarrow}{\Rightarrow}}}{d\sigma^{\stackrel{\leftarrow}{\Leftarrow}} + d\sigma^{\stackrel{\rightarrow}{\Rightarrow}}} = \frac{d\sigma^{\stackrel{\leftarrow}{\Leftarrow}} + d\sigma^{\stackrel{\rightarrow}{\Rightarrow}}}{2d\sigma_0}. \qquad (2.55)
$$

where σ_0 is the unpolarized cross section. Similarly, for a transversely polarized target, one can define the transverse spin asymmetry:

$$A_\perp = \frac{d\sigma^{\leftarrow\Uparrow} - d\sigma^{\rightarrow\Uparrow}}{d\sigma^{\leftarrow\Uparrow} + d\sigma^{\rightarrow\Uparrow}} = \frac{d\sigma^{\leftarrow\Uparrow} - d\sigma^{\rightarrow\Uparrow}}{2d\sigma_0}. \tag{2.56}$$

Then $g_1(x,Q^2)$ and $g_2(x,Q^2)$ can be extracted by measuring longitudinal asymmetry $A_\parallel$, transverse asymmetry $A_\perp$, and the unpolarized cross section:

$$\begin{aligned} g_1(x,Q^2) &= \frac{MQ^2}{4\alpha^2}\frac{y}{(1-y)(2-y)}2\sigma_0\left[A_\parallel + \tan^2\frac{\theta}{2}A_\perp\right], & (2.57)\\ g_2(x,Q^2) &= \frac{MQ^2}{4\alpha^2}\frac{y^2}{2(1-y)(2-y)}2\sigma_0\left[-A_\parallel + \frac{1+(1-y)\cos\theta}{(1-y)\sin\theta}A_\perp\right]. & (2.58)\end{aligned}$$

2.2.5 Virtual Photon-Nucleon Absorption Cross Section

In the above sections, the inclusive inelastic cross sections can be written in terms of structure functions $F_{1,2}$ and $g_{1,2}$. As shown in Fig. 2-1, the main process of scattering occurs with the exchange of a virtual photon by the electron and nucleon. All three particles (electron, virtual photon, and nucleon) in this interaction have spin, and the relative spin direction of each affects the probability of the scattering interaction. In the virtual photon notation, the inclusive inelastic cross section can be written in terms of a virtual photon flux factor and four partial cross sections (σ_L, σ_T, σ_{TT}, σ_{LT})[32]:

$$\frac{d^2\sigma}{d\Omega\, dE'} = \Gamma_V\left[\sigma_T + \epsilon\sigma_L - hP_x\sqrt{2\epsilon(1-\epsilon)}\sigma_{LT} - hP_z\sqrt{1-\epsilon^2}\sigma_{TT}\right], \tag{2.59}$$

where $h = \pm 1$ refers to the helicity state[1] of the longitudinally polarized electron, and P_z (P_x) is the target polarization parallel (perpendicular) to the direction of the virtual photon in the scattering plane of the electron, ϵ is the photon polarization

$$\epsilon = \frac{1}{1+2(1+\nu^2/Q^2)\tan^2(\theta/2)}\ , \tag{2.60}$$

---

[1] Helicity is defined as $\frac{\vec{S}\cdot\vec{P}}{|\vec{S}\cdot\vec{P}|}$.

and the flux factor Γ_V is

$$\Gamma_V = \frac{\alpha E' K}{2\pi^2 E Q^2 (1-\epsilon)} \ , \tag{2.61}$$

with K the "equivalent photon energy". K is convention-dependent and is expressed in Hand's convection[33]:

$$K = \nu(1-x) = \frac{W^2 - M^2}{2M} \ . \tag{2.62}$$

The cross section σ_L (σ_T) arises from the absorption of a longitudinal (transverse) polarized virtual photon while σ_{TT} (σ_{LT}) is the transverse-transverse (longitudinal-transverse) interference terms. For the unpolarized case at the real photon limit $Q^2 = 0$, the total cross section reduces to σ_T since the real photon is only transversely polarized. The two spin-flip (interference) cross sections, σ_{TT} (σ_{LT}), can only be measured by double-polarization experiments.

The partial cross section transverse (spin-averaged) σ_T and transverse-transverse (spin-dependent) interference σ_{TT} can be expressed in terms of helicity dependent cross section $\sigma_{1/2}$ and $\sigma_{3/2}$:

$$\sigma_T = \sigma_{1/2} + \sigma_{3/2}, \tag{2.63}$$

$$\sigma_{TT} = \sigma_{1/2} - \sigma_{3/2}, \tag{2.64}$$

where $\sigma_{1/2}$ and $\sigma_{3/2}$ are corresponding to excitations of intermediate states with spin projections $3/2$ and $1/2$, respectively, as shown in Fig. 2-3.

The four independent virtual-photon absorption cross sections are functions of Q^2 and ν and are related to the structure functions $F_{1,2}$ and $g_{1,2}$ as follows:

$$\begin{aligned}
\sigma_T &= \sigma_{1/2} + \sigma_{3/2} = \frac{4\pi^2\alpha}{MK} F_1, && (2.65)\\
\sigma_L &= \frac{4\pi^2\alpha}{MK} \Big[\frac{1+\gamma^2}{\gamma^2 \nu} F_2 - \frac{1}{M} F_1\Big], && (2.66)\\
\sigma_{TT} &= \sigma_{1/2} - \sigma_{3/2} = \frac{4\pi^2\alpha}{MK} (g_1 - \gamma^2 g_2), \text{ and} && (2.67)\\
\sigma_{LT} &= \frac{4\pi^2\alpha}{MK} \gamma (g_1 + g_2), && (2.68)
\end{aligned}$$

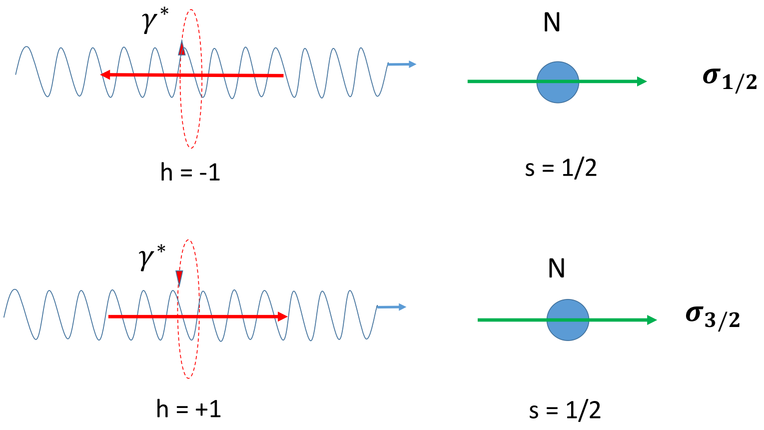

Figure 2-3: Helicity projections for the virtual photo-absorption cross sections $\sigma_{1/2}$ and $\sigma_{3/2}$. The quantities h and s represent the virtual photon helicity and the target spin.

where

$$\gamma = \frac{2Mx}{Q} = \frac{Q}{\nu}\ . \tag{2.69}$$

Two independent virtual photon-nucleon asymmetry, $A_1(x, Q^2)$ and $A_2(x, Q^2)$, can be defined:

$$A_1 = \frac{\sigma_{TT}}{\sigma_T} = \frac{g_1 - \gamma^2 g_2}{F_1}, \tag{2.70}$$

$$A_2 = \frac{\sigma_{LT}}{\sigma_T} = \gamma \left[\frac{g_1 + g_2}{F_1}\right]. \tag{2.71}$$

Likewise, the structure functions can be written as:

$$g_1(x, Q^2) = \frac{F_1(x, Q^2)}{1+\gamma^2}\left[A_1(x, Q^2) + \gamma A_2(x, Q^2)\right], \tag{2.72}$$

$$g_2(x, Q^2) = \frac{F_1(x, Q^2)}{1+\gamma^2}\left[-A_1(x, Q^2) + \frac{A_2(x, Q^2)}{\gamma}\right]. \tag{2.73}$$

If one knows the absorption asymmetries $A_{1,2}(x, Q^2)$ and structure function $F_1(x, Q^2)$, one can extract the $g_2(x, Q^2)$ structure function.

Using the optical theorem, the absorption of the virtual photon by the nucleon can be related to the imaginary part of the forward virtual photon-nucleon scattering amplitudes. More details will be discussed in Sec. 2.6.

2.3 Structure Functions in the Quark-Parton Model

The structure functions $F_{1,2}(x, Q^2)$ and $g_{1,2}(x, Q^2)$ are useful to describe the structure of the nucleon. However, these structure functions alone do not provide us an intuitive picture of the nucleon. In this section, a physical interpretation of these structure functions is presented.

2.3.1 Quark-Parton Model

After the observation of scaling of structure functions, the parton model [34] was proposed by Feynman, which provided a clear physical interpretation. Since the structure functions is Lorentz invariant, the parton model can be formulated in an infinite momentum frame (the scaling limit), where the nucleon is moving close to the speed of light. The interaction time (boosted by a factor $1/\sqrt{1 - v^2/c^2}$) in the nucleon is so long that the nucleon configuration is essentially frozen. On the other hand, in the rest frame, the virtual photon-parton interaction time is of order $1/Q$ which is much shorter than the strong interaction time of order of $1/\Lambda_{QCD}$. Therefore the nucleon can be approximately as a collection of collinear, non-interacting constituents, and each carries a fraction of the nucleon four-momentum. This approximation implies that the electron scattering at Bjorken limit behaves analogously to elastic lepton-lepton scattering as shown in Fig. 2-4. The elementary quark tensor $w_{\mu\nu}(x, q, s)$ is the same as the leptonic tensor $L_{\mu\nu}$, with the replacements $k^\mu \to xP^\mu$, $k'^\mu \to xP^\mu + q^\mu$ and multiplied the square of charge q_i^2 of quark i:

$$w_{\mu\nu}(x, q, s) = q_i^2 \, [w^{(S)}_{\mu\nu}(x, q) + i w^{(A)}_{\mu\nu}(x, q, s)] \tag{2.74}$$

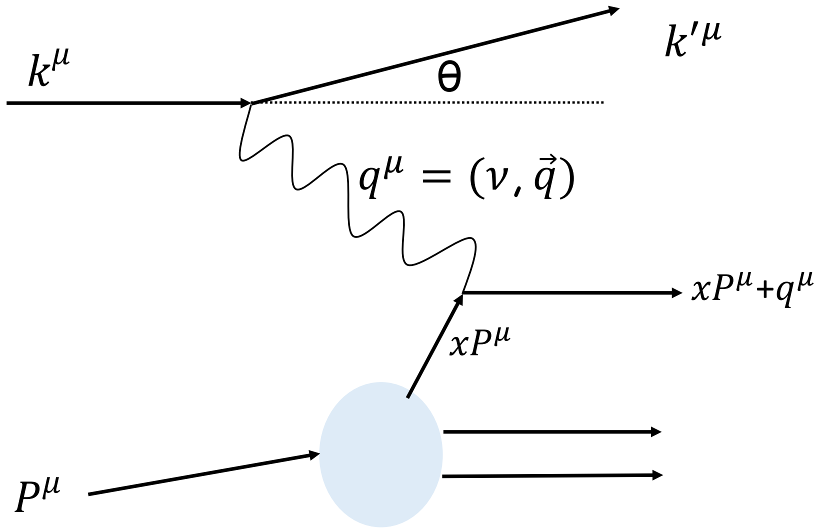

Figure 2-4: Parton model description of electron-nucleon scattering.

with

$$w^{(S)}_{\mu\nu}(x,q) = 2\,[2x^2 P_\mu P_\nu + xP_\mu q_\nu + xq_\mu P_\nu - x(P\cdot q)g^{\mu\nu}], \tag{2.75}$$

$$w^{(A)}_{\mu\nu}(x,q,s) = -2m_i\;\varepsilon_{\mu\nu\alpha\beta}\;s^\alpha q^\beta, \tag{2.76}$$

where s is the spin of the struct quark and its mass is $m_i = xM$ for consistency. The electron scattering cross section is the sum of the incoherent sum of all cross sections of the individual quarks and antiquarks. Define $n_i(x', s; S)$ as the number density of quark i which carries four-momentum fraction x', the hadronic tensor, Eq. 2.18, becomes[35]:

$$\begin{aligned} W_{\mu\nu}(q;P,S) &= W^{(S)}_{\mu\nu}(q;P) + iW^{(A)}_{\mu\nu}(q;P,S) \\ &= \sum_{i,s} q_i^2\,\frac{1}{M}\frac{1}{2P\cdot q}\int_0^1 \frac{dx'}{x'}\;\delta(x'-x)\;n_q(x',s;S)\;w_{\mu\nu}(x',q,s)\,, \end{aligned} \tag{2.77}$$

where the extra factor $1/x'$ is due to the normalisation converting from the parton flux to the the proton flux. Substitute Eq. 2.74 and Eq. 2.75, Eq. 2.77 can be written as

$$
\begin{aligned}
&W_{\mu\nu}(q;P,S) = W^{(S)}_{\mu\nu}(q;P) + iW^{(A)}_{\mu\nu}(q;P,S) \\
&= \sum_{i,s} e_i^2 \, \frac{1}{2MxP\cdot q}\left\{\left[2x^2P_\mu P_\nu + xP_\mu q_\nu + xq_\mu P_\nu - x(P\cdot q)g^{\mu\nu}\right] + i[-2m_i \, \varepsilon_{\mu\nu\alpha\beta} \, s^\alpha q^\beta]\right\}.
\end{aligned}
\tag{2.78}
$$

By applying the structure function projection operators $P^{\alpha\beta}_{1,2,3,4}$ discussed in Sec. 2.2.3.1 and Sec. 2.2.4, one can obtain the well known "naive" Parton Model predictions for the unpolarized nucleon structure functions:

$$
F_1(x) = \frac{1}{2}\sum_i q_i^2 \; q_i(x), \text{and} \tag{2.79}
$$

$$
F_2(x) = x\sum_i q_i^2 \; q_i(x) = 2xF_1(x)\,, \tag{2.80}
$$

and the polarized nucleon structure functions:

$$
g_1(x) = \frac{1}{2}\sum_i e_i^2 \; \Delta q_i(x), \tag{2.81}
$$

$$
g_2(x) = 0, \tag{2.82}
$$

where $q_i^\uparrow(x)$ and $q_i^\downarrow(x)$ are the number of density of quark i that carries the fraction x of the momentum of nucleon with spin aligned and anti-aligned to the nucleon spin direction, respectively. $q_i(x) = q_i^\uparrow(x) + q_i^\downarrow(x)$ is the unpolarized quark number densities of quark i while $\Delta q_i(x) = q_i^\uparrow(x) - q_i^\downarrow(x)$ the polarized quark number densities.

In this naive quark-parton model, the quark transverse momentum (relative to the nucleon spin direction) and the interaction between the struck quark and gluons is ignored. Any quantities originated from such process, such as g_2, have no simple interpretation.

2.3.2 Scaling Violation

The scaling of structure functions is only exact in the Bjorken limit. In fact, at finite Q^2, the photon exchange, shown in Fig. 2-1, is only the major process through which the electron interacts with the hadronic matter. Other higher-order processes, such as soft gluon radiations, cannot be separated from the single-photon exchange in reality and also contribute to the cross section. Fig. 2-5 shows the leading order process of gluon radiation, in which either the incident quark or scattered quark emits a gluon. By renormalizing the gluon radiations, the calculated cross section shows a logarithmic dependence on Q^2. Fig. 2-6 shows the experimental Q^2-dependence of proton structure function F_2^p[36]. At large value of x, F_2^p decreases as Q^2 increases, which indicates the larger probability that the exchanged photon probes a quark that has radiated a gluon. However, the trend is opposite at small values of x, which means that the higher probing energy (the better spatial resolution), the larger distribution of low x quarks and anti-quarks are found. These low x distributions are originated from the very gluons that were radiated at high x.

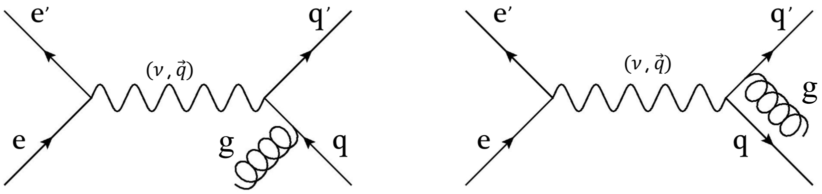

Figure 2-5: Angular Kinematics of polarized electron scattering.

The variation of the structure functions with Q^2 is referred as QCD evolution. The expression of structure functions can be generalized to have a Q^2 dependence:

$$F_1(x) = \frac{1}{2}\sum_i e_i^2\, q_i(x,Q^2) = \frac{1}{2}\sum_i e_i^2 \left[q_i^{\uparrow}(x,Q^2) + q_i^{\downarrow}(x,Q^2)\right] \quad (2.83)$$

$$g_1(x) = \frac{1}{2}\sum_i e_i^2\, \Delta q_i(x,Q^2) = \frac{1}{2}\sum_i e_i^2 \left[q_i^{\uparrow}(x,Q^2) - q_i^{\downarrow}(x,Q^2)\right] \quad (2.84)$$

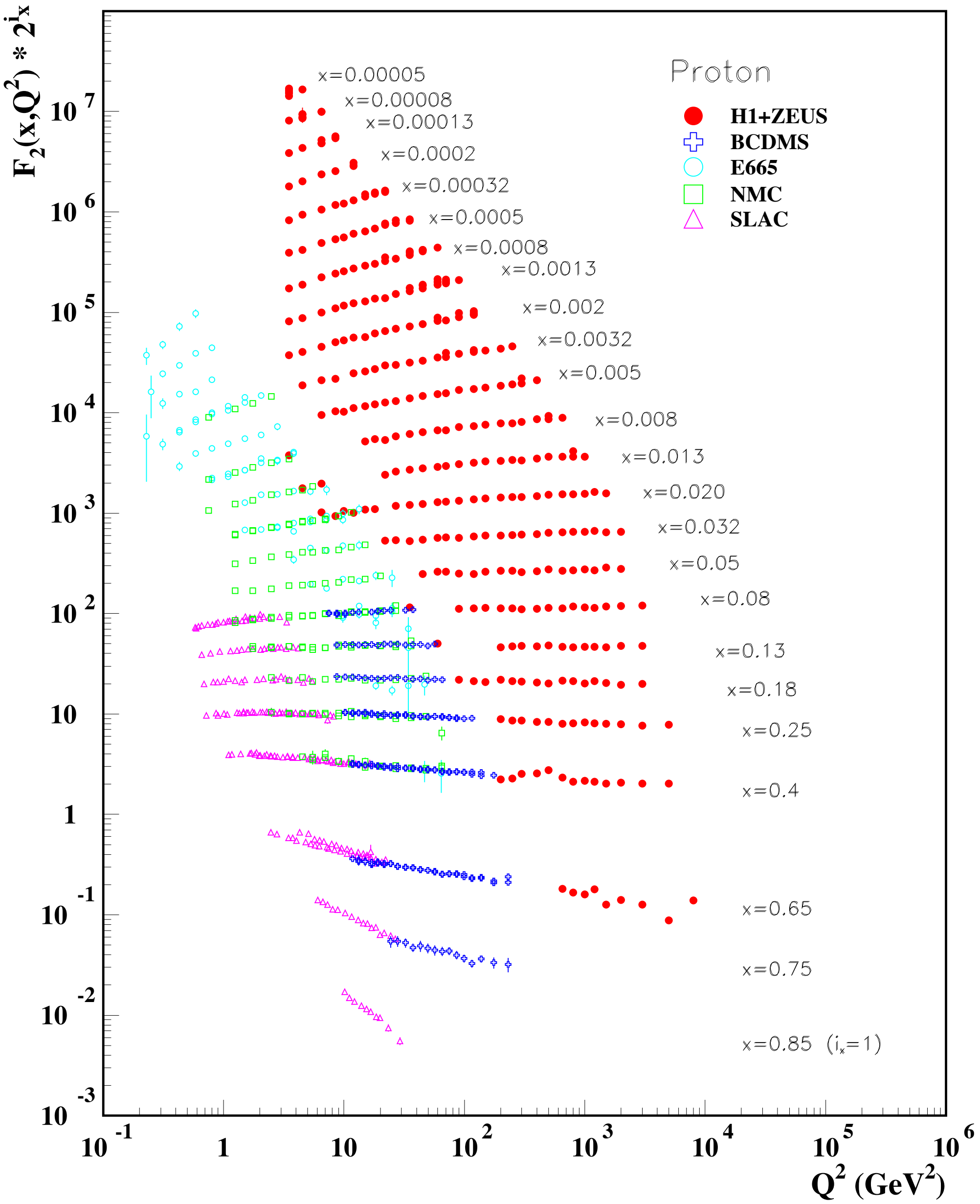

Figure 2-6: The proton structure function F_2^p measured in electromagnetic scattering of electrons and positrons off protons (collider experiments H1 and ZEUS for $Q^2 \geq 2GeV^2$) and for electrons (SLAC) and muons (BCDMS, E665, NMC) on a fixed target. The data are plotted as a function of Q^2 in bins of fixed x. For the purpose of plotting, F_2^p has been multiplied by 2^{i_x}, where i_x is the number of the x bin, ranging from $i_x = 1$ ($x = 0.85$) to $i_x = 24$ ($x = 0.00005$). Plot reproduced from [36].

where $q_i^{\uparrow}(x)$ and $q_i^{\downarrow}(x)$ are the number of density of quark i that carry fraction x of the momentum of nucleon with spin aligned and anti-aligned to the nucleon spin direction, respectively, when viewed by the probe with a resolution $\sim 1/\sqrt{Q^2}$.

The Q^2-evolution of the parton distributions can be calculated in pQCD by the DGLAP equations developed by Dokshitzer[37], Gribov, Lipatov[38], Altarelli and Parisi [39]. Once the parton distributions are known at one particular scale, they can be calculated at any other scale where QCD is applicable.

2.4 g_2 in Operator Product Expansion

From the discussion in Sec. 2.3.1, the spin-dependent structure function g_2, unlike g_1 and $F_{1,2}$, does not have an intuitive interpretation in the simple quark-parton model. At finite Q^2, the scaling of structure functions is only a good approximation. A different theoretical frame is needed to calculate the cross section and to understand the nucleon structure properly. In this section, the operator product expansion (OPE) method will be discussed.

2.4.1 Operator Product Expansion

The OPE method was introduced by K. Wilson in 1969[40] to conduct non-perturbative calculations of the quantum field theory (QFT). It has no model dependence and its main results, such as sum rules, can be derived using general results from quantum field theory. The OPE method separates the perturbative part of the product of two operators $\mathcal{O}_a(\xi)\mathcal{O}_b(0)$ from the non-perturbative part by expansion in local operators as the four dimensional spatial vector $\xi \to 0$[41]:

$$\lim_{\xi \to 0} \mathcal{O}_a(\xi)\mathcal{O}_b(0) = \sum_k c_{abk}(\xi)\mathcal{O}_k(0), \tag{2.85}$$

where the Wilson coefficient $c_{abk}(\xi)$, containing all the spatial information, can be calculated perturbatively, because the coupling constant is small at short distances d in QCD. All non-perturbative effects occur at scales which are much larger than ξ, and thus do not affect the computation of the coefficient functions.

OPE can also be applied in the momentum space. In the limit that $q \to \infty$, the

Fourier transform of Eq. 2.85 forces $\xi \to 0$. The operator product can be expressed with q-dependent coefficient functions[41]:

$$\lim_{q\to\infty} \int d^4\xi \, e^{iq\cdot\xi} \mathcal{O}_a(\xi)\mathcal{O}_b(0) = \sum_k c_{abk}(q)\mathcal{O}_k(0). \tag{2.86}$$

This expansion is valid for all matrix elements of QCD provided q is much larger than the characteristic scale Λ_{QCD}. Recall that the inclusive electron scattering cross section $d\sigma \approx L^{\mu\nu}W_{\mu\nu}$ with the hadronic tensor:

$$W_{\mu\nu}(q; P, S) = \frac{1}{4\pi M} \int d^4\xi e^{iq\cdot\xi} \langle N_S(P)|J_\mu(\xi)J_\nu(0)|N_S(P)\rangle, \tag{2.87}$$

Eq. 2.86 can be applied to the current product $J_\mu(\xi)J_\nu(0)$ by using quark and gluon operators with dimension D and spin n (For quark field, $D = 3/2$ and $n = 1/2$, while for gluon field tensor, $D = 2$, $n = 1$). The contribution of any operator to the cross section is of order:

$$(P\cdot q)^n (\frac{M}{Q})^{D-2-n} = (P\cdot q)^n (\frac{M}{Q})^{\tau-2} \tag{2.88}$$

where the twist τ is defined as

$$\text{twist} = \tau = D - n = \text{dimension} - \text{spin}. \tag{2.89}$$

Since any gauge invariant operator contains at least two quark fields or two gluon field tensors, the lowest twist is 2. From Eq. 2.88, at high Q^2, the most important operators in OPE are those with the lowest possible twist since each additional unit of τ produces a factor of order M/Q, while higher twists are expected to be important and are not ignorable at low Q^2. The parton model discussed in Sec. 2.3.1 can also be related to OPE. Its reliable part can be mapped onto the OPE's leading twist part corresponding to scattering off asymptotically free quarks[42], while OPE's other twist contributions, with no interpretation in the simple parton model, arise from quark-gluon correlations and non-zero quark masses. Higher-twist processes can be described in terms of coherent parton scattering in which more than one parton from a particular hadron participates[43].

2.4.2 g_2 Intepretation

From Sec. 2.4.1, g_2 can be related to hadronic matrix elements of current operators in OPE. The twist expansion leads to the well-known Cornwall-Norton (CN) moments[44]:

$$\int_0^1 x^{n-1} g_1(x,Q^2)dx = \frac{1}{2}a_{n-1} \quad \text{for} \quad n=1,3,5, \tag{2.90}$$

$$\int_0^1 x^{n-1} g_2(x,Q^2)dx = \frac{n-1}{2n}(d_{n-1}-a_{n-1}) \quad \text{for} \quad n=3,5, \tag{2.91}$$

where a_{n-1} and d_{n-1} are matrix elements of the quark and gluon operators for twist-2 and twist-3, respectively, and the contribution from higher twist are ignored. The fact that there exist expansions only over n-odd integers is due to the structure function's symmetry under charge conjugation. Up to twist-3, g_1 receives the twist-2 operators only, whereas g_2 receives contribution from both twist-2 and twist-3 operators.

Combine Eq. 2.90 and Eq. 2.91 together, the leading twist term is canceled:

$$\int_0^1 x^{n-1}\left[g_1(x,Q^2)+\frac{n}{n-1}g_2(x,Q^2)\right]dx = \frac{d_{n-1}}{2}, \quad \text{for n = 3,5.} \tag{2.92}$$

Assume the twist-3 contribution is negligible compared to that of twist-2, Eq.. 2.92 becomes:

$$\int_0^1 x^{n-1}\left[g_1(x,Q^2)+g_2(x,Q^2)\right]dx = \frac{1}{n}\int_0^1 x^{n-1}g_1(x,Q^2). \tag{2.93}$$

By applying the Mellin transforms to Eq. 2.93[45], one can obtain the Wandzura-Wilczek relation[46]:

$$g_2^{ww} = g_2(x,Q^2) = -g_1(x,Q^2) + \int_x^1 \frac{dy}{y} g_1(y,Q^2),, \tag{2.94}$$

where g_2^{ww} is denoted to ignore the higher twists. This relation shows that the leading twist part g_2^{ww} is determined completely by g_1 and can be interpreted in the parton model.

Now the $g_2(x, Q^2)$ can be separated into two components up to twist-3: a twist-2 part, g_2^{ww}, and a mixed twist part, $\bar{g}_2(x, Q^2)$:

$$g_2(x, Q^2) = g_2^{ww}(x, Q^2) + \bar{g}_2(x, Q^2) \tag{2.95}$$

with the $\bar{g}_2(x, Q^2)$ term

$$\bar{g}_2(x, Q^2) = -\int_x^1 \frac{\partial}{\partial y}\left[\frac{m}{M} h_T(y, Q^2) + \xi(y, Q^2)\right]\frac{dy}{y}. \tag{2.96}$$

where $h_T(x, Q^2)$ is a leading twist-2 term arises from transversely polarized quark distributions and is suppressed by the smallness of the quark mass and $\xi(x, Q^2)$ is a twist-3 contribution due to the quark-gluon interactions within a nucleon.

The physical interpretation of twist-3 contribution of g_2 can be understood from the virtual Compton scattering (g_2 is the imaginary part of the spin-dependent Compton amplitude, see Sec. 2.2.5 and Sec. 2.6):

$$\gamma^*(+1) + N(1/2) \to \gamma^*(0) + N(-1/2), \tag{2.97}$$

where γ^* and N represent the virtual photon and nucleon respectively, and the corresponding helicity is labeled in the parentheses. As one can see, the process 2.97 involves a t-channel helicity change, and this change must be carried by the intermediate parton when factorized in terms of parton subprocesses. However, for a massless fermion, the helicity is conserved in the electromagnetic interaction. In QCD, the required helicity exchange is allowed in two ways. One way is through single quark scattering in which the quark carries one unit of orbital angular momentum through its transverse momentum, the other is through quark scattering with an additional transversely-polarized gluon from the nucleon target[43]. Fig. 2-7 illustrates the two helicity exchanges allowed in the virtual Compton scattering process. The left plot of Fig. 2-7 shows the first helicity exchange process where scattering takes place on a single quark (twist-2 contribution), while the right plot shows the second helicity exchange when scattering involves a quark and gluon (twist-3 contribution).

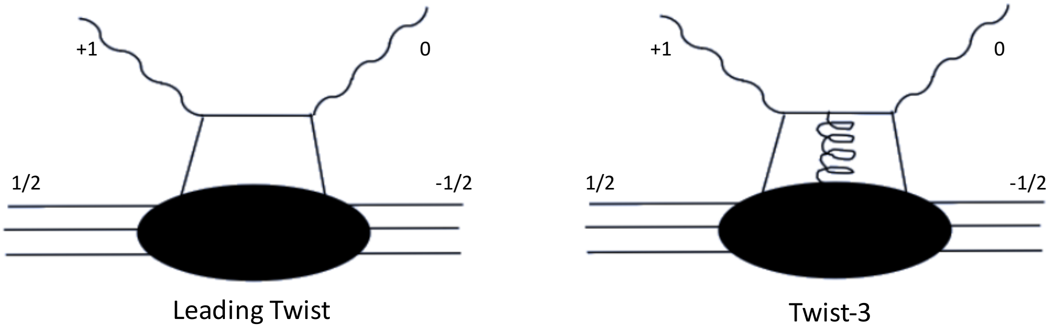

Figure 2-7: Twist-two and twist-three contributions to virtual Compton scattering.

The higher twist corrections increase at low energy with $\frac{1}{Q^{\tau}}$, reflecting the confinement of nucleon. Hence a full understanding of the interaction among nucleon constituents must be studied by looking into contributions beyond the leading twist. At typical JLab kinematics, g_2 is strongly deviated from the the leading twist behavior described by the Wandzura-Wilczek relation[47, 48]. Therefore, the measurement of g_2 provides a clean and direct way to study the higher-twist correlations among partons (quarks and gluons), opening a unique window on the confinement of quarks and gluons inside the nucleon.

2.5 Chiral Perturbation Theory

In Sec. 2.4.1, the Operator Product Expansion (OPE) is introduced to calculate the cross section at finite Q^2. However, it will fail at low Q^2 because the twist expansion breaks down. At low Q^2, the strong coupling constant α_s becomes large (an order of 1), and the relevant degrees of freedom in QCD are no longer the elementary of quarks and gluons. An effective theory known as chiral perturbation theory (χPT)[28, 49], based on the hadronic degree of freedom, allows us to study QCD in the low-energy regime.

QCD is a non–abelian gauge theory of strong interaction between colored quarks and gluons. The complete QCD Lagrangian is[50]

$$\mathcal{L}_{\mathrm{QCD}} = \sum_{f=\substack{u,d,s,\\ c,b,t}} \bar{q}_f (i\not{D} - m_f) q_f - \frac{1}{4}\mathcal{G}_{\mu\nu,a}\mathcal{G}^{\mu\nu}_{a}, \tag{2.98}$$

where g is the coupling constant (g=$\sqrt{4\pi\alpha_s}$), $G_{\mu\nu}$ is the strength of the gluon field, q is the quark spinor and m_f is the quark mass of flavor f. At an energy of $\sim$ 1GeV, the absolute values of running quark masses of u, d, s quark ($m_u \simeq 5$ MeV, $m_d \simeq 9$ MeV, $m_s \simeq 175$ MeV) are small compared to the typical light hadronic mass like the ρ meson (770 MeV) or the proton (938 MeV). For a massless fermion, the chirality is identical to the particle's helicity $h = \frac{\vec{\sigma}\cdot\vec{p}}{|\vec{\sigma}\cdot\vec{p}|}$. And the left and right-handed quark wavefunctions are written as:

$$q_L = \frac{1}{2}(1-\gamma_5)\, q, \tag{2.99}$$

$$q_R = \frac{1}{2}(1+\gamma_5)\, q. \tag{2.100}$$

Consider the limit of light quark mass $m_{u,d,s} \approx 0$, the left-handed and right-handed quark fields are decoupled from each other in the QCD Lagrangian as[51]:

$$\mathcal{L}^{0}_{\mathrm{QCD}} = \sum_{l=u,d,s} (\bar{q}_{R,l} i\not{D}\, q_{R,l} + \bar{q}_{L,l} i\not{D}\, q_{L,l}) - \frac{1}{4}\mathcal{G}_{\mu\nu,a}\mathcal{G}^{\mu\nu}_{a}. \tag{2.101}$$

which means the left and right handed quarks do not interact with each other. Hence the whole theory admits an $SU(3) \times SU(3)$ symmetry and the invariance of the Lagrangian under this group is referred to as the chiral symmetry.

However, the ground state of QCD does not have the full symmetry. Otherwise each hadron would have a partner of the same mass but opposite parity. In fact, the chiral symmetry is spontaneously broken down to the vectorial subgroup $SU(3)_V$ with the appearance of 8 massless pseudoscalar mesons, the Goldstone bosons[52]. In nature, these Goldstone bosons are not exactly massless but acquire a small mass due to the explicit symmetry breaking from the quark masses, $M_P^2 \sim \mathcal{M}$, where P is a generic symbol for the pions ($\pi^{\pm}$, π^0), the kaons ($K^{\pm}$, $\bar{K}^0$, K^0) and the eta (η). From the hadron spectrum $M_\eta \simeq M_K \gg M_\pi$, one can immediately conclude that $m_s \gg m_d \simeq m_u$ since the pions do not contain any strange quarks.

At the low energy limit, the effective χPT Lagrangian can be constructed as:

$$\mathcal{L}_{QCD} = \mathcal{L}^0_{QCD} + \mathcal{L}^p_{QCD}, \tag{2.102}$$

where $\mathcal{L}^0_{QCD}$ is the chiral symmetric part and the symmetry breaking part:

$$\mathcal{L}^p_{QCD} = -\bar{q}\mathcal{M}q \tag{2.103}$$

can be treated as a χPT perturbation. The effective Lagrangian systematically incorporates the symmetries and symmetry breaking patterns of the fundamental theory of QCD. The degrees of freedom are the Goldstone bosons.

The χPT expansion should be represented the same low energy expansion as QCD itself. A power series expansion in terms of small mass or momentum of the interacting particles, is typically performed for any matrix element or amplitude derived from the effective χPT Lagrangian. The convergence radius is expected limited, and can be tested by the measurement of quantities calculable in χPT.

χPT calculations can be also applied to baryons, however, there is a complication that the baryon mass does not vanish in the chiral limit and adds a new scale to the theory[53]. Therefore there is no guarantee that the small momentum expansion holds an exact one-to-one relation to one-loop graphs. Theorists have considered two main approaches for dealing with this complication: Heavy Baryon χPT (HBχPT) and Relativistic Baryon χPT (RBχPT). In the HBχPT approach, the baryons are considered as very heavy and allows for a consistent power counting scheme as an expansion in the inverse powers of the baryon mass[54, 55]; while RBχPT is a relativistically invariant formulation and involves infrared regularization that the regular part can be absorbed into low-energy constants of the effective Lagrangian, whereas the chiral expansion of the infrared part leads to the non-trivial momentum and quark-mass dependences of χPT[56].

Both HBχPT and RBχPT have been used to study the spin-dependent structure functions and their moments, and polarizablity sum rules[57, 58, 59, 60]. These moments and spin polarizability will be discussed in Sec. 2.6.

2.6 Sum rules and Moments

In previous sections, four structure functions $F_{1,2}(x, Q^2)$ and $g_{1,2}(x, Q^2)$ are introduced to describe the internal structure of the nucleon. While the fundamental theoretical tools, such as lattice QCD and chiral perturbation theory, can not calculate the complete structure functions directly, they can be used to provide calculations of moments of structure functions, and polarizability sum rules which relate the moments of the spin structure functions to real or virtual Compton scattering amplitudes. These moments and sum rules provide good opportunities to test theoretical predictions and study fundamental properties of the nucleon.

The absorption of the virtual photon ($\gamma^* N \rightarrow X$) in the inclusive electron scattering can be related to the doubly virtual photon-nucleon Compton scattering (VVCS) (with a virtual photon $q = q'$ and $q^2 = -Q^2 < 0$). Actually, the hadronic tensor $W_{\mu\nu}(q; P, S)$ in Eq. 2.18 is proportional to the forward virtual Compton tensor[28]

$$T_{\mu\nu}(q, P; q, P) = \imath \int d^4\xi e^{iq\cdot\xi} \langle N(P)|\mathcal{T} J_\mu(\xi) J_\nu(0)|S(P)\rangle \tag{2.104}$$

by

$$W_{\mu\nu}(q; P, S) = \frac{1}{2\pi M} \text{Im } T_{\mu\nu}(q, P; q, P), \tag{2.105}$$

where $\mathcal{T}$ in Eq. 2.104 is the time ordering operator. Similarly to the case of hadronic tensor in Eq. 2.20, the Compton tensor is constructed with the most general form that satisfies parity conservation and gauge invariance:

$$\begin{aligned}T_{\mu\nu}(q,P;q,P) = \left(-g^{\mu\nu} + \frac{q^\mu q^\nu}{q^2}\right) T_1(\nu,\, Q^2) \\ + \frac{1}{P\cdot q}\left(P^\mu - \frac{P\cdot q}{q^2}\, q^\mu\right)\left(P^\nu - \frac{P\cdot q}{q^2}\, q^\nu\right) T_2(\nu,\, Q^2) \\ + \frac{i}{M}\,\epsilon^{\mu\nu\alpha\beta}\, q_\alpha S_\beta\, S_1(\nu,\, Q^2) \\ + \frac{i}{M^3}\,\epsilon^{\mu\nu\alpha\beta}\, q_\alpha\,(P\cdot q\; S_\beta - S\cdot q\; p_\beta)\; S_2(\nu,\, Q^2),\end{aligned} \quad (2.106)$$

where all four terms T_1, T_2, S_1 and S_2 have the same dimension of mass and is co-variant under Lorentz transform. S_1 and S_2 are spin-dependent Compton amplitudes and can be expressed in terms of two other commonly used VVCS amplitudes g_{TT} and g_{LT}:

$$S_1(\nu,\, Q^2) \;=\; \frac{\nu\, M}{\nu^2 + Q^2}\left(g_{TT}(\nu,\, Q^2) + \frac{Q}{\nu}\, g_{LT}(\nu,\, Q^2)\right) \quad (2.107)$$

$$S_2(\nu,\, Q^2) \;=\; -\frac{M^2}{\nu^2 + Q^2}\left(g_{TT}(\nu,\, Q^2) - \frac{\nu}{Q}\, g_{LT}(\nu,\, Q^2)\right), \quad (2.108)$$

where the imaginary part of amplitude g_{TT} and g_{LT} directly relate to the photo-absorption cross section by optical theorem as follows:

$$\mathrm{Im}\; g_{TT}(\nu,\, Q^2) \;=\; \frac{K}{4\pi}\sigma_{TT}(\nu,\, Q^2), \quad (2.109)$$

$$\mathrm{Im}\; g_{LT}(\nu,\, Q^2) \;=\; \frac{K}{4\pi}\sigma_{LT}(\nu,\, Q^2). \quad (2.110)$$

Apply Eq. 2.109 and Eq. 2.110 into Eq. 2.107 and Eq. 2.108, one obtains:

$$\mathrm{Im}\; S_1(\nu,\, Q^2) \;=\; \frac{\nu\, M}{\nu^2 + Q^2}\,\frac{K}{4\pi}\left(\sigma_{TT} + \frac{Q}{\nu}\,\sigma_{LT}\right) = \frac{e^2}{4M}\,\frac{M}{\nu}\, g_1(\nu,\, Q^2) \quad (2.111)$$

$$\mathrm{Im}\; S_2(\nu,\, Q^2) \;=\; -\frac{M^2}{\nu^2 + Q^2}\,\frac{K}{4\pi}\left(\sigma_{TT} - \frac{\nu}{Q}\,\sigma_{LT}\right) = \frac{e^2}{4M}\,\frac{M^2}{\nu^2}\, g_2(\nu,\, Q^2) \quad (2.112)$$

In the following sections, three g_2 related sum rule – Burkhardt-Cottingham sum rule, generalized forward spin polarizability γ_0 and transverse-longitudinal polarizability δ_{LT} – will be discussed.

2.6.1 Burkhardt-Cottingham Sum Rule

The spin-dependent VVCS amplitude S_2 is odd in ν, which leads to the unsubtracted dispersion relation:

$$\begin{aligned}\mathrm{Re}\ S_2(\nu,\, Q^2) &= \frac{2\nu}{\pi}\,\mathcal{P}\int_0^\infty \frac{\mathrm{Im}\ S_2(\nu',\, Q^2)}{\nu'^2-\nu^2}\,d\nu' \\ &= \mathrm{Re}\ S_2^{\mathrm{pole}} + \frac{2\nu}{\pi}\,\mathcal{P}\int_{\nu_0}^\infty \frac{\mathrm{Im}\ S_2(\nu',\, Q^2)}{\nu'^2-\nu^2}\,d\nu'\,, \end{aligned} \tag{2.113}$$

where the pole part Re S_2^{pole} is elastic contribution, $\mathcal{P}$ denotes the principle value integral, ν_0 is the pion-production threshold of the nucleon. If assume S_2 at high energy follows

$$S_2(\nu, Q^2) \to \nu^{\alpha_2}\,, \qquad \text{for } \ \nu\to\infty\,, \qquad \text{with } \ \alpha_2 < -1\,, \tag{2.114}$$

the unsubtracted dispersion relation can be also applied for the amplitude $\nu\, S_2$, which is even in ν:

$$\begin{aligned}\mathrm{Re}\ (\nu\, S_2(\nu,\, Q^2)) &= \frac{2}{\pi}\,\mathcal{P}\int_0^\infty \frac{\nu'^2\mathrm{Im}\ S_2(\nu,\, Q^2)}{\nu'^2-\nu^2}\,d\nu' \\ &= \mathrm{Re}\ (\nu\, S_2)^{\mathrm{pole}} + \frac{2}{\pi}\,\mathcal{P}\int_{\nu_0}^\infty \frac{\nu'^2\mathrm{Im}\ S_2(\nu,\, Q^2)}{\nu'^2-\nu^2}\,d\nu'\,. \end{aligned} \tag{2.115}$$

Compare Eq. 2.115 with $\nu\times$Eq. 2.113, one obtains the "superconvergence relation" for *any* value of Q^2:

$$0 = \int_0^\infty \mathrm{Im}\ S_2(\nu,\, Q^2)\, d\nu\ . \tag{2.116}$$

From Eq. 2.112, one can rewrite Eq. 2.116 as the integral of $g_2(x,\, Q^2)$ structure function at a fixed Q^2:

$$0 = \int_0^1 dx\, g_2\,(x,\, Q^2)\,. \tag{2.117}$$

Eq. 2.116 (or Eq. 2.117) is the well known Burkhardt-Cottingham (BC) sum rule[61] and is valid for *any* value of Q^2 and could be violated if either of the following two circumstances happens[62]:

- g_2 is singular enough that the integral $\int_0^1 dx\, g_2\,(x,\, Q^2)$ does not exist.
- g_2 has a delta function singularity at $x = 0$.

A direct test of the BC sum rule can be performed either in the DIS region (high Q^2) or the low-energy region (low Q^2). It should be pointed out that BC sum rule is not from OPE since OPE does not include the $n = 1$ term of the g_2 expansion in Eq. 2.91.

2.6.2 Generalized Spin Polarizability γ_0 and δ_{LT}

The generalized forward spin polarizability γ_0 and and longitudinal-transverse polarizability δ_{LT} describe a relation between the nucleon structure functions and virtual Compton amplitudes, and are powerful tools to study fundamental properties of the nucleon structure and to test theoretical predictions from QCD. Similar to the magnetic or electric polarizability which describes the nucleon response to the electromagnetic field, the spin polarizability characterizes the nucleon spin's response to the field from the virtual photon[63]. The spin polarizability sum rules can be determined using dispersion relations and the optical theorem.

The spin-flip VVCS amplitude $g_{TT}(\nu, Q^2)$, which is odd in ν, can be applied with unsubtracted dispersion relation when assuming an appropriate high-energy converge behavior:

$$\mathrm{Re}[g_{TT}(\nu, Q^2) - g_{TT}^{\mathrm{pole}}(\nu, Q^2)] = (\frac{\nu}{2\pi^2})\mathcal{P}\int_{\nu_0}^{\infty} \frac{K(\nu', Q^2)\sigma_{TT}(\nu', Q^2)}{\nu'^2 - \nu^2} d\nu', \tag{2.118}$$

where g_{TT}^{pole} is the nucleon pole (elastic) contribution and K is the virtual photon flux factor. Expand Eq. 2.118 at low energy, one obtain:

$$\mathrm{Re}\; g_{TT}(\nu,\, Q^2) - \mathrm{Re}\; g_{TT}^{\mathrm{pole}}(\nu,\, Q^2) = \left(\frac{2\alpha}{M^2}\right) I_A(Q^2)\nu + \gamma_0(Q^2)\nu^3 + \mathcal{O}(\nu^5)\,. \tag{2.119}$$

The $\mathcal{O}(\nu)$ term in Eq. 2.118 leads to a generalization of the GDH sum rule[64]:

$$
\begin{aligned}
I_A(Q^2) &= \frac{M^2}{\pi\, e^2} \int_{\nu_0}^{\infty} \frac{K(\nu, Q^2)}{\nu} \frac{\sigma_{TT}\,(\nu,\, Q^2)}{\nu}\, d\nu, \\
&= \frac{2\, M^2}{Q^2} \int_0^{x_0} dx \left\{ g_1\,(x,\, Q^2) - \frac{4M^2}{Q^2}\, x^2\, g_2\,(x,\, Q^2) \right\}\,, \qquad (2.120)
\end{aligned}
$$

while the $\mathcal{O}(\nu^3)$ term yields the generalizated forward spin polarizability:

$$
\begin{aligned}
\gamma_0\,(Q^2) &= \frac{1}{2\pi^2} \int_{\nu_0}^{\infty} \frac{K(\nu, Q^2)}{\nu}\, \frac{\sigma_{TT}\,(\nu,\, Q^2)}{\nu^3}\, d\nu \\
&= \frac{e^2\, 4M^2}{\pi\, Q^6} \int_0^{x_0} dx\, x^2 \left\{ g_1\,(x,\, Q^2) - \frac{4M^2}{Q^2}\, x^2\, g_2\,(x,\, Q^2) \right\}\,. \qquad (2.121)
\end{aligned}
$$

Similarly to $g_{TT}(\nu, Q^2)$, one can apply the unsubtracted dispersion relation to longitudinal-transverse interference amplitude $g_{LT}(\nu, Q^2)$, which is even in ν:

$$
\text{Re } g_{LT}(\nu, Q^2) = \text{Re } g_{LT}^{\text{pole}}(\nu, Q^2) + \frac{1}{2\pi^2}\mathcal{P} \int_{\nu_0}^{\infty} \frac{\nu' K(\nu, , Q^2)\sigma_{LT}(\nu, Q^2)}{(\nu'^2 - \nu^2)} d\nu'. \qquad (2.122)
$$

and then perform a low energy expansion to obtain:

$$
\text{Re } g_{LT}(\nu,\, Q^2) - \text{Re } g_{LT}^{\text{pole}}(\nu,\, Q^2) = \left(\frac{2\,\alpha}{M^2}\right) Q I_3(Q^2) + Q\delta_{LT}(Q^2)\nu^2 + \mathcal{O}(\nu^4). \qquad (2.123)
$$

The leading term of Eq. 2.123 gives $I_3(Q^2)$:

$$
\begin{aligned}
I_3(Q^2) &= \frac{M^2}{\pi\, e^2} \int_{\nu_0}^{\infty} \frac{K(\nu\,, Q^2)}{\nu}\, \frac{1}{Q}\, \sigma_{LT}\,(\nu,\, Q^2)\, d\nu \\
&= \frac{2\, M^2}{Q^2} \int_0^{x_0} dx\, \left\{ g_1\,(x,\, Q^2)\, +\, g_2\,(x,\, Q^2) \right\}\,. \qquad (2.124)
\end{aligned}
$$

Meanwhile the $\mathcal{O}(\nu^2)$ term of Eq. 2.123 leads to a generalized longitudinal-transverse polarizability:

$$\begin{aligned}\delta_{LT}\,(Q^2) &= \frac{1}{2\pi^2}\int_{\nu_0}^{\infty}\frac{K(\nu,\,Q^2)}{\nu}\,\frac{\sigma_{LT}(\nu\,,Q^2)}{Q\,\nu^2}\,d\nu \\ &= \frac{e^2\,4M^2}{\pi\,Q^6}\int_0^{x_0} dx\,x^2\,\left\{g_1\,(x,\,Q^2)\,+\,g_2\,(x,\,Q^2)\right\}\,. \qquad (2.125)\end{aligned}$$

If the spin structure functions $g_{1,2}$ are measured through inclusive double-polarized electron scattering experiments using virtual photons across a wide x spectrum, the generalized spin polarizability can be formed and evaluated. With the Q^2 dependence, the generalized polarizabilities are powerful tools to probe the nucleon structure covering the whole range from the partonic to the hadronic region, and a benchmark test of χPT (see Sec. 2.5) predictions at low Q^2.

2.7 Proton Hyperfine Structure

Calculations of the Proton Hyperfine Structure

The spin structure functions also provide important inputs for calculations of atomic physics. The hyperfine splitting of hydrogen has been measured to very high precision of 10^{-13}[65]:

$$\Delta E = 1420.405\ 751\ 766\ 7(9)\ \text{MHz}. \qquad (2.126)$$

However, calculations of this fundamental quantity from QED only shows precision to a few parts per million[66]. The splitting can be expressed in terms of the Fermi energy E_F as

$$\Delta E = (1+\delta)E_F, \qquad (2.127)$$

with the correction δ given by

$$\delta = 1 + (\delta_{\text{QED}} + \delta_R + \delta_{small}) + \Delta_S, \qquad (2.128)$$

where δ_{QED} accounts for the QED radiative correction which is known to a very high precision, δ_R represents the recoil effects, δ_{small} is the relatively small corrections (hadronic and muonic vacuum polarizations, and weak interaction), and Δ_S is the proton structure correction and has the largest uncertainty. The Δ_S term depends on the ground and excited state properties of the proton and can be split into two terms:

$$\Delta_S = \Delta_Z + \Delta_{\text{pol}}. \tag{2.129}$$

The Δ_Z term can be expressed as

$$\Delta_Z = -2\alpha m_e r_Z \left(1 + \delta_Z^{\text{rad}}\right) \tag{2.130}$$

where δ_Z^{rad} is the radiative correction, and r_Z is the Zemach radius depends on the electric and magnetic form factors of the proton which can be determined from elastic scattering[67]:

$$r_Z = -\frac{4}{\pi}\int_0^\infty \frac{dQ}{Q^2}\left[G_E(Q^2)\frac{G_M(Q^2)}{1+\kappa_p} - 1\right]. \tag{2.131}$$

The second term in Eq. 2.129, Δ_{pol}, contains contributions from the excited states of the proton:

$$\Delta_{\text{pol}} \sim (\Delta_1 + \Delta_2), \tag{2.132}$$

where Δ_1 involves the inelastic Pauli form factor F_2 and the g_1 structure function, and Δ_2 depends only on the g_2 structure function:

$$\Delta_1 = \frac{9}{4}\int_0^\infty \frac{dQ^2}{Q^2}\left\{F_2^2(Q^2) + \frac{8m_p^2}{Q^2}B_1(Q^2)\right\} \tag{2.133}$$

$$\Delta_2 = -24m_p^2\int_0^\infty \frac{dQ^2}{Q^4}B_2(Q^2) \tag{2.134}$$

with integrals B_1 and B_2:

$$B_1(Q^2) = \int_0^{x_{\text{th}}} dx\, \beta_1(\tau)g_1(x,Q^2) \tag{2.135}$$

$$B_2(Q^2) = \int_0^{x_{\text{th}}} dx\, \beta_2(\tau)g_2(x,Q^2) \tag{2.136}$$

and

$$\begin{aligned}\beta_1(\tau) &= \frac{4}{9}\left[-3\tau+2\tau^2+2(2-\tau)\sqrt{\tau(\tau+1)}\right], &(2.137)\\ \beta_2(\tau) &= 1+2\tau-2\sqrt{\tau(\tau+1)}. &(2.138)\end{aligned}$$

Here $\tau = \nu^2/Q^2$, and the upper integration limit x_{th} represents the pion production threshold.

The correction term Δ_2 is dominated by the low Q^2 region as shown in Fig. 2-8. Due to the lack of g_2 data at low Q^2, the calculation of Δ_2 currently rely heavily on models. A precise measurement of g_2 at low Q^2 can thus have significant impact on calculations of the hydrogen hyperfine splitting.

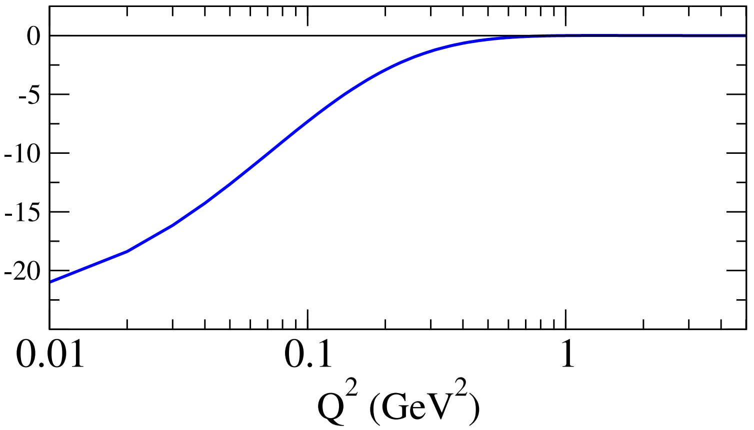

Figure 2-8: The integrand of Δ_2 in Eq. 2.129 from MAID [68] model prediction. Plot reproduced from [69].

2.8 Existing Measurements

2.8.1 Structure Function g_2

From Sec. 2.2, the spin-dependent structure function g_2 can be extracted from combined measurements of both the longitudinal and the transverse target spin cross section differences $\Delta\sigma_{\parallel}$ and $\Delta\sigma_{\perp}$ (Eq. 2.53 and Eq. 2.56), or the corresponding asymmetries $A_{\parallel}$, $A_{\perp}$ together with the unpolarized cross section σ_0 (Eq. 2.57 and Eq. 2.58).

The earliest results for g_2 were obtained in the DIS region at SLAC[70] by measuring both the longitudinal and the transverse asymmetries. At the same period, the SMC collaboration at CERN extracted $g_{1,2}$ in the DIS by using a polarized muon beam scattering off a polarized proton target[71]. The value of g_2 tends to be relatively small in DIS kinematics, and a high luminosity are usually needed in these measurements. The most precise g_2 data in the DIS is from the dedicated SLAC E155X[72] which measured g_2 for both the proton and deuteron with neutron g_2 extracted from their difference. The kinematic range was $0.02 \leq x \leq 0.8$ and $0.7 \leq Q^2 \leq 20$ GeV^2. E143[73] and E155[74] also contribute to the measurement of proton g_2, and their combined results are shown in Fig. 2-9. The general trend of the data points are consistent with the solid curve which represents the twist-2 g_2^{WW} (Eq. 2.94) using g_1 data, with some deviations for the proton, especially at small x. With the high polarized beam, JLab also provides very high precise data in DIS. JLab experiment E97-103[75] measured g_2 for the neutron in DIS using a polarized ^{3}He target to study its Q^2 dependence. The kinematics of the experiment covered $0.58 < Q^2 < 1.36$ GeV^2 and $x \approx 0.2$. Fig. 2-10 shows g_2 results from E97-103[75], E99-117[76] and SLAC E155. The precision is improved by more than an order of magnitude compared to SLAC data[72]. The g_2 data is consistently higher than leading twist g_2^{WW} which clearly indicates that higher-twist effects become significantly positive at Q^2 values below 1 GeV^2.

In addition to the study of g_2 in DIS, several experiments performed the measurement of g_2 in the nucleon resonance region ($W < 2$ GeV) over a wide range in Q^2, to study the internal structure of the nucleon resonance states. The first experiment that measured g_2 in this region is the SLAC E143 with a beam energy of 9.7 GeV to cover the resonance region at $Q^2 = 0.5$ GeV^2 and 1.2 GeV^2 [77]. At JLab, the g_2 at resonance region were investigated by E94-010 (for the neutron)[48] and the Resonance Spin Structure (RSS) collaboration (for the proton)[47]. Experiment E94-010 at JLab collected extensive data for the neutron at low Q^2 by extracting directly from cross section differences for polarized electrons scattering off a ^{3}He target polarized both along and transverse to the beam, as shown in Fig. 2-11. The g_2 data of ^3He

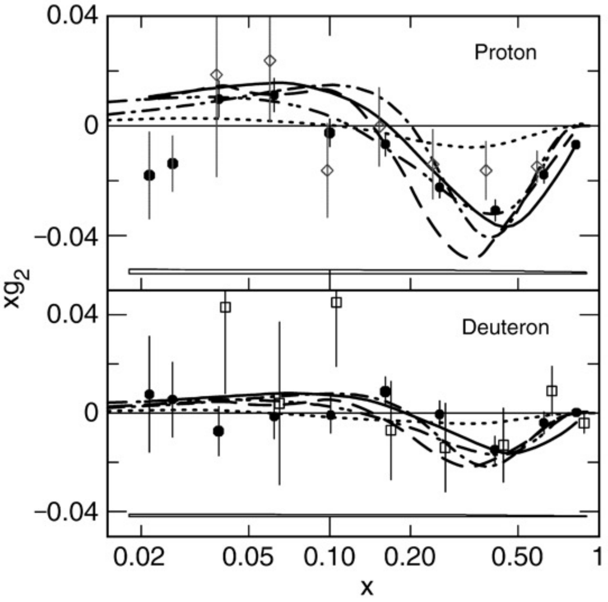

Figure 2-9: Q^2-averaged structure function xg_2 for the proton and the deuteron in DIS region. This plot includes data from E155X[72] (solid circle), E143[73] (open diamond) and E155[74] (open square). The errors are statistical; systematic errors are shown as the width of the bar at the bottom. Also shown is our twist-2 g_2^{WW} at the average Q^2 of this experiment at each value of x (solid line), the bag model calculations of Stratmann[78] (dash-dot-dot) and Song[79] (dot) and the chiral soliton models of Weigel and Gamberg[80] (dash dot) and Wakamatsu[81] (dash). Plot reproduced from [72].

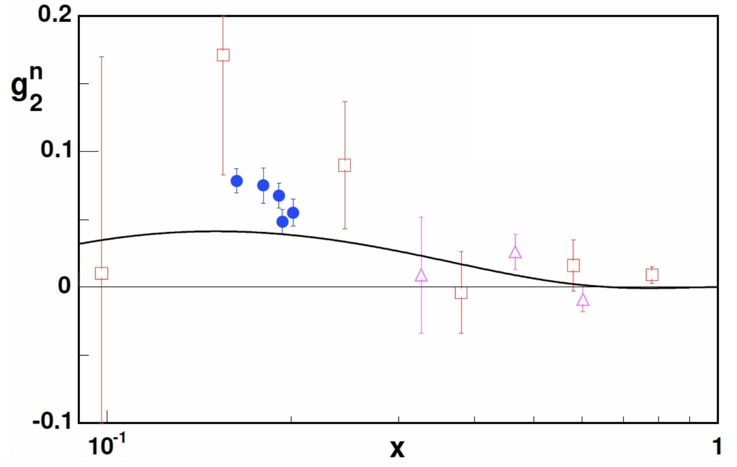

Figure 2-10: g_2 results for the neutron in DIS and low Q^2 region. This plot includes data from includes E97-103[75] (solid circle), E99-117[76] (open triangle) and SLAC E155[74] (open square). The solid curve shows predicted g_2^{WW} at $Q^2 = 1$ GeV^2. Plot reproduced from [75].

shows a positive response in the $\Delta(1232)$ resonance region and a strong deviation from the leading twist g_2^{WW} estimation. The lowest Q^2 measurement of proton g_2 is from the RSS experiment in Hall C. It measured g_2 for the proton in the resonance region at an average $Q^2 = 1.3$ GeV^2 and the result is shown in Fig. 2-12. It is clear that the leading twist g_2^{WW} is insufficient to describe the data in the low Q^2 region.

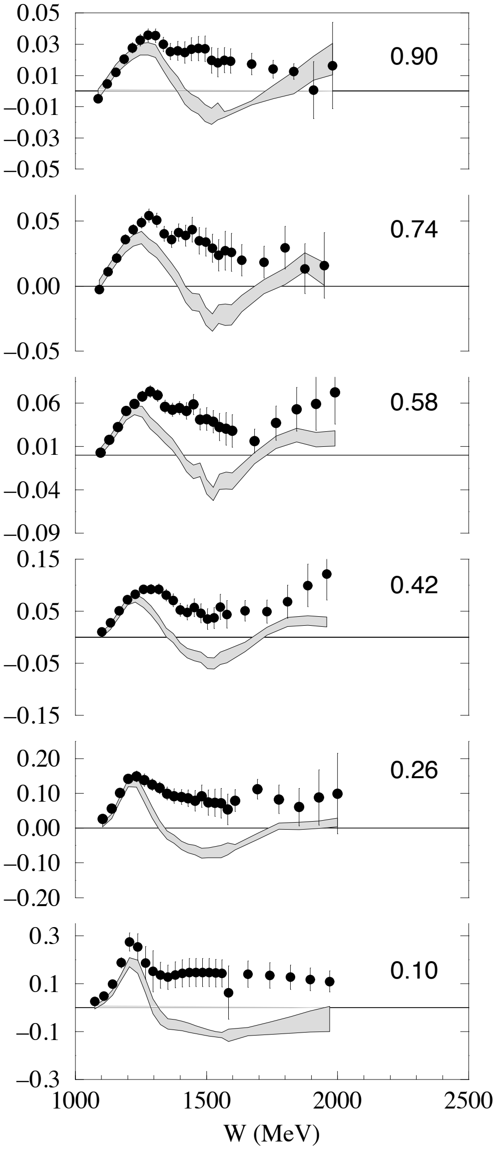

Figure 2-11: ^{3}He g_2 data from E94-010. The average Q^2 for each data set are indicated in GeV^2 with the grey bands representing the g_2^{WW} expectations. Plot reproduced from [48].

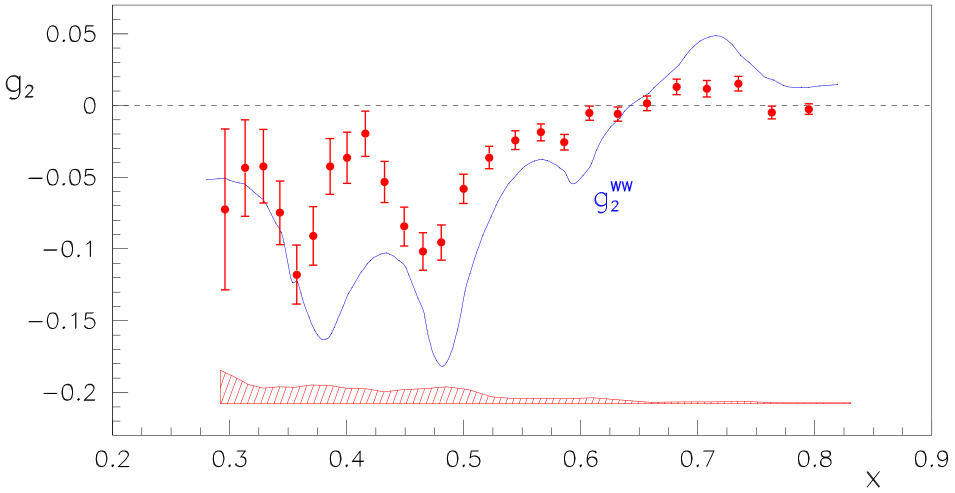

Figure 2-12: Proton g_2 data from RSS experiment compared with the g_2^{WW} (line) expectations at an averaged $Q^2 = 1.3$ GeV^2. The $\Delta(1232)$ resonance is at $x \approx 0.7$. Plot reproduced from [47].

2.8.2 Burkhardt-Cottingham (BC) sum rule

From Eq. 2.117 in Sec. 2.6, the BC sum rule states that the first moment of g_2 is zero ($\Gamma_2(Q^2) = \int_0^1 dx\ g_2(x, Q^2) = 0$) and is expected to be valid for any value of Q^2.

SLAC E155X performed the first measurement of the moment $\Gamma_2(Q^2)$ for proton, deuteron, neutron (extracted from the difference of deuteron and proton). After this, JLab Hall A conducted a series of experiments (E94-010 [48], E97-110 [82] and E01-012 [83]) to measure the neutron $\Gamma_2(Q^2)$ with a polarized ^{3}He target in a wide range of kinematics. The measurement of the proton $\Gamma_2(Q^2)$ was performed in the RSS experiment in Hall C at an average Q^2 of 1.3 GeV^2.

Fig. 2-13 shows existing world data for $\Gamma_2(Q^2)$ for the proton (top) and the neutron (bottom). The open symbols represent the experimentally measured data which typically cover the resonance region, and the solid squares are the complete integral including the unmeasured $x = 1$ (elastic) and low x contributions. The nucleon elastic contribution at $x = 1$ can be easily evaluated using the well-known form factors, and the unmeasured low x contribution is estimated using the Wandzura-Wilczek relation (Eq.2.94). For the neutron, the BC sum rule has been satisfied within uncertainties, across several different experiments and a large range of Q^2.

The BC sum rule for the proton is largely untested, see the top panel of Fig. 2-13, due to lack of data. The proton data from SLAC E155X[72] appears to be inconsistent with the BC sum rule at the 2.75 σ level. E155X covered the x range $0.02 \leq x \leq 0.8$ with an averaged $Q^2 \approx 5$ GeV^2 and the full coverage is $0.8 \leq Q^2 \leq 8.2$ GeV^2. In addition to the large experimental uncertainty, there is also an uncertainty from the low-x extrapolation, assumed $g_2 = g_2^{ww}$, which is difficult to quantify. The preliminary result from JLab RSS agrees with the BC sum rule prediction within the experimental uncertainty.

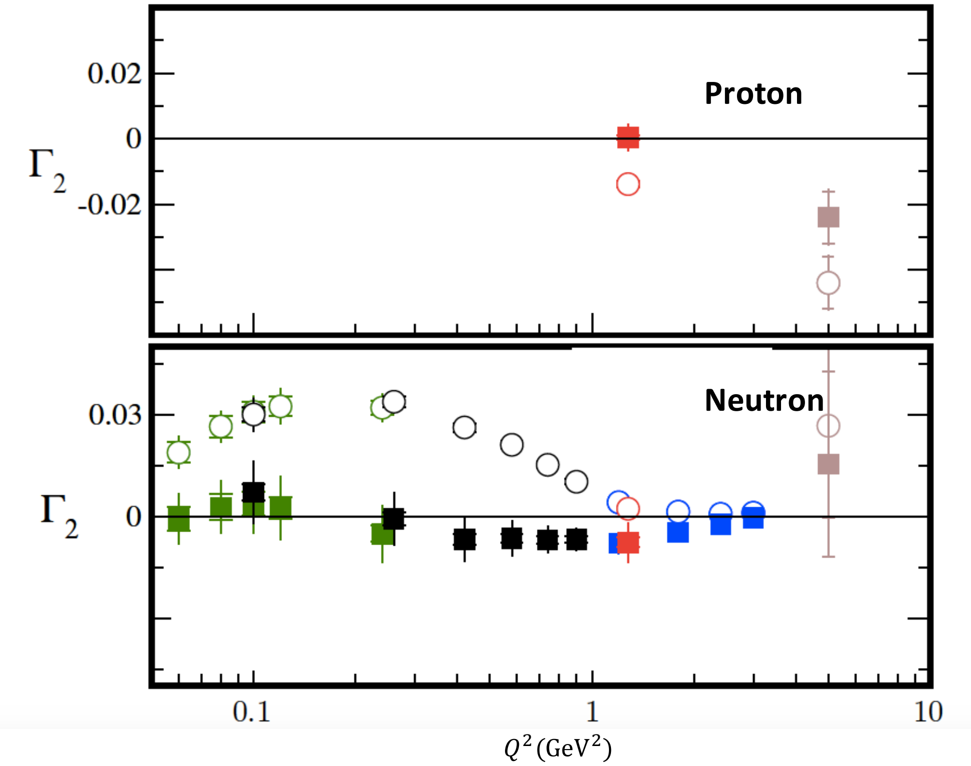

Figure 2-13: Tests of the BC sum rule for the proton (top) and neutron (bottom). The data is from Hall C RSS (Red) and Hall A experiments E94-010 [48](Black), E97-110 [82](Green) and E01-012 [83] (Blue), together with SLAC E155x[72] (Brown). The open symbols are the measured values and the solid symbols are the total moments, including the elastic and estimated contributions from the unmeasured high-energy region. The data from experiments RSS and E97-110 are still preliminary. Plot reproduced from [69].

2.8.3 Generalized Spin Polarizability γ_0 and δ_{LT}

From Eq. 2.121 and Eq. 2.125, the generalized polarizabilities γ_0 and δ_{LT} have an extra $1/\nu^2$weighting and thus converge much faster than the first moments. In this case, the unmeasured large-ν region will contribute less to the integral which minimizes the uncertainty due to extrapolation. At low Q^2, the generalized polarizabilities have been calculated in χPT calculations (see Sec. 2.5). Measurements of the generalized spin polarizabilities γ_0 and δ_{LT} provides perfect tools to understand the dynamics of QCD in the chiral perturbation region. Fig. 2-14 shows the comparison between experimental results and the χPT calculations.

The neutron results of $\gamma_0(Q^2)$ and $\delta_{LT}(Q^2)$, blue dots in the neutron panel of Fig. 2-14 were obtained from Hall A E94-010 at Jefferson Lab [84]. Top right plot shows the neutron $\gamma_0^n(Q^2)$ data at the two lowest Q^2 values of 0.10 and 0.26 GeV^2 with χPT calculations and MAID predictions. The statistical uncertainties of the experimental data are smaller than the size of the symbols in the plot. At the lowest Q^2 point ($Q^2 = 0.1$ GeV^2), the experimental result agree with the infrared-regularized (IR) version RBχPT[60] calculation including the resonance contributions (red bands), but disagree with HBχPT[59] calculation without explicit resonance contributions (blue dashed line), which indicates that the resonance contribution is significant for the heavy baryon approximation at this Q^2. The MAID prediction is consistent with the higher-Q^2 data, but overestimates the strength at lower Q^2. Refs.[59, 60] have pointed out that δ_{LT} is insensitive to the Δ resonance while γ_0 is sensitive, so δ_{LT} should be more suitable than γ_0 to serve as a testing ground for the χPT calculations.

The bottom-right panel of Fig. 2-14 shows the result of δ_{LT} compared with χPT calculations and the MAID predictions. The MAID predictions are in good agreement with the data, however, the predictions from both the HBχPT and (the IR version of) RBχPT are in significant disagreement with the data even at the lowest Q^2 of 0.1 GeV^2, which is known as the "δ_{LT} puzzle". The puzzle presents a challenge to the Chiral Perturbation Theory. However, the most recent calculation using leading-order and next-to-leading-order RBχPT[85] (blue bands) shows reasonable agreement

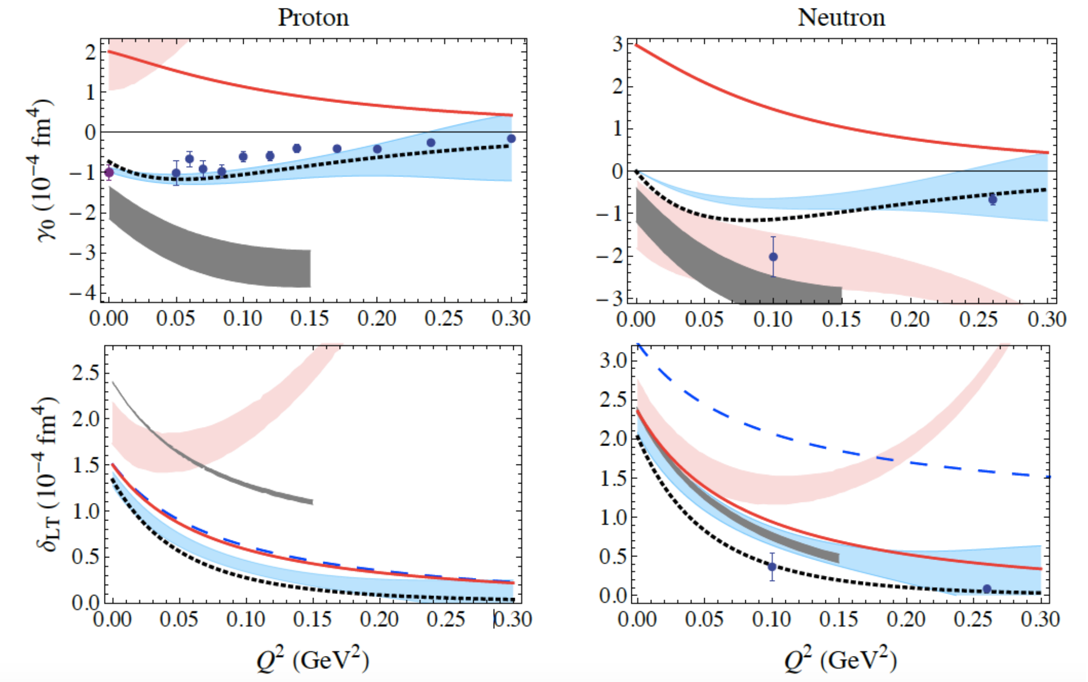

Figure 2-14: Generalized spin polarizability γ_0 and δ_{LT} for the proton (left) and the neutron (right). All the neutron data points are from E94-010 experiment[84]. The proton data at $Q^2 = 0$ (purple dot) are from ELSA[86], and at finite Q^2 (blue dots) from EG1 experiment at JLab[87]. The blue dashed line is the HBχPT calculation[59], off the scale in the upper panels. The red bands shows the IR version of the RBχPT calculation[60]. The grey bands are the recent RBχPT calculation from Ref.[88] while the red solid lines and blue bands shows the latest LO and NLO RBχPT calculations respectively[85]. Black dotted lines represent the empirical evaluation using the MAID model. Plot reproduced from [85].

with δ_{LT} data, which might suggest the puzzle is solved. The proton δ_{LT} is absent in Fig. 2-14.

2.9 Motivation Summary

At low and moderate Q^2, data on the proton g_2 structure function are scarce. Measurements of the proton g_2^p structure function at low Q^2 will provide a benchmark test of Chiral Perturbation Theory (χPT), examine the Burkhardt-Cottingham (BC) sum rule, and bring important inputs to calculations of the proton hyperfine structure.

Chapter 3

The g_2^p experiment

Experiment E08-027 (the g_2^p experiment)[69] was conducted in Hall A at Thomas Jefferson National Accelerator Facility (JLab) from March to May in 2012. The experiment aims to measure the proton spin-dependent structure function g_2 in the low Q^2 region ($0.02 < Q^2 < 0.2$ GeV^2). As mentioned in Chapter 2, the measured proton g_2^p data will provide a benchmark test of Chiral Perturbation Theory (χPT) by extracting the generalized longitudinal-transverse spin polarizability δ_{LT}, examine the Burkhardt-Cottingham (BC) sum rule for the proton, and bring important inputs to the proton hyperfine structure calculation.

During the experiment, a longitudinal polarized electron beam of energies between 1.157 and 3.350 GeV scattered off a transversely polarized NH_3 (proton) target, to measure the transverse polarized cross section difference $\sigma_\perp$. Then g_2 can be extracted using Eq. 2.57 and Eq. 2.58 when combined with the longitudinal cross section difference $\sigma_\parallel$ from the Hall B EG4 experiment[89]. One set of $\sigma_\parallel$ data were also collected in E08-027 at a beam energy of 2.254 GeV with the goal of verifying the EG4 data. The scattered electrons were detected by the Hall A High Resolution Spectrometers (HRS). The standard HRS can reach a minimum angle 12.5$^\mathrm{o}$ respect to the beam direction. To access the low Q^2 of this experiment, detection of smaller scattering angles is desirable. Therefore a so-called "septum" magnet was installed in front of the HRS to bend the scattered electron into HRS. The minimum angle reached using septum was $\approx 5.77^\circ$. The kinematic configurations are listed in Table. 3.1. For some low energy settings, a 2.5 T target field was used to reach the minimum possible Q^2 because a transverse 5 T field would deflect scattered electrons outside of the acceptance of the Hall A spectrometers.

Fig. 3-1 shows the kinematic coverage of the experiment. In each configuration, with a different beam energy or target field, a series of different momentum settings was used to measure a wide kinematic range of scattered electrons. After obtaining g_2 in a wide coverage of ν and x, the sum rule and moments (in Sec. 2.6) can then be formed and the corresponding theory can be tested.

This chapter will describe the experimental setup and the instrumentation used for the E08-027 experiment.

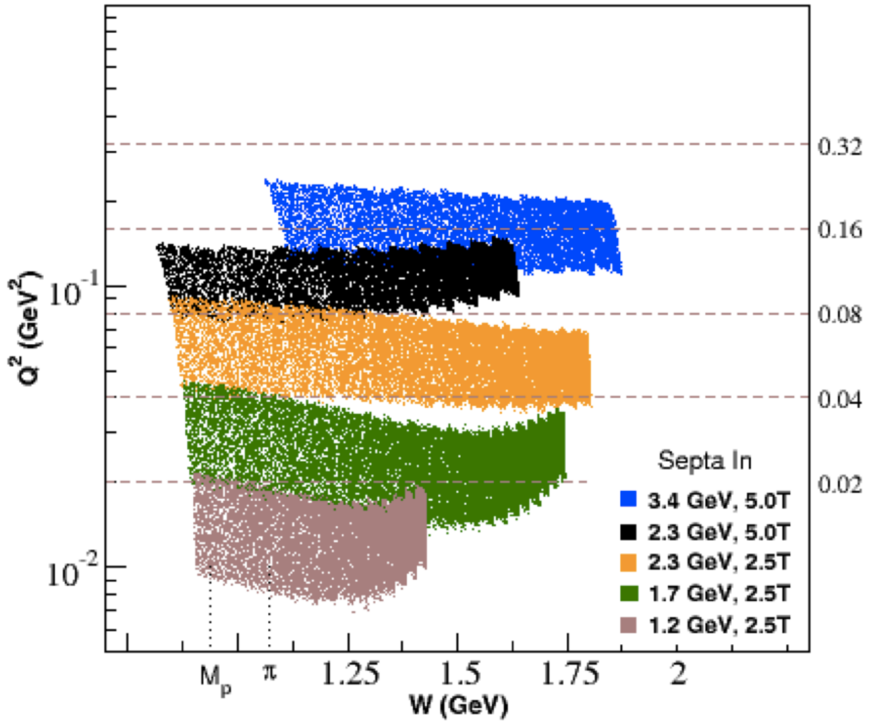

Figure 3-1: Kinematic coverage of experiment E08-027. The legends show the beam energy and target field strength for each setting.

	Beam Energy (GeV)	Field (T)	Field Angle (degree)	Septum
1	2.254	0	N/A	48-48-16
2	2.254	2.5	90	48-48-16
3	2.254	2.5	90	40-32-16
4	1.710	2.5	90	40-00-16
5	1.157	2.5	90	40-00-16
6	2.254	5	0	40-00-16
7	2.254	5	90	40-00-16
8	3.350	5	90	40-00-16

Table 3.1: Beam energy, target field and septum configurations for the E08-027 experiment. Previously, either right or left septum magnet has three pairs of coils with (48 - 48 - 16) turns on top and (16 - 48 - 48) turns on bottom. The septum configurations listed here represent the number of turns of coils for the top right septum, see Sec. 3.5.

3.1 The Electron Accelerator

The Continuous Electron Beam Accelerator Facility (CEBAF) at JLab provides multi-GeV continuous-wave (cw) polarized electron beams for medium energy physics study. The electron accelerator consists of one polarized electron source, two superconducting linear accelerators (linac), two re-circulation arcs (magnets), and magnetic elements to extract the beam to the three Halls (named Halls A, B, C). After the accelerator upgrade in 2014-15, a fourth Hall (Hall D) was added.

The layout of the electron accelerator is shown in Fig. 3-2. As required by many experiments, the CEBAF beam is usually highly polarized. The polarized electrons are produced from a strained gallium arsenide (GaAs) cathode by shining the 780 nm circularly polarized laser light at the injector. The spin of photo-emitted electrons can be flipped by switching the circular polarization state of the laser light, which is achieved by changing the voltage of the Pockels cell. The Pockels Cell is a crystal that acts as a quarter-wave retardation plate when a high voltage is applied on it, and flipping the polarity of the high voltage can thus flip the light circular polarization direction. During E08-027, the beam helicity was flipped at 960.02 Hz to be compatible with other experimental halls. The sequence for beam helicity states followed a quartet pattern, either $+--+$ or $-++-$, and the sequence of the quartet was random. This pattern eliminates the linear background and minimizes the low frequency systematic uncertainty[90]. To control the helicity dependent systematic effects, an insertable half-wave plate (IHWP) can be placed upstream of the Pockels cell in the photon beamline, to reverse the beam helicity manually several times per day[91].

On the photocathode, electrons are then extracted and accelerated to the injector under a constant, -100 kV electric field. At the injector, electrons are accelerated from an initial energy of 100 keV to 45 MeV by two and a quarter cryomodule, and then injected into the north linac, which consists of 20 consecutive cryomodules: with each full pass of the accelerator, the electrons gain $400 - 600$ MeV in each linac. Between north and south linacs, electrons are bended in the recirculation arc (a radius of around 80 m) for continuous accelerating. Each pass of electron needs a different set of recirculation arcs. The electrons can be accelerated up to 5 passes, reaching a maximum energy of 6 GeV (before the upgrade). After the accelerator upgrade, the maximum energy became 11 GeV to Halls A, B, C and 12 GeV to Hall D.

The entire accelerator is operated at a radio frequency (RF) of 1497 MHz, and the electron bunches are splitted to 499 MHz for each hall. After passing the south linac and reaching the required beam energy of one hall, RF separators and beam septa can allow particular bunch trains and energies to be extracted and sent to the experimental hall. By using this technique, CEBAF can provide beams with independent currents and at different but correlated energies to three halls simultaneously. The maximum total current available among the three halls is around 200 μA and the average beam polarization is about 85%. Typically, Halls A and C take beam currents 1-100 μA, whereas Hall B typically runs at less than 100 nA.

During the E08-027 experiment, electron beams were delivered into Hall A with current $I_e \sim 50$ nA and five beam energies (1.1, 1.7, 2.2, 3.3 GeV) for production data taking. The average beam polarization during the experiment was $\approx 85\%$.

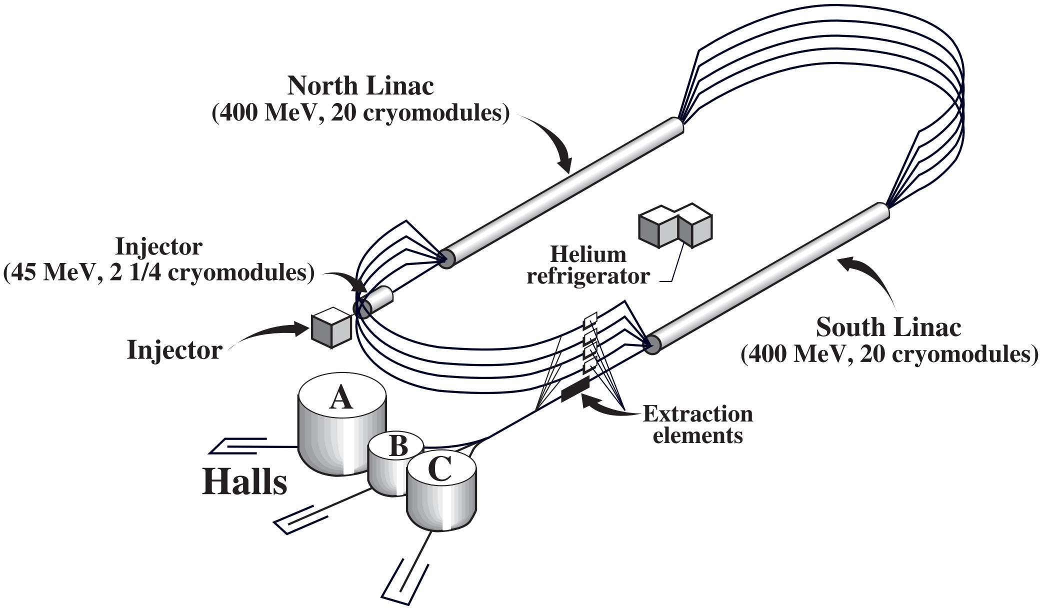

Figure 3-2: Layout of the CEBAF facility in the 6 GeV era[92]. The electron beam is produced at the injector and accelerated in the two superconducting linacs up to 5 times. The linac energies shown are for operation at 4 GeV while each linac operates at 600 MeV for 6GeV. The electron beam can be extracted simultaneously to each of the three experimental halls A, B and C.

3.2 Overview of Hall A

Hall A is the largest experimental Hall among the existing halls with a floor diameter of 53 m. Fig. 3-3 shows the top and the side view of Hall A during E08-027 experiment. The key elements include the beam line, the polarized NH_3 target, septum magnets, High Resolution Spectrometers and their detector packages, which will be discussed in following sections.

3.3 Hall A beamline

During the E08-027 experiment, the JLab-UVA polarized ammonia target was used in Hall A for the first time. This target utilized the Dynamical Nuclear Polarization (DNP) technique to polarize the solid ammonia at a temperature around 1 K and a magnetic field about 5 T. However, the strong transverse 5T field would signifi-

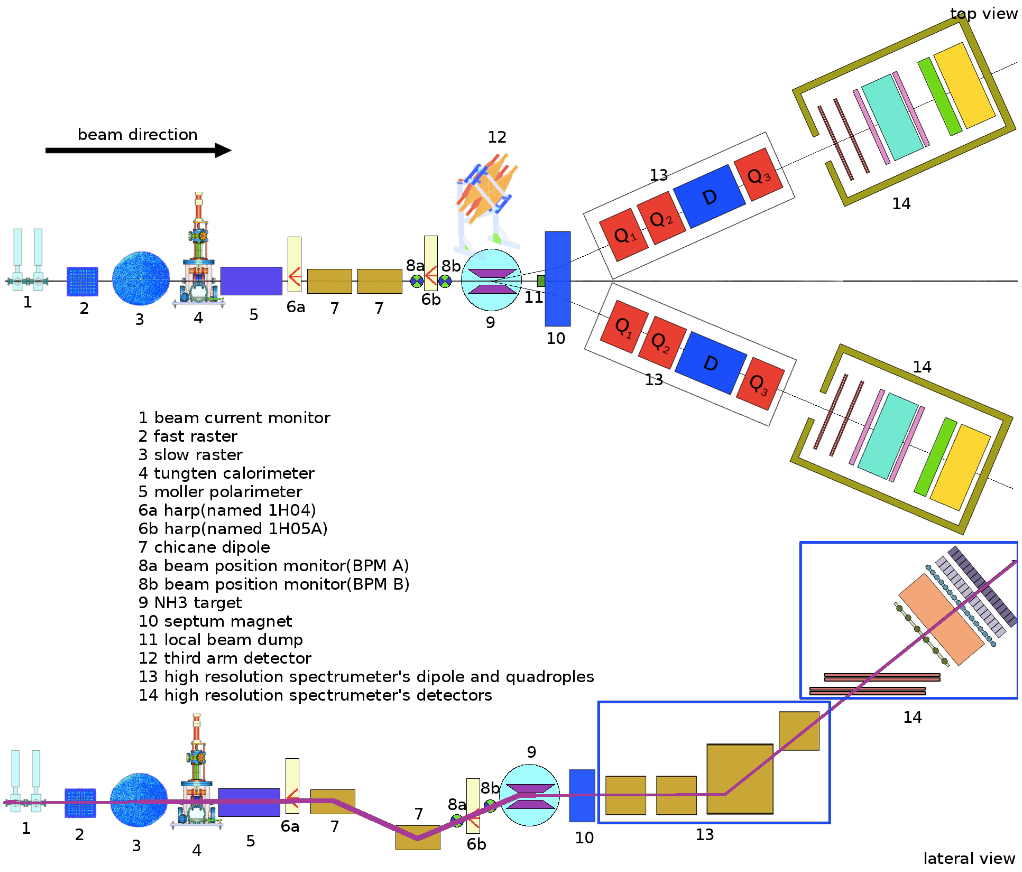

Figure 3-3: Schematic of Hall A during E08-027[93].

cantly bend the electron beam and the scattered electrons. To properly transport the electron beam in the presence of the target field, two chicane dipoles were installed upstream of the target to compensate for the bending effect of the target field, and a local dump was installed downstream of target for the energy setting ($E_e = 3.3$ GeV) where the electron beam cannot reach the standard beam dump of Hall A. To minimize the beam-introduced depolarization effect on the target, a pair of slow rasters was also used in Hall A for the first time to spread the beam uniformly over the target, and a very low beam current $I_e \sim 50$ nA was required. Since the typical Hall A experiments before g_2^p all used current between 1 μA and 100 μA, such a low current required new beam current monitors (BCMs) and beam position monitors (BPMs) that work at low currents. The elements of the beam line are labeled as $1 - 8b$ in Fig. 3-2.

3.3.1 Beam Energy Measurement

The beam energy during the E08-027 experiment was measured using the Arc method[92]. The principle of this method is that the momentum P of a charged particle is related to the bending angle θ in a given magnetic field as:

$$P = k\frac{\int \vec{B} \cdot \vec{l}}{\theta}, \tag{3.1}$$

where $\int \vec{B} \cdot \vec{l}$ (in T·m) is the integral of the transverse magnetic field along the trajectory, and $k = 0.299792$ GeV·rad·T^{-1}m^{-1}/c.

Fig. 3-3 shows the layout of the Arc measurement. Eight dipole magnets are used to produce the magnetic field for bending, but cannot be probed directly since they are located in the vacuum. Their integral $\int \vec{B} \cdot \vec{l}$ is measured using a 9th identical dipole (reference magnet) located outside of the arc and connected in series with the other 8. Two sets of superharps (wire scanners) are installed at both the entrance and the exit of the arc to monitor any deviation from the nominal bending angle (34.4°). The Arc energy measurement provides an absolute measurement to the 2×10^{-4} GeV level. However, the Arc method is invasive and cannot be made in parallel to the production data taking.

During production running, the beam energy was monitored by the "Tiefenbach" measurement[92]. The Tiefenbach beam energy value is calculated from the current values of the arc $\int \vec{B} \cdot \vec{l}$ and the arc beam position monitors (BPM), and is recorded in the data stream continuously. The energy from this method is accurate to the 5×10^{-4} GeV level.

3.3.2 Beam Current Monitor

In the E08-027 experiment, the beam current was measured by two beam current monitors (BCMs), labeled as id 1 in Fig. 3-3. The whole system contains two RF cavities, an Unser monitor, and a BCM receiver with a data-acquisition system.

The two RF cavities are stainless steel cylindrical high-Q($\approx$ 3000) waveguides

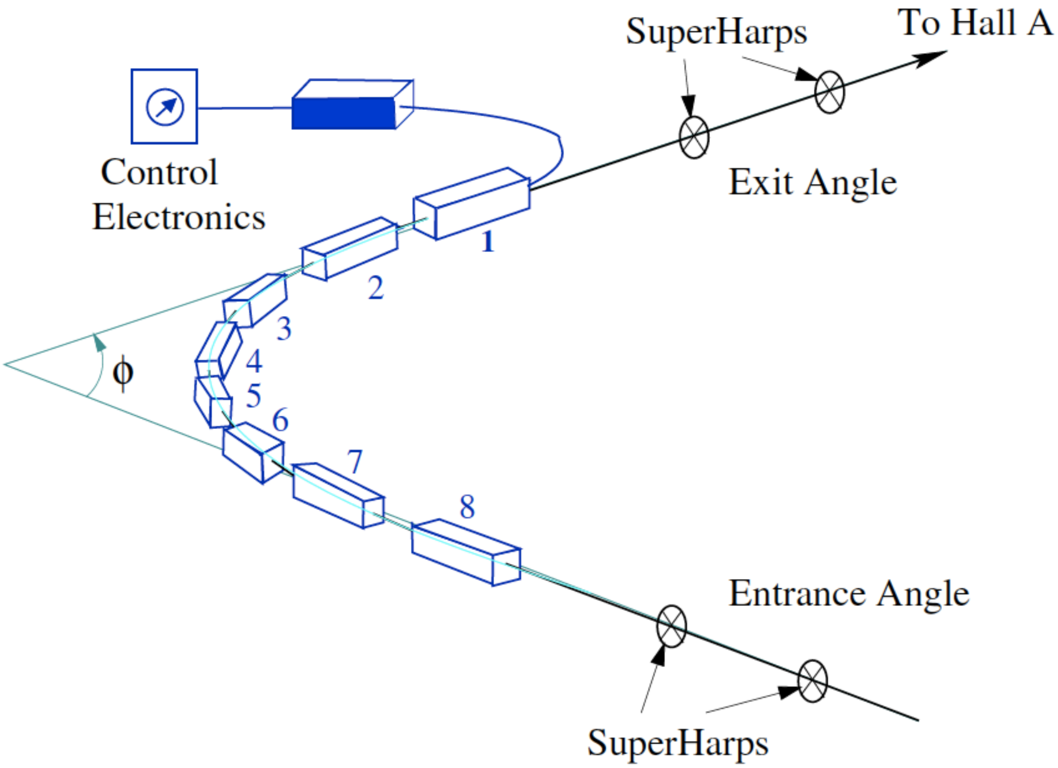

Figure 3-4: Schematic of the arc energy measurement. Plot reproduced from [94].

located 23 m upstream of the the target center. Their response is tuned to the frequency of the electron beam (1497 MHz). When the electron beam passes through the cavity, the cavity will output a signal with voltage proportional to the beam current.

The BCM receiver converts raw signals to be compatible with the DAQ system. Since the original RMS-to-DC converter works linearly only within 1 to 200 μA and did not work at the low current of 50 nA[95], a new BCM receiver was designed and built by the JLab instrumentation group to achieve a reasonable signal/noise (S/N) ratio in the beam current range of several nA to several μA[96]. The new BCM receiver consists of an analog part and a digital part. The analog part converts the ratio frequency (RF) signal to the intermediate frequency (IF) signal by a mixer and then amplifies it, while the digital part digitizes the signal by a 36 MSPS ADC and then applies two filters to increase the S/N ratio before converted back to 0-10V analog signal to match the existing Hall A DAQ system. The voltage signal is converted to frequency signal by a voltage-to-frequency module in the DAQ system and then counted by the scaler.

The BCMs are traditionally calibrated with a Faraday cup in the injector, and double-checked by the Unser monitor located between the two RF cavities. However, both Unser and Faraday cup could not work at low currents. Therefore a tungsten calorimeter[97] (id 4 in Fig. 3-3) was installed for calibrating the BCMs. The tungsten calorimeter is pumped into vacuum to minimize the heat loss so that its temperature change is dominated by the energy deposited from the electron beam. The typical heat loss is around 0.2% if the measurement takes less than 20 min[97]. The relation between the total charge Q and the temperature change ΔT can be expressed as

$$Q = \frac{eK_w \Delta T}{E_e}, \tag{3.2}$$

where E_e is the beam energy, $K_w = (8555.5 \pm 50)$ J/K is the heat capacity of the tungsten measured before the experiment[98], and e is the electron charge to convert the unit of E_e (in eV) to Joules. Then the BCM readout signal can be calibrated with the charge Q by:

$$N = (CI + C_0)t, \tag{3.3}$$

where N is the BCM scaler reading, C_0 is the pedestal value of BCM, and C is the calibration constant and I is the current. During the E08-027 experiment, the calibration constant uncertainties were below 0.7% for 90% of the runs[99].

3.3.3 Rasters

The size of the beam spot is around 100 μm when it enters Hall A, which will bring significant depolarization and heating to the target. In E08-027 experiment, besides the use of low current beams (around 50 nA), two raster systems, a fast raster and a slow raster (id 2 and 3 in Fig. 3-3), were installed at around 17 m upstream of the target to distribute the beam uniformly to a size of 20 mm in diameter at the target by time-varing dipole magnetic fields. The fast raster and the slow raster are labeled 2 and 3 in Fig. 3-3, respectively, and each consists of two dipole magnets.

The fast raster is a standard Hall A beamline component. The same current as the standard operation, in a triangular waveform with frequency 25 kHz, was used to drive the two dipoles to move the beam in x and y directions. A rectangular pattern of about 2 mm×2 mm was formed, as shown in Fig. 3-5.

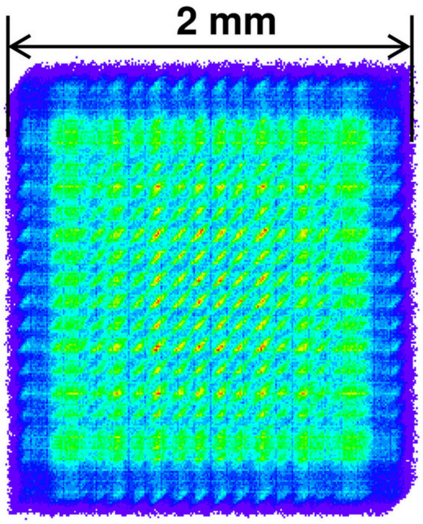

Figure 3-5: Fast raster pattern, produced from the magnet current signal[100].

For the g2p experiment, in addition to the existing fast raster system, a slow raster system was installed the first time in Hall A to be able to uniformly cover the large target cross section which has a ≈ 25 mm diameter. The waveforms for the x and y directions are generally independently from a dual-channel function-generator (Model agilent 33522A):

$$\begin{aligned} I_x &= A_x f(t^{1/2}) \sin(\omega t), \\ I_y &= A_y f([t+t_0]^{1/2}) \sin(\omega t + \phi), \end{aligned} \tag{3.4}$$

where A_x and A_y are the maximum amplitudes, t_0 (ϕ) is the AM (sin phase) difference between x and y waveforms, $\omega = 99.4124$ Hz is the frequency, $f(t^{1/2})$ is a parametric function responsible for generating a uniform circular pattern and includes four periodic piece-wise function: the first term is $t^{1/2}$, the second term is $(T/2 - t)^{1/2}$, the third term is $-(t - T/2)^{1/2}$, and the final term -$(T - t)^{1/2}$, with each term account for one quarter cycle $T/4$. The cycled function has a frequency of 30 Hz. During the E08-027 experiment, $t_0 = 0$ is manually set to 0 to avoid nonuniform distortion, the phase $\phi = \pi/2$ is locked by the function generator, and the period of cycled function is $T = 1/30$ s. A typical slow raster pattern 2 cm×2 cm is shown in Fig. 3-6. A 2.2 cm circular rastered beam was achieved by combining these two rasters.

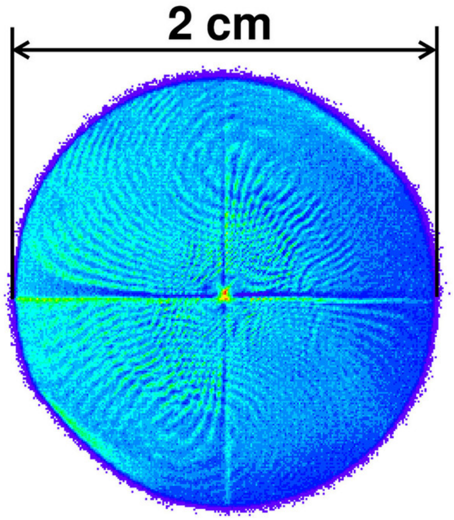

Figure 3-6: Slow raster pattern, produced from the magnet current signal[100].

3.3.4 Beam Position Monitor

For the E08-027 experiment, the beam position and directions were measured by two Beam Position Monitors (BPMs), labeled as id 8a and 8b in Fig. 3-3. Each BPM contains four antennas (marked as u_+, u_- and v_+, v_-) parallel to the beam direction and are oriented at 45° from the horizontal and vertical planes in a vacuum chamber, as shown in Fig. 3-7. When the beam passes through the BPM chamber, each antenna picks up signals that are inversely proportional to the distance from the beam.

Assuming the antennas did not affect each other and neglect the edge effect due to the finite length of the chamber, the signal amplitude picked up by each antenna can be expressed as[101, 102]

$$\phi_i = \phi_0 I \frac{R^2 - \rho^2}{R^2 + \rho^2 - 2R\rho\cos(\theta_i - \theta_0)}, \tag{3.5}$$

where ϕ_i is the signal received in the antenna, and i is the channel u_+, u_-, v_+ or v_-, ϕ_0 is a constant related to the geometry of the BPM chamber and the output resistance, I is the beam current, R is the radius of the BPM vacuum chamber, ρ is the radial position of the beam, and $\theta_i - \theta_0$ is the angle difference between the antenna and the beam in the polar coordinate. The beam position can then be extracted in the BPM local coordinates using Eq. 3.5:

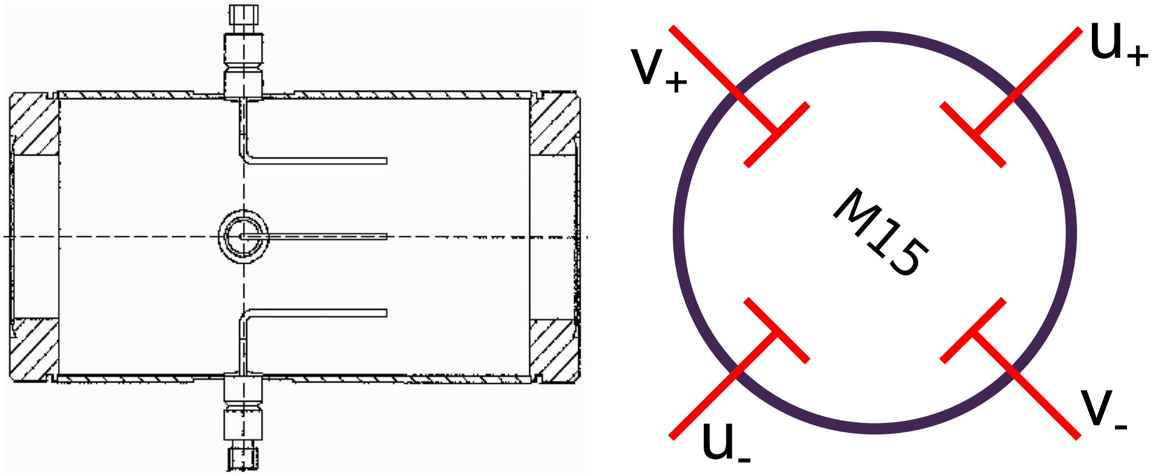

Figure 3-7: Diagram of BPM[100].

$$U = RD_U\left(\frac{1}{D_u^2 + D_v^2} - \frac{1}{\sqrt{D_u^2 + D_v^2}}\sqrt{\frac{1}{D_u^2 + D_v^2} - 1}\right), \tag{3.6}$$

where U denotes u or v, and D_u (D_v) is the ratio of the signal difference to signal sum in the u (v) direction:

$$D_U = \frac{\phi_{U+} - \phi_{U-}}{\phi_{U+} + \phi_{U-}}. \tag{3.7}$$

The BPMs were calibrated by two superharps: one installed between the BPMs and the other installed upstream of the upstream chicane magnet, as shown in Fig. 3-3. Each harp consists of three wires with a thickness of 50 μm, oriented vertically and at ±45° respectively, and is fixed to a chassis controlled by a step motor[103], as shown in Fig. 3-8. The original position of each wire is surveyed with a precision of 0.1 mm. During a harp scan, the electron beam is sensed by the three wires one by one in the harp. The absolute beam position could be calculated with the recorded wire signal combined with the survey result. Then the BPMs can be calibrated by comparing the harp result with the BPM signal in that scan. The two BPMs were placed very close to each other due to the space limitation between the second chicane magnet and the target: one BPM was placed 95.5 cm upstream of the target while the other was placed 69 cm upstream. After obtaining the beam position information at the BPM location, transport functions were fitted to transport the beam position from the BPMs to the target, to account for the strong target magnetic field effect. The short distance between BPMs (26.5 cm) magnified the position uncertainty from the BPMs to target.

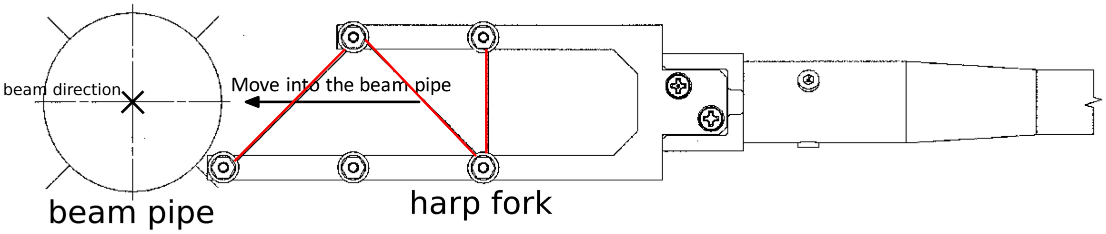

Figure 3-8: Diagram of harp. The harp is made of 3 wires (red), arranged on a fork-shape holder that can be moved in and out of the beam with a motor[100].

As mentioned in Sec. 3.3.3, the beam was spread by a fast raster at 25 kHz. The BPM cannot provide the beam position event by event, only the center of the raster pattern. Therefore, beam position and the angle at the target are extracted event-by-event by combining information from the BPMs (average value) and the signals from the rasters (event dependent).

For the E08-027 experiment, the uncertainty of beam position at target was previously reported to be $1 \sim 2$ mm, while the uncertainty for the incident angle was $1 \sim 2$ mrad[100]. However, these still need further investigation.

3.3.5 Beam Polarization Measurement

For the E08-027 experiment, the polarization of the electron beam was measured by the Møller polarimetry, labeled as id 5 Fig. 3-3. The principle is that the cross section of polarized electrons (beam) scattering off polarized atomic electrons in a magnetized foil (target), $\vec{e^-} + \vec{e^-} \rightarrow e^- + e^+$, depends on the beam and target polarizations P_b and P_t as[92]

$$\sigma \propto (1 + \sum_{i=X,Y,Z} (A_{ii} P_{b,i} P_{t,i})), \tag{3.8}$$

where $i = Z$ represent the projection of polarization along beam direction, while $i = Y$ represents the projection perpendicular to the scattering plane X-Z). A_{ii} is the analyzing power that depends on the scattering angle in the center of mass (CM) frame (θ_{CM}), and can be expressed as:

$$\begin{aligned} A_{ZZ} &= -\frac{\sin^2\theta_{CM} \cdot (7 + \cos^2\theta_{CM})}{(3 + \cos^2\theta_{CM})^2}, \\ A_{XX} &= -A_{YY} = -\frac{\sin^4\theta_{CM}}{(3 + \cos^2\theta_{CM})^2}. \end{aligned} \tag{3.9}$$

As one can see, the analyzing power does not depend on the beam energy.

The main purpose of the polarimeter is to measure the longitudinal beam polarization, which corresponds to analyzing power A_{ZZ}. At $\theta_{CM} = 90°$, the analyzing power has its maximum $A_{ZZ,max} = 7/9$.

The setup for the Møller polarimetry polarimeter is shown in Fig. 3-9. A thin magnetically saturated ferromagnetic foil is used as the polarized electron target with an average electron polarization of about 8% at 24 mT[92]. The scattered electrons are selected by a magnetic spectrometer consists of a sequence of three quadrupole magnets and a dipole magnet, and then measured by the detector consists of scintillators and lead-glass calorimeter modules in two arms in order to detect the two scattered electrons in coincidence. A pair of asymmetry is measured at two different target angles ±20° with respect to the beam in the horizontal plane and the two asymmetry results are averaged to cancel the possible contribution from transverse polarization of the target, whose asymmetries would have opposite signs for these target angles. The beam longitudinal polarization is measured as:

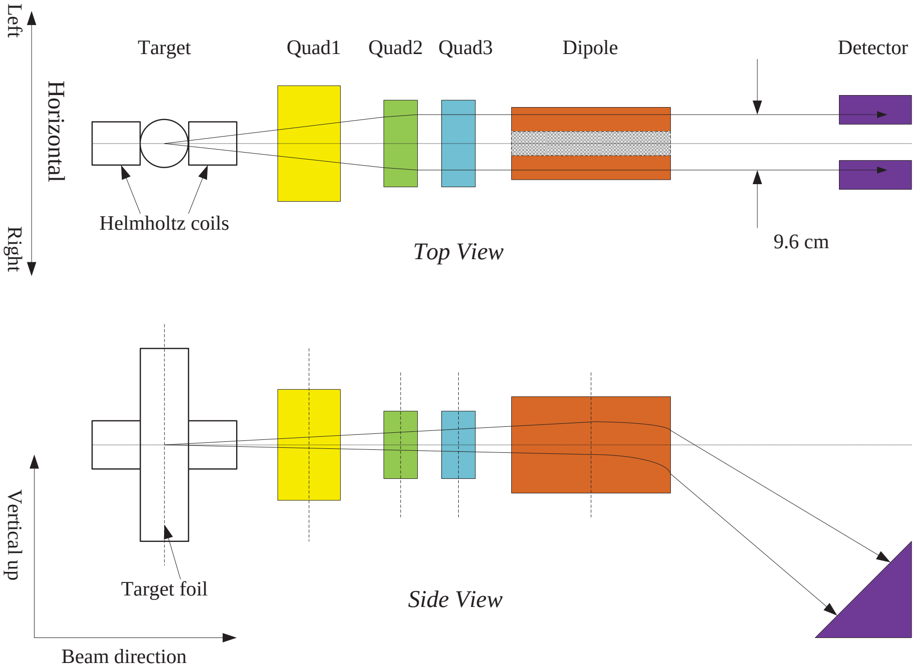

Figure 3-9: Schematic diagram of the Møller polarimeter[92, 104].

$$P_{b,Z} = \frac{N_+ - N_-}{N_+ + N_-} \cdot \frac{1}{P_t \cdot \cos\theta_t \cdot < A_{ZZ} >}, \tag{3.10}$$

where N_+ and N_- are the event counting rates with two opposite mutual orientation of the beam and target polarization, $< A_{ZZ} >$ is obtained from a Monte-Carlo calculation of the Møller spectrometer acceptance, P_t is the target polarization derived from special magnetization measurements of the foil samples, θ_t is the target angle measured using a scale which is engraved on the target holder and seen with an TV camera. Eq. 3.10 is used at different values of the target angle θ_t.

The Møller measurement is invasive and takes a couple of hours to complete. Dur-

#	Date	Polarization and Statistical Error (%)	Systematic Error (%)
1	03/03/2012	79.91±0.20	±1.7
2	03/30/2012	80.43±0.46	±1.7
3	03/30/2012	79.89±0.58	±1.7
4	04/10/2012	88.52±0.30	±1.7
5	04/23/2012	89.72±0.29	±1.7
6	05/04/2012	83.47±0.57	±1.7
7	05/04/2012	81.82±0.59	±1.7
8	05/04/2012	80.40±0.45	±1.7
9	05/15/2012	83.59±0.31	±1.7

Table 3.2: Results of the Møller measurements during E08-007[105].

ing the E08-027 experiment, it was often scheduled immediately after long unavailable beam periods or configuration changes in the accelerator. Nine measurements were taken during the experiment and the results are shown in Table. 3.2. The relative systematic uncertainty 1.7% is dominated by the knowledge of the foil polarization[106].

3.3.6 Chicane Magnets

In the E08-027 experiment, the strong transverse magnetic field in the target region caused the electron beam deflect downwards when the beam passed through. Two chicane magnets were placed in front of the target and the BPMs to pre-bend the beam upwards to compensate for the bending in the target region, as shown as id 7 in Fig. 3-3. The first chicane magnet was installed at 5.92 m upstream from the target center while the second one at 2.66 m upstream. The beam was bent downwards of the horizontal plane in the first chicane magnet, and then bent back towards the target in the second magnet at an angle to compensate the bending in the target field. In different beam energy or target field configurations, the vertical positions of the two chicane magnets were adjusted so that the beam could incident straightly on the target. Fig. 3-10 shows the two chicane magnets installed for the E08-027 experiment.

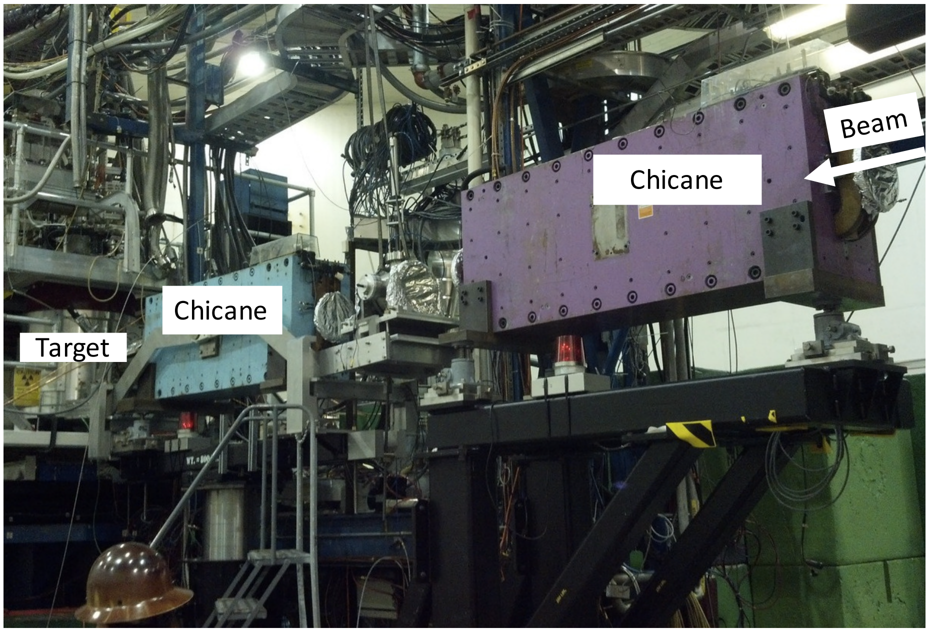

Figure 3-10: Chicane dipole magnets upstream of the target.

3.3.7 Local Beam Dump

For the 5 T longitudinal and the 2.5 T transverse target field settings, the beam, can reach the standard Hall A dump. However, due to the limited installation space for the chicane magnets, the beam cannot be bent back to the Hall A dump under the 5 T transverse target field. At this low beam current (around 50 nA), a local beam dump (id 11 in Fig. 3-3) was allowed to be installed downstream of the target center and upstream of the septum magnet to stop the electron beam. The local dump consisted of a series of tungsten and copper plates. Fig. 3-11 shows the local dump used in the experiment.

3.4 The polarized NH_3 Target

During the E08-027 experiment, a polarized ammonia (NH_3) target was used to provide the polarized proton for electron scattering. The protons in the irradiated NH_3 were polarized using Dynamic Nuclear Polarization (DNP) technique at a tem-

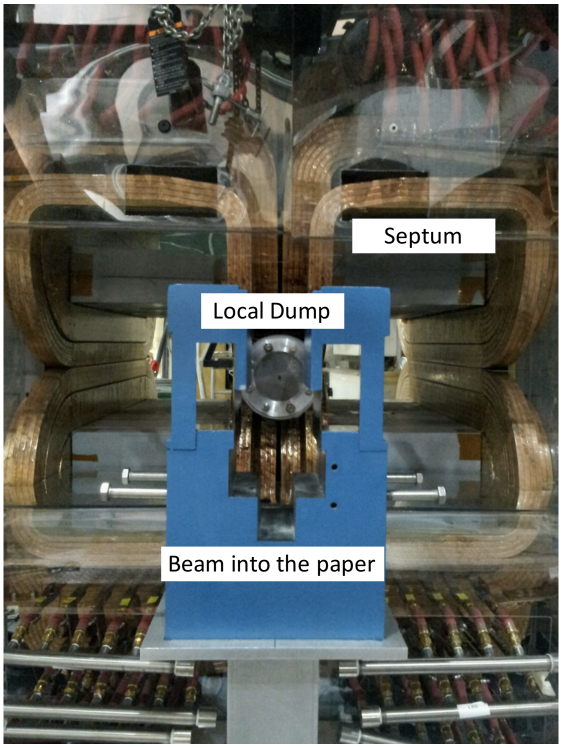

Figure 3-11: Local beam dump (blue one) in front of the septum magnet.

perature of 1 K and at fields of 2.5 and 5.0 T, and their polarization was measured by Nuclear Magnetic Resonance (NMR). The 2.5 T transverse field configuration was used at the low energy settings to reach the minimum possible Q^2 because a transverse 5 T field would strongly deflect scattered electrons outside the acceptance of the Hall A spectrometers due to the power and construction limit for the chicane dipole magnet. Providing much lower proton polarizations.

There are several advantages to choose polarized ammonia as a polarized proton source: it is capable of reaching high proton polarizations, above 90% at the 5 T magnetic field settings; it can be polarized very quickly, within 30 minutes or less; and it holds up very well to radiation damage, which was important to minimize beam down time during the run period. In this section, the principle of Dynamic Nuclear Polarization, the target setup, and the polarization measurement will be discussed.

3.4.1 Principles of Dynamic Nuclear Polarization

At a magnetic field B and temperature T, the spin-1/2 particles are polarized according to the Boltzmann statistics with thermal equilibrium polarization:

$$P_{TE} = \frac{e^{\frac{\mu B}{kT}} - e^{\frac{-\mu B}{kT}}}{e^{\frac{\mu B}{kT}} + e^{\frac{-\mu B}{kT}}} = \tanh\left(\frac{\mu B}{kT}\right), \tag{3.11}$$

where $k = 1.38 \times 10^{-23}$ J/K is the Boltzmann constant and μ is the magnetic moment of the particle. For a typical configuration during E08-027 experiment, temperature $T = 1$K, $B = 2.5$T, electron polarization is approximately 92% according to Eq. 3.11 with $\mu_e = 9.2740 \times 10^{-24}$ J/T. However, the proton polarization is only 0.25% since proton's magnetic momentum $\mu_p = 1.4106 \times 10^{-26}$ J/T is about 1/660 of μ_e. This small thermal polarization of proton is clearly not practical for spin-structure measurements. On the other hand, it is very difficult to reach a magnetic field far beyond 2.5T and a temperature far below 1K, other approaches must be pursued to achieve a high polarization for the proton.

A DNP technique was developed to enhance the polarization by transferring the polarization of free electrons in the medium to the nucleon via electron-proton coupling using an additional microwave field[107, 108]. For the electron-proton system, the Hamiltonian can be expressed as

$$H = \vec{\mu}_e \cdot \vec{B} + \vec{\mu}_p \cdot \vec{B} + H_{ss}, \tag{3.12}$$

where H_{ss} represents the spin-spin interaction between the electron and the proton. As a result of hyper-fine splitting from the spin-spin interaction, the ground state of the proton is split to four sublevels, as shown in Fig. 3-12. By carefully tuning the RF frequency ν_μ from the microwave generator, the coupled electron and proton spin system can be pumped to the desired state as:

$$e_\downarrow p_\downarrow \to e_\uparrow p_\uparrow \text{ if } \nu_{\mu-} = \nu_{EPR} - \nu_{NMR}, \text{ or} \tag{3.13}$$

$$e_\downarrow p_\uparrow \to e_\uparrow p_\downarrow \text{ if } \nu_{\mu+} = \nu_{EPR} + \nu_{NMR}, \tag{3.14}$$

where $e_\downarrow$ and $p_\downarrow$ ($e_\downarrow$ and $p_\downarrow$) represents the state with the electron and the proton spin aligned (anti-aligned) to the magnetic field, ν_{EPR} is the electron's EPR (electron paramagnetic resonance) frequency, respectively, and ν_{NMR} is the proton's NMR (nuclear magnetic resonance) frequency. From the pumping processes (Eq. 3.13 and 3.14), either positive or negative proton polarizations can be achieved in the same magnetic field by using the microwave frequency $\nu_{\mu-}$ or $\nu_{\mu+}$. The pumped electron-proton spin state is not permanent and relax back to the lowest energy state later. At temperature 1K, the proton' spin relaxes on the order of tens of minutes, whereas the electron's spin relaxation time is very fast with an order of milliseconds. Therefore, the rapid relaxed electron can then be used to pump another proton by the microwave. If the pump rate is greater than or equal to the proton spin relaxation rate, a high proton polarization can be achieved and maintained.

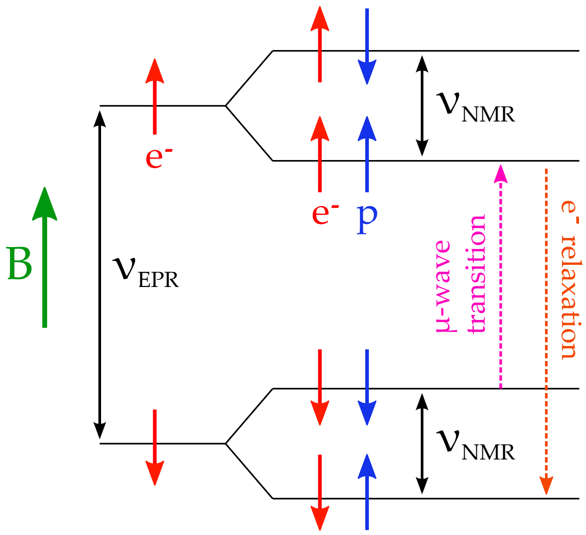

Figure 3-12: Dynamic Nuclear Polarization method to positively polarize protons. Plot reproduced from [109].

3.4.2 Setup

The polarized ammonia target system used in E08-027 is shown in Fig. 3-13. To optimize the DNP process, the magnetic field must be not only very strong, but also very uniform over the volume of the target material. For this target, a field nonuniformity $\Delta B/B$ of less than 10^{-4} over a cylindrical volume with 2 cm in diameter and 2 cm long, was achieved by a superconducting magnet maintained at 4 K with a reservoir of liquid helium [110]. The open geometry of the magnet can allow the beam to pass through in both longitudinal and transverse configurations. An aluminum scattering chamber, with multiple thin windows for the electron to pass, is evacuated to approximately 10^{-7} torr and provides an insulating vacuum for the cryogenic components inside. The target sample is placed in the magnet center via a target insert and maintained at 1 K in a helium container (referred to as the target nose) with the ^{4}He evaporation refrigerator and Roots pump set. The cooling power is about 3 W in the experimental condition.

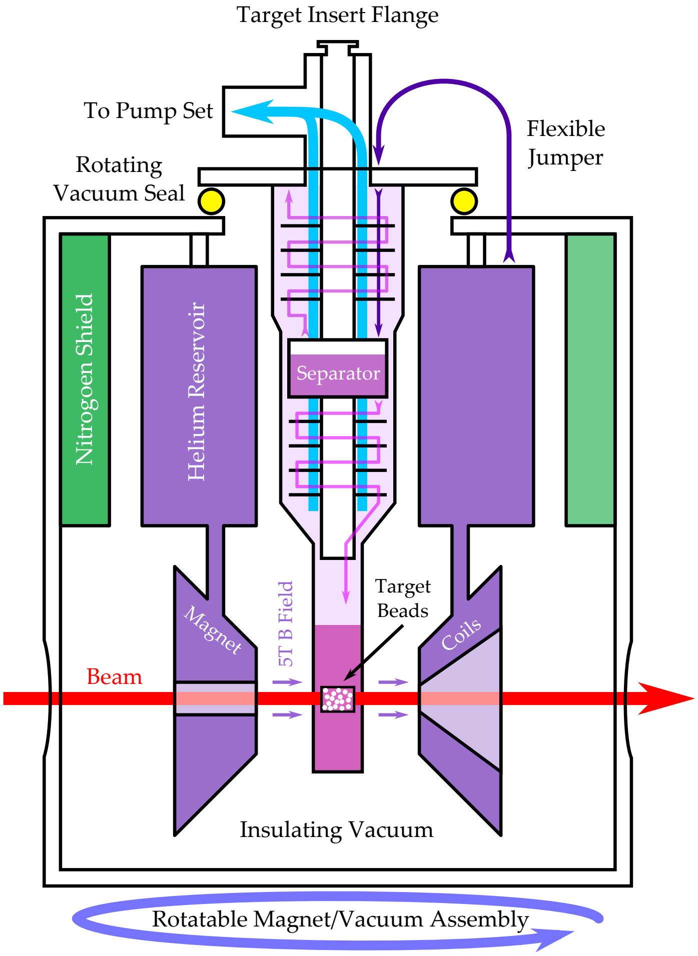

Figure 3-13: A cross section of the polarized target setup showing the location of the magnet, the NMR coil, and liquid helium and nitrogen reservoirs used to cool the setup[110].

The target insert contained several cells: a NH_3 cell, a CH_2 hole, a carbon hole, a second NH_3 cell, a dummy cell and a carbon cell from top to bottom, as shown in Fig. 3-14. The two NH_3 cells, filled with ammonia beads and covered by thin aluminium foils, are used for production data taking. A short Cu-Ni capillary coil was also installed in the cell for NMR measurement. A dummy cell identical to the NH_3 cell but without any ammonia beads was used for dilution study. The carbon cell was used for optics study. The CH2 hole and the carbon hole were designed to load the CH2 foil and the carbon foil, also for optics study. The position of the target insert can be moved vertically to select different cells by a remote controlled stepper motor.

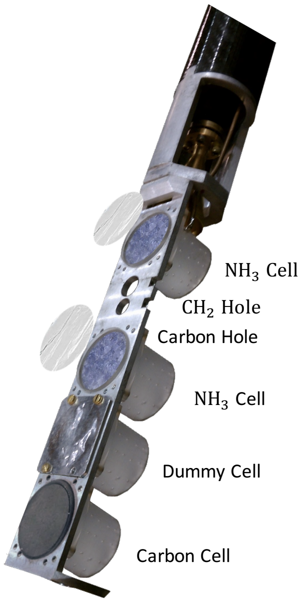

Figure 3-14: The end of the target insert with a NH_3 cell, a CH_2 hole, a carbon hole, a NH_3 cell, a dummy cell and a carbon cell from top to bottom.

Before the experiment, the ammonia beads were irradiated with a 10 MeV linear accelerator at the National Institute of Standards and Technology (NIST) to produce a few additional radicals in the material. The irradiation causes the normally colorless frozen ammonia beads to turn a deep purple color, as shown in Fig. 3-15. The radicals can speed up the DNP process but also increase the proton depolarization rate, so the number of radicals in the material must be carefully balanced to maintain a high polarization. As more electron beam is delivered to the ammonia, the more of the excess radicals, the less efficient of the DNP process. Therefore, the ammonia beads need to be heated between 70 and 100 K for 10 to 60 minutes to force the radicals to recombine after a long beam run. This process is called annealing the target. While anneals allow polarization recovery for a given ammonia sample, the sample still have a limited lifetime due to creation of bad radicals from accumulated radiation damage and thus need to be replaced periodically[111].

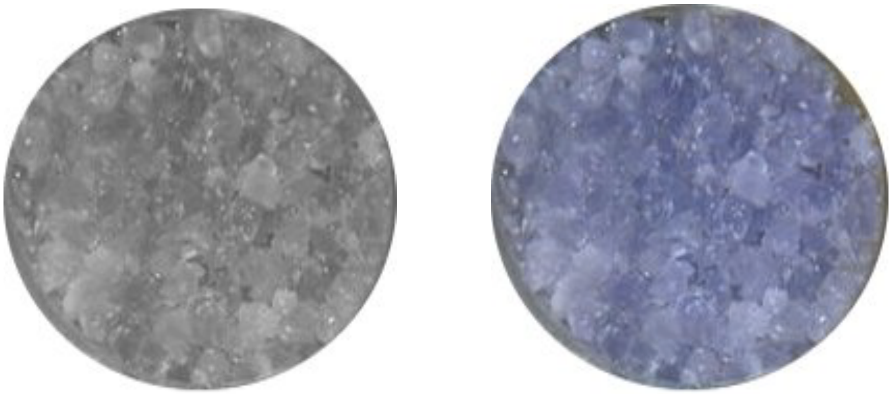

Figure 3-15: NH_3 beads before (left) and after (right) irradiation.

The microwaves to drive the spin transition in DNP are provided via an Extended Interaction Oscillator (EIO) tube and carried via waveguides to a horn positioned near the ammonia cup. The optimal frequency of the microwave radiation is not a constant value due to the radiation damage and need to be tweaked during the run period.

3.4.3 Target Polarization Measurement

To measure the proton polarization, a nuclear magnetic resonance (NMR) system is used. When the spin system is irradiated by a RF field at the Larmor frequency perpendicular to the static target field, the spin system can either absorb or emit some energy as the spins flip. The system response to the RF irradiation is described by its magnetic susceptibility $\chi(\omega)$, which can be expressed as a dispersive term $\chi'(\omega)$

and an absorptive term $\chi''(\omega)$[112]:

$$\chi(\omega) = \chi'(\omega) - i\chi''(\omega). \tag{3.15}$$

The integral of the absorptive portion $\chi''(\omega)$ over frequency is proportional to the polarization[113]:

$$P = K \int_0^\infty \chi''(\omega) d\omega, \tag{3.16}$$

where the constant K accounts for the correction factor for the NMR system properties, such as spin density and gyromagnetic ratio. The absorptive signal can be observed using the NMR coil via a Q-meter. The NMR circuit surrounds or is embedded in the target material with inductance L_C and resistance r_C, and its impedance can be changed under an inductive coupling between spins in the material and the coil's magnetic field as:

$$\begin{aligned} Z_C &= r_C + i\omega L_C \big[1 + 4\pi\eta\chi'(\omega) - i4\pi\eta\chi''(\omega)\big] \\ &= r_C + 4\pi\omega L_C \eta\chi''(\omega) + i\Big[\omega L_C\big(1 + 4\pi\eta\chi'(\omega)\big)\Big], \end{aligned} \tag{3.17}$$

where η is the filling factor of the coil. The Q-meter is connected to the NMR coil via a coaxial transmission cable, a capacitor C, and a damping resistance R that forms a series LRC circuit with resonance $\omega_0 = \sqrt{L_C C}$ at the proton's Larmor frequency. When scanning RF frequency through ω_0, the inductance is changed as the target material absorbs or emits energy, and so does the complex output voltage $V(w, \chi)$ since it is proportional to χ. In the absence of χ, $V(w, 0)$ is measured, and is often referred as the Q-curve. For a positive target polarization, the impedance is increased around ω_0 of the particle since target spins absorb energy from the RF to flip from aligned (low energy) to anti-aligned (high energy), while the impedance is decreased around ω_0 for a negative polarization. The signal difference between the polarized case and the Q-curve (baseline) gives the NMR signal[112]:

$$S(\omega) = Re[V(w, \chi) - V(w, 0)] \approx \chi''(\omega). \tag{3.18}$$

Therefore, integrating the dip or the peak in the signal due to absorption or emission provides a proportional measure of the material's polarization. The left plot of Fig. 3-16 shows the the raw signal in red with the baseline signal in blue, while the right plot shows the subtracted NMR signal.

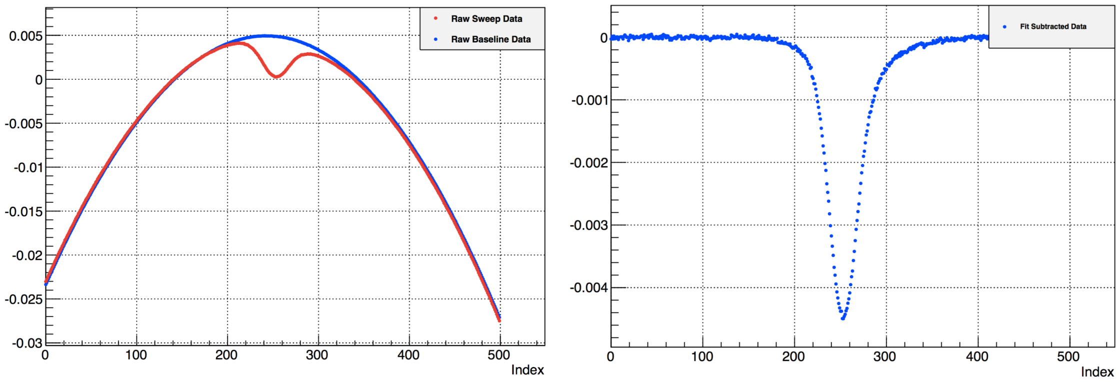

Figure 3-16: An typical NMR signal for the polarized ammonia target. The horizontal axis index is proportional to the frequency of the RF generator. The left plot shows the raw signal (red) and the Q-curve signal (blue), while the right plot shows the NMR signal after subtracting the Q-curve from the raw signals. Plot reproduced from [114].

The NMR method is a relative proton polarization measurement and needs to be calibrated. In the E08-027 experiment, it was calibrated with thermal equilibrium measurements with known polarization P_{TE} shown in Eq. 3.11. The absolute proton polarization can then be expressed as

$$P = \frac{\int_0^\infty S_{enh}(\omega)d\omega}{\int_0^\infty S_{TE}(\omega)d\omega} P_{TE}, \tag{3.19}$$

where S_{TE} is the NMR signal at thermal equilibrium and S_{enh} is the NMR signal during experimental run. The calibrated polarization for the 2.5 T target field is shown run-by-run with an average polarization of 15% in Fig. 3-17, while the average polarization was $\approx$ 70% for the 5T target field, shown in Fig. 3-18. The target polarization uncertainty is still being finalized. There are two major contributions to the uncertainty: one is from the uncertainty of the NMR signal; the other is the uncertainty in the magnetic field and temperature readings of the TE measurement.

The current estimate of the uncertainty is about 1% relative for the sample with 8 TE measurements, and 5% relative for the worst case where only one TE measurement was performed.

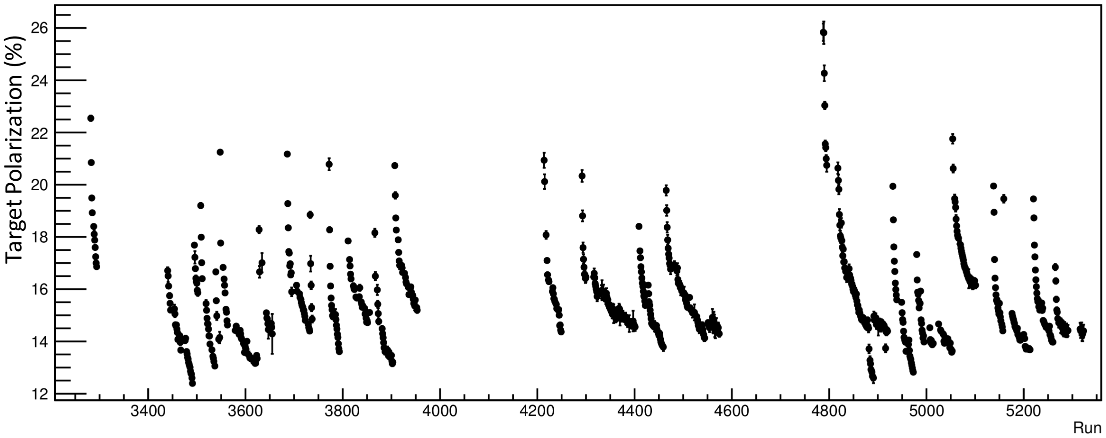

Figure 3-17: Target polarization for the 2.5 T field configuration for each run. Plot reproduced from [114].

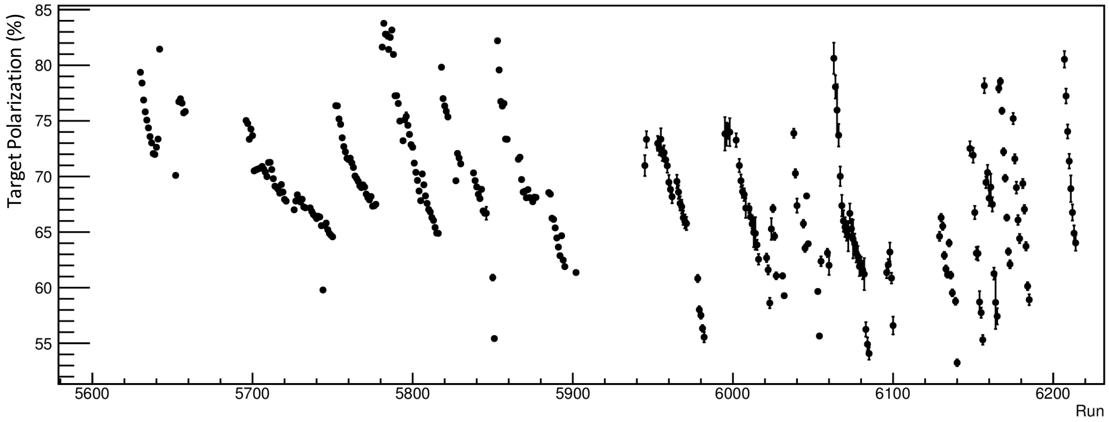

Figure 3-18: Target polarization for the 5 T field configuration for each run. Plot reproduced from [114].

3.5 Septum Magnets

During the g_2^p experiment, a pair of room temperature septum magnets (id 10 in Fig. 3-3) were used to bend the scattered electrons from a scattering angle of 5.77° into the minimum achievable central angle of HRS (12.5°). Each magnet has three pairs of coils with $(48-48-16)$ turns on the top and $(48-48-16)$ turns on the bottom, as shown in Fig. 3-19. Unfortunately, the right top septum electrical lead was burnt twice, and the burnt wires were shorted to iron, which resulted in $(40-32-16)$ turns and $(40-00-16)$ turns, respectively. The left septum coils remained unchanged. The septum configurations in Table 3.1 refer to the top right septum coil status during the run.

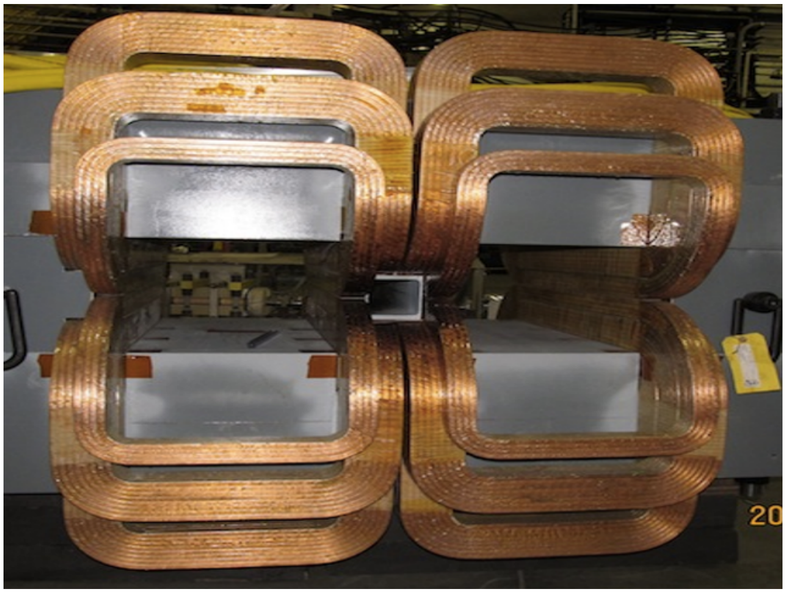

Figure 3-19: Picture of the septum magnet pair. The unscattered beam hit in the pipe between the septums (perpendicular to the paper).

3.6 High Resolution Spectrometers

E08-027 experiment used the two standard and nearly identical Hall A high resolution spectrometers (HRS) to detect the scattered electrons, located 12.5° respect to the beam line on each side. Each HRS consists of three superconducting quadrupole and one superconducting dipole magnets in a QQDQ configuration, as shown in Fig. 3-20. The first quadrupole Q1 is convergent in the dispersive (vertical) plane while Q2 and Q3 provide a transverse focusing. The dipole bends the electrons 45° in the vertical direction with a momentum resolution at the 10^{-4} level. The main characteristics of the HRS are summarized in Table 3.3.

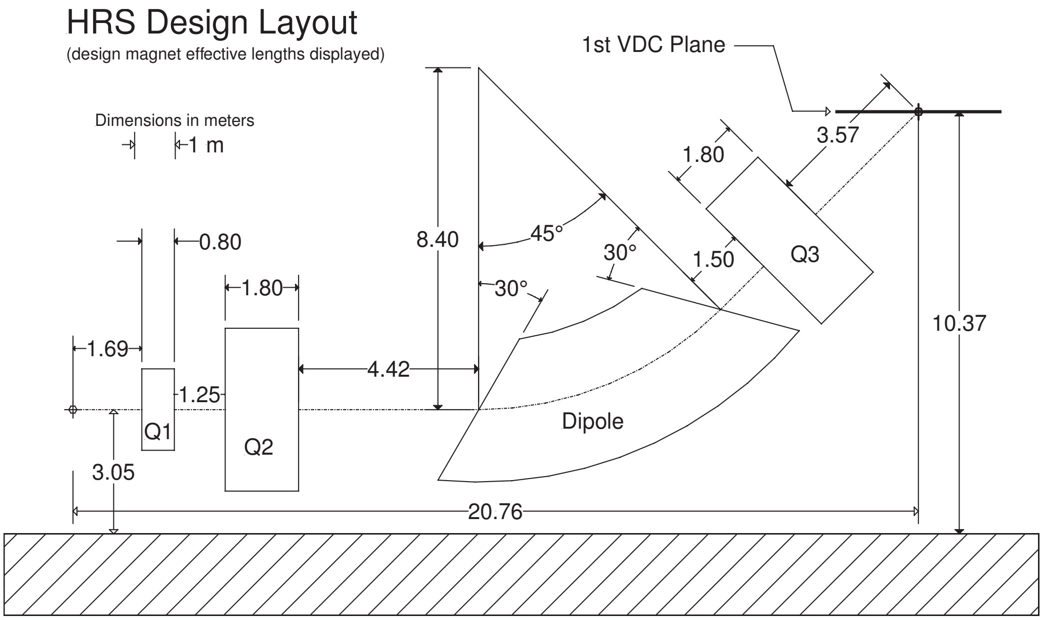

Figure 3-20: Sideview of the Hall A High Resolution Spectrometer's magnet system[92].

3.7 Detector Package

The detector package for each HRS is installed in a shield hut with the data acquisition electronics (DAQ) at the end of the HRS magnet group (id 14 in Fig. 3-4). For E08-027 experiment, the detector configuration are shown in Fig. 3-21.

Details of these detectors will be discussed in this section.

Configuration	QQDQ vertical bend
Bending angle	45°
Optical lengh	24.2 m
Momentum range	0.3-4.0 GeV/c
Momentum acceptance ($\delta p/p$)	$\pm 4.5\%$
Momentum resolution	2×10^{-4}
Dispersion at the focus (D)	12.4 m
Radial linear magnification (M)	-2.5
D/M	5.0
Horizontal angular acceptance	± 30 mrad
Vertical angular acceptance	$\pm$ 60 mrad
Horizontal resolution	1.5 mrad
Vertical resolution	4.0 mrad
Solid angle at $\delta p/p = 0, y_0 = 0$	6 msr
Transverse length acceptance	± 5 cm
Transverse position resolution	2.5 mm

Table 3.3: Main characteristics of the standard Hall A high resolution spectrometers[92]. The resolution values shown are the FWHM values.

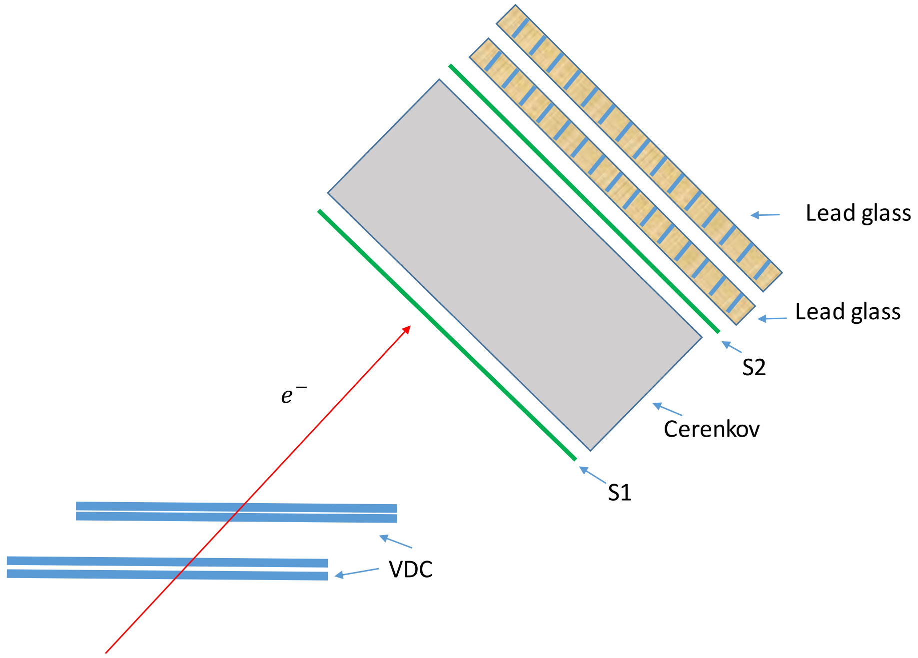

Figure 3-21: Detector package for HRS.

3.7.1 Vertical Drift Chambers

A pair of vertical drift chambers (VDC) are used to provide the particle tracking information in each HRS. The tracking information combined with the spectrometer optics can be used to reconstruct the position, angle, and momentum of the scattered particles at the interaction point at the target.

The two VDCs are placed horizontally, with the long edge along the nominal particle dispersive direction. The two chambers are separated by 335 mm, as shown in Fig. 3-22. Each chamber is made of two wire planes (368 sense wires spaced by 4.24 mm per plane) in a UV configuration. Each plane is oriented at 90° to each other and at 45° with respect to the dispersive direction.

The frame is applied at a negative high voltage of -4 kV and the wires are kept at the ground level. The drift chambers are filled with a mixture of 62% argon and 38% ethane. Argon serves as the ionizing medium while ethane absorbs the photons produced from ionization. When a charged particle crosses the VDC planes, it ionizes the atoms along its path and leaves a track of electrons and ions along its trajectory behind. The ionized electrons drift along the electric field lines at a velocity of $\approx$ 50 μm/ns and produce an electron avalanche as they approach the sense wires where the electric field is the strongest. This avalanche fires the sense wires and generates a timing signal which is then read out by a time to digital converter (TDC). Electrons that travel across the wires at an angle 45° typically fire four to six wires, as shown in Fig. 3-23. The "start" for the TDC is the signal from the sense wire while the event trigger supervisor provides the "stop". The drift distance for each wire in a cluster is determined by the drift velocity and the TDC signal. A linear fit of the drift distance gives the cross-over point at the sense wire plane. The trajectory of the particles can be reconstructed by the VDC accurately with a position and an angle resolution of 100 μm and 0.5 mrad, respectively.

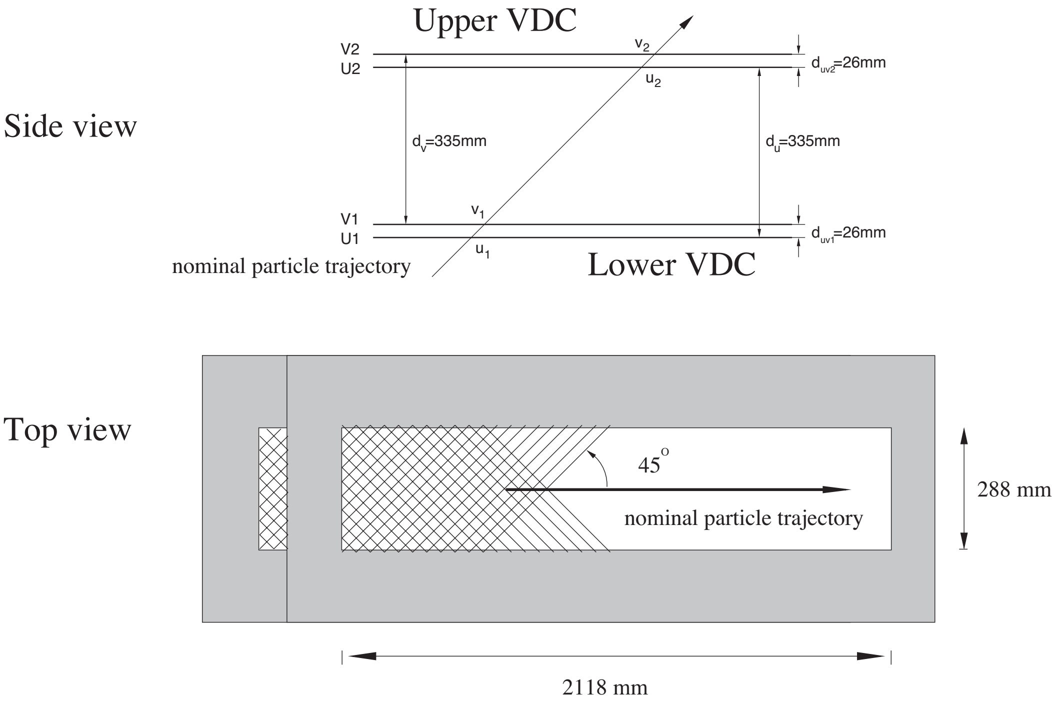

Figure 3-22: Top and sideview of the VDCs[92].

3.7.2 Scintillator Planes and Trigger Electronics

In E08-027 experiment, two scintillator planes, S1 and S2m, were used to form the trigger for the DAQ system. Both planes are composed of overlapping paddles of plastic scintillators[92], and are separated 2 m apart with S1 before the Cherenkov detector and S2m after, as shown in Fig. 3-24. The S1 plane is comprised of 6 overlapping paddles, while there are 12 paddles for S2m. Each paddle is viewed by two photomultiplier tubes (PMTs) placed at its two ends. The timing resolution for each plane is about 0.3 ns. The main trigger T3 (T1) on Left HRS or LHRS (Right HRS or RHRS) is formed as follows:

- A paddle in S1 is defined to be fired if there are signals from both its left and right PMTs;

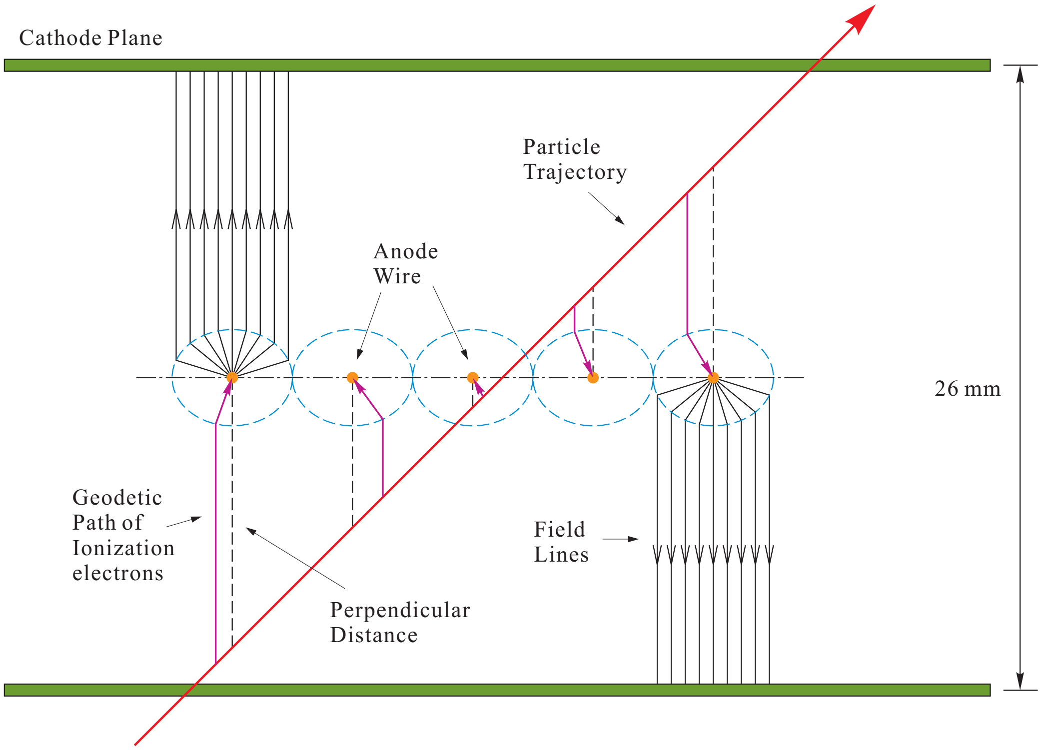

Figure 3-23: Configuration of wire chambers[92, 104].

- A paddle in S2m is defined to be fired if there are signals from both its left and right PMTs;
- One S1 paddle and one S2m paddle are both fired within a specified timing window.

These main T3(T1) triggers represent "good" events. In order to monitor the efficiency of the main trigger T3 (T1), a secondary trigger T4 (T2) was formed on LHRS (RHRS). These efficiency triggers are formed exclusive to the main triggers as:

- Either the S1 or S2m plane fires, but not both.
- The event caused the gas Cherenkov to fire.

The T4 (T2) triggers represent possible "good" events but one of the scintillator planes failed to detect.

All triggers are counted by helicity-gated scalers (deadtime-less) and sent to the trigger supervisor (TS). The TS synchronizes all the detector readouts and determine

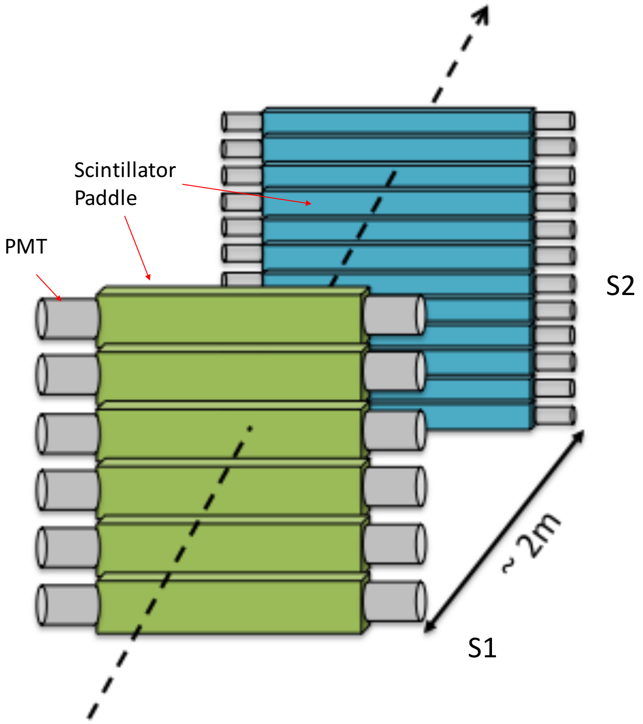

Figure 3-24: A diagram of the S1 and S2m scintillator planes. Plot reproduced from [115].

if the event should be sent to the DAQ system. When the event rate is high, the DAQ system cannot read all events and has a deadtime (DT). The deadtime comes from two sources: computer deadtime, which is related to the speed of data processing and can be decreased by scaling the incoming events with a prescale value (ps) at the TS; electronic deadtime, arises due to the response of the detectors and is usually negligible compared to the computer deadtime. The fraction of events recorded by the DAQ is called the livetime $LT = 1 - DT$ and can be measured as:

$$LT^{\pm} = \frac{ps \cdot T^{\pm}_{acc}}{T^{\pm}_{tot}}, \tag{3.20}$$

where ± denote the helicity status, $T^{\pm}_{acc}$ is the number of triggers accepted by the DAQ for the corresponding helicity, and $T^{\pm}_{tot}$ is the total number of triggers for that helicity recorded by the scaler.

The trigger efficiency is defined as:

$$\eta = \frac{T_{main}}{T_{main} + T_{eff}}, \tag{3.21}$$

where T_{main} and T_{eff} are the total numbers of trigger counts for the main and the efficiency triggers, respectively. Fig. 3-25 shows the trigger efficiency during E08-027 experiment. The trigger efficiency was very high (mostly above 99%) for all production runs, which contributes less than 1% correction to the cross section.

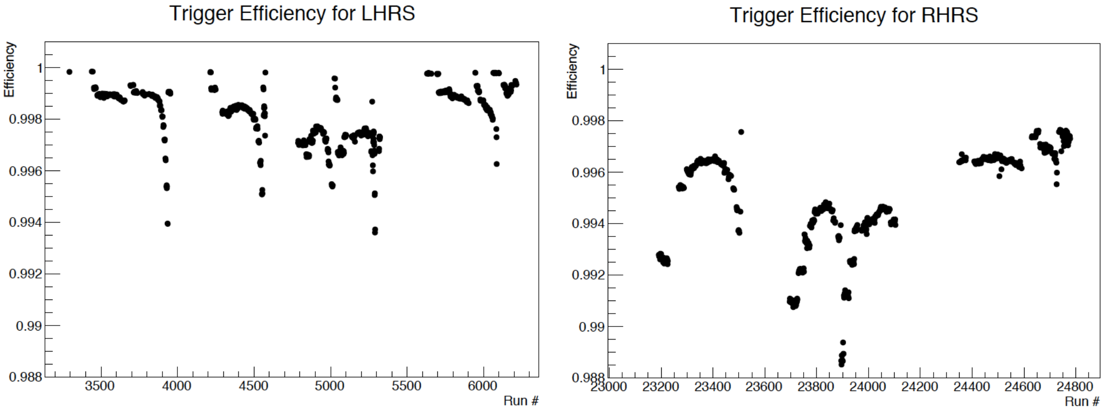

Figure 3-25: Trigger efficiencies for LHRS (left) and RHRS (right), using Eq. 3.21. Plot reproduced from [116].

3.7.3 Gas Cherenkov Detector

E08-027 experiment measured inclusive electron scattering, thus the particle detection must be able to distinguish electrons from background particles (mostly pions). The gas Cherenkov detector was sandwiched between two scintillator planes to provide the PID information, together with two layers of lead glass calorimeter, which will be discussed in Sec. 3.7.4.

The principle is that when a charged particle travels through a transparent material (with refraction index n) at a speed higher than the light in that material, the disturbance to the local electromagnetic field accumulates in the medium as a result of limited response speed (light speed c/n), thus a coherent shockwave is radiated at an angle $\theta = \arccos(\frac{1}{n\beta})$ with respect to the particle direction. This phenomenon is known as Cherenkov radiation. Fig. 3-26 shows the geometry of the Cherenkov radiation. The threshold for the production of Cherenkov radiation is given by

$$\beta c \geq \frac{c}{n} \quad \text{or} \quad \beta \geq \frac{1}{n} \tag{3.22}$$

which means the momentum of the particle of mass m must satisfy:

$$p = \frac{mv}{\sqrt{1-(\frac{v}{c})^2}} \geq \frac{mc}{\sqrt{n^2-1}}. \tag{3.23}$$

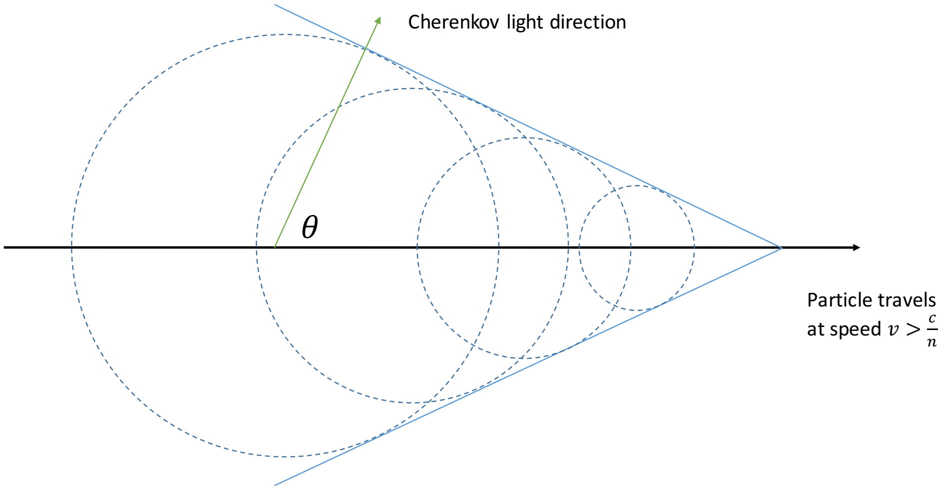

Figure 3-26: Cherenkov radiation is emitted in a cone with $\theta = \arccos(\frac{1}{n\beta})$.

During the experiment, the Cherenkov tanks in both HRSs are filled with carbon dioxide gas with refraction index $n = 1.00041$[92]. From Eq. 3.23, the momentum threshold for electrons is 0.018 GeV/c, whereas the threshold for pions is 4.87 GeV/c. Thus, in the designed HRS momentum range 0.3 $\sim$ 4.0 GeV/c, electrons emit Cherenkov radiation, but pions do not. So the gas Cherenkov detector can be used to identify electrons from pions.

The path length for a particle to travel in the Cherenkov detector is about 1.5 m. 10 spherical mirrors were installed partially overlapped to focus the Cherenkov light to 10 PMTs. The signal from the PMTs passes through an analog-to-digital converter (ADC) and is then summed together to represent the total light output for the corresponding event. However, particles, such as pions can still have a small probability to generate Cherenkov light by producing δ-electrons. These contamination events can be further cleaned by using the lead-glass calorimeter in Sec. 3.7.4.

3.7.4 Lead Glass Calorimeters

In E08-027 experiment, two layers of lead glass in each HRS were used to provide additional pion rejection capability in addition to that of the gas Cerenkov counter. When high energy charged particles pass through a dense material like lead glass, an electromagnetic shower of photons and electron-positron pairs are produced. The total amount of light radiated is proportional to the energy deposited in the material and can be detected by PMTs mounted at the ends of lead glass blocks. For electrons, as well as positrons and photons, most of their energy will be deposited in HRS's calorimeters. However, charged hadrons, such as pions, have a low probability to produce an electromagnetic shower, and they trigger only a small signal from ionization energy loss. Therefore one can separate electrons and pions by looking at the deposited energy difference.

The left and the right HRS calorimeters are slightly different in construction[92]. For LHRS, both layers of lead glass are oriented perpendicular to the particle's track and each contained 34 lead glass blocks of size 14.5 cm×14.5 cm×30 cm (first layer) or 14.5 cm×14.5 cm×35 cm (second layer). The first layer is often referred as pionrejector 1, while the second layer pionrejector 2. For RHRS, the first layer (preshower) consisted of 48 10 cm×10 cm×35 cm lead glass blocks oriented perpendicular to the particle track. The second layer (shower) is composed of 80 15 cm×15 cm×35 cm blocks and oriented parallel to the particle track. The major difference is that the scattered electrons deposit their full energy in the RHRS calorimeter, while for the LHRS they deposit only about 95% of energy at a momentum of 1 GeV and this fraction varies with energy.

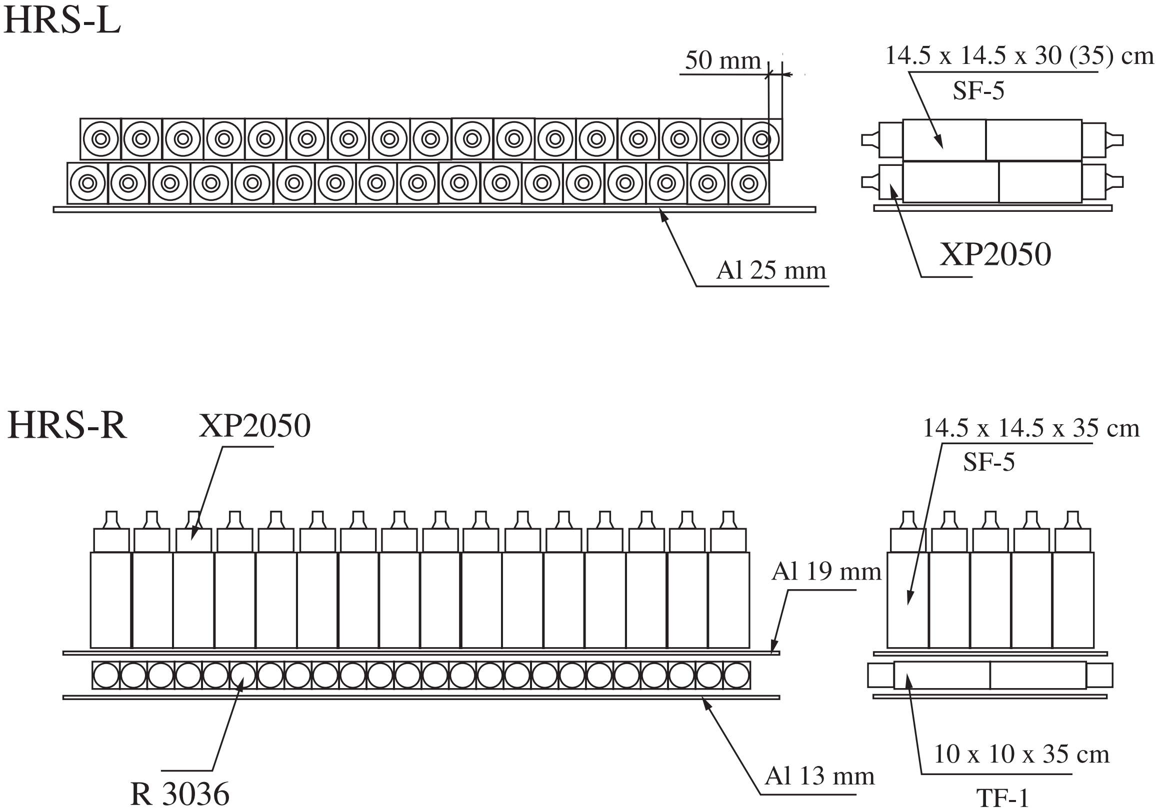

Figure 3-27: The electromagnetic calorimeters in the HRS[92]. The scattered particles direction is from bottom to top.

Chapter 4

Data Analysis

In E08-027 experiment, the proton spin structure functions are extracted from asymmetries and unpolarized cross sections measured using the polarized electron beam scattering off polarized NH_3 (proton) target, according to Eq. 2.57 and Eq. 2.58. This chapter will present an overview of the data analysis.

4.1 Asymmetries and Cross-Sections

The longitudinal and transverse physics asymmetries are defined as the ratio of the difference in polarized cross sections to the sum, and can be measured experimentally:

$$A_{\parallel,\perp}^{phys} = \frac{A_{\parallel,\perp}^{raw}}{f P_b P_t}, \tag{4.1}$$

where f is a dilution factor to account for events arising from unpolarized material in the target, P_b is the beam polarization, P_t is the target polarization, A_{raw} is the raw asymmetry and can be calculated from the measured quantities (number of events $N^{\pm}$, live time $LT^{\pm}$, charge $Q^{\pm}$) in the $\pm$ helicity state:

$$A_{raw} = \frac{\frac{N^+}{LT^+Q^+} - \frac{N^-}{LT^-Q^-}}{\frac{N^+}{LT^+Q^+} + \frac{N^-}{LT^-Q^-}}. \tag{4.2}$$

The Born asymmetries, which is commonly used to compare with theoretical results (applied in Eq. 2.57 and Eq. 2.58), can then be calculated from the physics asymmetry by applying internal and external radiative corrections:

$$A_{\parallel,\perp}^{Born} = A_{\parallel,\perp}^{phys} + A_{\parallel,\perp}^{ext} + A_{\parallel,\perp}^{int}. \tag{4.3}$$

The physics unpolarized cross section is defined as the unpolarized cross section from interested particle (proton) only, and can be expressed as the product of the total raw unpolarized cross section σ_0^{raw} and the dilution factor:

$$\sigma_0^{phys} = f\sigma^{raw}. \tag{4.4}$$

σ_0^{raw} can be calculated in terms of measurable quantities:

$$\sigma_0^{raw} = \frac{d^2\sigma^{raw}}{d\Omega\ dE'} = \frac{ps \cdot N_{acc}}{LT \cdot \epsilon_{det}} \frac{1}{N_{in}\rho\Delta z} \frac{1}{\Delta\Omega\Delta E'} \tag{4.5}$$

where N_{acc} is the number of events survive the HRS acceptance and PID cuts, ps is the prescale factor, LT is the livetime, ϵ_{det} is the product of hardware and software cut detector efficiencies, $N_{in} = Q/e$ is the number of electrons incident on the target measured from BCMs, ρ is the target density, $\Delta\Omega$ ($\Delta E'$) are the solid angle (momentum) acceptance seen by the spectrometer, and Δz is the target length.

The unpolarized Born cross section can be determined after applying external and internal radiative corrections:

$$\sigma_0^{Born} = \sigma_0^{phys} + \sigma_0^{int} + \sigma_0^{ext}. \tag{4.6}$$

Finally, the cross section difference can be expressed as

$$\Delta\sigma_{\parallel,\perp}^{phys} = 2A_{\parallel,\perp}^{phys}\sigma_0^{phys}, \tag{4.7}$$

and also need be radiative corrected to be compared with theoretical predictions.

4.2 Detector Calibration and Efficiencies

The detector efficiency ϵ_{det} in Eq. 4.5 can be expressed as:

$$\epsilon_{det} = \epsilon_{cer}\epsilon_{cal}\epsilon_{T}\epsilon_{VDC} \tag{4.8}$$

where ϵ_{VDC} is the VDC efficiency, ϵ_T is the trigger efficiency, ϵ_{cer} and ϵ_{cal} are the Cherenkov and lead glass calorimeter cut efficiencies respectively. The product ϵ_{PID}=$\epsilon_{cer}\cdot\epsilon_{cal}$ is also called the PID efficiency.

4.2.1 Gas Cherenkov

As discussed in Sec. 3.7.3, the Gas Cherenkov provides part of the particle identification for E08-027 experiment. In this section, the calibration procedure and its cut efficiency will be discussed.

4.2.1.1 Calibration

The gas Cherenkov contains 10 individual mirrors to focus the Cherenkov light to 10 individual PMTs. The signal sum of the 10 ADC signals of PMTs is used as one of the PID cuts to select electron events. Calibration of the gas Cherenkov is to align the response of all 10 ADC signals by setting their single photo-electron (SPE) peaks at one particular ADC channel. A good electron event usually produces multiple photoelectrons in the gas Cherenkov, while the SPE events result from secondary scattering (such as pion-induced δ electrons) within the detector or from noise in the photomultiplier tube.

A typical signal for the ADC of one PMT is shown in the left plot of Fig. 4-1. To isolate the SPE peak (around 120) cleanly, one needs to remove the contribution from the pedestal and the main peak. Fig. 4-2 shows the geometric cut combined with tight timing cuts that are applied to exclude the pedestal and the main peak contributions. The isolated peak is fitted with a Landau-Gaussian convolution function to account for the residual background tail leftover after cuts are applied, as shown in the right

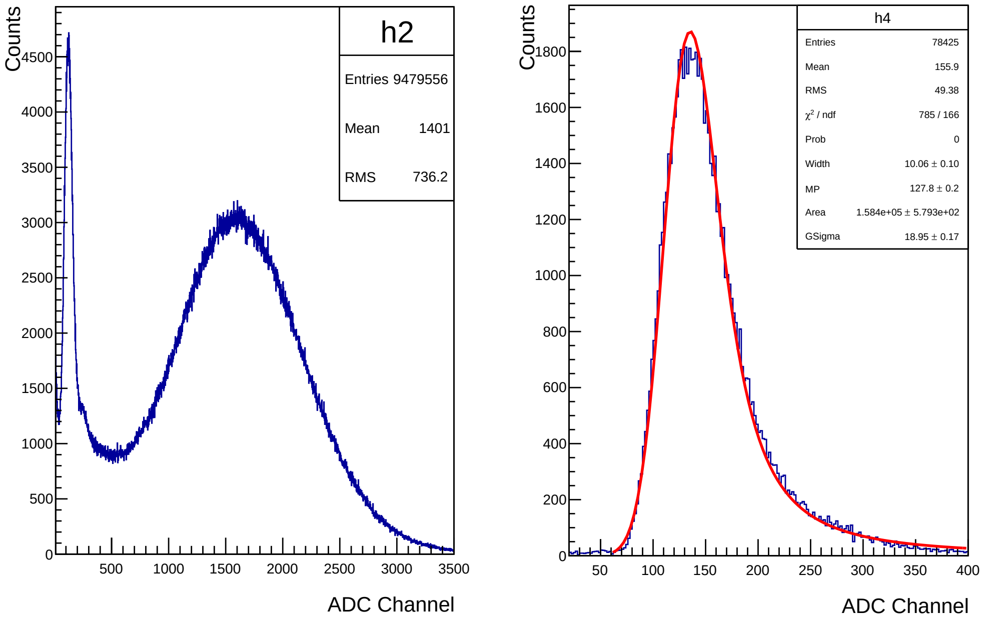

Figure 4-1: A typical ADC signal from one PMT of Gas Cherenkov.

plot of Fig. 4-1. Once the center of the peak is determined from the fit, a calibration constant is obtained to shift that peak to channel 100 for all 10 PMT signals.

4.2.1.2 Cut Efficiency

Gas Cherenkov is used to identify good electron events to be used in the final analysis by cutting out other events, such as pions. As seen in Fig. 4-1, on the left side of the ADC spectrum, there are some pedestal or δ-electron events and these events need be removed. The Cherenkov cut is optimized to maximize the pion rejection efficiency while minimizing the inefficiency caused by removing good electron events.

To determine the cut efficiency for Cherenkov on the LHRS, a electron sample was chosen in the lead glass calorimeter which are well separated from the pedestal or pion events, while a pion sample was selected to be away from the good electron events, as shown in the left plot of Fig. 4-3. The electron cut efficiency ϵ_{cer} can be

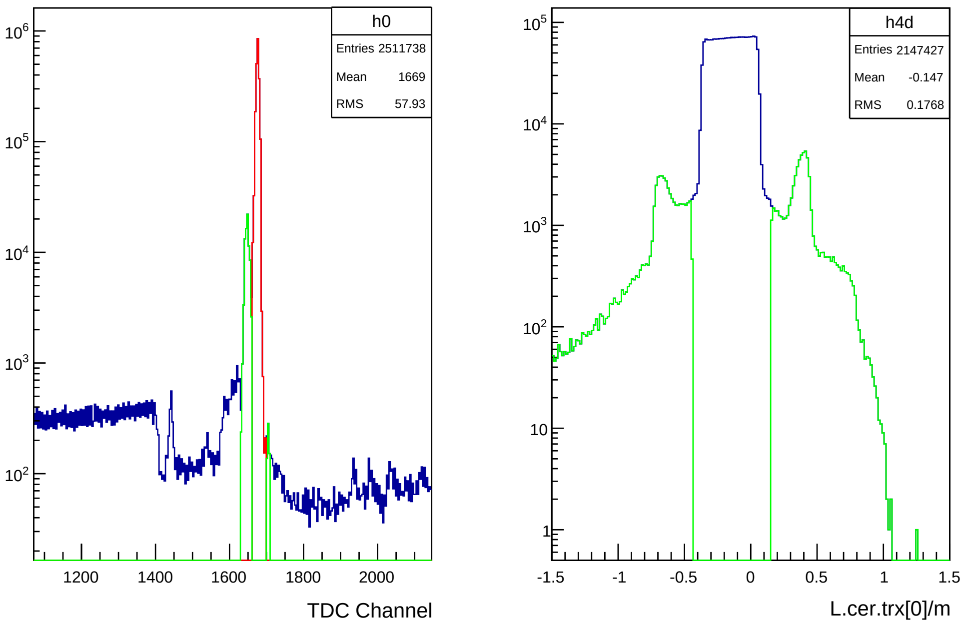

Figure 4-2: The geometric cut (right) and a tight timing cut (left) to isolate the SPE peak. The green curve are the selected events for both plots. The geometric cut is to exclude the main peak events, while the timing cut is to minimize the noise background. Most of selected events come from photon leakage of adjacent mirrors.

defined as:

$$\epsilon_{cer} = \frac{N_{e-acc}}{N_{e-tot}}, \tag{4.9}$$

where N_{e-acc} is the number of events in the electron sample (with total sample number N_{e-tot}) that survive the Cherenkov cut selection, and the pion rejection efficiency η_{cer} is defined by

$$\eta_{cer} = \frac{N_{\pi-acc}}{N_{\pi-tot}}, \tag{4.10}$$

where $N_{\pi-acc}$ is the number of events in π sample (total sample number $N_{\pi-tot}$) that survive the Cherenkov cut selection.

The cut optimization for Cherenkov cut is shown in the right plot of Fig. 4-3. The cut is defined as the sum of 10 ADC signals above a chosen ADC channel. The electron cut efficiency remains flat when cutting below ADC channel 200 and then decreases, while the pion rejection efficiency increases rapidly till 120 and then slightly increases for higher cut. During data analysis, the gas Cherenkov cut was placed at channel 150 for RHRS, while on the LHRS the cut was placed at channel 200. The electron cut efficiency is maintained high for both cases, as shown in Fig. 4-4.

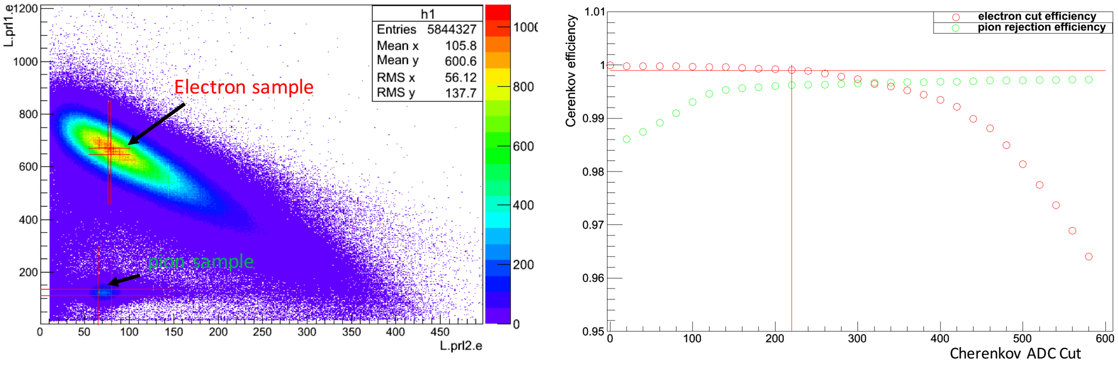

Figure 4-3: An optimization of Cherenkov Cut. The left plot shows the sample selection using left HRS pion rejectors while the right shows the electron cut and pion rejector efficiencies versus cut. The red vertical line located at ADC channel 210 shows the electron cut with an electron efficiency 99.9%.

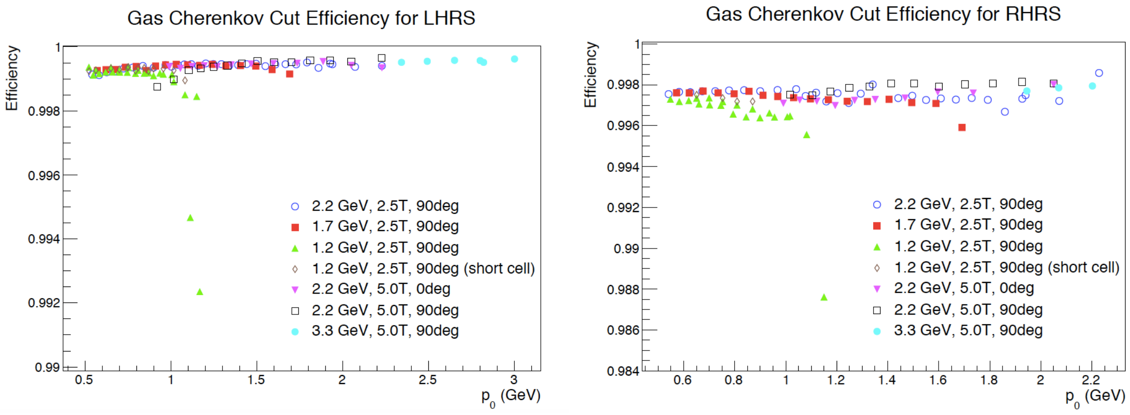

Figure 4-4: Electron cut efficiencies for the gas Cherenkov on the left and right HRS. The data points include one representative run for each kinematic setting. Plot reproduced from [117].

4.2.2 Lead Glass Calorimeter

As discussed in Sec. 3.7.4, the lead glass calorimeter provides particle identification in addition to the Gas Cherenkov for E08-027 experiment. In this section, the calibration procedure and its cut efficiency will be discussed.

4.2.2.1 Calibration

There are two layer of lead glass in each HRS. The layers of the LHRS calorimeter are referred as the first and second layer of the pion rejector (prl1 and prl2), while the two layers of the RHRS are referred as the preshower and shower for RHRS. The calibration is to convert the raw ADC signal from each PMT to the energy deposited within the corresponding lead glass block. Since the cascade of secondary particles is typically spread over several adjacent blocks of lead glass, the output of these blocks are summed to give the deposited energy.

As mentioned in Sec. 3.7.4, the calorimeter on RHRS is a full energy absorber (thickness around 20 radiation length) that absorbs the total energy of electrons. Its calibration is very straightforward, and the calibration constant can be obtained from the χ^2 minimization:

$$\chi^2 = \sum_{i}^{n} \left[\sum_{j} C_j \cdot (A_j^i - p_j) + \sum_{k} C_k \cdot (A_k^i - p_k) - P_{kin^i} \right]^2 \tag{4.11}$$

where i is for summing over all events used for the calibration; for each event, j (k) is the j-th (k-th) block in the preshower (shower), A_j^i (A_k^i) is the ADC value of the j-th (k-th) block in the preshower (shower), p_j (p_k) is the pedestal value of the j-th (k-th) block in the preshower (shower), P_{kin}^i is the momentum of the i-th event, and C_j (C_k) is the calibration constant to be determined for the preshower (shower).

However, for the LHRS, the electron energy is not fully deposited. Assuming the nominal electron track direction as the longitudinal direction, the average longitudinal shower profile can be described by a gamma distribution[118]:

$$\frac{dE}{dt} = E_0\beta(\beta t)^{\alpha-1}\frac{e^{-\beta t}}{\Gamma(\alpha)} \tag{4.12}$$

where t is the shower depth expressed in radiation length, $t^{\alpha-1}$ describes the rising part of the shower profile where particle multiplication occurs, $e^{-\beta t}$ represents the absorption process (Compton and photo effect for photons, stopping of electrons due to ionization) dominating at larger distance, α and β are parameters, $\Gamma(\alpha) = \int_0^\infty e^{-z}z^{\alpha-1}dz$. The shower max is found to grow logarithmically with energy E_0 of the incident particle

$$t_{max} = \frac{\alpha - 1}{\beta} = ln(\frac{E_0}{E_c}) - 0.5. \tag{4.13}$$

Therefore, the pion rejector can be calibrated in two steps:

The first step of calibration is to align the signal response for all blocks in each layer. As shown in Fig. 4-5, the pedestal signal is fitted with Gaussian function for the 22-th block in pion rejector 1 in the left plot, while the main signal is fitted with Gauss-Landau function in the right plot. The difference in the two peak positions defines the response of the block.

The second step is to obtain the proportional gain for each layer to convert to the deposited energy by fitting for all events:

$$\rho E'_{prl1} + \mu E'_{prl2} = \int_0^T \frac{dE}{dt} \tag{4.14}$$

where E'_{prl1} and E'_{prl2} are the sum of all aligned ADC signal (main peak signal subtracted by the corresponding pedestal) in pion rejector 1 and 2 respectively, ρ and μ are the gain factor to be determined from the calibration, and T is the radiation thickness of the trajectory. For the pion rejector, the lead glass type SF-5 has radiation length $X_0 = 2.55$ cm and critical energy $E_c = 15.8$ MeV, and a total radiation thickness $T = 11.3\ X_0$ for a nominal trajectory. Fig. 4-6 shows the reconstructed total energy versus momentum for all production momentum settings after calibrations.

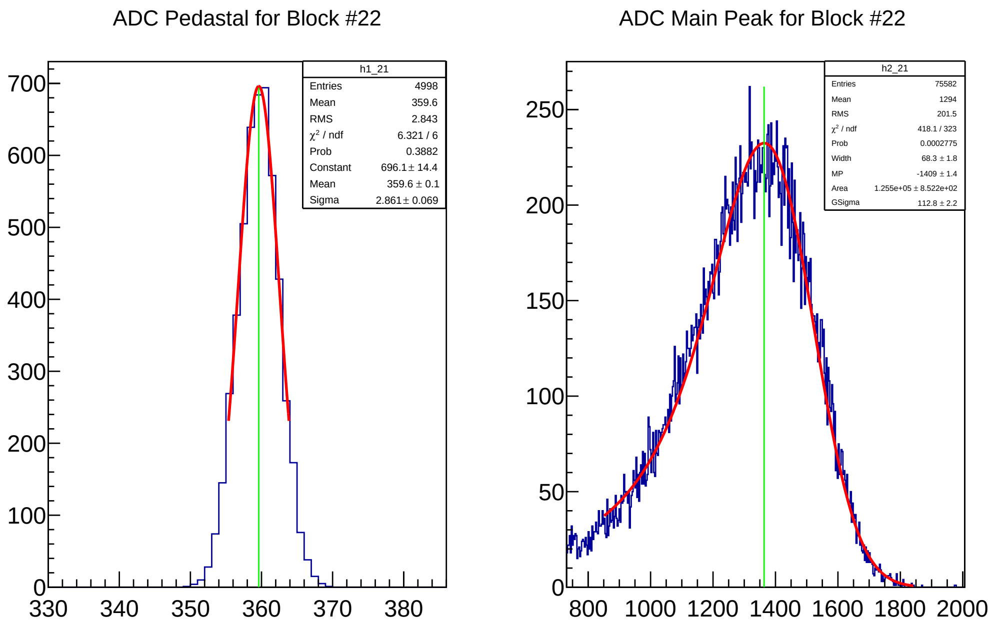

Figure 4-5: Pedestal signal (left) and Main signal (right) for the 22-th block in pion rejector 1.

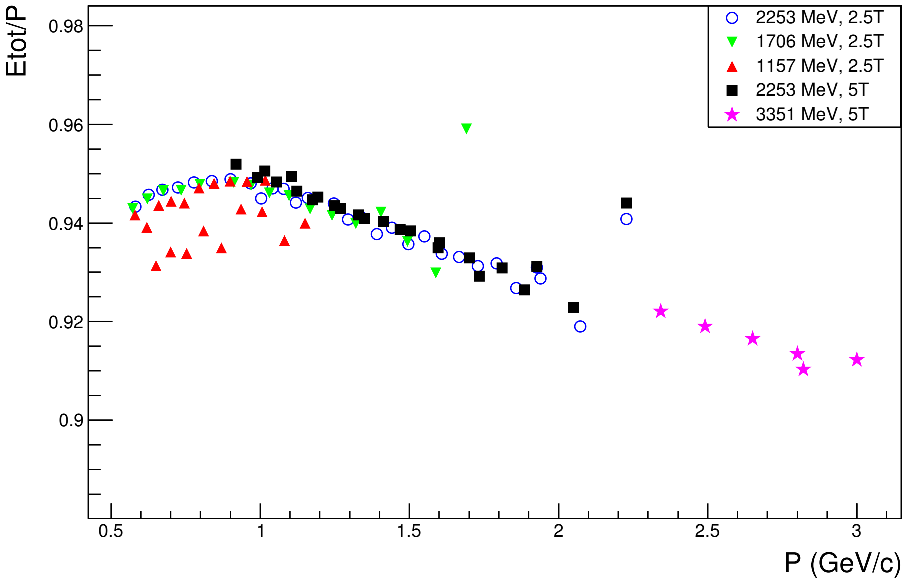

Figure 4-6: Reconstructed total energy versus momentum for pion rejector.

4.2.2.2 Cut Efficiency

Lead glass calorimeter was used to provide two standard PID cuts: one cut on the first layer of lead glass, the other on the total energy deposited in the calorimeter. Similar to the optimizing of Cherenkov cut, the lead glass cuts are studied using pure/clean electron sample events selected using the Cherenkov signal, and the cuts are optimized that the overall electron detection efficiency does not fall below 99%. The cuts are momentum dependent. The electron cut efficiency for lead glass is shown in Fig. 4-7.

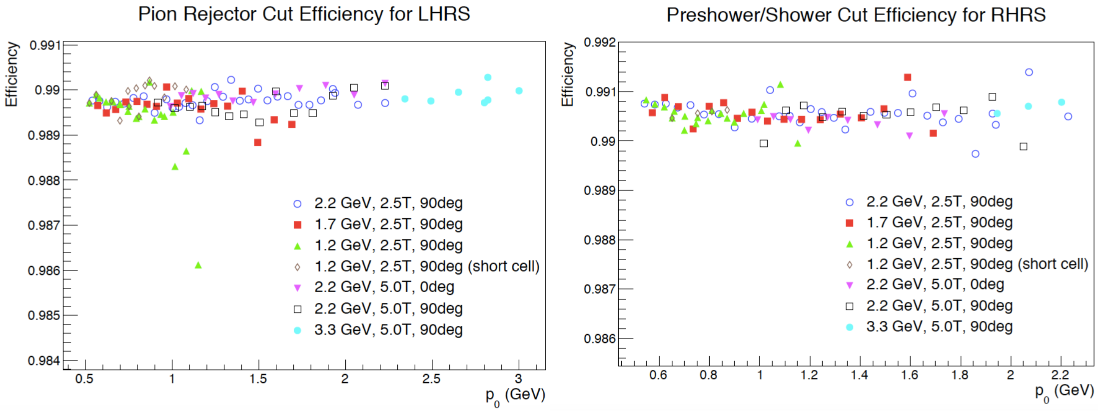

Figure 4-7: Electron cut efficiencies for the lead glass on the left and the right HRS. The data points include one representative run for each kinematic setting. Plot reproduced from [117].

After applying both Cherenkov cuts and lead glass cuts, the level of residual pion contamination is very low, with $\pi/e < 0.0052$ for all kinematic settings for both the left and right HRS[117].

4.2.3 VDC

As discussed in Sec. 3.7.1, the VDC provides particle tracking information for E08-027 experiment. In this section, the calibration procedure and its efficiency will be discussed.

4.2.3.1 Calibration

The VDC provides the tracking information by measuring the timing difference of signals in all sensed wires when a particle passes through. To compare the drift time spectrum from all the sensed wires, one need to remove timing offset due to the different cable length or signal processing for different wires. The calibration is to provide a reference timing position t_0 for the TDC spectrum of each wire in the plane. This reference position is determined by differentiating the region of short drift times channel by channel to select the max-slope and then extrapolating the max-slope point linearly to the channel axis. The point of intersection is chosen as t_0. Then the TDC spectrum is shifted so the t_0 is positioned at 0. Fig. 4-8 shows a typical time spectrum after t_0 correction.

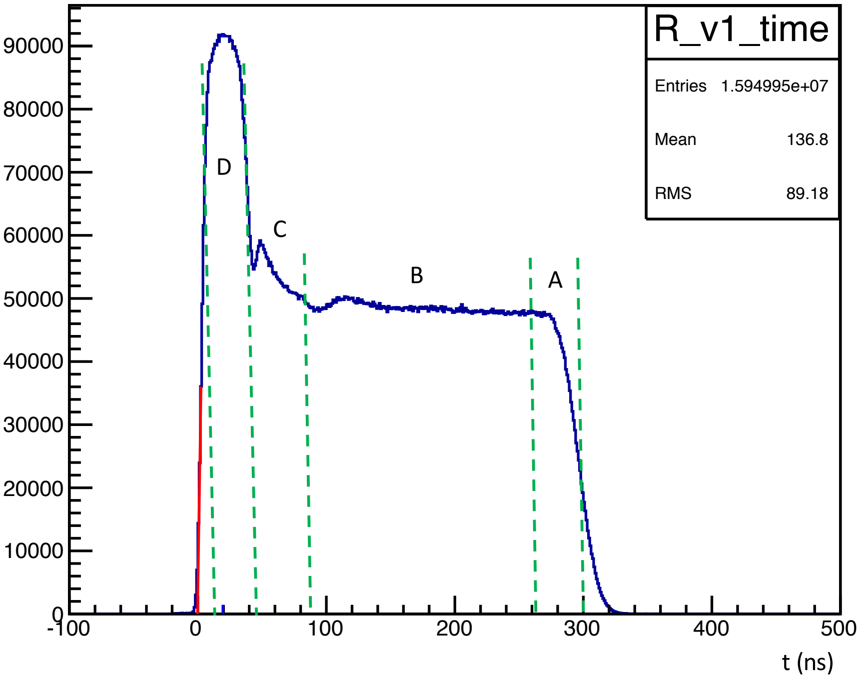

Figure 4-8: A typical time spectrum after t_0 correction for all wires on one VDC plane for one run. The red linear curve is the max-slope point extrapolated to the horizontal axis, to check the t_0 correction.

The time spectrum of Fig. 4-8 is not flat and has several features. Assuming a uniform number of trajectories crossing the VDC area, in an element of drift cell, the number of events per time bin can be expressed as:

$$\frac{dN}{dt} = \frac{dN}{ds}\frac{ds}{dt} \tag{4.15}$$

where ds is an element of distance along an electric field line in the drift cell, dN/ds is the linear density of tracks along ds, and ds/dt is the mean drift velocity of the ionization within ds. The distinct regions of the time spectrum can be understood as follows[119]:

- **Region A**: region near the HV frame, particles has larger trajectory angles and intersecting a smaller portion of the cell near the HV frame, which results in a less detecting probability (smaller dN/ds) and a long drifting time.
- **Region B**: a flat respond region with all the field lines are parallel, and hence a constant dN/ds and ds/dt.
- **Region C**: the transition region where field lines begin to change from parallel to quasi-radial closer to the sense wires, dN/ds begins to increase while ds/dt remains more or less constant.
- **Region D**: the region very close to the sense wires where the drift velocity ds/dt increases drastically and dN/ds goes through a maximum.

4.2.3.2 Efficiency

The VDC efficiency is defined as the fraction of good events with a successful track reconstruction to the total events.

For the HRS set-up, we can use the PID and acceptance cuts to select a clean sample of electrons and study how many of these events have valid tracks as well as blocks along such tracks to verify good track reconstruction. The VDC efficiency can then be redefined as:

$$\epsilon_{VDC} = \frac{N_{good}}{N_{tot}} \tag{4.16}$$

where N_{tot} is the total number of events that survive the acceptance and PID cuts (sample), and N_{good} is the number of events with a successful track reconstruction and which is also verified by the lead glass calorimeter signal. PID cuts used here in N_{tot} are the combination of Cerenkov and lead glass cuts and do not contain any track information.

Under normal conditions, each detected particle leaves only one track in the VDC, but multi-track events can occur when there is noise or several particles passing through VDC simultaneously. For most of 6 GeV era experiments in Hall A, the event rate is low and only a small fraction of events has multi-tracks. Usually, only events with a single track are used in the physics analysis for convenience, thus the physics result need be corrected for the loss due to multi-track events. Since the fraction of multi-track events is tiny, one can simply assume the multi-track events contains at least one good track and have the similar distribution with the single-track events, then Eq. 4.16 can be written as:

$$\epsilon_{VDC} = \frac{N_{singletrack}}{N_{tot}} \tag{4.17}$$

where the $N_{singletrack}$ is the number of events with good single-track events in the sample.

For kinematics settings with higher event rates, the fraction of multi-track events also become higher. Fig. 4-9 shows the main trigger (T_3) raw rate versus momentum in the top plot while the fraction of multi-track event is shown in the bottom plot. Form Fig. 4-9, one can see that the fraction of multi-track events can reach 30% for some kinematic settings. The multitrack events must be examined carefully to determine whether or not the event has one or more good track reconstructed in the VDC.

4.2.3.2.1 Geometry Correction

In principle, the PID cuts are usually applied in terms of the sum of ADCs in the detector, and thus the PID efficiency does not depends on the accuracy of knowing the

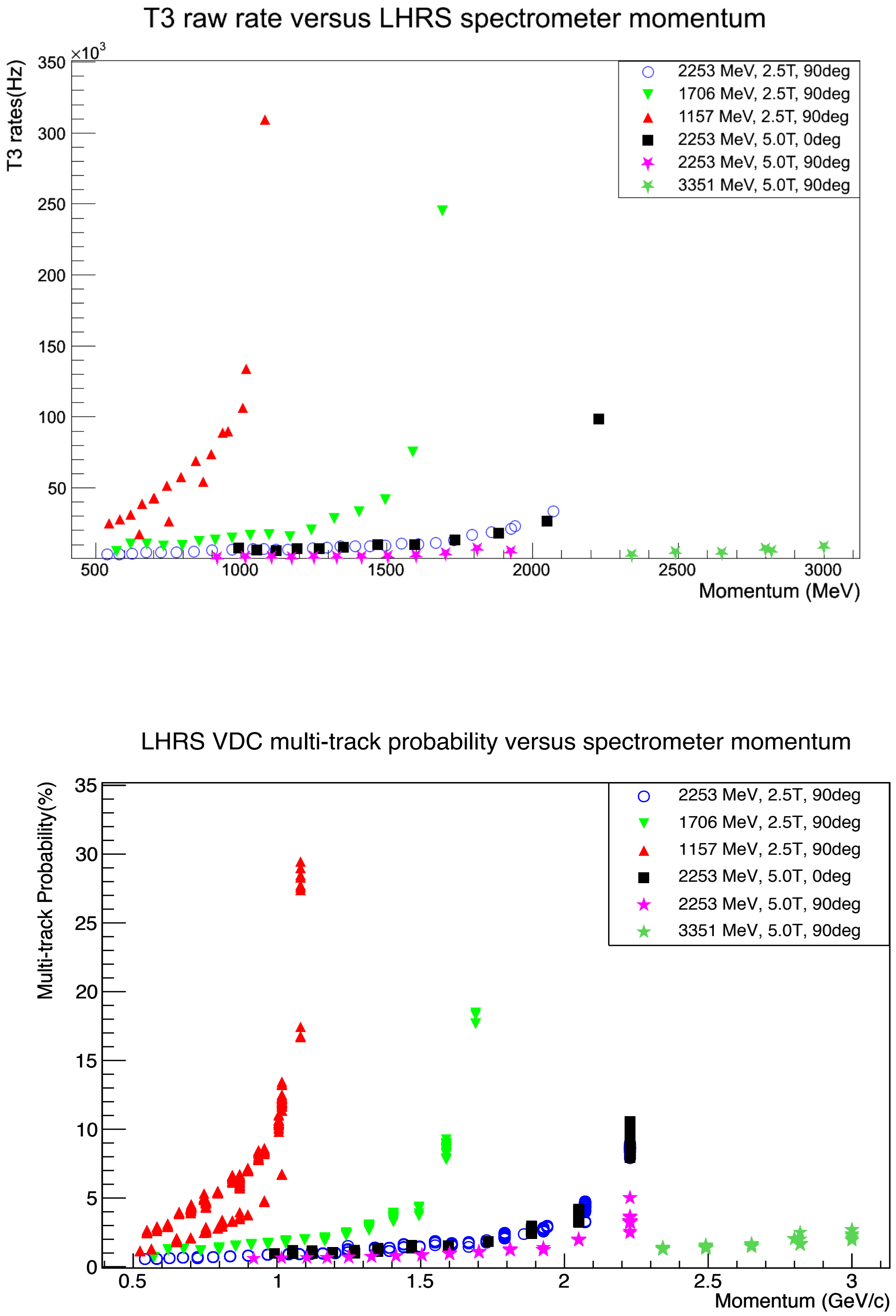

Figure 4-9: T_3 raw rate (top) and fraction of multi-track events (bottom) versus momentum. In both plots, each symbol represent one run in one momentum setting. In the top plot, only runs with continuous beam are selected.

.

position for the detectors as long as they cover the whole acceptance for all trajectories from the HRS. However, in order to precisely reconstruct the VDC track information, the position of the detector package, especially the lead glass calorimeters respect to the VDC, must be measured or known accurately. One can then point the VDC trajectory to the correct location in the calorimeter to sum up the total deposited energy in the adjacent blocks. However, the position of the calorimeter was not measured in the experiment.

Fortunately, this information can be recovered from data. Fig. 4-10 shows the pointing from VDC to the pion rejector using the VDC track information and the geometry (such as distance and orientation between the VDC and the lead glass) in the Hall A Analyzer database. Each layer of lead glass consists of 2×17 blocks arranged as in Fig. 4-11. The reconstructed track location in the pion rejector is shown in Fig. 4-12. The top plot of Fig. 4-12 shows the events in the center blocks (8-th and 25-th) of pion rejector 1 with the previous geometry configuration, while the bottom plots shows the events in two groups of blocks (one group is 3-th and 20-th, the other is 11-th and 28-th) separated by a distance of 8 blocks. The top plot tells the offset of pion rejector in the $\hat{x}$ (vertical) direction compared to the database, while the bottom plot tells the offset along the nominal particle direction $\hat{z}$. From Fig. 4-12, the pion rejector prl1 and prl2 were moved ≈ 42 cm along the $\hat{z}$ direction and ≈ 21 cm in the $\hat{x}$ direction compared to the previous geometry stored in the Hall A Analyzer database.

After correcting the geometric information of the lead glass blocks in the database, a cross check was done by comparing the reconstructed center in the pion rejector (using VDC tracking information) with the cluster center of the energy deposited in the pion rejector. The cluster center is the ADC signal weighted location of the 2×3 blocks (2 blocks along $\hat{y}$ and 3 blocks along $\hat{x}$) around the block with the maximum ADC signal. The comparison is shown in Fig. 4-13. For around 99.6% of good single-track electron events, the reconstructed track center is located within half of a block compared to the averaged cluster center of the deposited energy in the pion rejector. The wave-like pattern is due to that most of the deposited energy ($\sim 90\%$)

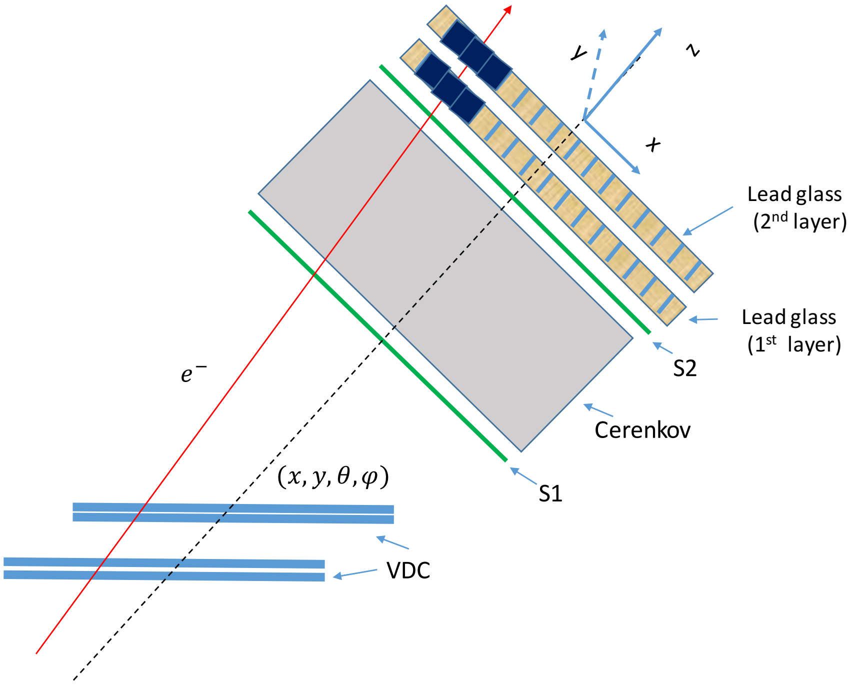

Figure 4-10: Pointing the track from VDC to the pion rejector.

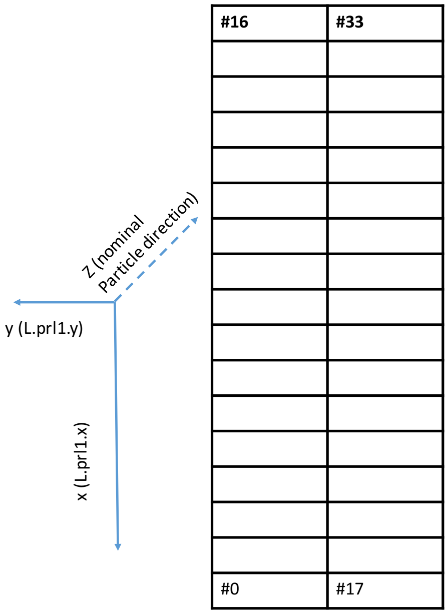

Figure 4-11: The arrangement of the blocks in one layer of lead glass (pion rejector).

was deposited in one block in the $\hat{x}$ direction. Similar procedure was followed for the RHRS preshower and shower geometric information and the cross check.

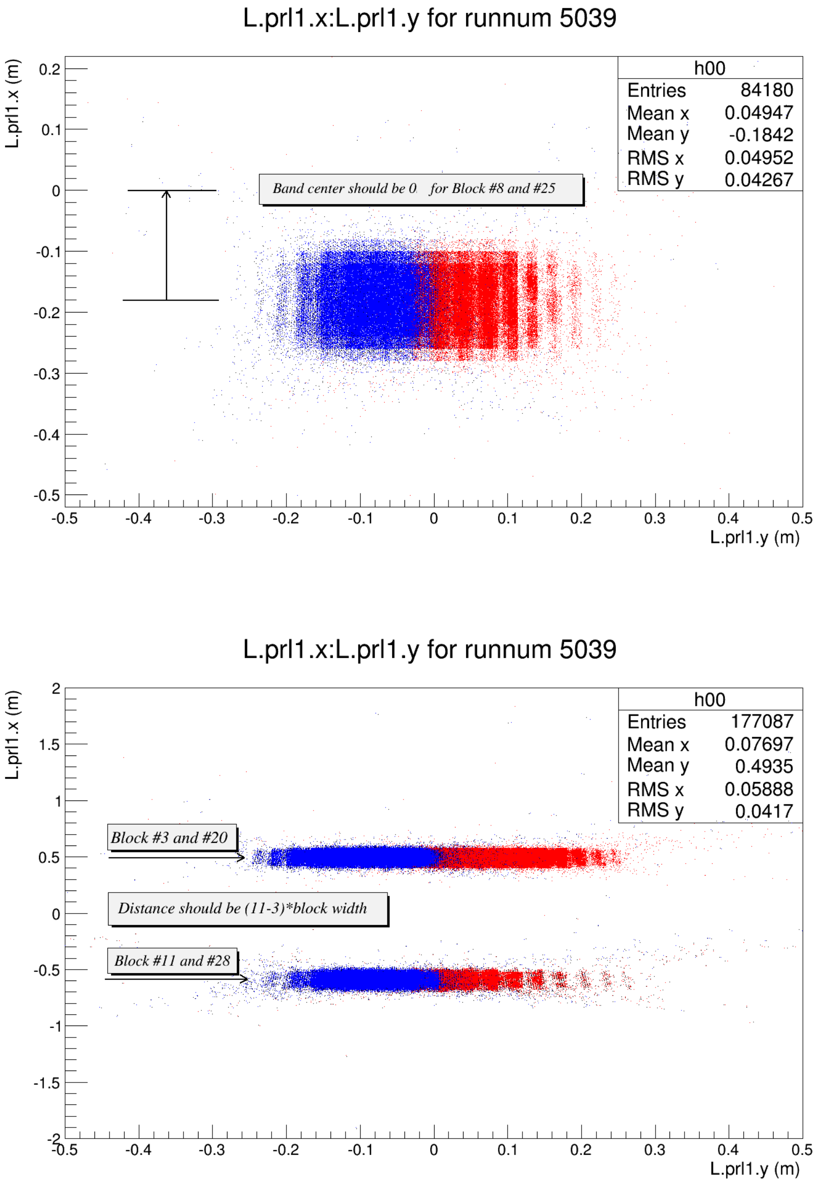

Figure 4-12: Positions check for pion rejector 1 (prl1) in LHRS. L.prl1.y and L.prl1.x is the pointed position at prl1 from VDC tracking information by using the values in the previous Hall A Analyzer Database. However, the distance between Block #3 and #11 was 8 block width (1.2 m) in reality but the plot shows 1.08 m. In addition, the Block #8 center would be located at the origin point according to the same database while the plot shows -19 cm. The block positions were moved 42 cm further in z and 21 cm in the x direction.

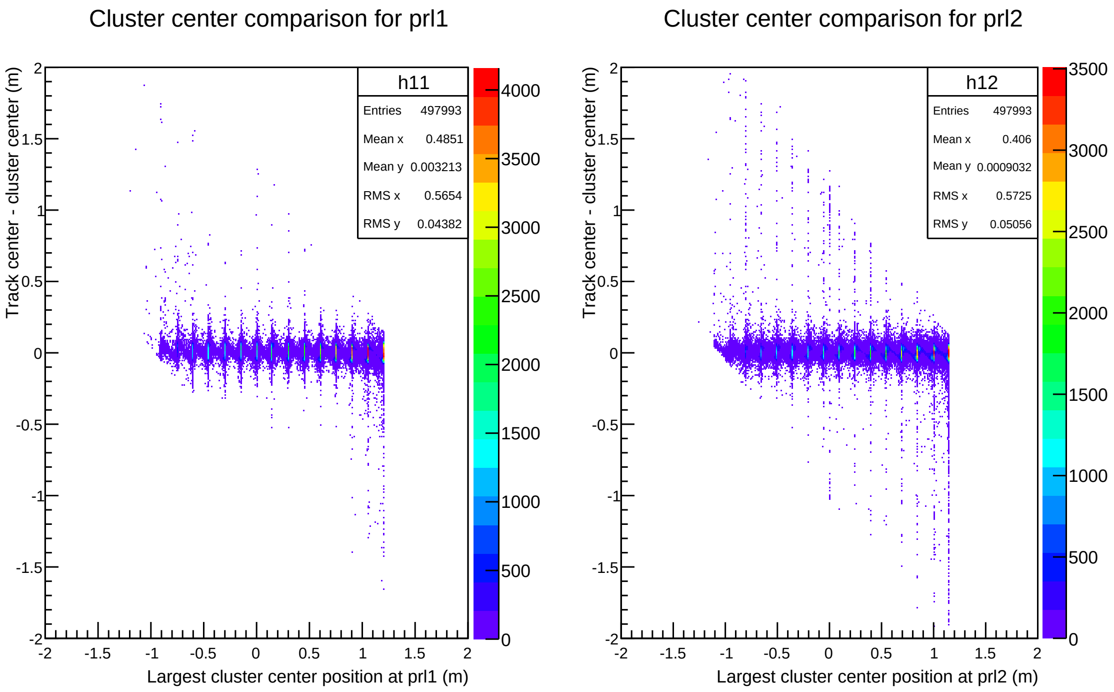

Figure 4-13: Distribution of reconstructed center compared with the real energy-averaged cluster center in the lead glass after updating the geometric information in the database.

4.2.3.2.2 Efficiency and Systematic Study

As mentioned in Sec. 4.2.3.2, for each multi-track event, a careful examination is needed to determine whether there is at least one good track reconstructed by the VDC. A multi-track event is expected to be good if the energy deposited in the calorimeter by one of the tracks satisfies the PID cuts and this track is also within the acceptance cuts used to select the sample. Fig. 4-14 shows the acceptance used for this study in LHRS. The track number distribution for the kinematics with beam energy $E_b = 1.157$ GeV and spectrometer momentum $P_0 = 1.082$ GeV is shown in Table 4.1.

After correcting the geometry in Sec. 4.2.3.2.1, the track information from VDC can be mapped to the energy deposited in the lead glass. Fig. 4-15 shows the deposited energy (sum of both layers) distribution in the pion rejector for track #1 (E_1) and track #2 (E_2) in two-track events. There are four distinct areas in Fig. 4-15:

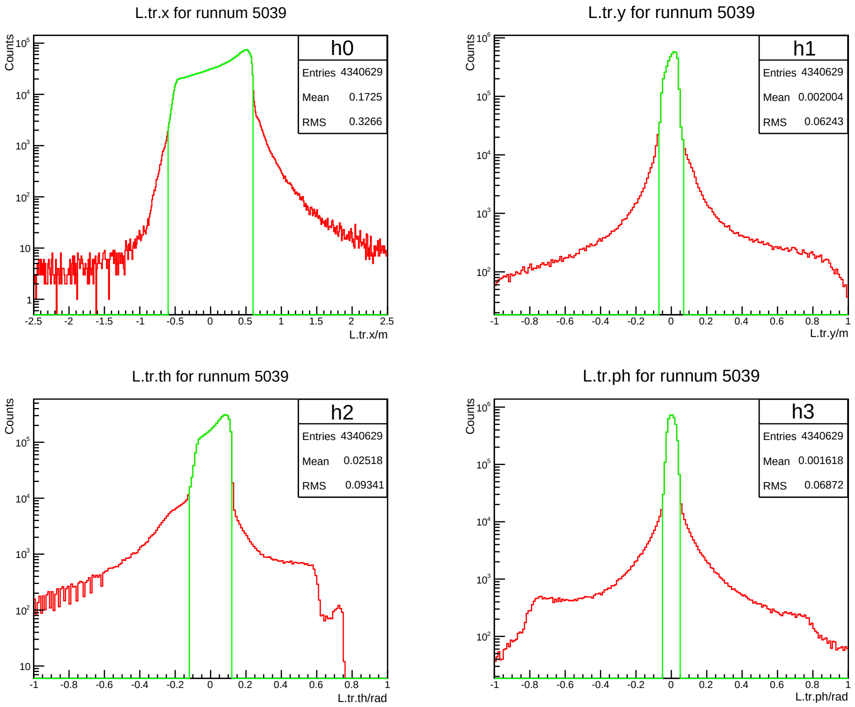

Figure 4-14: LHRS acceptance cuts. The red line represents the raw variable and the green line indicates the selected events.

Number of tracks	0	1	2	3	4	5	6	7	More than 7
Probability (%)	0.11	71.37	18.05	7.13	2.10	0.76	0.28	0.11	0.09

Table 4.1: Track number distribution for the kinematic setting with beam energy $E_b = 1.157$ GeV and spectrometer momentum $P_0 = 1.082$ GeV.

- **Region A**: $E_1 < E_{PID}$ and $E_2 < E_{PID}$ where E_{PID} is the PID cut for the total energy deposited in the two layers of lead glass. In this area, the events could not pass through PID cuts, so no good track is expected.

- **Region B**: $E_1 \geq E_{PID}$ and $E_2 < E_{PID}$. If the first track is within acceptance and its energy deposited in the first layer of lead glass also satisfies the PID energy cut in the first layer (this is the other PID cut only on the first layer of lead glass, see Sec. 4.2.2), track 1 is expected to be good not track 2.

- **Region C**: $E_1 < E_{PID}$ and $E_2 \geq E_{PID}$, similar to **Region B**, but now track 2 is good but not track 1.

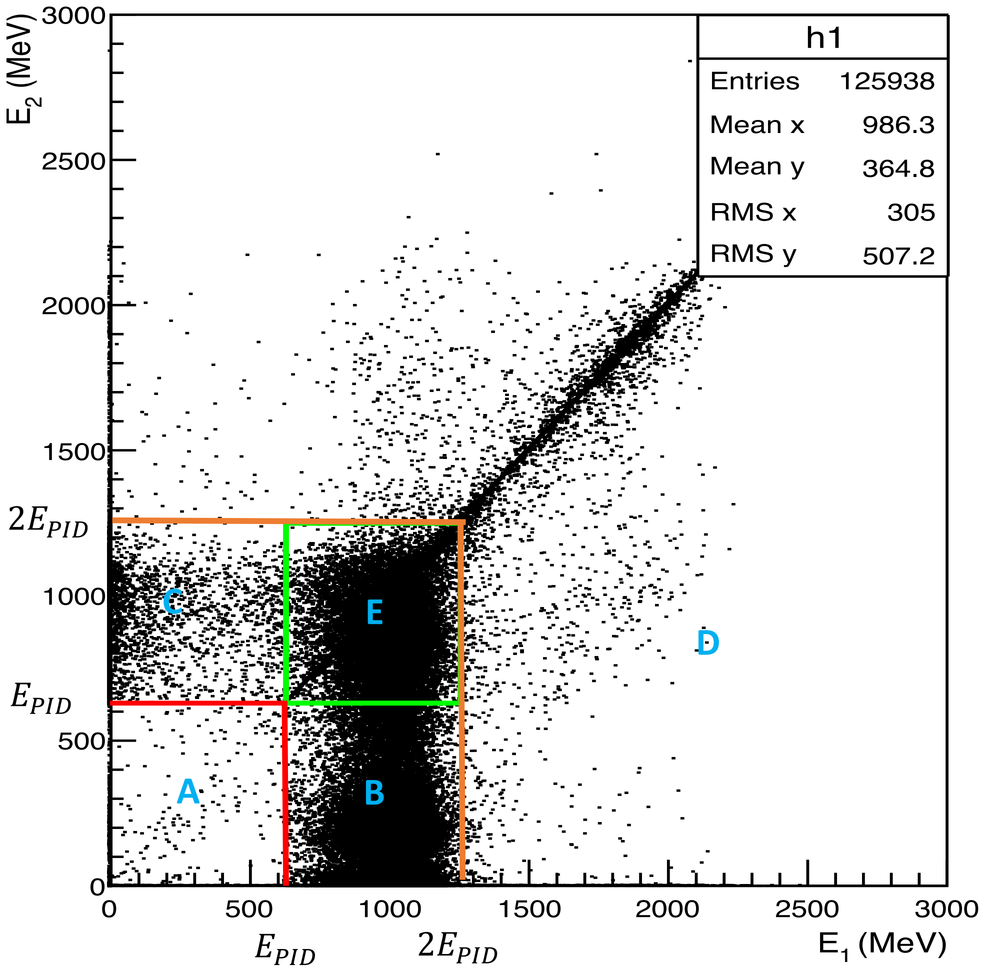

Figure 4-15: Distribution of deposited energy in the LHRS pion rejector for track #1 (E_1) and track #2 (E_2) in two-track events for Run 5039 with spectrometer momentum $P_0 = 1.082$ GeV. The green square represents the cut $E_{PID} < E_1, E_2 < 2E_{PID}$.

- **Region D**: $E_1 > 2E_{PID}$ or $E_2 > 2E_{PID}$. if one track is within acceptance and its energy deposited in the first layer of lead glass also satisfies the PID energy cut in this layer (this is the other PID cut only on the first layer of lead glass, see Sec. 4.2.2), at least one good track is expected.

- **Region E**: the green square with $E_{PID} < E_1, E_2 < 2E_{PID}$. These events can arise from two good tracks, or one good track and one noise track, or two noise tracks, so need be treated more carefully. Fig. 4-16 shows the distance between two tracks for these events in both x and y directions.

- **Case I**: there is at least one block distance between the pointed blocks at lead glass, it is safely to count at least one good track, since typically around 95% of energy is deposited in one lead glass.
- **Case II**: two tracks came into the lead glass within a distance of one block width (no block between them), which is the peak distribution in the left plot of Fig. 4-16. In this case, two tracks overlapped in the energy deposition and it is difficult to separate the energy contribution from each track. Several kinds of cluster overlaps are shown in Fig. 4-17. If one cluster energy subtracts twice the energy deposited in the directly pointed blocks by another track, satisfying the PID and acceptance cuts, we can also expect it to have at least one good track. These events may occur due to knock-out δ electrons or misconstructed tracks in the VDC.

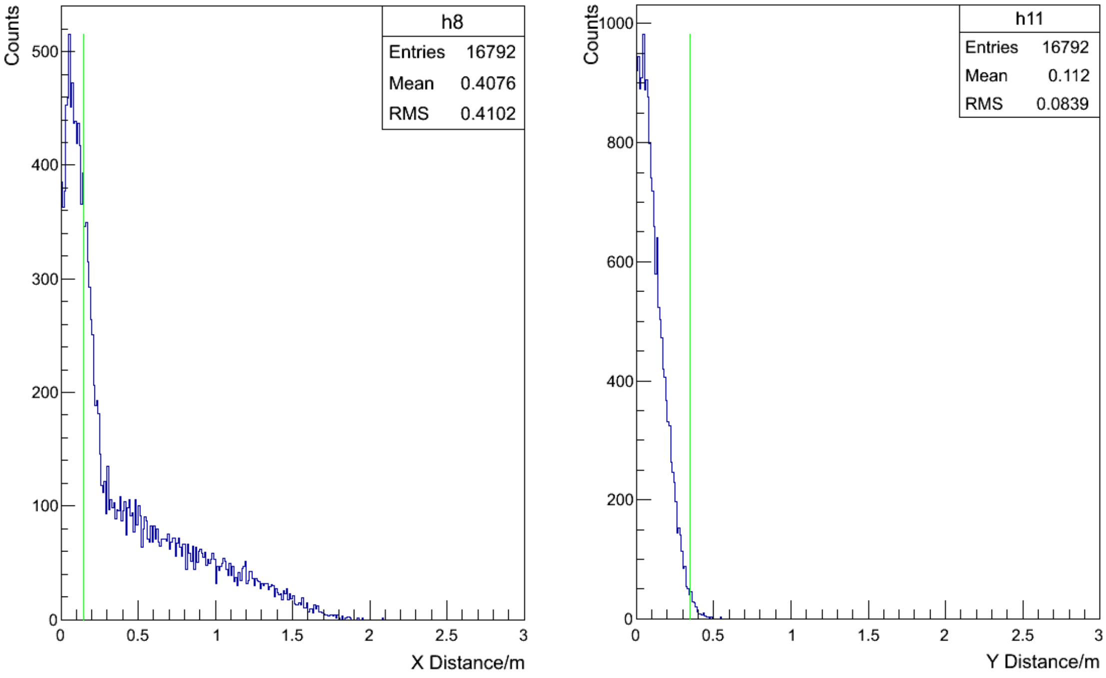

Figure 4-16: Distance distribution in x (left) and y (right) for two track events with $E_{PID} < E_1, E_2 < 2E_{PID}$. The Green curves indicates the size of one single block.

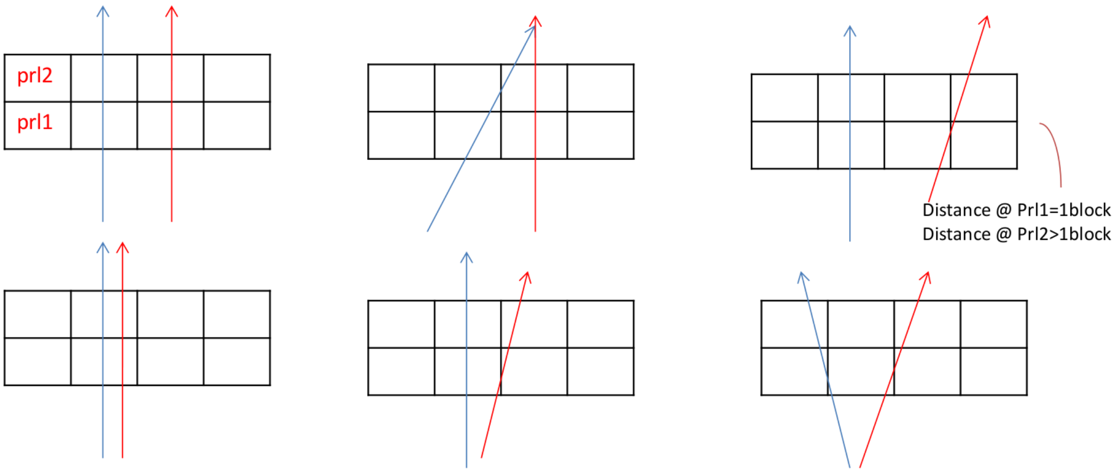

Figure 4-17: Several kinds of cluster overlap between two tracks in pion rejector. Red and blue line represents two trajectory.

The VDC inefficiency gives the upper limit of systematic uncertainty of VDC efficiency while the unresolved tracks bring the lower limit of systematic uncertainty. For run number 5039, with the beam energy $E = 1.157GeV$ and momentum $p_0 = 1.082GeV/c$, the two-track event probability is 18.05% and the good two-track events is $17.72^{+0.33}_{-0.78}\%$. Fig. 4-18 shows the fraction of good events in the two-track events among the sample.

A software was developed to analyze the multi-track events up to 7-track. For the run number 5039, the probability for an event entry to have one or more good tracks is $98.81^{+1.19}_{-1.67}\%$ while the probability for an event entry to have only one track and be good is 71.10%. For multi-track events that have two or more good electrons, the probability is very low at this $\sim$ 100 ns TDC timing window and the effects is expected to be properly corrected by the deadtime. The distribution of total VDC track efficiency (at least one good track) versus spectrometer momentum is shown in Fig. 4-19 for LHRS and Fig. 4-20 for RHRS.

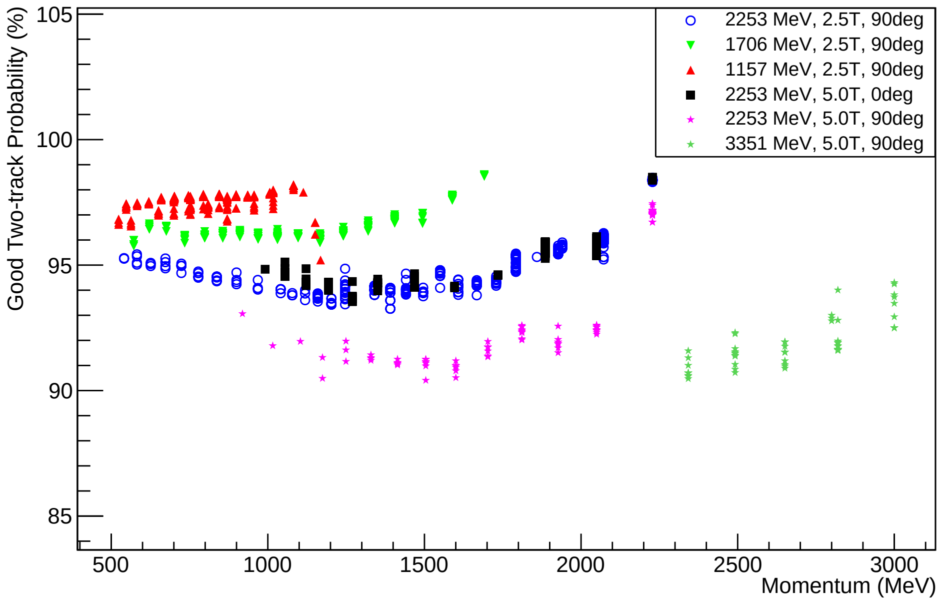

Figure 4-18: The fraction of events with at least one good track among the two-track events in the sample.

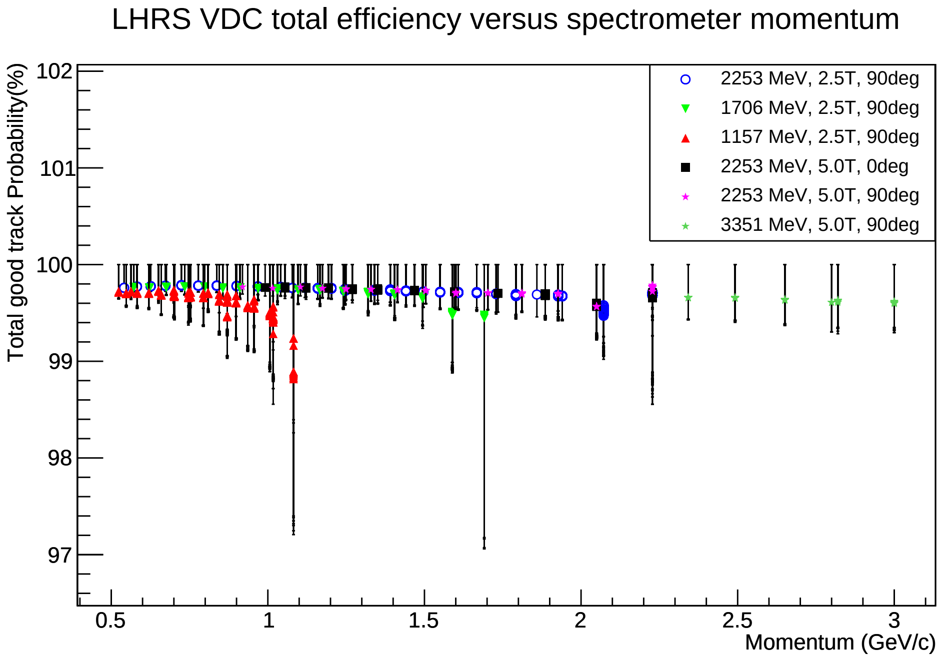

Figure 4-19: LHRS VDC efficiency with systematic uncertainty

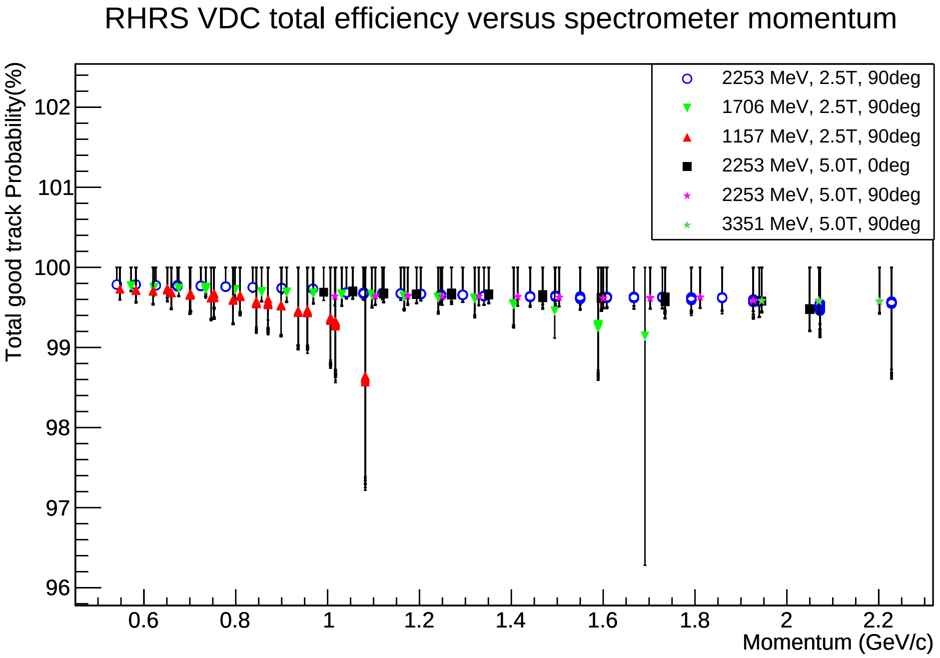

Figure 4-20: RHRS VDC efficiency with systematic uncertainty

4.3 Packing Fraction Analysis

In E08-027 experiment, the ammonia beads were used as the target material and filled into a 2.83 cm length cell and immersed in liquid helium, as shown in Fig. 4-21. Due to the size and shape of the ammonia beads, some liquid Helium also filled the space between beads. The packing fraction (pf), or the effective length of ammonia target material immersed in the liquid helium, can change for each material sample and must be understood. The packing fraction can be extracted from data collected using the NH_3 target, the dummy target, the empty target (same as dummy target, but no endcaps and NMR coils), and the carbon target described in Sec. 3.4[120]. These runs obtained from non-NH_3 target are referred as "dilution runs".

In general, the normalized yields from a given material x can be written as:

$$Y_x = \frac{AN_A\rho_x L_x\sigma_x}{M_x} \tag{4.18}$$

where N_A is Avogadro's number, A is the experimental acceptance factor, ρ_x is the

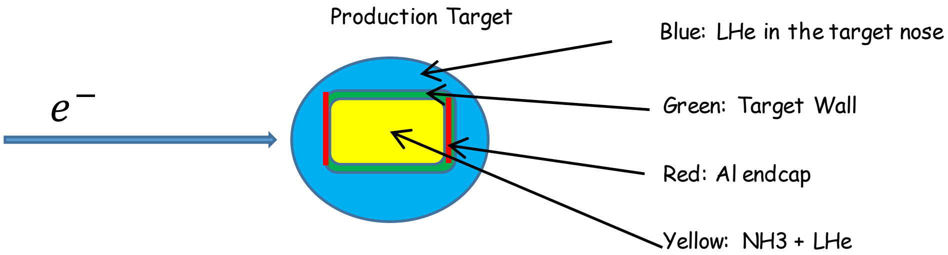

Figure 4-21: NH_3 target in the target nose. The target nose is 4.20 cm in diameter, the target cell length is 2.83 cm, each of the aluminum endcap has a thickness of 0.7 mil.

material density, M_x is the molar mass, L_x is the material thickness, and σ_x is the cross section for the material with radiative effects included.

Denote the measured yields for NH_3 target, the dummy target, the empty target and the carbon target as Y_{prod}, Y_{dummy}, Y_{empty}, Y_{carbon}. Following Eq. 4.18, these yields can be expressed as:

$$Y_{prod} = AN_A \left[\frac{\rho_{NH_3} L_{cell} \cdot pf}{M_{NH_3}} (\sigma_N + 3\sigma_H) + \frac{\rho_{He}(L_{total} - L_{cell} \cdot pf)\sigma_{He}}{M_{He}} + \frac{\rho_{Al} L_{Al} \sigma_{Al}}{M_{Al}} \right], \tag{4.19}$$

$$Y_{empty} = AN_A \frac{\rho_{He} L_{total} \sigma_{He}}{M_{He}}, \tag{4.20}$$

$$Y_{dummy} = AN_A \left[\frac{\rho_{He} L_{total} \sigma_{He}}{M_{He}} + \frac{\rho_{Al} L_{Al} \sigma_{Al}}{M_{Al}} \right], \tag{4.21}$$

$$Y_{carbon} = AN_A \left[\frac{\rho_C L_C \sigma_C}{M_C} + \frac{\rho_{He}(L_{total} - L_C)\sigma_{He}}{M_{He}} \right], \tag{4.22}$$

where pf is the packing factor, L_{tg} is the cell thickness 2.83 cm, and L_{total} is the effective length (3.70 cm) of the target nose along the beam line. From Eqs. 4.19-4.22, the production yields Y_{prod} can then be expressed in terms of dilution run yields Y_{dummy}, Y_{empty}, Y_{carbon} as

$$pf = \frac{Y_{prod} - Y_{dummy}}{\left(\frac{M_C \rho_{NH_3} L_{cell} \cdot pf}{M_{NH_3} \rho_C L_C}\right) \left(Y_{carbon} - \frac{L_{total} - L_C}{L_{total}} Y_{empty}\right)(a + 3b) - c\frac{L_{cell}}{L_{total}} Y_{empty}}, \tag{4.23}$$

where a represents the factor used to scale σ_C (carbon target) to σ_N (in the ammonia target), b represents the factor used to scale σ_C (carbon target) to σ_H (in the ammonia target), and c represents the factor used to scale σ_{He} (empty target) to σ_{He} (in the ammonia target), see detailed discussions about the scaling factor a, b, c in Ref.[120]. In the DIS region, an approximation for factor a is to take the ratio of the number of constituent nucleons in each material as $\sigma_{^{14}N} = \frac{7}{6}\sigma_C \to a = \frac{7}{6}$ if radiation thickness is the same for NH_3 and carbon targets.

A calculated packing fraction versus the energy transfer ν for material ID 19 is shown in Fig. 4-22. A linear fit is performed in the large ν region where there is a good approximation for cross section scaling[120, 121, 122] to obtain the packing fraction with $pf = 0.597 \pm 0.025$. In E08-027 experiment, a total of 10 different ammonia samples were used. The results are shown in Table 4.2. See Ref. [120] for more details about packing fraction analysis.

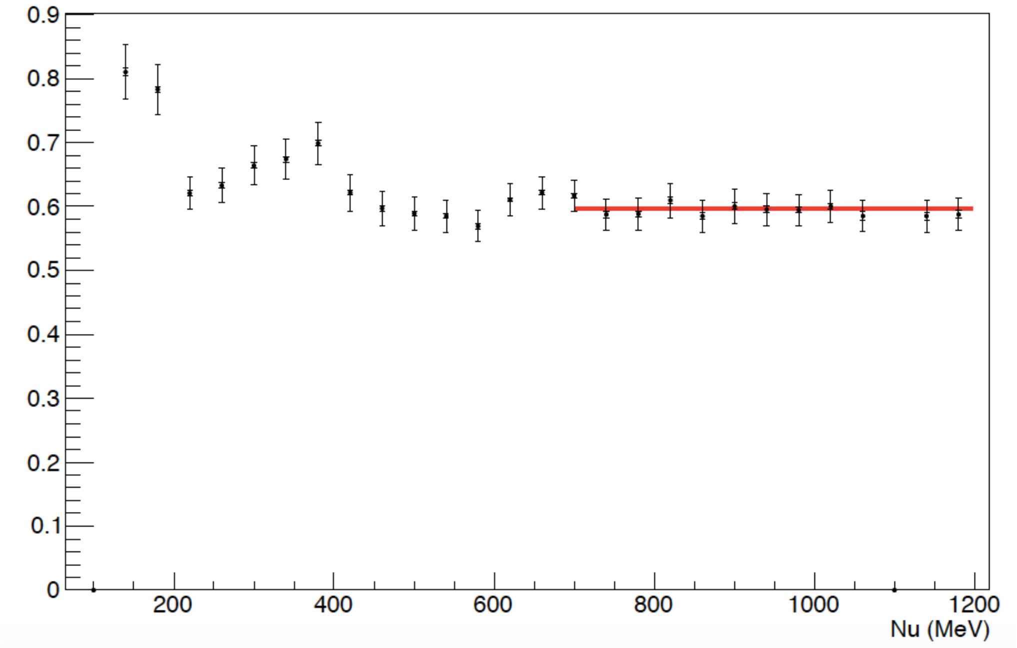

Figure 4-22: Calculated packing fraction with a linear fit at large ν for material ID 19. Each points represents a run configuration. Plot reproduced from [120].

Beam Energy (GeV)	Field (T)	Field Angle (degree)	Material ID	Packing Fraction
2.254	5	0	17	0.516±0.019
2.254	5	0	18	0.581±0.019
2.254	5	90	19	0.597±0.025
2.254	5	90	20	0.610±0.028
3.350	5	90	19	0.644±0.015
3.350	5	90	20	0.544±0.011
2.254	2.5	90	7	0.630±0.048
2.254	2.5	90	8	0.658±0.051
1.710	2.5	90	7	0.770±0.059
1.710	2.5	90	8	0.850±0.066

Table 4.2: Packing fractions for each kinematics. For 1.1 GeV setting, the packing fraction of material ID 11, 12, and 14 are still being studied. The parking fraction obtained were different for the same material in different kinematic setting, which may due to fact that the target cells were changed out and warmed up during the kinematic setting change. Table reproduced from [120].

4.4 Dilution Analysis

The measured asymmetry is diluted by contributions from the unpolarized material in the target, such as nitrogen, liquid helium and the aluminum foil end caps on the ammonia target cups, and thus needs be corrected by a dilution factor to remove the contamination to get physics asymmetry as shown in Eq. 4.1.

The raw asymmetry can be written as:

$$A_{raw} = \frac{Y_H^+ - Y_H^-}{Y_H^+ + Y_H^- + Y_{bg}}, \tag{4.24}$$

where Y_H^+ and Y_H^- are the yields arise from polarized proton with positive and negative helicity states, respectively, and Y_{bg} is the yields of electrons scattered from various unpolarized materials:

$$\begin{aligned} Y_{bg} &= Y_N + Y_{He} + Y_{Al} \\ &= AN_A \left[\frac{\rho_{NH_3} L_{cell} \cdot pf}{M_{NH_3}} (\sigma_N) + \frac{\rho_{He}(L_{total} - L_{cell} \cdot pf)\sigma_{He}}{M_{He}} + \frac{\rho_{Al} L_{Al} \sigma_{Al}}{M_{Al}} \right], \end{aligned} \tag{4.25}$$

where pf is the packing fraction determined in the previous section. Similar to the packing fraction analysis, Y_{bg} can be formed using dilution run data from carbon, dummy, empty targets. Then Eq. 4.25 can be written as the yields of these dilution runs:

$$Y_{bg} = \left(\frac{M_C \rho_{NH_3} L_{cell} \cdot pf}{M_{NH_3} \rho_C L_C}\right)\left(Y_{carbon} - \frac{L_{total} - L_C}{L_{total}} Y_{empty}\right) a - c\frac{L_{tg}}{L_{total}} Y_{empty}, \tag{4.26}$$

where a and c are the scaling factors discussed in Sec. 4.3.

Comparing Eq. 4.1 and Eq. 4.24, the dilution factor D_f can be calculated as:

$$\begin{aligned} D_f &= 1 - \frac{Y_{bg}}{Y_{prod}} \\ &= 1 - \frac{\left(\frac{M_C \rho_{NH_3} L_{cell} \cdot pf}{M_{NH_3} \rho_C L_C}\right)\left(Y_{carbon} - \frac{L_{total} - L_C}{L_{total}} Y_{empty}\right) a - c\frac{L_{tg}}{L_{total}} Y_{empty}}{Y_{prod}}, \end{aligned} \tag{4.27}$$

The dilution results calculated via Eq. 4.27 are shown in Fig. 4-23 and Fig. 4-24. The uncertainty is dominated by systematic uncertainties. The largest contribution is from the model used for cross section scaling, typically (5-10)% depending on the target. The dilution results for $E_b = 1.1$ GeV and $E_b = 3.3$ GeV setting are still being studied. See Ref.[120] for more details about dilution analysis.

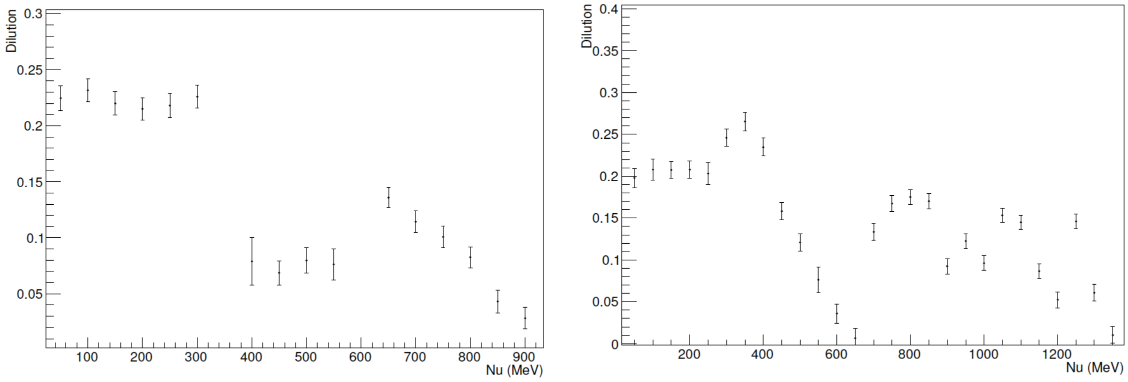

Figure 4-23: Dilution factors for $E_b = 1.710$ GeV, field 2.5 T transverse setting (left) and $E_b = 2.254$ GeV, field 2.5 T transverse setting (right). Plot reproduced from [120].

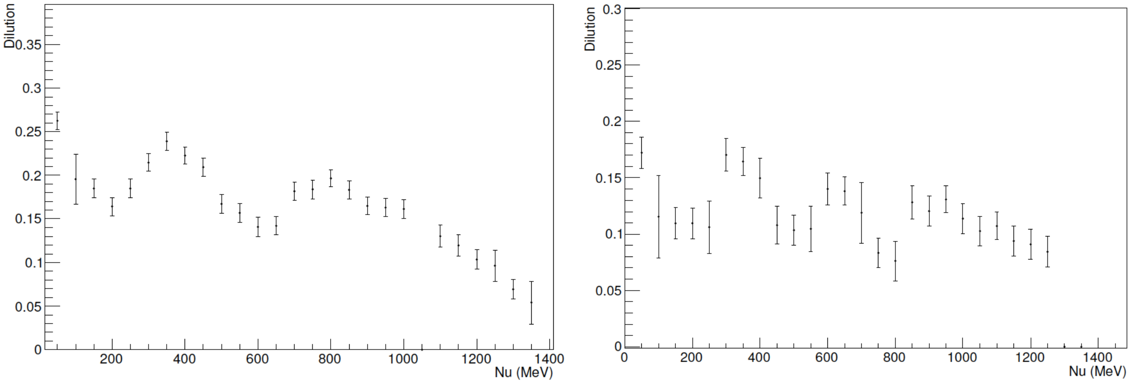

Figure 4-24: Dilution factors for $E_b = 2.254$ GeV, field 5 T transverse setting (left) and $E_b = 2.254$ GeV, field 5 T longitudinal setting (right). Plot reproduced from [120].

4.5 Optics and Simulation

4.5.1 Spectrometer Optics Study

As discussed in Sec. 3.7.1, the VDC provides the particle tracking information by determining the raw wire hits and drift times. Two spatial and two angular variables are extracted from VDC signals to represent the event in the focal plane (fp) coordinate system. The kinematic variables at the target of each event can then be reconstructed from the focal plane coordinates using the spectrometer optics. The spectrometer optics describes the property of the magnet system of the spectrometer in which the charged particle travels like light through lenses. In the standard HRS (or HRS + septum) configuration, a single calibrated matrix is introduced to describe the optics. In E08-027 experiment, the strong transverse field makes the single matrix method challenging. Instead, a two-step reconstruction was used to separate the target field effects from the standard magnets system[123]. In the target region, the motion of particles is calculated using the equation of motion of charged particles in the magnetic field, while a optics matrix is optimized to describe the particles' motion outside of the target region. In this section, an overview of the procedures of spectrometer optics is discussed, more details can be found in Ref. [123].

4.5.1.1 Coordinate System

A short overview of the target and focal plane coordinate systems used in the spectrometer optics study is presented. More details can be found in reference [124].

4.5.1.2 Hall Coordinate System (HCS)

Fig. 4-25 shows the definition of HCS: the origin is the Hall A center, $\vec{z}$ is along the beam line and points downstream, $\vec{y}$ is vertically up.

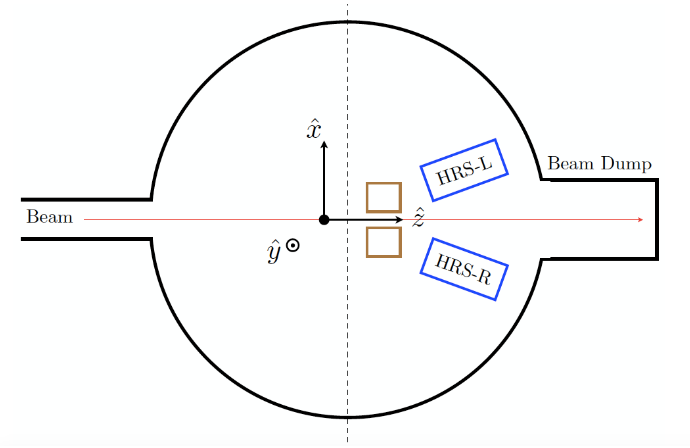

Figure 4-25: Hall coordinate system (top view). Plot reproduced from [123].

4.5.1.3 Target Coordinate System (TCS)

Each spectrometer defines its own TCS. The central ray of the spectrometer, which is the line perpendicular to the plane of the sieve slit passing through the center point of the central sieve slit hole, defines $\vec{z}_{\text{tg}}$ axis. The $\vec{x}_{\text{tg}}$ points vertically down and $\vec{y}_{\text{tg}}$ points to the right facing the spectrometer. The offsets between TCS center and HCS center should be zero in the ideal case, but in reality there are non-zero offsets D_x and D_y defined in the vertical and horizontal directions in TCS, respectively. Fig. 4-26 illustrates the TCS with respect to the HCS and definitions of the offsets. The kinematics of each scattering event are described by four variables (δ, θ_{tg}, y_{tg},

ϕ_{tg}) in TCS. δ is related to the momentum P of scattered particle and the central spectrometer momentum P_0 as $\delta = (P - P_0)/P_0$. y_{tg} is the y coordinate of the interception point of the particle trajectory and the $\phi_{\text{tg}} = 0$ plane. The out-of-plane angle θ_{tg} and the in-plane angle ϕ_{tg} are given by the tangent of the actual angles. For events passing through a hole on the sieve slits with position (x_{sieve}, y_{sieve}), these are simply $\theta_{\text{tg}} = dx_{\text{sieve}}/L$ and $\phi_{\text{tg}} = dy_{\text{sieve}}/L$, with L the drift length of the particle.

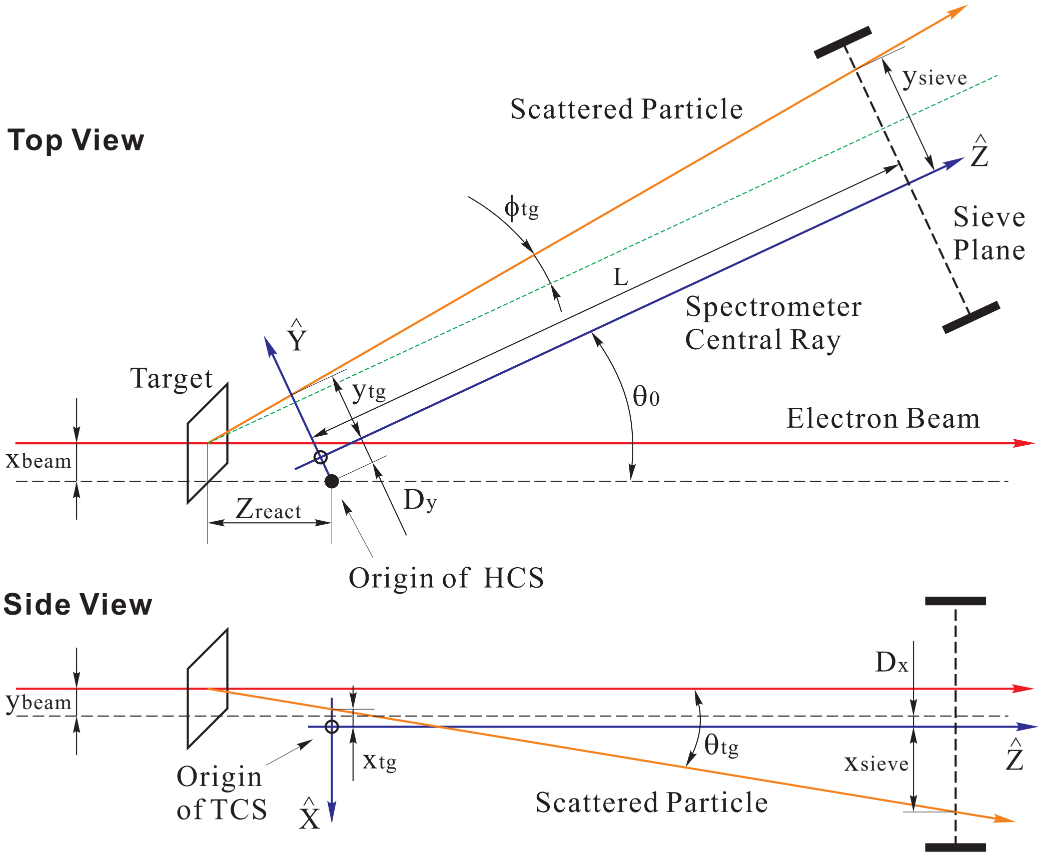

Figure 4-26: Target coordinate system (top and side view). Plot reproduced from[104].

4.5.1.4 Detector Coordinate System (DCS)

The Detector Coordinate System (DCS) is defined by the positions of the VDC planes, as shown in Fig. 4-27. The origin of DCS is defined by the intersection of wire 184 of the VDC1 U1 plane and the perpendicular projection of wire 184 in the VDC1 V1 plane onto the VDC U1 plane. $\vec{z}$ is perpendicular to the VDC U1 plane pointing vertically up while $\vec{x}$ is along the long symmetry axis of the lower VDC pointing downstream.

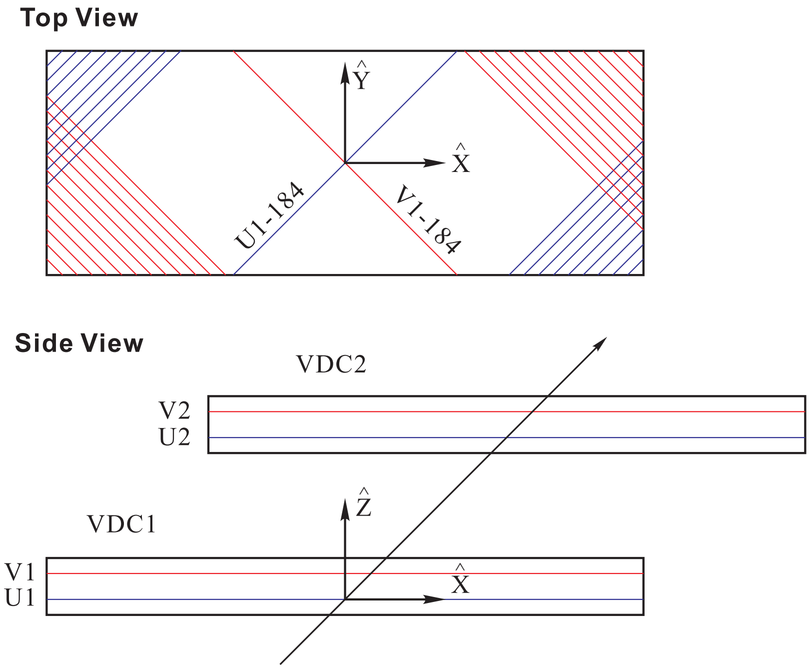

Figure 4-27: Detector coordinate system (top and side view). Plot reproduced from[104].

4.5.1.5 Transport Coordinate System (TRCS)

The TRCS at the focal plane (plane U1) is generated by rotating the DCS clockwise around its y axis by 45°.

4.5.1.6 Focal Plane Coordinate System (FCS)

This is the coordinate system for optics analysis. Because of the focusing of the HRS magnet system, particles from different scattering angles with the same momentum will be focused at the focal plane. The FCS is defined by rotating the DCS around its y-axis by an varying angle $\rho\ (x_{\rm tr})$ that the new z-axis is always parallel to the local central ray with scattering angle $\theta_{\rm tg} = \phi_{\rm tg} = 0$, as shown in Fig. 4-28. In this rotated coordinate system, the dispersive angle $\theta_{\rm fp}$ is small all over the focal plane and is approximately symmetric distributed with respect to $\theta_{\rm fp} = 0$, thus the expansions of the optics matrix will converge faster during the optics calibration if the rotated system is used.

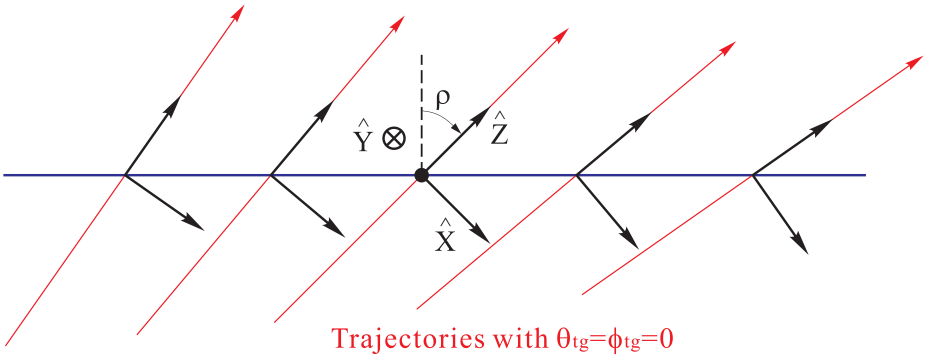

Figure 4-28: Rotated focal plane coordinate system. Plot reproduced from[104].

4.5.1.7 Optics Calibration

For the standard configuration (without the target field), an optics matrix is optimized to map the measured focal plane variables (x_{fp}, θ_{fp}, y_{fp}, ϕ_{fp}) to the TCS variables (δ, θ_{tg}, y_{tg}, ϕ_{tg}). The first order optics matrix can be expressed as,

$$\begin{pmatrix} \delta \\ \theta \\ y \\ \phi \end{pmatrix}_{\mathrm{tg}} = \begin{pmatrix} <\delta|x> & <\delta|\theta> & 0 & 0 \\ <\theta|x> & <\delta|\theta> & 0 & 0 \\ 0 & 0 & <y|y> & <y|\phi> \\ 0 & 0 & <\phi|y> & <\phi|\phi> \end{pmatrix} \cdot \begin{pmatrix} x \\ \theta \\ y \\ \phi \end{pmatrix}_{\mathrm{fp}} . \tag{4.28}$$

In practice, the matrix is more complicated with a set of tensors $D_{jkl}, T_{jkl}, Y_{jkl}$ and P_{jkl} to relate the focal plane coordinates to each target variable:

$$\delta = \sum_{jkl} D_{jkl} \theta_{\mathrm{fp}}^{j} y_{\mathrm{fp}}^{k} \phi_{\mathrm{fp}}^{l}, \tag{4.29}$$

$$\theta_{\mathrm{tg}} = \sum_{jkl} T_{jkl} \theta_{\mathrm{fp}}^{j} y_{\mathrm{fp}}^{k} \phi_{\mathrm{fp}}^{l}, \tag{4.30}$$

$$y_{\mathrm{tg}} = \sum_{jkl} Y_{jkl} \theta_{\mathrm{fp}}^{j} y_{\mathrm{fp}}^{k} \phi_{\mathrm{fp}}^{l}, \tag{4.31}$$

$$\phi_{\mathrm{tg}} = \sum_{jkl} P_{jkl} \theta_{\mathrm{fp}}^{j} y_{\mathrm{fp}}^{k} \phi_{\mathrm{fp}}^{l}, \tag{4.32}$$

where the tensors D_{jkl}, T_{jkl} and P_{jkl} are polynomials in x_{fp}. For example,

$$D_{jkl} = \sum_{i=0}^{m} C^{D}_{ijkl} x^{i}_{\text{fp}}. \tag{4.33}$$

where C_{ijkl} are the optics matrix elements. The matrix elements can be determined from the data with the coordinates known at both the target plane and focal plane by minimizing the χ^2:

$$\chi^2(w) = \sum_{N} \left(\frac{\sum_{ijkl} C^{w}_{ijkl} x^{i}_{\text{fp}} \theta^{j}_{\text{fp}} y^{k}_{\text{fp}} \phi^{l}_{\text{fp}} - w^0}{\sigma^{N}_{w}} \right)^2, \tag{4.34}$$

where N is the total number of events, w can be any target variable (δ, θ_{tg}, y_{tg} or ϕ_{tg}), w^0 is the nominal value for the corresponding variable. Typically, sieve slits hole data are used to determine θ_{tg} and ϕ_{tg}, and carbon foils are used to determine δ or y_{tg}. The sieve slit is a 0.2 inch-thick tungsten plate with holes arranged in a grid pattern covering the angular acceptance, as shown in Fig. 4-29.

For E08-027 experiment, a two-step approach was developed to accommodate the effect from the strong transverse magnetic field of the polarized NH_3 target. The first step is to remove the target effects and obtain the effective reference values (x_{ref}, θ_{ref}, y_{ref}, ϕ_{ref}) at target coordinates, as shown in Fig. 4-30. These effective reference values are determined by simulating a large number of electrons drifting in the magnetic field from the target reaction point to the holes of sieve slit. When the simulated point (x_{drift}, y_{drift}) is within the tolerance of the actual hole position (x_{sieve}, y_{sieve}), the effective reference values are obtained by linearly projecting it back to the target plane:

$$\begin{aligned} x_{\text{ref}} &= x_{\text{drift}} - L\theta_{\text{drift}}, & (4.35)\\ \theta_{\text{ref}} &= \theta_{\text{drift}}, & (4.36)\\ y_{\text{ref}} &= y_{\text{drift}} - L\phi_{\text{drift}}, & (4.37)\\ \phi_{\text{ref}} &= \phi_{\text{drift}}, & (4.38)\\ & & (4.39) \end{aligned}$$

where L is the distance from the sieve slit to the TCS origin. Fig. 4-31 shows the effective reference values (θ_{ref}, ϕ_{ref}) for the $P_0 = 1.710$ GeV configuration.

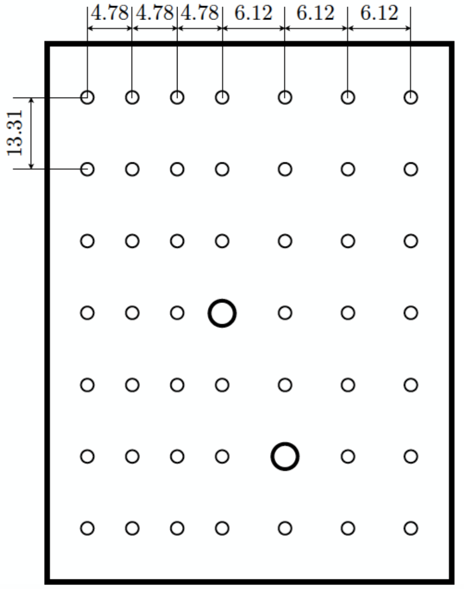

Figure 4-29: The design of the sieve slit used during the g2p experiment. during E08-027. The dimensions are in mm. There are two kinds of holes: small hole (diameter 1.4 mm); large holes (diameter 2.7 mm). The two large holes are used to determine the orientation of the sieve slit. Plot reproduced from[123]

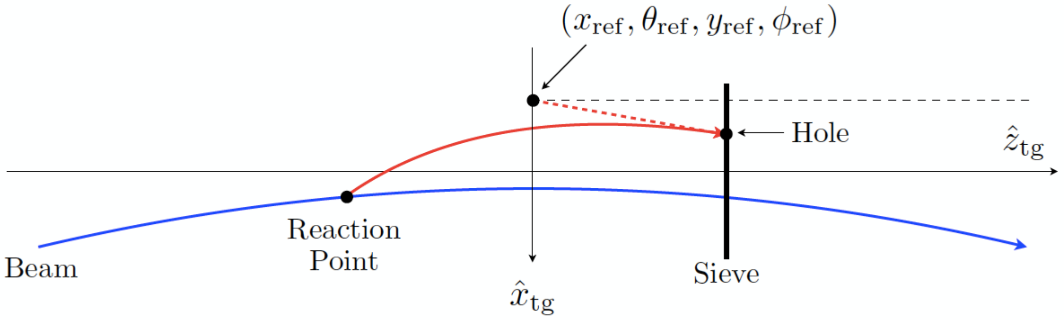

Figure 4-30: Determine the new reference values for the optics optimization with simulation. Plot reproduced from[123].

The second step for optics calibration is a standard procedure as the case without target field by minimizing with effective reference value as the nominal value w_0. Thus

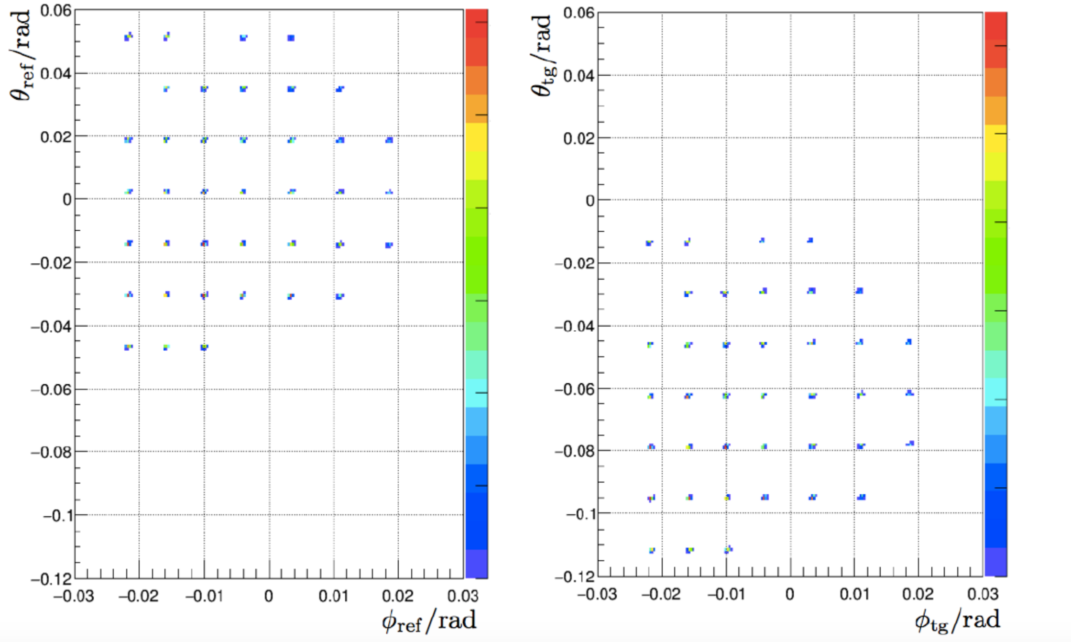

Figure 4-31: The effective reference values ($\theta_{\rm ref}$, $\phi_{\rm ref}$) for 1.710 GeV (left) and the corresponding actual target plane angle at the reaction point (right). Plot reproduced from[123].

the target variables or the effective reference variables must be precisely known, which can be obtained using the survey results combined with a sieve-slit collimator and a foil target and some well-known physics process like elastic scattering. A set of data was taken on single carbon foil with the sieve slit in to optimize the matrix. For each set of optics data, a delta scan was performed by setting the spectrometer momentum 0%, ±1%, ±2%, ±3% of the carbon elastic peak to cover the spectrometer momentum acceptance, and a beam position scan was performed at (±4, 0) mm and (0, ±4) mm in HCS by manually adjusting the point beam to increase the $y_{\rm tg}$ coverge. Since the sieve slit was in during optics data taking, the spectrometer angle acceptance ($\theta_{\rm tg}$ and $\phi_{\rm tg}$) was also covered. After obtaining the optics matrix, the reconstruction of target variables (δ, $\theta_{\rm tg}$, $y_{\rm tg}$, $\phi_{\rm tg}$) is shown in Fig. 4-32. The effective variables ($x_{\rm ref}$, $\theta_{\rm ref}$, $y_{\rm ref}$, $\phi_{\rm ref}$) are obtained via the matrix directly. The effective variables are projected linearly to the sieve slits and then traced back to target plane in the target field with simulation. Due to the poor resolution of $y_{\rm tg}$ calibration at small scattering angles[92, 123], the $y_{\rm tg}$ is determined from BPM readout instead.

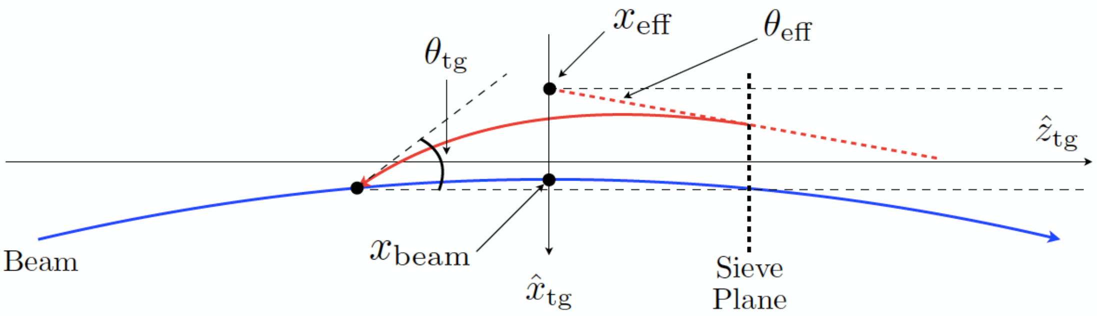

Figure 4-32: Reconstruction of the target kinematic variables. Plot reproduced from[123].

In E08-027 experiment, the HRS field and the septum field were set proportional to the central momentum, so the optical property does not change when the electron momentum setting changes. However, due to the broken of the septum magnet, this situation changed and the matrix needs to be re-calibrated. The optics performance is summarized in Table 4.3. The resolution of each variable is evaluated as:

$$Res(w) = \sqrt{\frac{1}{N}\sum_{s=1}^{N}(w_s - w_0)^2}, \tag{4.40}$$

where N is the total number of events used in the optimization, w is the calculated value with optics matrix for the target variable and w_0 is the reference values. See Ref. [123] for more details about optics study.

4.5.2 Simulation

For E08-027 experiment, a Monte-Carlo simulation package, called "g2psim", was developed to simulate the entire physics process of this experiment. This program consists of the target region raytracing (see Sec. 4.5.1.7), transport functions from Snake (See Ref. [125]), cross section models (inelastic: P. Bosted Model[126], quasi-free-scattering (QFS) model[127]; elastic: H[128], ^{4}He[129], ^{12}C[130, 131], ^{14}N[129]),

HRS	E_{beam} (GeV)	Field (T)	Field Angle	Septum	δ_{res}	θ_{res} (mrad) (mrad)	ϕ_{res} (mrad)
LHRS	2.254	2.5	90°	48-48-16	2.0×10^{-4}	1.7	1.7
LHRS	2.254	2.5	90°	40-32-16	2.2×10^{-4}	1.8	1.8
LHRS	1.710	2.5	90°	40-00-16	2.4×10^{-4}	2.4	1.5
LHRS	1.157	2.5	90°	40-00-16	3.2×10^{-4}	2.1	1.3
LHRS	2.254	5.0	0°	40-00-16	2.2×10^{-4}	1.6	1.2
RHRS	2.254	2.5	90°	48-48-16	1.8×10^{-4}	1.6	1.2
RHRS	2.254	2.5	90°	40-32-16	2.5×10^{-4}	2.2	1.8
RHRS	1.710	2.5	90°	40-00-16	2.3×10^{-4}	2.7	1.7
RHRS	1.157	2.5	90°	40-00-16	3.4×10^{-4}	1.9	1.5

Table 4.3: Summary of optics performance with the target field. The resolutions are calculated using Eq. 4.25. Table reproduced from [123].

and energy loss and radiation processes. In this section, the energy loss processes and multiple scattering in the simulation will be discussed.

4.5.2.1 Radiation in Simulation

A charge particle will experience several kinds of interactions when passing through material. It will lose energy and be deflected from initial direction. These interactions include: inelastic collisions with atomic electrons in the material, scattering off nuclei, bremesstrahlung, emission of Cherenkov radiation, and nuclear reactions. The bremesstrahlung can be divided into external and internal ones, depending on whether the interaction occurs on the scattering nuclei or some other nuclei. For g2p experiment, most of these processes are electromagnetic effects and are calculable in QED. However, to study the detector acceptance, the QED calculation involving the analytical integration over the photonic phase space is complicated or not desirable because it requires knowing specifics of the detector geometry and resolutions. The Monte Carlo simulation which provides the radiative effects is very crucial to help study this issue. Ionization, internal and external bremesstrahlung are the most contributing radiative effects in addition to the primary scattering.

Ionization is due to the charged particle colliding atomic electrons. The average energy loss per unit path length for an electron is described by the modified Bethe-

Bloch formula[132]:

$$\frac{dE}{dx} = 2\pi N_A r_e^2 m_e c^2 \rho \frac{Z}{A}\frac{1}{\beta^2}\left[\ln(\frac{\tau^2(\tau+2)}{2(I/(m_e))^2} - F(\tau) - \delta - 2\frac{C}{Z}\right], \tag{4.41}$$

where N_A is Avogadro‘s number, r_e is the classical electron radius (2.818 fm), I is the mean excitation potential of material, ρ is the density of the absorb material, Z (A) is the atomic number (weight) of the material, $\beta = v/c$ is for the incident electron, δ is the shell correction, C is the density correction due to the the fact that the incident electron polarizes atoms along its path and this polarization shields the full electric field intensity for the atomic electrons far away from the path, τ and $F(\tau)$ are factors:

$$\tau = \frac{E - m_e c^2}{m_e c^2}, \quad \text{and} \tag{4.42}$$

$$F(\tau) = 1 - \beta^2 + \frac{\tau^2/8 - (2\tau+1)\ln 2}{(\tau+1)^2}. \tag{4.43}$$

For a given electron passing through the media, the energy loss is not always equal to the mean value given by Eq. 4.41 because of the statistical nature in the number of collisions and the associated energy loss in each collision. In the simulation package, the ionization energy loss is divided to discrete and continuous energy loss. The discrete energy loss represents the energy loss due to the explicit production of a δ electron. The cross section for generating a δ electron is determined by the δ electron production threshold. The random sampling of the δ electron energy is based on [133, 134]. The discrete energy loss is above the δ electron production threshold.

The cumulative effect of ionization below the δ-ray production threshold is counted as continuous energy loss. A parameterised model by L. Urbán is applied for the fluctuation of energy loss. It is assumed that the atoms have only two energy levels with binding energy E_1 and E_2. The particle-atom interaction will then be an excitation with energy loss E_1 or E_2, or an ionisation with an energy loss distributed according to a function $g(E) \sim 1/E^2$. See more details in Ref.[133, 134].

In addition to ionization energy loss, the electron also lose energy by interacting with the Coulomb field of the transverse medium. The lost energy is emitted as a forms of photons due to bremesstrahlung. The external bremesstrahlung describes the bremesstrahlung in the field of other nuclei, not the actual nucleus the electron scatters. The probability for an electron of E_0 to radiate $\Delta E = E_0 - E$ through a distance of t radiation length in the target is given by[135]:

$$I(E_0, E, t) = bt(E_0 - E)^{-1}\left[\frac{E}{E_0} + \frac{3}{4}\left(\frac{E_0 - E}{E}\right)^2\right]\left(\ln\frac{E_0}{E}\right)^b t, \tag{4.44}$$

where b is

$$b = \frac{3}{4}\left[1 + \frac{1}{9}\frac{Z+1}{Z+\phi}\right]\ln(183Z^{-1}), \tag{4.45}$$

with

$$\phi = \ln(1440Z^{-2/3})/\ln(183Z^{-1}). \tag{4.46}$$

In the simulation, the distribution of Eq. 4.44 is sampled with the acceptance and rejection method. After each sampling, the energy of the electron decreases by ΔE but direction is kept the same direction in approximation since bremsstrahlung is very forwardly peaked.

Internal bremsstrahlung is defined as energy loss due to photon emission resulting from the primary nuclear interaction. The radiation effects on the cross section can be decomposed to vacuum polarization correction, noninfrared vertex contribution, and the radiative tail. The sum of vacuum and vertex corrections is:

$$\delta_v = \frac{2\alpha}{\pi}(-\frac{14}{9} + \frac{13}{12}\ln\frac{-q^2}{m^2}), \tag{4.47}$$

with m the electron mass and contributed contributes as $e^{-\delta_v}$ to scale the Born cross section. While the radiative tail can be approximated by the equivalent radiator concept[135], with one before and after scattering, each of thickness

$$t_{equiv} = \frac{-\alpha}{\pi}(\ln\frac{-q^2}{m^2} - 1). \tag{4.48}$$

In the simulation, the probability distribution of internal bremesstrahlung is computed the same approach as for external bremesstrahlung by using t_{equiv} in place of t in Eq. 4.44 and calculated separately for before and after scattering.

4.5.2.2 Multiple Scattering

As the charged particle passes through the material, it will be deflected by many small-angle scatterings. Most of these deflections are due to Coulomb scattering from nuclei as described by the Rutherford cross section. The probability distribution for the deflected angle θ can be approximated with a Gaussian distribution. Assume the scattering happens only in one plane, the standard deviation σ_θ for traveling t radiation length in the relativistic limit is[136]:

$$\sigma_\theta = \frac{0.0136}{E} 2\sqrt{t}\left[1 + 0.038\ln(t)\right], \tag{4.49}$$

where E is the energy of the particle. In the simulation, the deflected angle is generated by a random Gaussian distribution.

4.5.2.3 Simulation Results

Fig. 4-33 shows the absolute yield comparison between simulation and data. The data are from a carbon run with no liquid helium, beam raster on, and at the longitudinal 5T target field configuration. The simulation agrees with data in the central region of acceptance -0.05 mrad$<\theta_{\mathrm{tg}} < 0.05$ mrad, which suggests the radiation model works well. For the region away from the center, deviations are found and are still under study. These deviations may be due to applying the optics (a coverage using point beam ±4 mm, see Sec. 4.5.1.7) to the large raster size (10mm in diameter) or due to the aperture in the Snake transportation functions.

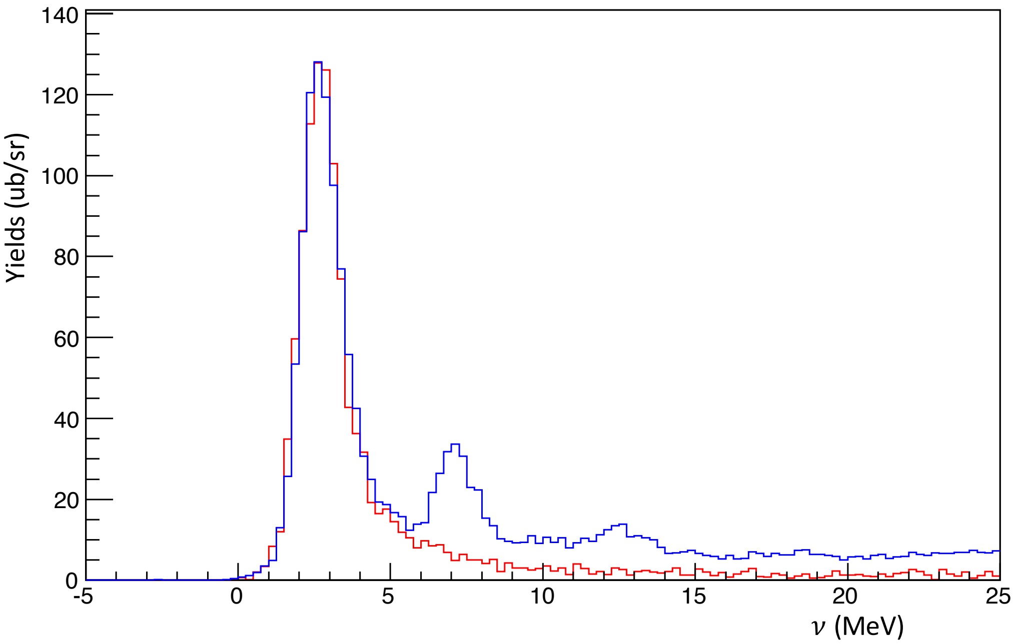

Figure 4-33: Yields comparison between simulation and experimental data. The data are from a carbon run with no liquid helium, raster on, and at the longitudinal 5T target field configuration. More updates can be found in [137].

4.6 Yield Drift Study

For the same experimental condition, the runs with the same kinematics setting should have the same yields:

$$Y = \frac{N_{acc} \cdot ps}{Q \cdot LT \cdot \epsilon_{det}}. \tag{4.50}$$

However, during the E08-027 experiment, there are 23/135 momentum settings where the yields differ by more than than 4% within the same kinematic setting. Fig. 4-34 shows the yields with a 7% deviation for the E_{beam} = 2.2 GeV, P = 1.6 GeV, 5T transverse setting. A method was developed to resolve the issue by studying the raster pattern, as shown in Fig. 4-35. The left plot shows the raster pattern in Happex DAQ which is triggered by the helicity signal (∼1 kHz). A cut in the raster pattern (block spot with 6 mm in diameter) can be used to extract the corresponding charge.

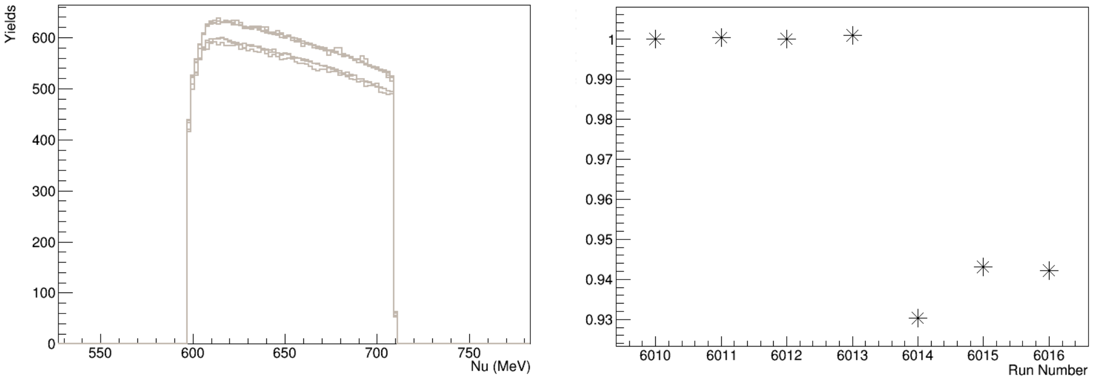

Figure 4-34: Yields versus ν for $E_{beam} = 2.2$ GeV, $P = 1.6$ GeV, 5T transverse setting (left); Relative yields versus number for the same setting (right).

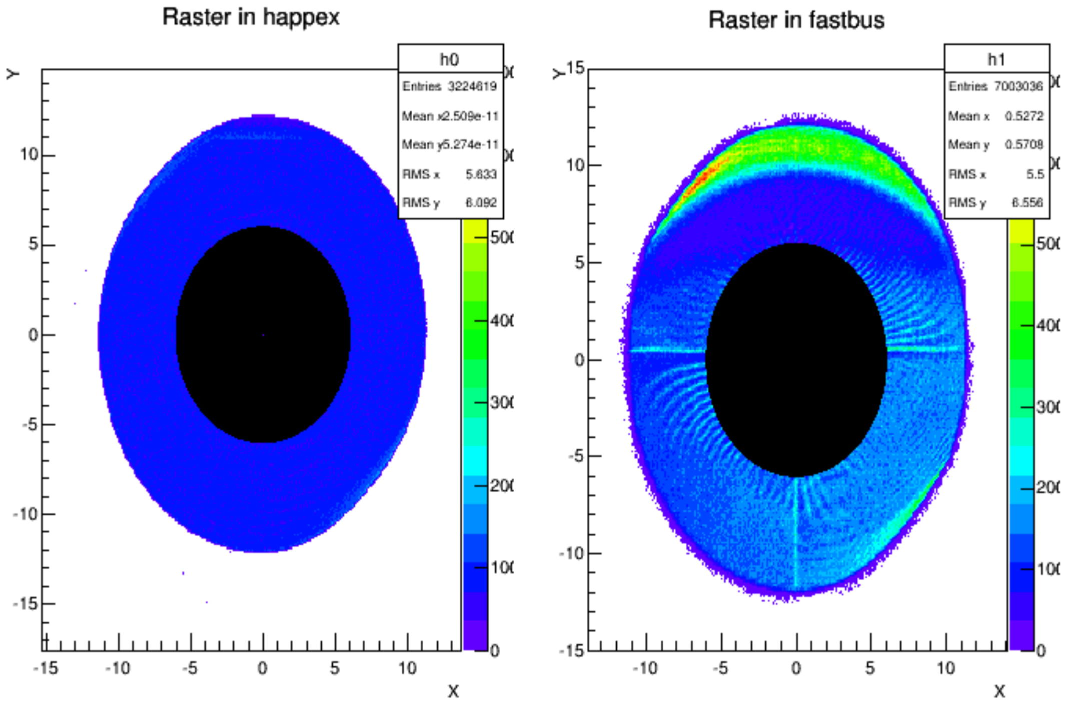

Figure 4-35: 6 mm raster cut (black spot) in both Happex (left) and Fastbus (right) DAQ. With these raster cuts, the uncertainty from the boundary of raster (right) is removed.

Meanwhile, the right plot shows the raster pattern in the Fastbus DAQ which is from the physics trigger ($\sim$ 6 kHz), so a cut in the raster size can be used to extract the

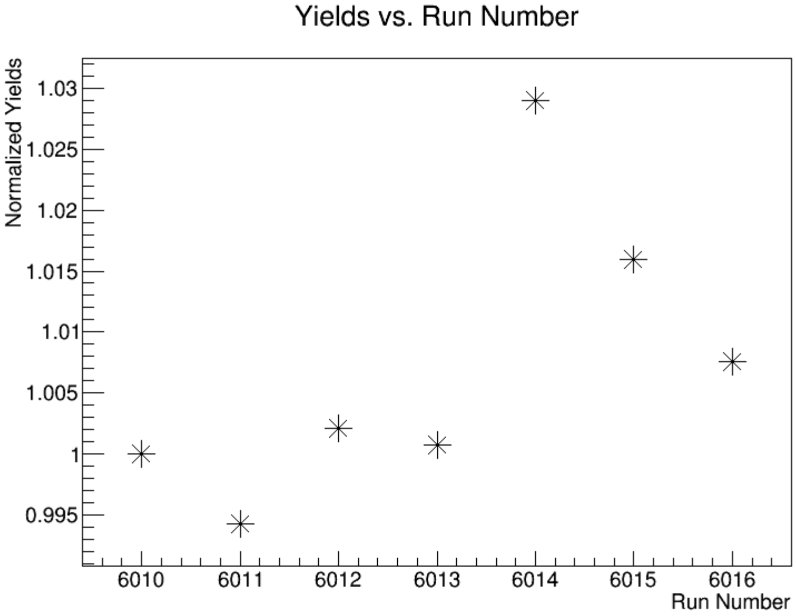

Figure 4-36: Relative yields versus run number for $E_{beam} = 2.2$ GeV, $P = 1.6$ GeV, 5T transverse setting after applying the 6 mm raster cut.

corresponding scattering events. Therefore, after applying the raster size cut, the corresponding yields and charge can be obtained. The yields spread becomes 3.5% as shown in Fig. 4-36. By applying this method, about half of the drifts are reduced to below 4%. More details can be found in [137].

Chapter 5

Preliminary Results

In this chapter, preliminary results are presented for asymmetries, polarized cross-section differences, the spin structure functions for the beam energy 2.254 GeV with the target field 5.0 T both longitudinal and transverse settings. The spin structure functions contribute to the spin polarizabilities γ_0 and δ_{LT} are also discussed. For other energy settings, the dilution and packing fraction analysis are still ongoing, and thus their results are not included here.

5.1 Asymmetry Results

The method to extract the asymmetry is described by Eq. 4.1. Each of the required parameters has been discussed in previous sections, such as beam charge Q in Sec. 3.3.2, beam polarization P_b in Sec. 3.3.5, target polarization P_t in Sec. 3.4, and dilution factor f in Sec. 4.4. The statistical uncertainty of the raw asymmetry can be written as:

$$\delta A_{raw} = \frac{2Y_+Y_-}{(Y_+ + Y_-)^2}\sqrt{\frac{S_+^2}{N_+} + \frac{S_-^2}{N_-}} \approx \frac{1}{2}\sqrt{\frac{S_+^2}{N_+} + \frac{S_-^2}{N_-}}, \tag{5.1}$$

where $Y_\pm$ is the yield corresponding to $\pm$ helicity state (Eq. 4.50), while $S_\pm = \sigma_{N_\pm}/\sqrt{N_\pm}$ is a correction factor. In general, the fluctuation in the number of events $N_\pm$ follows the Poisson distribution with $\sigma_{N_\pm} = \sqrt{N_\pm}$, therefore $S_\pm$=1. However, when the raw trigger rate is high enough, a prescale factor is used to scale the DAQ event rate, and thus the correction factor $S_{\pm}$ is changed due to an additional source contribution from acceptance fluctuation[138]:

$$S = \sqrt{1 - LT \cdot R(1 - \frac{1}{ps})}, \tag{5.2}$$

where LT is the livetime correction of the DAQ system, ps is the prescale factor, and R is the acceptance for useful events which can be obtained form the number of accepted events to the number of recorded events. From Eq. 4.1, the statistical uncertainty of physics asymmetry can be written as:

$$\delta A_{phys} = \frac{1}{f P_t P_b} \delta A_{raw}, \tag{5.3}$$

where the uncertainties of the target and beam polarizations and dilution factor are considered as systematic uncertainties, and not considered here.

The asymmetry results are often formed in each bin of W (or ν) to show the evolution. During the experiment, several runs were taken for each momentum setting, and therefore the asymmetry calculated from corresponding runs are combined using a statistically weighted average:

$$A = \frac{\sum_i A_i/\delta A_i^2}{\sum_i 1/\delta A_i^2}, \tag{5.4}$$

with

$$\delta A = \sqrt{\frac{1}{\sum_i 1/\delta A_i^2}}, \tag{5.5}$$

where A_i is the asymmetry calculated for the i-th run and δA_i is the corresponding statistical uncertainty.

Fig. 5-1 shows the physics asymmetry at beam energy 2.254 GeV setting with the target field 5.0 T both longitudinal and transverse. The error bars shown are statistical uncertainties.

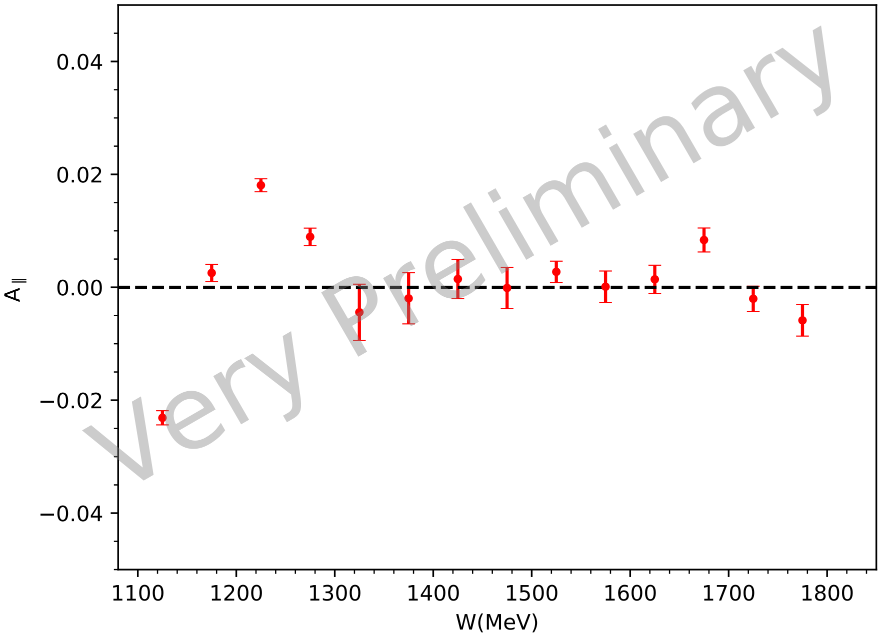

(a) Longitudinal configuration.

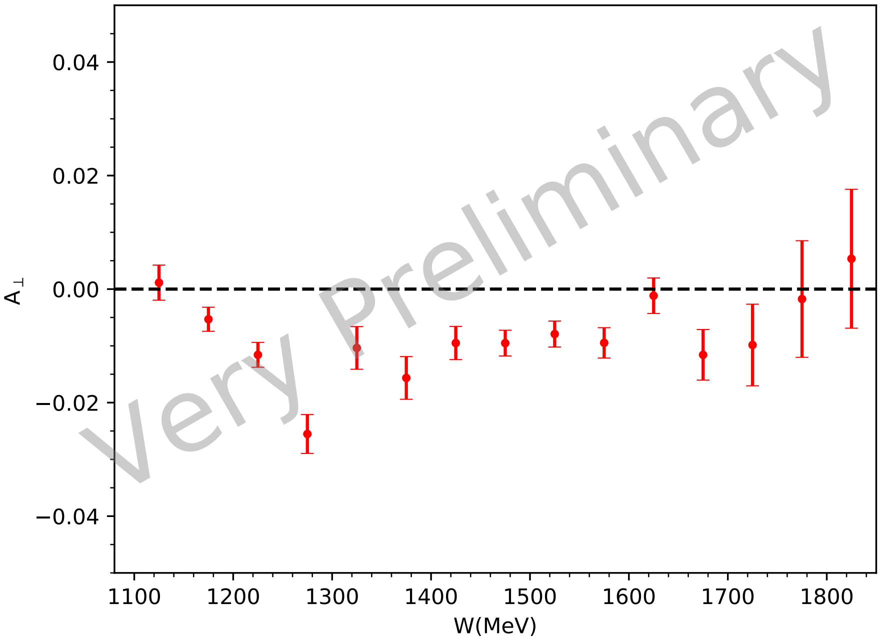

(b) Transverse configuration.

Figure 5-1: Physics asymmetries for the configurations with 2.254 GeV beam energy and 5.0 T target field. Only the statistical uncertainty is shown in the error bar.

5.2 Radiative Corrections

The electron scattering diagram in Fig. 2-1 shows only the leading order process of one photon exchange, which is usually considered in the theoretical predictions. However, as mentioned in Sec. 4.5.2.1, ionization, vacuum polarization and vertex correction, internal and external bremesstrahlung, are contained in the experimental data. Therefore, the quantities extracted from the data, such as asymmetries and cross sections, need be corrected to compare with theoretical calculations, and this correction is referred as the radiative correction.

For the preliminary results presented here, the radiative corrections to the asymmetry is based on model predictions. The MAID model[139] is used to generate the polarized cross section difference. The internal radiative effects are calculated using the POLRAD formalism[140], while the external parts (ionization and external bremesstrahlung) are determined using the methods developed by Mo and Tsai[141]. The polarized elastic tail contributions are also taken into account by using the MASCARD code[142] combined with the corresponding form factors.

The unpolarized cross section is generated by the fits of P. Bosted[126]. The inelastic radiative effects are calculated with the fits of P. Bosted as inputs for both the internal and external corrections, while the elastic tail is again from Mo and Tsai formalism.

Fig. 5-2 shows the radiated and unradiated asymmetries compared with model predictions for 2.254 GeV beam energy setting with 5.0 T target field both longitudinal and transverse. The input for the scattering angle represents the average scattering angle determined from the data.

The difference between the radiated and unradiated asymmetry curves in Fig. 5-2 are applied to the data asymmetry $A_{\text{uncorrected}}$ as the radiative correction:

$$A_{\text{corrected}} = A_{\text{uncorrected}} + \Delta_{\text{RC}}^{\text{model}}, \tag{5.6}$$

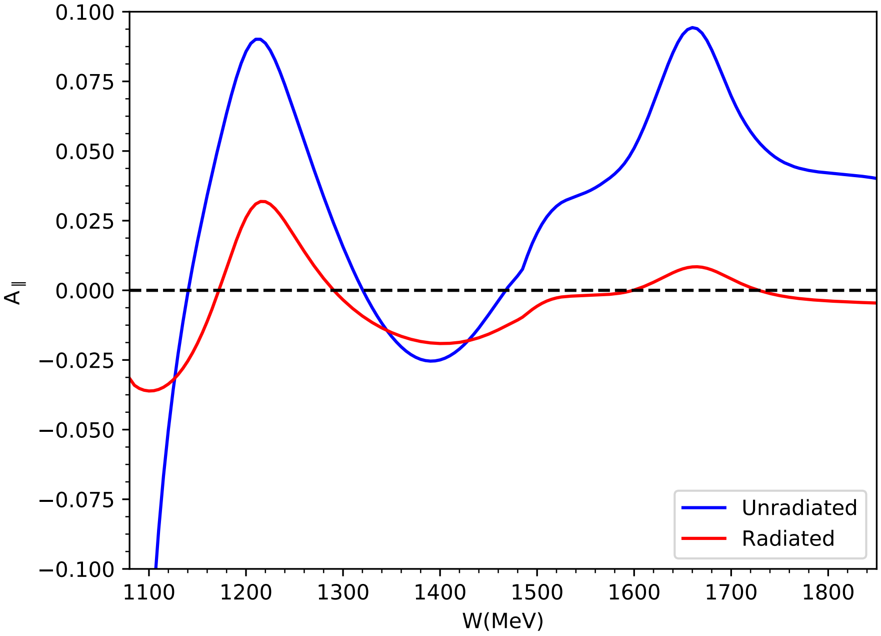

(a) Longitudinal configuration.

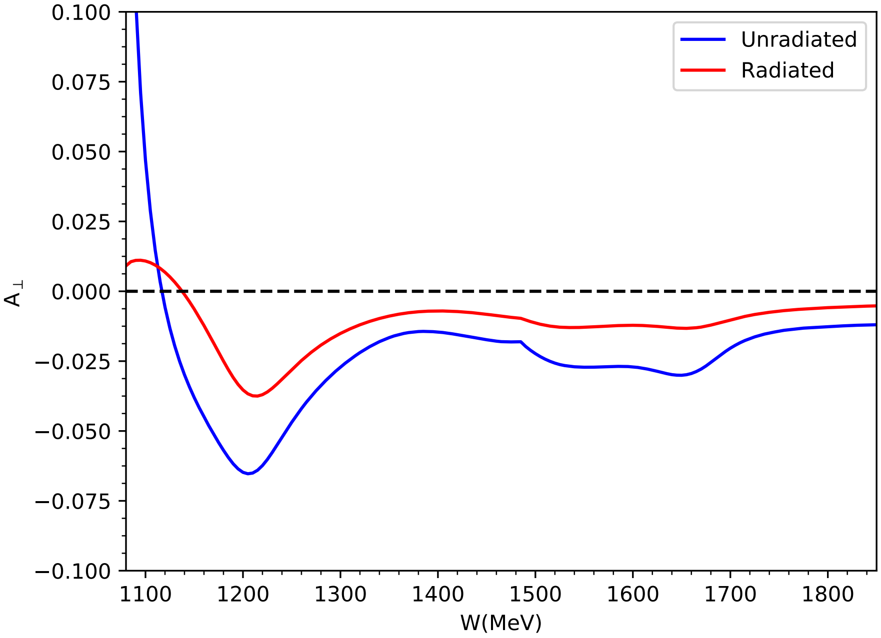

(b) Transverse configuration.

Figure 5-2: Comparison of the radiated and unradiated model predictions for the asymmetries with 2.254 GeV beam energy and 5.0 T target field both longitudinal and transverse.

with

$$\Delta_{\rm RC}^{\rm model} = A_{\rm unrad}^{\rm model} - A_{\rm rad}^{\rm model}. \tag{5.7}$$

The radiative-corrected and uncorrected physics asymmetries are shown in Fig. 5-3. The grey band shows the estimated systematic uncertainty. The current status of systematic uncertainty is given by

$$\delta A_{phys}^{sys} = \sqrt{(\frac{\partial A}{\partial f}\delta_f)^2 + (\frac{\partial A}{\partial P_t}\delta_{P_t})^2 + (\frac{\partial A}{\partial P_b}\delta_{P_b})^2 + (\delta A_\pi)^2 + (\delta A_Q)^2 + (\delta A_{LT})^2 + (\delta_{\Delta RC})^2} \tag{5.8}$$

where

- **Dilution Factor** (f): The systematic uncertainty is around 6.0% for the longitudinal setting, while 6.5% for the transverse setting, see Sec. 4.4.
- **Beam Polarization** (P_b): the uncertainty on the Moller measurement is given as 1.7%, see Sec. 3.3.5.
- **Target Polarization** (P_t): the target polarization uncertainty is (2-4.5)% depends on run, see Sec. 3.3.5.
- **Livetime Asymmetry** (A_{LT}): $\delta A_{LT} \approx 5.5 \times 10^{-6}$, see Ref.[115].
- **Charge Asymmetry** (A_Q): $\delta A_{LT} \approx 1.1 \times 10^{-4}$, see Ref.[115].
- **Pion Asymmetry** (A_π): $\delta A_\pi \approx 4.5 \times 10^{-5}$, see Ref.[115].
- **Radiative Correction** (ΔRC): since the MAID model predictions are not tested at the kinematics of this experiment, the difference between the measured data asymmetry (blue points in Fig. 5-3) and the radiated MAID model predictions (blue dashed line in Fig. 5-3) is taken as the uncertainty for radiative correction. It contributes the leading error currently, but will be reduced when the cross sections of this experiment are available.

Other contributions, such as acceptance effects, are still being studied.

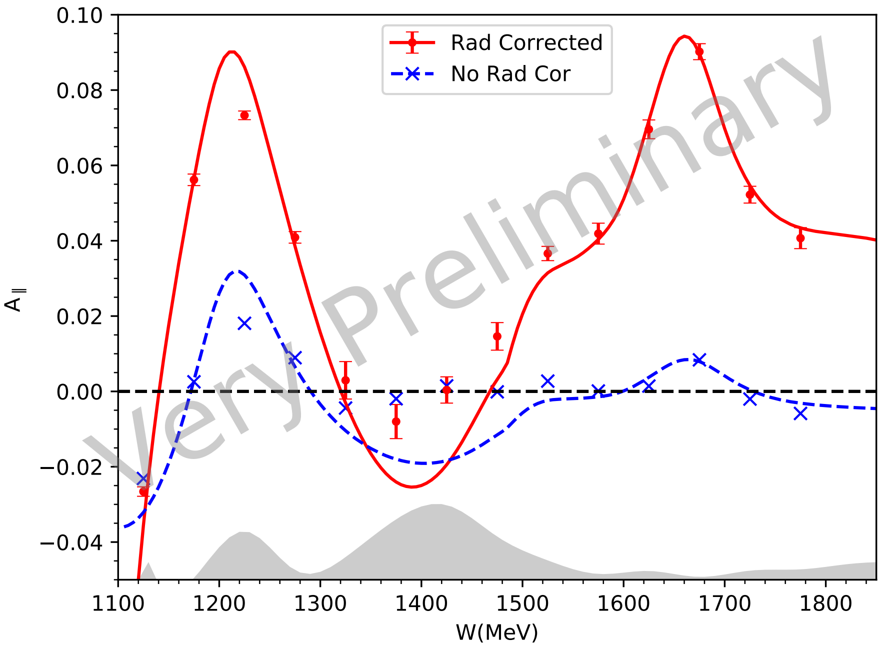

(a) Longitudinal configuration.

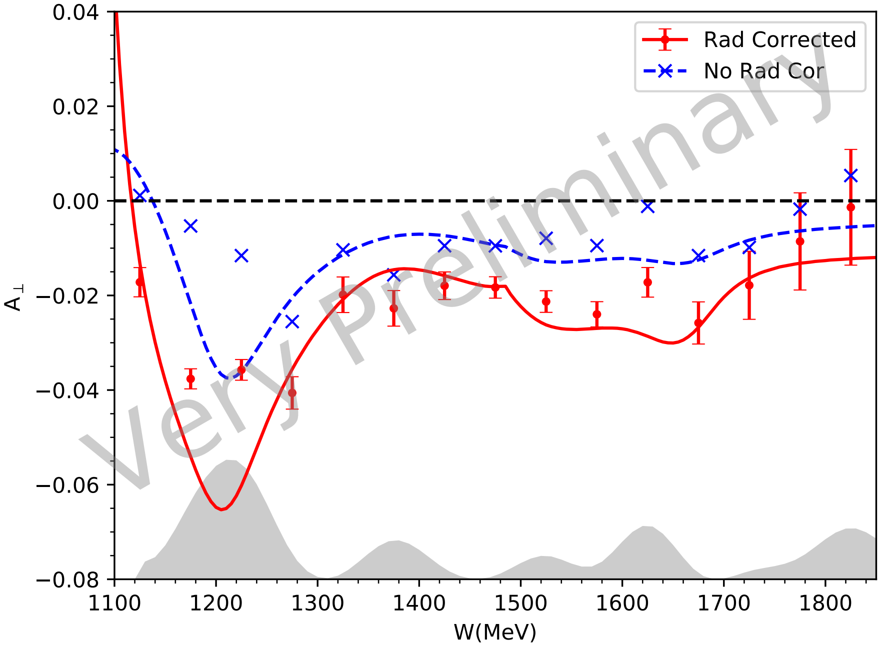

(b) Transverse configuration.

Figure 5-3: Comparison of the radiative-corrected and uncorrected physics asymmetries for the kinematic settings with 2.254 GeV beam energy and 5.0 T target field both longitudinal and transverse. The statistical uncertainty is shown as the error bar on each data point, while the systematic is shown as the grey band. The errors for the uncorrected asymmetry are not shown in this plot.

5.3 Polarized Cross-Section Differences

The polarized cross-section differences can be calculated using Eq. 4.7. Since the unpolarized cross section is still being studied, the fits of P. Bosted [126] are used as the unpolarized cross-section. The radiative-uncorrected polarized cross section difference can be evaluated as

$$\Delta\sigma_{\parallel,\perp}^{\text{uncorrected}} = 2A_{\parallel,\perp}^{\text{uncorrected}} \cdot \sigma_0^{\text{uncorrected}}, \tag{5.9}$$

where $A_{\parallel,\perp}^{\text{uncorrected}}$ is from Eq. 4.1 and $\sigma_0^{\text{uncorrected}}$ is the radiated version of the fits of P. Bosted, while the radiative-corrected polarized cross section difference is given by

$$\Delta\sigma_{\parallel,\perp}^{\text{corrected}} = 2A_{\parallel,\perp}^{\text{corrected}} \cdot \sigma_0^{\text{corrected}}, \tag{5.10}$$

where $A_{\parallel,\perp}^{\text{corrected}}$ is from by Eq. 5.6 and $\sigma_0^{\text{corrected}}$ is the fits of P. Bosted.

The radiative-corrected and uncorrected cross-section differences are shown in Fig. 5-4. The systematic uncertainty of radiative-corrected cross-section difference results has two major contributions. One is the systematic uncertainties of the asymmetries $A_{\parallel,\perp}$ discussed in Sec. 5.2, the other is from the unpolarized cross-sections $\sigma_0^{\text{uncorrected}}$ which is estimated to be 5% when calculated using fits of P. Bosted.

5.4 Spin Structure Function g_2^p

As discussed in Sec. 2.2.4, the polarized structure functions g_1 and g_2 can be written in terms of the cross section differences $\Delta\sigma_{\parallel,\perp}$ by Eqs. 2.53 and 2.54. In the analysis of this thesis, the $\Delta\sigma_{\parallel,\perp}$ results were obtained using asymmetries measured in E08-027 combined with model predictions for σ_0 in Sec. 5.3. Since the kinematics of the longitudinal and transverse settings are not the same (field bending differently), the cross section difference cannot simply be combined to extract the structure functions. We combine MAID predictions $\Delta\sigma_{\parallel}$ to extract g_2 from the transverse setting result of $\Delta\sigma_{\perp}$ using Eq. 2.54. Because the transverse setting cross section difference

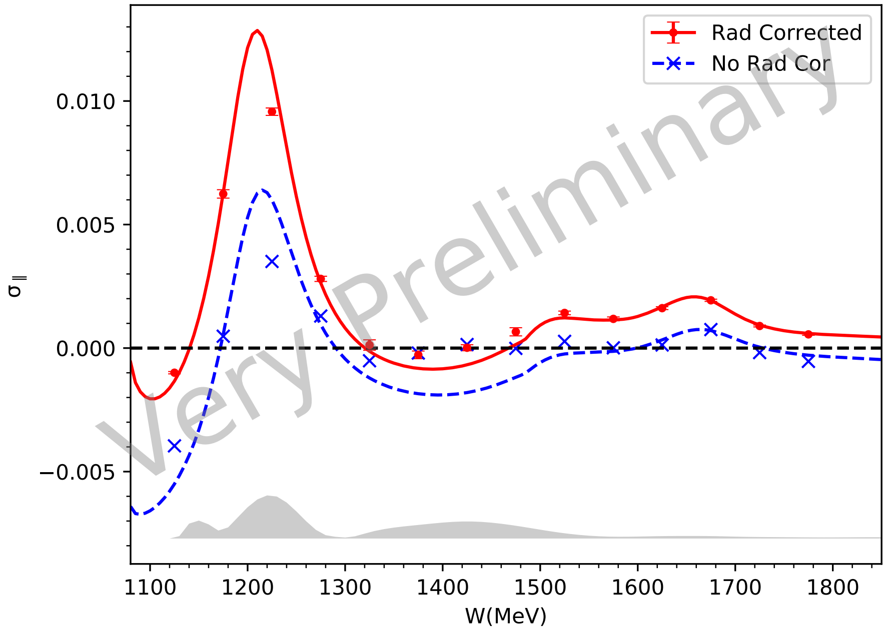

(a) Longitudinal configuration.

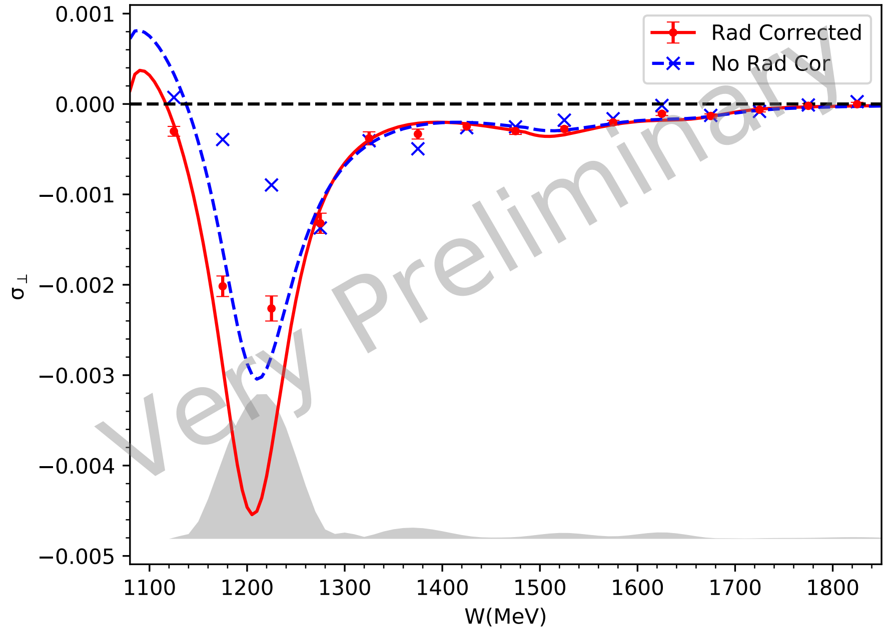

(b) Transverse configuration.

Figure 5-4: Comparison of the radiative-corrected and uncorrected cross-section difference for the kinematic settings with 2.254 GeV beam energy and 5.0 T target field both longitudinal and transverse. The statistical uncertainty is shown as the error bar on each data point, while the systematic is shown as the grey band. The errors for the uncorrected asymmetry are not shown in this plot.

is dominated by g_2 (see Eq. 2.52), the systematic uncertainty due to using MAID is minimized. Similarly, the MAID predictions for $\Delta\sigma_\perp$ is combined with $\Delta\sigma_\parallel$ from the longitudinal setting data to evaluate g_1. The MAID model input is assumed 40% relative uncertainty for both cases. The extracted g_1 and g_2 results are shown in Fig. 5-5. The statistical uncertainties are propagated from Sec. 5.3, while the systematic uncertainties is propagated from Sec. 5.3 with additional contribution from MAID model predictions.

5.5 Burkhardt-Cottingham Sum Rule

With a preliminary result for g_2 from Sec. 5.4, the contribution to the first moment of g_2 can be formed. Fig. 5-6 shows the integrand value versus Bjorken x for the transverse setting. The longitudinal setting is not shown since the g_2 is dominant by the model predictions for $\Delta\sigma_\perp$ in that case. The statistical uncertainty is shown as the black error bar, while the total uncertainty shown as the red error bar. From Fig. 5-6, one can see that the contribution from the measured resonance region to the integral is overall negative, which is consistent to RSS results shown in Fig. 2-13.

5.6 Spin Polarizability γ_0 and δ_{LT}

As discussed in Sec. 2.6.2, the generalized spin polarizabilities γ_0 and δ_{LT} can be expressed as moments of g_1 and g_2 by Eq. 2.121 and Eq. 2.125, respectively. The integrals need to be evaluated from $x = 0$ to the pion threshold ($x \approx 0.25$ at this setting). Fig. 5-7 and Fig. 5-8 shows the integrand value versus x using the preliminary results from Sec. 5.4 . The statistical uncertainty is shown as the black error bar, while the total uncertainty is shown as the red error bar. The unmeasured low x region will be assumed to follow g_2^{ww} (Eq. 2.94) and expected to be suppressed fast due to the x^2 weighting in the integrals.

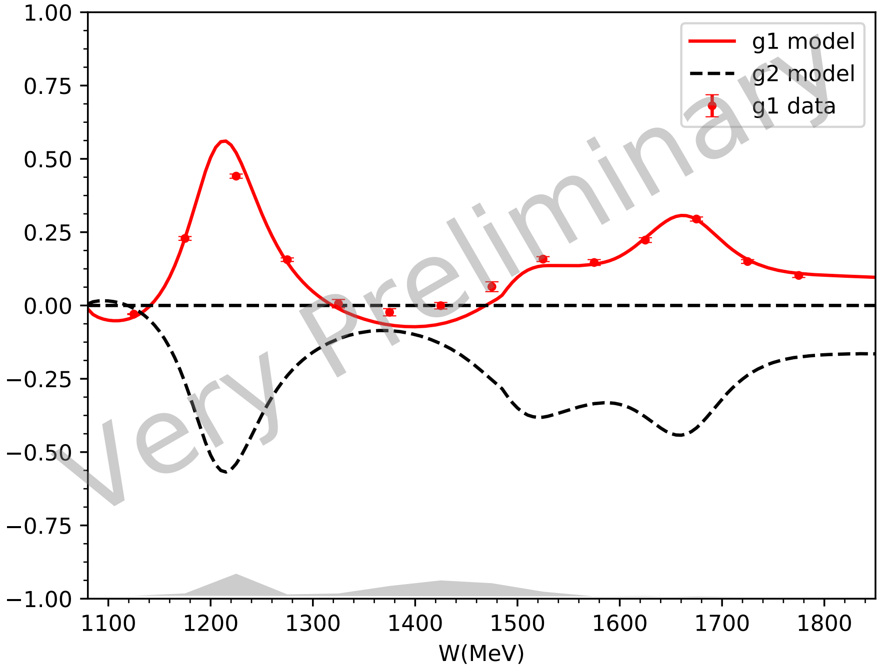

(a) Longitudinal configuration. MAID model calculation for $\Delta\sigma_{\perp}$ was combined with data to extract the g_1^p.

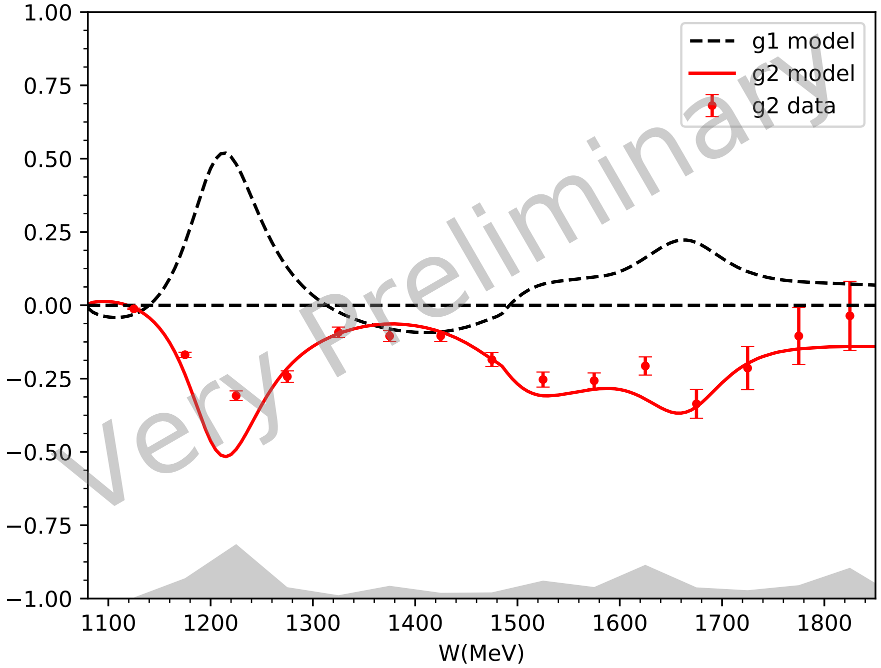

(b) Transverse configuration. MAID model calculation for $\Delta\sigma_{\parallel}$ was combined with data to extract the g_2^p.

Figure 5-5: g_1 and g_2 results for the kinematic settings with 2.254 GeV beam energy and 5.0 T target field both longitudinal and transverse. The statistical uncertainty is shown as the error bar on each data point, while the systematic is shown as the grey band. The errors for the uncorrected asymmetry are not shown in this plot.

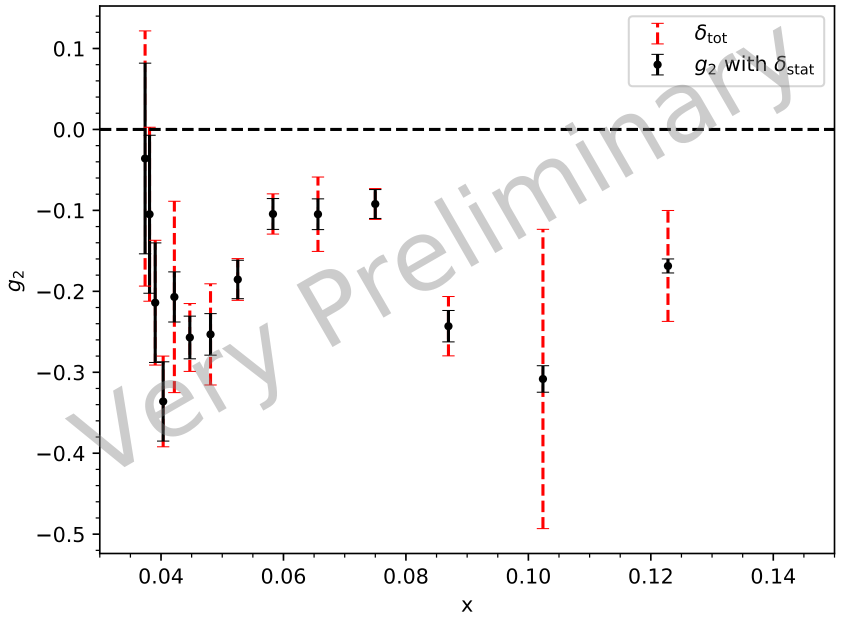

Figure 5-6: g_2 versus Bjorken x for the kinematic setting with 2.254 GeV beam energy and 5.0 T transverse target field. The black error bars show the statistical uncertainty δ_{stat} while the red error bars show the total uncertainty δ_{tot}.

5.7 Summary and Outlook

The E08-027 experiment successfully collected data to extract the proton g_2 structure function in the Q^2 range of $(0.02 - 0.2)$ GeV^2. In this thesis, the preliminary results of the asymmetry at 2.254 GeV beam energy and 5.0 T target field (both longitudinal and transverse) are presented. The polarized cross sections difference $\Delta\sigma_{\parallel,\perp}$ are obtained and presented with inputs from models and world data, because the analysis of cross section is still ongoing. Once the acceptance is finalized and the cross section is ready, the model prediction inputs will be replaced and the preliminary radiative correction will be improved with proper tuning to the data. These studies will improve the systematic uncertainties.

For the 2.254 GeV and target field 5.0 T setting, both longitudinal and transverse data were collected. While the transverse data will eventually provide precision results on $\Delta\sigma_\perp$ as described above, the longitudinal data will be used to extract $\Delta\sigma_\parallel$ as a cross check of another JLab experiments, EG4, which focused on measuring g_1^p using

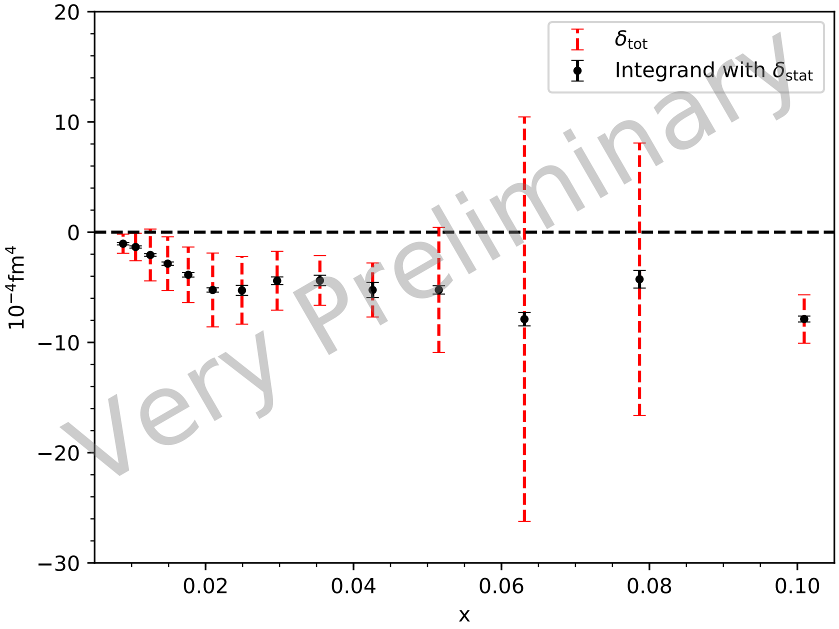

(a) Longitudinal configuration. MAID model calculation for $\Delta\sigma_{\perp}$ was combined with data to extract the δ_{LT} integrand.

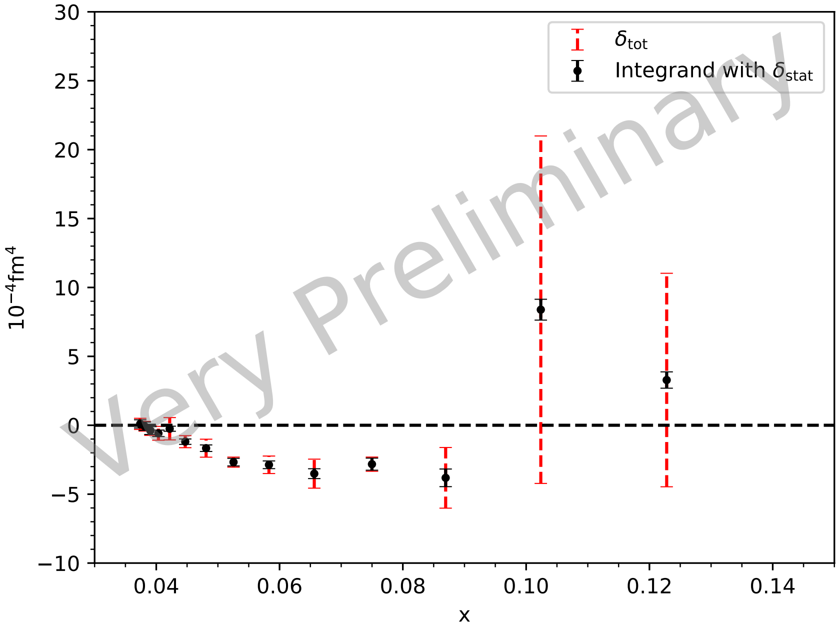

(b) Transverse configuration. MAID model calculation for $\Delta\sigma_{\parallel}$ was combined with data to extract the δ_{LT} integrand.

Figure 5-7: Preliminary results for the δ_{LT} integrand, $\frac{4e^2M^2}{\pi Q^6}x^2\left[g_1(x,Q^2)+g_2(x,Q^2)\right]$, for the kinematic settings with 2.254 GeV beam energy and 5.0 T target field both longitudinal and transverse. The average Q^2 is ≈0.1 GeV^2 for this setting. The black error bars show the statistical uncertainty δ_{stat} while the red error bars show the total uncertainty δ_{tot}.

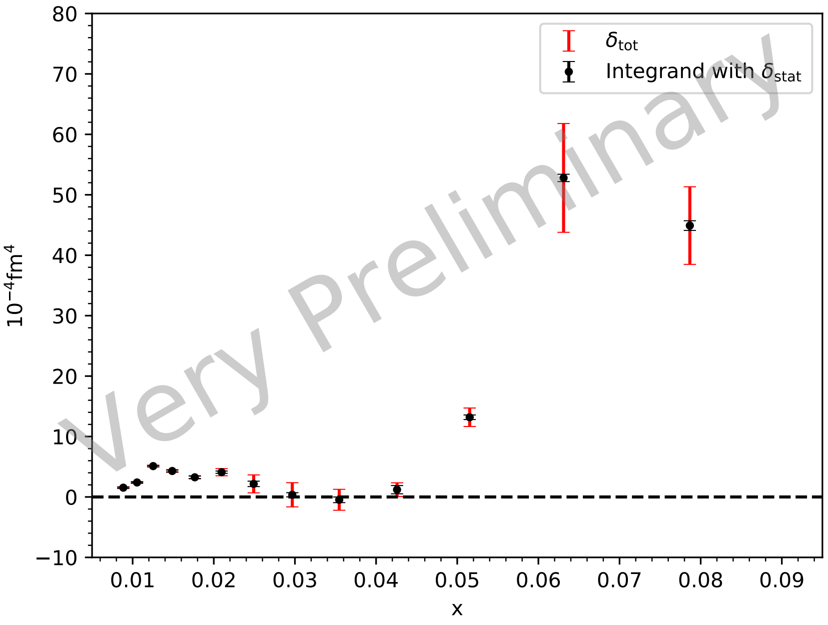

(a) Longitudinal configuration. MAID model calculation for $\Delta\sigma_\perp$ was combined with data to extract the γ_0 integrand.

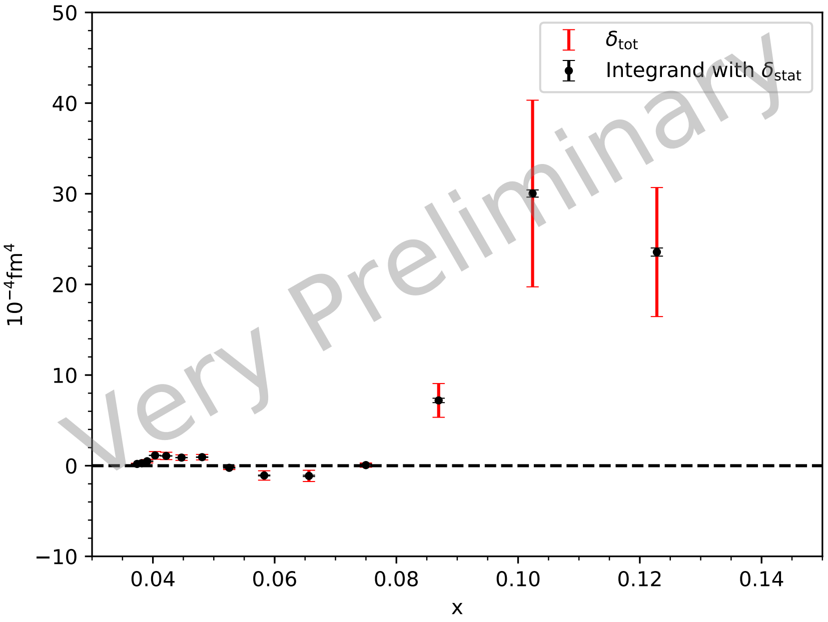

(b) Transverse configuration. MAID model calculation for $\Delta\sigma_\perp$ was combined with data to extract the γ_0 integrand.

Figure 5-8: Preliminary results for the γ_0 integrand, $\frac{4e^2M^2}{\pi Q^6}x^2\left[g_1 - \frac{4M^2}{Q^2}x^2g_2\right]$, for for the kinematic settings with 2.254 GeV beam energy and 5.0 T target field both longitudinal and transverse. The average Q^2 is ≈0.1 GeV^2 for this setting. The black error bars show the statistical uncertainty $\delta_{\rm stat}$ while the red error bars show the total uncertainty $\delta_{\rm tot}$.

CLAS in Hall B at very low Q^2. The analysis on the longitudinal data presented in the previous paragraph paves the way for such cross check in the near future. For energies of E08-027 other than 2.254 GeV (and target field 5.0 T), only transverse target data were collected.

For all beam energy settings of E08-027, eventually the high precision results on $\Delta\sigma_\perp$ will be combined with $\Delta\sigma_\parallel$ results from Hall B EG4 to extract both g_1^p and g_2^P at low Q^2.

Once the studies mentioned above are done, the precision proton spin structure function g_2 will be used to provide the first test of BC sum rule at low Q^2 for proton, which has remained largely untested until now. The generalized spin polarizabilities γ_0 and δ_{LT} can also be formed to provide a benchmark test of χPT theory calculations. The E08-027 collaboration will continue the work to finalize these important physics quantities.

Chapter 6

JLab Polarized ^{3}He Target

This chapter will discuss the application of polarized ^{3}He gas in JLab-based nuclear physics.

6.1 Introduction

Polarized targets are essential for nucleon spin structure study. Because a free neutron target cannot be made dense due to its short lifetime (885.7±0.8s [136]) , polarized light nuclear targets such as deuteron and ^{3}He are typically used as effective polarized neutron targets. For a ^{3}He nucleus, as shown in Fig. 6-1, its ground state is dominated by an S-wave configuration in which the two proton spins are aligned opposite to one another and the neutron accounts for the nuclear spin [143]. Polarized ^{3}He targets have been widely used in the neutron electromagnetic form factor and spin structure function studies at MIT-Bates, SLAC, DESY, MAMI and JLab. At JLab, thirteen 6 GeV experiments (GDH [48, 84, 144, 145], G_M^n[146, 147], A_1^n[76, 148], g_2^n[75], Spin-duality[83], Small-Angle-GDH[82], G_E^n[149], Transversity[150, 151], A_y-DIS[152], d_2^n[153], A_y-QE[154], $(e, e'd)$[155] and A_y-$(e, e'n)$[156]) have successfully utilized the polarized ^{3}He target.

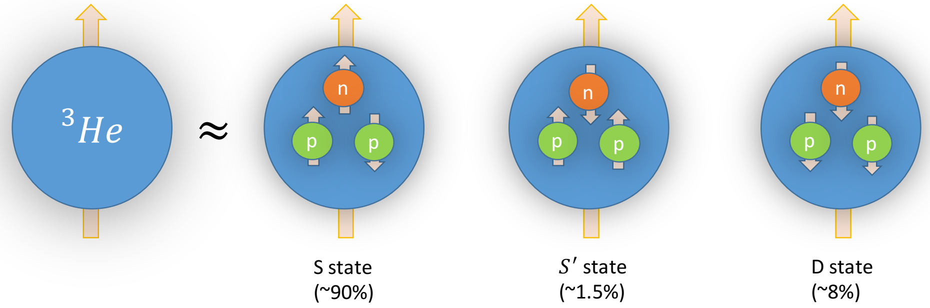

Figure 6-1: The ^{3}He wave function.

6.2 Spin-Exchange Optical Pumping

For ^{3}He atoms, the ground state 1^1S_0 is a single state with total electronic angular momentum J=0. Its total angular momentum F is equal to the nuclear spin I, F=I=1/2, and the thermal equilibrium nuclear polarization follows Boltzmann distribution:

$$P_{thermal} = \tanh \frac{\mu_{^3\mathrm{He}} B}{k_B T}, \tag{6.1}$$

where $\mu_{^3\mathrm{He}} = 1.0746 \times 10^{-26} J/T$ is the magnetic momentum, $k_B = 1.3806 \times 10^{-23} J/K$ is the Boltzmann constant, B is the magnetic field, and T is the temperature. For a 25 G field and room temperature, $P_{thermal} \approx 6.64 \times 10^{-9}$.

There have been two methods used to polarize ^{3}He nuclei beyond its thermal equilibrium value. The first one is based on metastability-exchange optical pumping (MEOP)[157], where the ^{3}He are optically pumped to the 2^3S_1 atomic metastable state (an excited state with a lifetime much longer than regular excited state, but shorter than the stable ground state, often functions as a temporary "energy trap") and the polarized meta-stable state $^3\vec{\mathrm{He}}(2^3S_1)$ subsequently transfer their polarization to the ground state nuclei $^3\mathrm{He}(1^1S_0)$ through metastability-exchange collisions $^3\vec{\mathrm{He}}(2^3S_1)+{}^3\mathrm{He}(1^1S_0)\rightarrow{}^3\vec{\mathrm{He}}(1^1S_0)+{}^3\mathrm{He}(2^3S_1)$. The efficiency of this method is determined by the amount and the lifetime of the metastable ^{3}He atoms. However, the presence of ^{3}He metastable states will lead to the depolarization of other ^{3}He metastable states through collisions, especially at pressure > 0.005 atm. So this approach is only suitable for low density targets. The second technique is based on spin exchange optical pumping (SEOP) [158], where a vapor of alkali-metal atoms is polarized by laser first and then the polarization is transferred to ^{3}He nuclei in a hyperfine spin-exchange interaction during collisions. The spin-exchange optical pumping method can be more easily applied to achieve high density targets (around 10 atm). This method was originally developed at SLAC and has been utilized for all the polarized ^{3}He related experiments at JLab since 1998. The details of SEOP will be discussed below.

6.2.1 Optical Pumping

The first step of SEOP is the optical pumping that polarize Rb vaporized atoms in a magnetic field by using a circularly polarized laser light. The magnetic filed is typically 25 G and is parallel to the laser propagation direction to split the Zeeman levels. Fig. 6-2 shows the D1 transition of Rb atoms from $5S_{1/2} \rightarrow 5P_{1/2}$, ignoring the effect of the nuclear spin. According to the angular momentum selection rule for dipole transition, only Rb atoms from the ground state $5S_{1/2}$ with $m_J = -1/2$ is excited to state $5P_{1/2}$ with $m_J = +1/2$ under the 795 nm right circularly polarized light. Then they decay back to two sub-levels of $5S_{1/2}$ with equal probability. So the Rb vapor is pumped to accumulate in the $m_J = +1/2$ $5S_{1/2}$ state. As shown in Fig. 6-2, the electron decays from $5P_{1/2}$ to $5S_{1/2}$ and emits a photon in all spatial direction. However, this photon is unpolarized and can be reabsorbed by other Rb atom, which depolarizes the Rb vapor. Fortunately, a small amount of N_2 ($\simeq$ 0.1 amg) added to the system can mitigate this effect[159]. The excited electron decays back to ground state mostly ($\approx$95%) through non-radiatively quenching since N_2 has vibrational and rotational degrees of freedom to absorb the energy.

For Rb vapor, there are two depolarization effects, caused by collisions between Rb atoms with the cell wall, and interatomic collisions. The Rb spin will reach an equilibrium population distribution determined by the optical pumping and the relaxation processes, which can be strongly deviated from the thermal equilibrium in Eq. 6.1. In other words, the Rb vapor can become highly polarized.

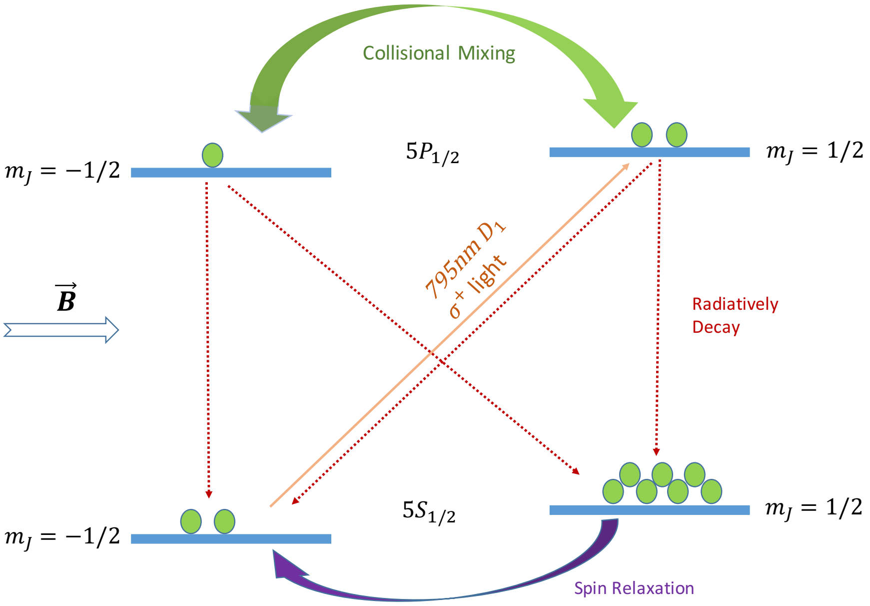

Figure 6-2: The Optical pumping of Rb.

The actual optical pumping is more complex than Fig. 6-2 if one also consider the hyperfine splitting between Rb nuclear spin ($I = 5/2$ for ^{85}Rb and $7/2$ for ^{87}Rb) and the electron angular momentum (S=1/2, L=0). As the external magnetic field is weak for this target, the hyperfine interaction is much stronger than Zeeman splitting. The hyperfine structure Hamiltonian for Rb ground state in the presence of static magnetic field $\vec{H} = H\hat{z}$ is

$$\begin{aligned}\mathcal{H}_{hfs} &= A_{hfs}\vec{I}\cdot\vec{S} - \vec{\mu}_s\cdot\vec{H} - \vec{\mu}_I\cdot\vec{H}\\ &= A_{hfs}\vec{I}\cdot\vec{S} - \frac{\mu_s}{S}S_zH_z - \frac{\mu_I}{I}I_zH_z,\end{aligned} \tag{6.2}$$

where A_{hfs} is the coupling coefficient, $\vec{I}$ is the nuclear spin, $\vec{S}$ is the electron spin, $\vec{\mu}_s = g_s\mu_B\vec{S}$ is the electron magnetic moment (g-factor $g_s = -2.0023$, Bohr magneton $\mu_B = 9.2740 \times 10^{-24}$ J/K, S=1/2), $\vec{\mu}_I = g_I\mu_N\vec{I}$ is the nuclear magnetic moment (g-factor $g_I = 0.5413$ for ^{85}Rb, nuclear magneton $\mu_N = 5.0508 \times 10^{-27}$ J/K). The eigenstates of $\mathcal{H}_{hfs}$ are described by quantum numbers F and m_F as $|F, m_F\rangle$. F is the total angular momentum of the state at field $H \to 0$ and m_F is the eigenvalue of $F_z = I_z + S_z$ at any field H. So the ground state $5S_{1/2}$ state actually splits to multi-levels $m_F = -F, -(F-1), ..., F-1, F$ with $F = I \pm 1/2$. The Rb atom is highly pumped to $m_F = F$ state under a right circularly polarized laser light and $m_F = -F$ for left-handed.

The pumping efficiency depends on the quality of the laser. The absorption line shape of Rb is broadened and shifted by the interatomic collisions[160, 161]. The Rb D_1 transition absorption spectrum has a FWHM of around 0.3 nm and the absorption peak fluctuates by typically 0.05nm due to the operational high pressure of ^{3}He (≈10 amg) and temperature (230 °C). If the laser light has a very large line width, a significant amount of light does not fall within the absorption line-width and is wasted. Moreover, the unusable light also adds to the thermal depolarization. In recent years, optical pumping has been greatly improved with the advance of laser techniques. Fig. 6-3 shows the light profile between different lasers with the same power 30 Watts. The newly available narrow-linewidth diode lasers (COMET, QPC, Raytum) with FWHM≈0.25 nm provide a much higher optical pumping efficiency than the broad-width diode lasers (Coherent) with FWHM≈1.5 nm and the in-beam ^{3}He target polarization subsequently increased from 50% (during GEN[149] in 2006) to 60%(during Transversity[150, 151] in 2009).

6.2.2 Spin Exchange

The second step is the spin exchange through which the polarized alkali atoms transfer their electron spin polarization to ^{3}He nuclei. The spin-exchange process is dominated by binary collisions. Alkali atoms interact with ^{3}He nuclei through both isotropic hyperfine interaction and spin-rotation interaction. The isotropic hyperfine interaction is the one produces spin-exchange and is described by Hamiltonian[162]:

$$H_{SE} = \alpha \vec{I} \cdot \vec{S}, \tag{6.3}$$

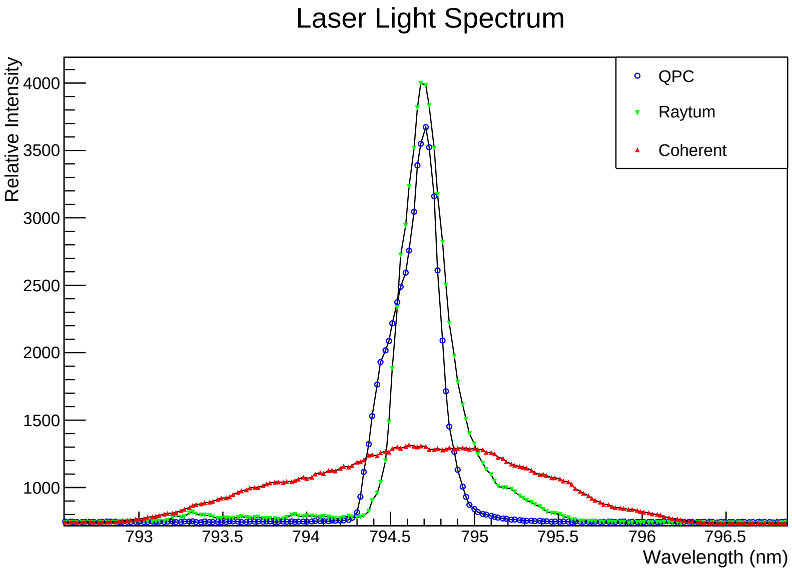

Figure 6-3: Comparison of laser wavelength spectrum between vendors. Coherent is the broad-width diode laser (FWHM≈1.5 nm) while QPC and Raytum are new narrow-width ones (FWHM≈0.25 nm).

where $\vec{I}$ is the ^{3}He nucleon spin, $\vec{S}$ is the spin of the alkali valence electron and α is the coupling constant for Fermi-contact interaction:

$$\alpha(R) = \frac{16\pi}{3}\frac{\mu_B \mu_{^3He}}{I}|\phi(R)^2| \tag{6.4}$$

where R is the internuclear separation between alkali and ^{3}He and $\phi(R)$ is the valence electron wave function at the position of the ^{3}He nucleus. During hyperfine interaction, the total spin is conserved, as shown in Fig. 6-4. The spin-rotation interaction contributes to the relaxation and depends on the coupling between rotational angular momentum of the alkali-^{3}He pair and the alkali valence electron spin.

The speed at which the Rb valence electron transfers its polarization to ^{3}He is defined as the spin exchange rate per ^{3}He atom

$$\gamma_{\mathrm{SE}}^{\mathrm{Rb}-^3\mathrm{He}} = k_{\mathrm{SE}}^{\mathrm{Rb}-^3\mathrm{He}}[Rb], \tag{6.5}$$

where [Rb] is the Rb number density, $k_{\mathrm{SE}}^{\mathrm{Rb}-^3\mathrm{He}}$=$6.8\times10^{-20}$ cm^3[163] is the spin-exchange constant for Rb$-^3$He collisions.

The spin exchange efficiency η is equal to the ratio of spin exchange rate to the total spin relaxation rate

$$\eta = \frac{\gamma_{\mathrm{SE}}^{\mathrm{Rb}}[^3\mathrm{He}]}{\Gamma_{\mathrm{Rb}}[\mathrm{Rb}]} = \frac{k_{\mathrm{SE}}^{\mathrm{Rb}}[^3\mathrm{He}]}{\Gamma_{\mathrm{Rb}}}, \tag{6.6}$$

where [Rb] ([^{3}He]) is the density for Rb (^{3}He), Γ_{Rb} is the total alkali spin relaxation rate. For Rb at 180 °C, η is around 0.02 when ^{3}He has a density of ~ 7 amg[164], which means 50 polarized Rb atoms are needed to polarized one initially unpolarized ^{3}He nucleus.

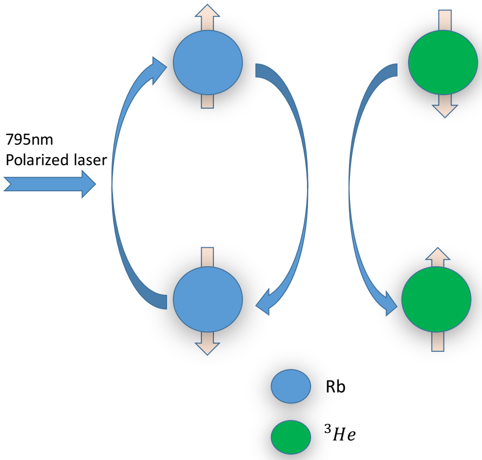

Figure 6-4: Spin exchange between Rb and ^{3}He due to binary collisions.

In recent years, an advanced technique called Rb-K hybrid spin-exchange optical pumping was developed and greatly improved the spin exchange efficiency η. The main reason is that K relaxation Γ_{K} is much slower than Rb, thus the spin exchange efficiency is about one order of magnitude higher as shown in Fig. 6-5, although $k_{\mathrm{SE}}^{\mathrm{K}-^3\mathrm{He}}$ $=5.5\times10^{-20}\mathrm{cm}^3< k_{\mathrm{SE}}^{\mathrm{Rb}-^3\mathrm{He}}$[165, 166]. However, there is no commercial and high-power narrow-width laser to polarize K directly. On the other hand, K can be polarized through the fast Rb-K spin-exchange and the K vapor can reach almost the same polarization as Rb vapor. Fig. 6-6 shows the additional spin exchange path Rb-K-He in the hybrid cell. The spin exchange efficiency was studied for various

K/Rb density ratios [166]. A ratio of [K]/[Rb]$\simeq$5 is usually chosen to make the target performance optimal. The hybrid pumping was utilized before narrow-diode lasers were available, and subsequently increase the in-beam ^{3}He target polarization from 40%(during A1n[76, 148] in 2001) to 50% (during GEN[149] in 2006).

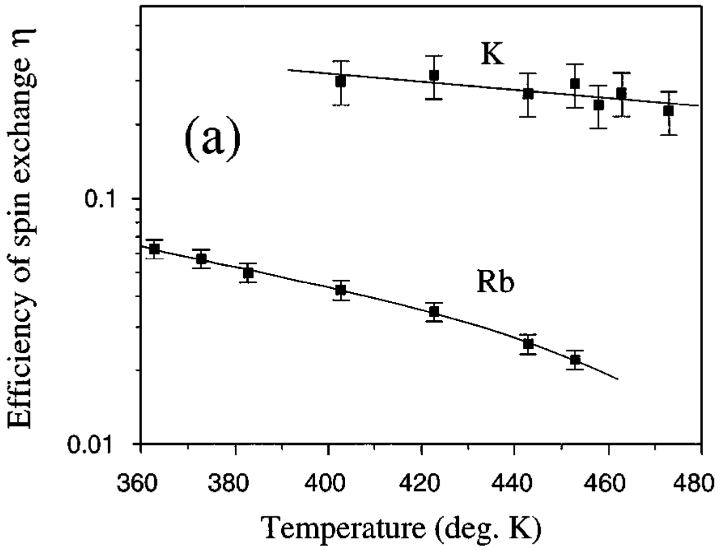

Figure 6-5: Spin exchange efficiency comparison (note logarithmic scale) for ^{3}He-Rb (7.0 amagat of ^{3}He) and ^{3}He-K (6.9 amagat of ^{3}He) versus temperature[164].

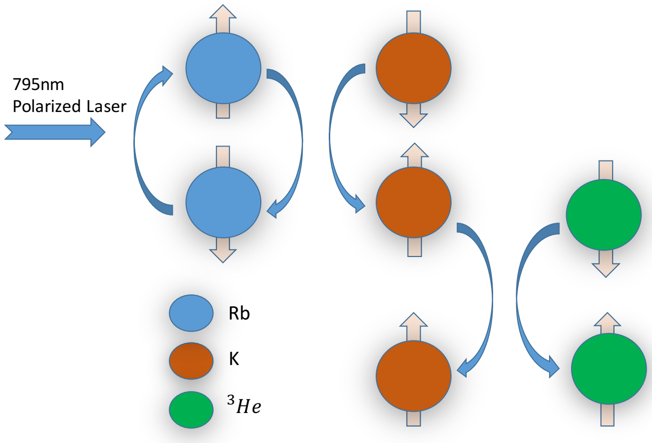

Figure 6-6: Spin exchange between Rb, K and ^{3}He.

6.2.3 Polarization Evolution over Time

Consider a single chamber cell, the ^{3}He polarization evolution over time can be described as

$$\frac{dP_{^3\mathrm{He}}}{dt} = \gamma_{\mathrm{SE}}(P_A - P_{^3\mathrm{He}}) - \Gamma_{\mathrm{R}} P_{^3\mathrm{He}}, \tag{6.7}$$

where P_A is the average alkali polarization, γ_{SE} is the alkali-^{3}He spin-exchange rate per ^{3}He atom, Γ_{R} is the overall relaxation rate of the ^{3}He. Solving Eq. 6.7, the ^{3}He polarization is

$$P_{^3\mathrm{He}}(t) = P_A \left(\frac{\gamma_{\mathrm{SE}}}{\gamma_{\mathrm{SE}} + \Gamma_{\mathrm{R}}} \right) \left(1 - e^{-(\gamma_{\mathrm{SE}} + \Gamma_{\mathrm{R}})t}\right). \tag{6.8}$$

From Eq. 6.8, one can define the spin up time constant:

$$t_{^3\mathrm{He}} = \frac{1}{\gamma_{\mathrm{SE}} + \Gamma_{\mathrm{R}}} \tag{6.9}$$

to describe how fast the ^{3}He can reach the maximum polarization and the theoretically achievable maximum ^{3}He polarization is

$$P_{^3\mathrm{He}} = P_A \left(\frac{\gamma_{\mathrm{SE}}}{\gamma_{\mathrm{SE}} + \Gamma_{\mathrm{R}}} \right). \tag{6.10}$$

To achieve the best ^{3}He polarization, an optimal condition need be found to maximize γ_{SE} or minimize Γ_{R}. To minimize Γ_{R}, one can choose a cell which has the best performance (minimize wall relaxation) under the same spin up conditions; to maximize γ_{SE}, one can increase the alkali vapor polarization by increasing usable laser power. The ^{3}He cell at JLab usually has two chambers, but the polarization evolution is similar between two chambers, see details in Sec. 6.3.4. Without the electron beam, a maximum ^{3}He polarization over 70% was reached with a well chosen cell (Brady) and around 60 W of usable laser light.

6.2.4 Polarized Target System at JLab

The polarized ^{3}He target at JLab is based on the SEOP method and a specific design is needed to fulfill the SEOP conditions: an optics system to produce the circularly polarized light for optical pumping, an oven system to keep the alkali vaporized, a holding magnetic field system to provide the Zeeman splitting energy levels for alkali atoms, and polarimetry to measure the ^{3}He polarization. Fig. 6-7 shows main elements of the target system in the latest Transversity experiment[150, 151]. More details will be discussed in the following sections.

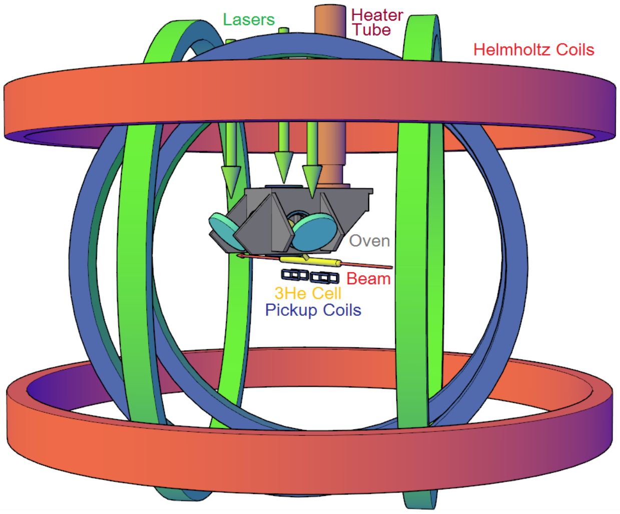

Figure 6-7: Polarized ^{3}He target setup during the Transversity experiment[167].

6.2.4.1 ^{3}He Diffusion Cell

The ^{3}He gas is contained in a hand-blown glass cell. The glass material must be free of magnetic material to not disturb the uniformity of the magnetic field. It is often constructed from an aluminosilicate glass called GE180 which contains very few magnetic compounds, can hold a high pressure (typically 10 atm) safely and has a relatively small radiation thickness.

To fit for the electron scattering experiment, the cell typically has a double chamber design as shown in Fig 6-8 and Fig 6-9. The spin-exchange optical pumping takes places in the upper "pumping chamber" and the electron beam passes through the lower 40 cm long "target chamber". The spherical shape of the pumping chamber is designed to reduce the surface relaxation (high surface/volume ratio) while the long tube shape of the target chamber is to maximize the beam-target interaction probability. The polarized ^{3}He gas diffuses from pumping chamber to target chamber through 9-cm long “transfer tube” and hence this design is referred to as "diffusion cell". The cell is filled to a pressure of about 7 atm with around 1% N_2 (in pressure) and a mixture of K and Rb. The alkali mixture is added in the upper 3 inches diameter sphere pumping chamber only. A small lip extending from the transfer tube is to prevent alkali flow down to transfer tube when the pumping chamber is heated up. The thickness of target chamber windows at the end (where the beam passes) is (100-150) μm, much thinner than the side wall thickness (about 1.5mm), to minimize the background electron scattering and electron energy loss. Fig. 6-9 shows the dimension of a typical ^{3}He cell. A cell can easily perform badly if any magnetic contamination is present or if the inner cell wall is not smooth. In order to achieve a ^{3}He relaxation time of 20 hours or above (at room temperature and without electron beam), the construction and filling processes must be performed very carefully.

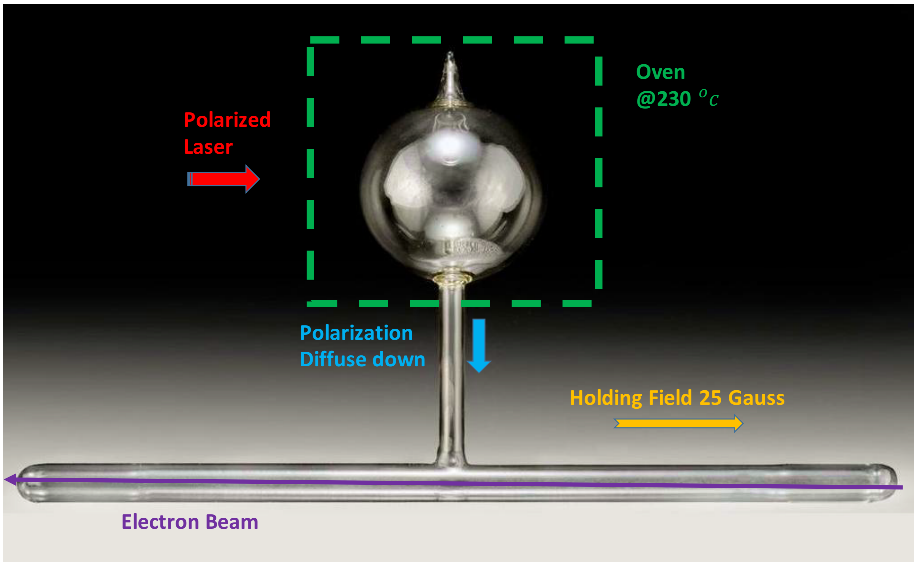

Figure 6-8: Image of a typical polarized ^{3}He Cell using during 6 GeV experiment[168].

6.2.4.2 Polarization Optics

The laser system consists of three narrow-width diode lasers, each with an unpolarized light output power of 30 W and a wavelength of 795 nm. A polarization optics

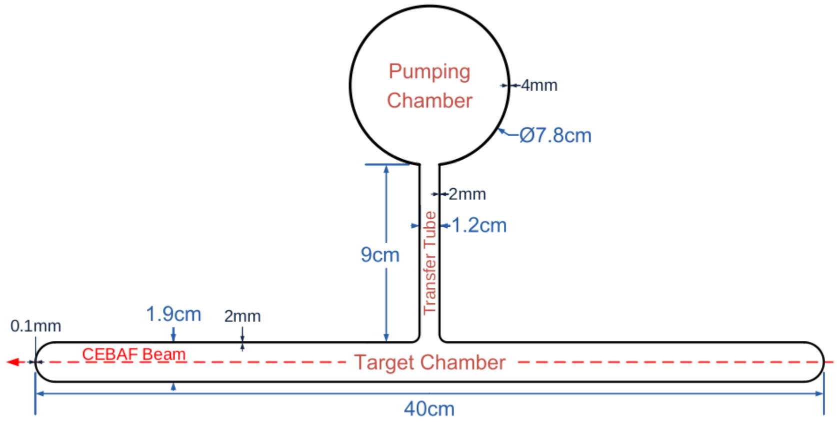

Figure 6-9: Geometry of a typical polarized ^{3}He Cell used by Transversity experiment[168].

system was developed to produce the circularly polarized light for optical pumping, as shown in Fig. 6-10. The output from the optical fiber of each laser is highly divergent and is focused by the convex lens with $f_1 = 8.83$ cm. The distance between fiber and lens is adjusted to make the aperture at the target match the pumping chamber size. The unpolarized light is split into a horizontal (P-wave) and a vertical (S-wave) linearly polarized components by the beam splitter. About 95% of the P-wave component transmits through the splitter and is reflected towards the target. All the S-wave gets reflected by the beam splitter, passes through a $\lambda/4$ wave plate, is reflected by a flat mirror, then passes through the $\lambda/4$ wave plate again, and becomes the P-wave component to transmit through the beam splitter. At this point, most of the unpolarized laser light becomes linearly polarized P-wave. After passing through the additional $\lambda/4$ plate with the correct orientation, both paths of the P-wave beam turn into circularly polarized light and are directed towards the pumping chamber of the ^{3}He cell. The helicity of the light and thus the spin direction of ^{3}He nuclei can be flipped by simply rotating the $\lambda/4$ plate by 90 degrees.

A small amount ($\approx$5%) of the original P-wave is reflected by the beam splitter together with the original S-wave. This portion of P-wave turns into S-wave after passing the $\lambda/4$ plate twice and then is reflected back to the optical fiber. A careful adjustment of the beam splitter is needed to minimize this back-reflection and to prevent damage to the fiber.

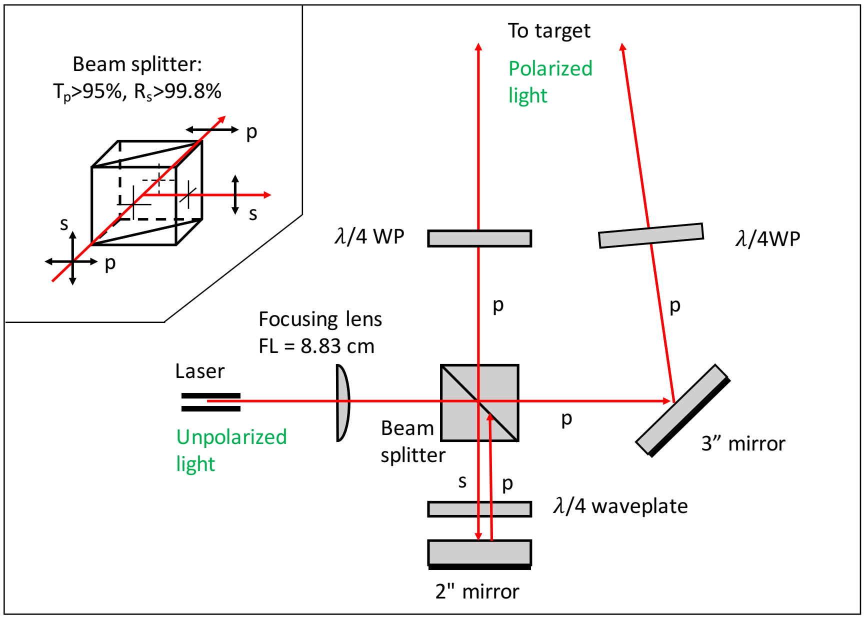

Figure 6-10: The optics system to produce circularly polarized light[94].

6.2.4.3 Holding Magnetic Field

For the polarized ^{3}He target, the ^{3}He nuclei are pumped to the $m_F = -F(+F)$ state which means the polarization direction can only be parallel (anti-parallel) to the holding field. Different polarized-^{3}He experiments may require different ^{3}He polarization directions with respect to the electron beam, requiring different holding field directions. Even during the same experiment, several polarization directions may be required. Three pairs of Helmholtz coils in orthogonal directions are typically used, see Fig. 6-7. Each pair is separately powered by independent power supplies to provide 3D tunable ability in both the field direction and the amplitude (between 25 G and 32 G). The diameters of coils are 1.27 m, 1.45 m, 1.83 m for horizontal along the beam, perpendicular to the beam and the vertical-direction field's Helmholtz coils respectively. Magnetic field uniformity is a very important parameter for the target system performance: the field gradient should be small enough to minimize the polarization loss during Nuclear Magnetic Resonance measurements and the polarization relaxation due to thermal motion in the inhomogeneous field, but should be large enough to suppress the masing effect (see Sec. 6.6.4). A pair of anti-Helmholtz coils can help make the gradient satisfied in the desired direction. If the gradient is too large, a pair of "anti"-Helmholtz can keep the gradient in the appropriate range along desired direction. The magnetic field gradient of the system is kept at roughly (5-30) mG/cm through the whole cell region.

6.2.4.4 Oven System

The oven heats the pumping chamber to keep the alkali vaporized for optical pumping. The oven is made of calcium-silicate based nonmagnetic material CS85. The heating source for the oven is provided by a hot flow of pressurized air. The air flow used (dry and filtered at room temperature) is provided by a dedicated compressor, and then passes through two heaters before entering the oven. The oven temperature can be adjusted by changing the air flow speed and the heat voltage. The oven internal air temperature is measured using a resistance temperature detector (RTD) and its read-back is fed into a digital proportional-integral-derivative (PID) controller to make the temperature stable by turning on/off one of the heat power automatically. The typical oven temperature is kept at (230±1) °C. The part of the cell outside the oven (including target chamber and part of transfer tube) is kept below 100 °C to prevent the alkali vapor from entering the target chamber. Any alkali vapor flowing down would liquidize and be collected by the "lip" on the transfer tube. This temperature gradient makes the ^{3}He gas to be much denser than 7 amg in the target chamber.

6.3 Polarimetry

For all 6 GeV experiments, two primary methods were used to measure the ^{3}He polarization – nuclear magnetic resonance (NMR) polarimetry and electron paramagnetic resonance (EPR) polarimetry. The NMR measures the electromagnetic signal induced by the ^{3}He spin reversal through the adiabatic fast passage (AFP) and is used to monitor the ^{3}He polarization relatively. The EPR measures the frequency shift on the EPR lines of the Rb atom caused by the polarized ^{3}He, and thus can provide an absolute polarization measurement to calibrate the ^{3}He NMR signal. These NMR and EPR polarimetry methods have been intensively cross-checked and confirmed by results from elastic scattering asymmetry off ^{3}He.

6.3.1 NMR Polarimetry

6.3.1.1 AFP Principle

NMR is based on flipping the ^{3}He spin using the AFP technique. AFP can be achieved by changing either the holding field amplitude or the oscillating RF field frequency.

When the ^{3}He nucleon is placed in a holding field $\vec{H} = H\hat{z}$, the ^{3}He nuclear spin does not align fully with the holding field, but precesses around it:

$$\frac{d\vec{M}}{dt} = \gamma \vec{M} \times \vec{H}, \tag{6.11}$$

where γ is the ^{3}He gyromagnetic ratio ($\gamma = -3.243$ kHz/G) and $\vec{M}$ is the magnetic moment ($\vec{M}$=$\gamma\vec{I}$) of ^{3}He with $\vec{I}$ the nuclear spin. It is useful to describe the system in a frame rotating with $\vec{\omega} = \omega\hat{z}$. Denote ($\hat{x}$, $\hat{y}$, $\hat{z}$) as the basis vector in the lab frame and ($\hat{x}'$, $\hat{y}'$, $\hat{z}'$) in the rotating frame:

$$\begin{aligned} \hat{x}' &= \hat{x}\cos\omega t + \hat{y}\sin\omega t, && (6.12)\\ \hat{y}' &= -\hat{x}\sin\omega t + \hat{y}\cos\omega t, && (6.13)\\ \hat{z}' &= \hat{z}. && (6.14) \end{aligned}$$

Their derivatives can be written as

$$\frac{d}{dt}\begin{pmatrix}\hat{x}' \\ \hat{y}'\end{pmatrix} = \vec{\omega} \times \begin{pmatrix}\hat{x}' \\ \hat{y}'\end{pmatrix}. \tag{6.15}$$

Notice that the left side of Eq.6.11 can be expressed in the rotating frame as

$$\begin{aligned}\left(\frac{d\vec{M}}{dt}\right)_{lab} &= \frac{d}{dt}(M_x'\hat{x}' + M_y'\hat{y}' + M_z'\hat{z}') \\ &= M_x'\frac{d\hat{x}'}{dt} + M_y'\frac{d\hat{y}'}{dt} + \hat{x}'\frac{dM_x'}{dt} + \hat{y}'\frac{dM_y'}{dt} + \hat{z}'\frac{dM_z'}{dt} \\ &= \vec{\omega} \times \vec{M} + \left(\frac{d\vec{M}}{dt}\right)_{rot},\end{aligned} \tag{6.16}$$

where the term $\left(\frac{d\vec{M}}{dt}\right)_{rot}$ represents the derivatives of $\vec{M}$ in the rotation frame. Combining Eq. 6.11 and Eq. 6.16 gives

$$\left(\frac{d\vec{M}}{dt}\right)_{rot} = \gamma\vec{M} \times (\vec{H} + \frac{\vec{\omega}}{\gamma}). \tag{6.17}$$

$\vec{M}$ will be static in the rotational frame if H is along $\hat{z}$ and one picks the frequency $\omega_0 = -\gamma H$. This frequency is called the Larmor frequency.

During an AFP, a small oscillating RF field $\vec{H_1} = 2H_1\cos(\omega t)\hat{x}$ (typically $H_1 \approx 90$ mG, frequency $\omega/2\pi \approx 91$ kHz) is applied in the vertical direction, as shown in Fig. 6-11. This RF field can be decomposed into two counter-rotating components with frequency $\pm\omega$ in the lab frame:

$$\vec{H_1} = [H_1\cos(\omega\mathrm{t})\hat{\mathrm{x}} + H_1\sin(\omega\mathrm{t})\hat{\mathrm{y}}] + [H_1\cos(\omega\mathrm{t})\hat{\mathrm{x}} - H_1\sin(\omega\mathrm{t})\hat{\mathrm{y}}]. \tag{6.18}$$

In the rotating frame, the first term in Eq. 6.18 becomes $\vec{H_1} = H_1\hat{x}'$. Ignoring the effect of the second term first, the motion of magnetization in the rotating frame from Eq. 6.17 is

$$\left(\frac{d\vec{M}}{dt}\right)_{rot} = \gamma\vec{M} \times [(H + \frac{\omega}{\gamma})\hat{z}' + H_1\hat{x}'], \tag{6.19}$$

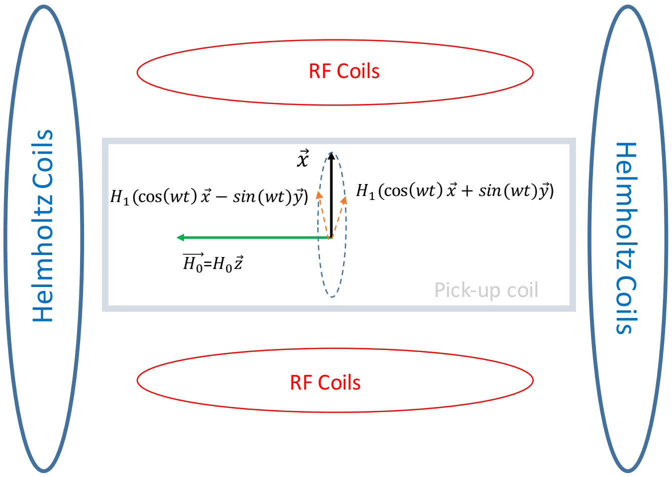

Figure 6-11: The field setup for NMR system.

where $H\hat{z}' = H\hat{z}$ is now the main holding field in the horizontal direction. The effective field then can be written as

$$\vec{H}_{eff} = (H + \frac{\omega}{\gamma})\hat{\mathrm{z}}' + H_1\hat{\mathrm{x}}'. \tag{6.20}$$

which is static in the frame with magnitude:

$$H_{eff} = \sqrt{(H + \frac{\omega}{\gamma})^2 + H_1^2}. \tag{6.21}$$

Therefore, if we change $(H + \frac{\omega}{\gamma})$ from positive to negative, the spin will follow the effective field direction and flip from -$\hat{z}$ to $+\hat{z}$, while the H_1 field ensures the field is not zero when it crosses the resonances.

The effect of the second term in Eq. 6.18 can be seen easily if establishing a new frame rotates with $\vec{\omega} = -\omega\hat{z}$[169]. Following the same procedure, the effective magnetic field in the new rotating frame is give by

$$\vec{H}'_{eff} = (H - \frac{\omega}{\gamma})\hat{\mathrm{z}} + H_1\hat{\mathrm{x}}, \tag{6.22}$$

which means that the magnetization vector processes about $\vec{H}'_{eff}$ with angular frequency $\omega' = \gamma H'_{eff} \approx 2\omega$ (note $\omega = -\gamma H$), and $\vec{H}'_{eff}$ deviates from the z axis by an angle $\theta = \arcsin(H_1/H'_{eff}) \approx H_1/(2H) \approx 0$. So, its effect is negligible and only the first term in Eq. 6.18 has a significant effect on the magnetization vector.

Therefore, the goal of AFP is for the spin to precess about $\vec{H}_{eff}$ which is chosen to be along $\hat{x}'$ only, until it flips. The AFP can be achieved by either changing the holding field strength (H, "field sweep") or RF field frequency (ω, "frequency sweep"). Fig. 6-12 shows the magnetic fields in both rotational and lab frame during a field sweep. As the holding field H increases, the $(H + \omega/\gamma)\hat{z}$ component of the effective field decreases first as in Case A, becomes zero as H reaches resonance field $H_0 = -\omega/\gamma$ as in Case B, and then changes to the opposite direction as $H > H_0$ as in Case C. As a result, the ^{3}He nucleus spin is flipped. The NMR sweep must satisfy the AFP condition, that is, the holding field in the field sweep (or RF field frequency in frequency sweep) changes slowly enough for ^{3}He spin to follow the effective magnetic field (adiabatic condition) and fast enough to pass the minimum effective field ($= H_1$)

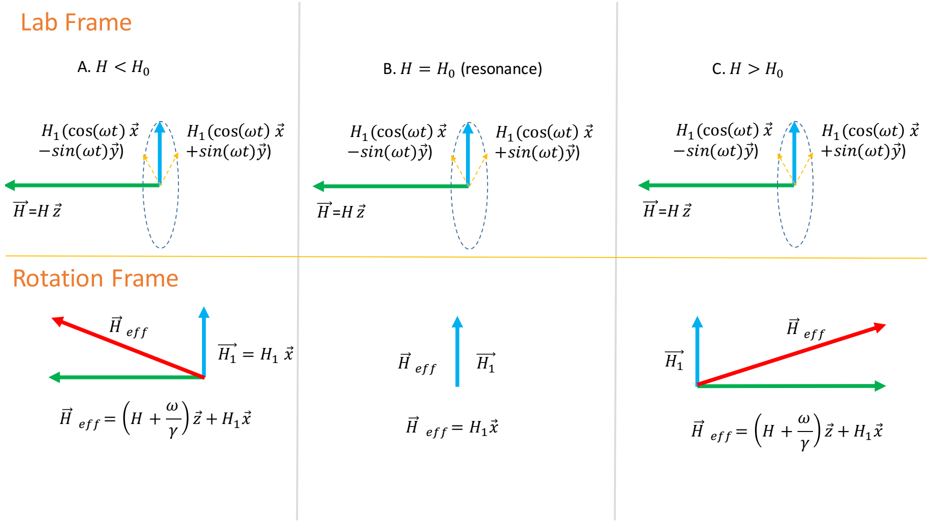

Figure 6-12: Fields in both the lab frame and the rotation frame. Case A shows the fields when the holding field H is smaller than the resonance field H_0; Case B shows the fields at resonance $H = H_0$; Case C shows the fields when the holding field H larger than the resonance field H_0 and the $\hat{z}$ component of the effective field direction flips.

to have less relaxation (fast condition):

$$\frac{D|H|^2}{{H_1}^2} \leq \frac{\frac{d}{dt}(H+\frac{\omega}{\gamma})}{H_1} \leq \gamma H_1, \tag{6.23}$$

where D is the ^{3}He diffusion rate. Use the setup at JLab, the AFP condition is

$$(10^2 s)^{-1} \leq \frac{\frac{d}{dt}(H+\frac{\omega}{\gamma})}{H_1} \leq (10^{-3} s)^{-1}. \tag{6.24}$$

Typically, a AFP field sweep is conducted at fixed frequency (91 kHz) and changing holding field H (scan rate 1.2 G/s) through the resonance (H_0 =28.06 G) from 25 G to 32 G and then scan back, while a AFP frequency sweep is done at a fixed holding field (25 G) but changing RF frequency (scan rate 4 kHz/s) through resonance (ω_0 = 81 kHz) from 78 kHz to 85 kHz and then scan back.

Most of the ^{3}He nucleus spin will undergo a spin reversal as the field scans through the resonance H_0. The percentage of polarization loss during the sweep is characterized as AFP loss, typically <1% for the NMR system.

In the lab frame, the ^{3}He spin precesses around $\omega\hat{z}$ with an angle with respect to the z-axis

$$\theta = \arctan(\frac{H_1}{\sqrt{(H+\frac{\omega}{\gamma})^2 + H_1^2}}). \tag{6.25}$$

This spin rotating will introduce a electro-motive forced (EMF) signal in both pick-up coils. The pick-up coils are put transverse to holding field and perpendicular to the RF field as shown in Fig. 6-13. The opposite orientations of the two pick-up coils are used to subtract the background and double the NMR signal. The induced signal is proportional to the transverse magnetization M_T and also the average ^{3}He polarization:

$$S_{NMR}(t) \propto M_T \propto \langle P_{^3\mathrm{He}}\rangle (H_{eff})_T \propto \langle P_{^3\mathrm{He}}\rangle \frac{H_1}{\sqrt{(H+\frac{\omega}{\gamma})^2 + H_1^2}}. \tag{6.26}$$

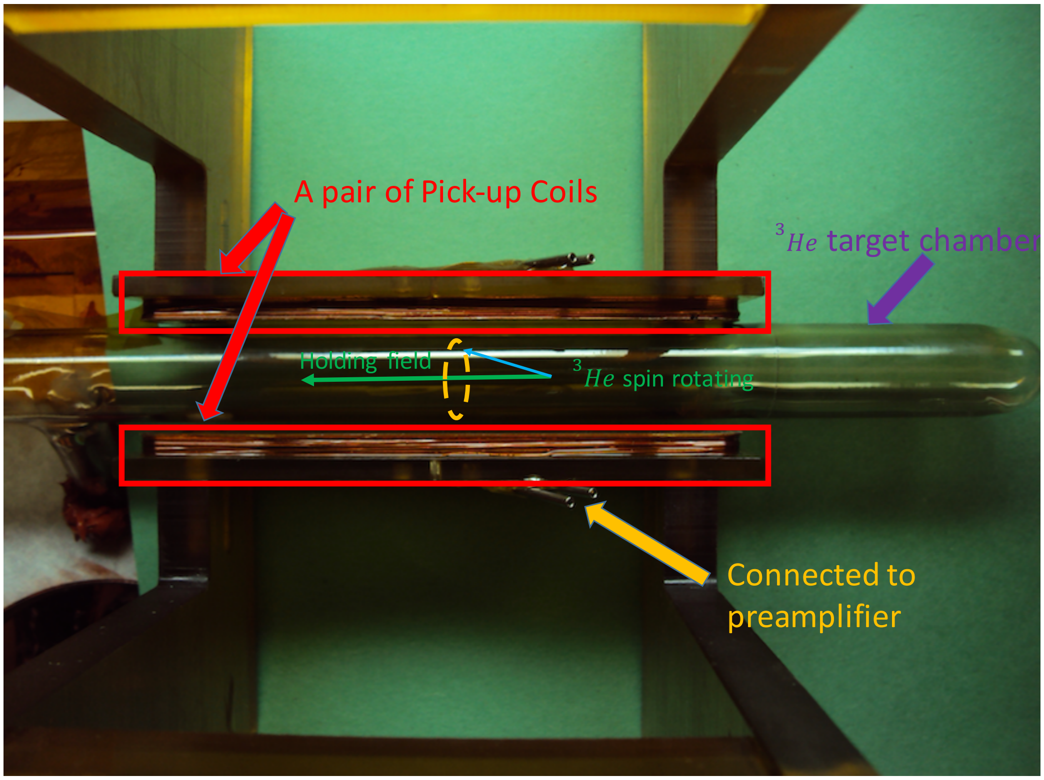

Figure 6-13: Pick-up coils for NMR.

6.3.1.2 NMR Measurement

Fig. 6-14 shows the setup for the NMR system. During the NMR measurement, the function generator (HP 3324A) provides a constant or sweeping RF signal to the RF coil and the pick-up coils detect the EMF signal at the same time. The EMF signal goes through the pre-amplifier (Model SR620) first, then is integrated by the Lock-in Amplifier (Model SR844) referenced at the RF frequency. The lock-in samples the signal every ∼10 ms and sends data via GPIB interface to be stored in computer.

Fig. 6-15 shows a typical NMR signal during field sweep. The NMR signal is fitted by several ansatz functions (eg. Eq. 6.26) which reproduce the NMR height within 1%. This 1% was included as a part of the systematic uncertainty for the final polarization. The fitted NMR height (signal height at resonance after removing background) is proportional to the averaged ^{3}He polarization but needs to be calibrated. One method for calibration is water NMR which measures the water thermal polarization signal

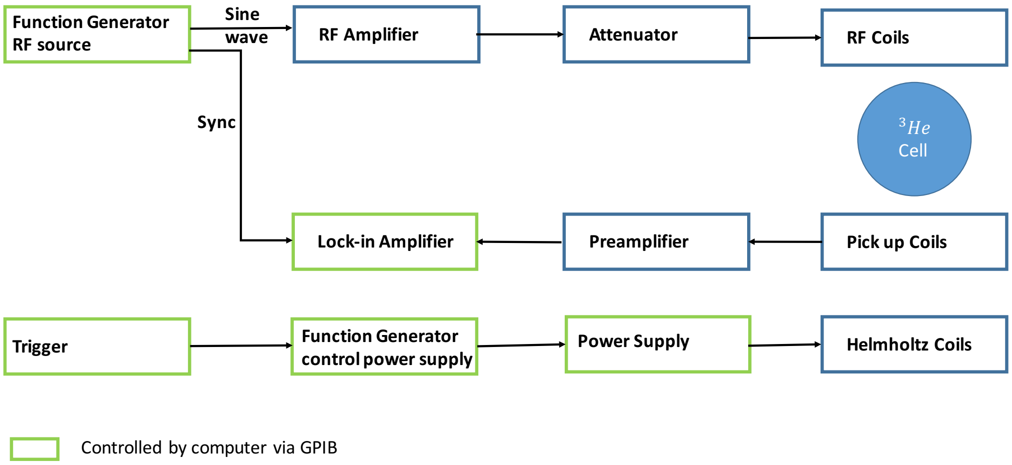

Figure 6-14: The electronic set up for the NMR measurements.

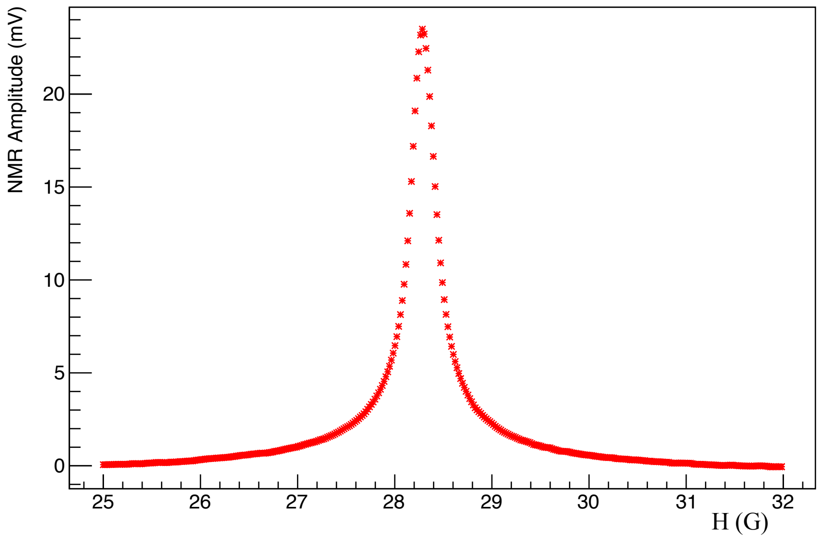

Figure 6-15: A typical NMR signal versus holding field H.

within a water cell with the same size and shape and located in the same position as the ^{3}He cell in the holding field, the other is EPR which will be discussed below.

6.3.2 EPR Polarimetry

EPR is a technique that detects transitions between the Rb electron's spin levels rather than ^{3}He nuclear ones. It measures the difference in the frequency shift of the Zeeman splitting of alkali atoms with the ^{3}He magnetization aligned and anti-aligned to the holding field, where the ^{3}He spin flip is done by an AFP measurement. From this difference one can precisely determine the additional magnetic field due to the polarized ^{3}He gas. Unlike the ^{3}He NMR mentioned above, EPR provides an absolute polarization measurement for the ^{3}He in the pumping chamber.

6.3.2.1 EPR Principle

In a field $\vec{H}$ of a few 10s of G, the interaction between the external magnetic field and the alkali atom is comparable to the hyperfine interaction, as discussed in Sec. 6.2.2 . The ground state of an alkali atom can be described by the Breit-Rabi formula[170]:

$$E_{F=I\pm 1/2,m_F} = -\frac{\Delta E_{hfs}}{2(2I+1)} - g_I \mu_N H m_F \pm \frac{\Delta E_{hfs}}{2}\sqrt{1+\frac{4m_F}{2I+1}x+x^2}, \tag{6.27}$$

where E_{hfs} is the hyperfine splitting energy measured in[171], $x = (g_I\mu_N - g_s\mu_B)H/\Delta E_{hfs}$ describes the strength of the Zeeman splitting compared to the hyperfine interaction.

EPR measures the resonance frequency ν_{EPR+} (ν_{EPR-}) for transition between $m_F = F(-F)$ and $m_F = F-1(-F+1)$ with $F = I+1/2$. The resonance frequency $\nu_{EPR\pm}$ can be calculated from Eq. 6.27 as

$$\begin{aligned} \nu_{EPR\pm} &= E_{F=I+1/2,m_F=\pm F} - E_{F=I+1/2,m_F=\pm(F-1)} \\ &= -\frac{H}{2}(g_I\mu_N + g_s\mu_B) + \left[\pm 1 \mp \sqrt{1 \pm 2\frac{2I-1}{2I+1}x + x^2}\right]\frac{\Delta E_{hfs}}{2}. \end{aligned} \tag{6.28}$$

When the ^{3}He spin is aligned or anti-aligned with the holding field, the total field experienced by the alkali atoms will change according to the ^{3}He spin direction as $H_{tot} = H \pm \Delta H$ where ΔH is the additional field generated by the ^{3}He spin. Since

$\Delta H \ll H$, the EPR frequency variation is very small. The change $\Delta\nu_{EPR}$ can thus be approximated as

$$\Delta\nu_{EPR} = \frac{d\nu_{EPR}}{dH}\Delta H = \frac{d\nu_{EPR}}{dH}(\Delta H_M + \Delta H_{SE}). \tag{6.29}$$

Here ΔH_{SE} is the contribution from spin exchange collisions between the alkali atoms and the ^{3}He atoms, and ΔH_M corresponds to ^{3}He magnetization which is proportional to the ^{3}He polarization $P_{^3He}$ and the ^{3}He number density $[n_{^3\mathrm{He}}]$

$$\Delta H_M = G\mu_0\mu_{^3\mathrm{He}}[n_{^3\mathrm{He}}]P_{^3\mathrm{He}}, \tag{6.30}$$

where $\mu_{^3\mathrm{He}}$ is the magnetic moment of ^{3}He, G is a geometric factor characterizing the cell (2/3 for a sphere cell). The variation in the EPR frequency $\Delta\nu_{EPR}$ is related to the ^{3}He polarization $P_{^3\mathrm{He}}$ as[172]

$$\Delta\nu_{EPR} = \frac{2\mu_0}{3}\frac{d\nu(F,m_F)}{dH}\kappa_0\mu_{^3\mathrm{He}}[n_{^3\mathrm{He}}]P_{^3\mathrm{He}}, \tag{6.31}$$

where $\frac{d\nu(F,m_F)}{dH}$ can be derived from Eq. 6.28[173] and $\kappa_0 = \frac{\Delta H_M + \Delta H_{SE}}{\Delta H_M}$ is a constant that parametrizes the spin-exchange effective field. κ_0 depends on the temperature but not on density, and has been measured[172, 174]:

$$\kappa_0^{^{39}\mathrm{K}}(T) = (5.99 \pm 0.11) + (0.0086 \pm 0.0020)(T - 200°C) \tag{6.32}$$

$$\kappa_0^{^{85}\mathrm{Rb}}(T) = 6.39 + (0.00916 \pm 0.00026)(T - 200°C). \tag{6.33}$$

The highest temperature at which κ_0 were measured is $200°C$ for K and thus need extrapolated to the JLab working condition ($\sim 230°$). The uncertainty is also extrapolated and contributes the largest source of systematic error (2-3%) in the pumping chamber's polarization EPR measurement.

For the typical JLab condition, the EPR frequency shift $2\Delta\nu_{EPR} = \nu_{EPR-} - \nu_{EPR+}$ is around 0.3% for potassium with statistical error $\delta(\Delta\nu_{EPR})/\Delta\nu_{EPR} < 0.2\%$, as shown in Fig. 6-16.

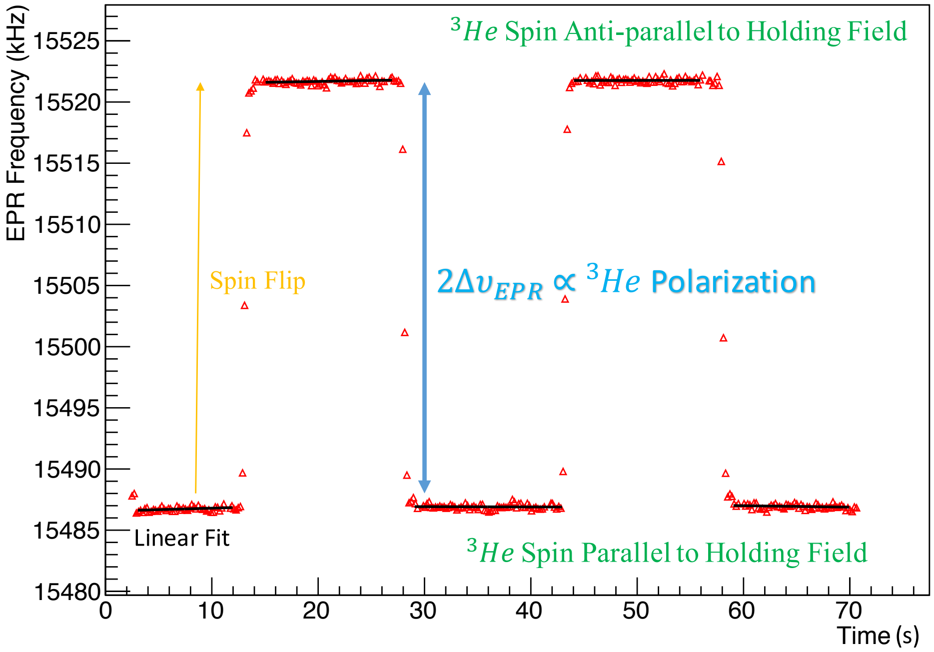

Figure 6-16: A typical EPR spectrum during AFP frequency sweep when pumped by σ_+ light.

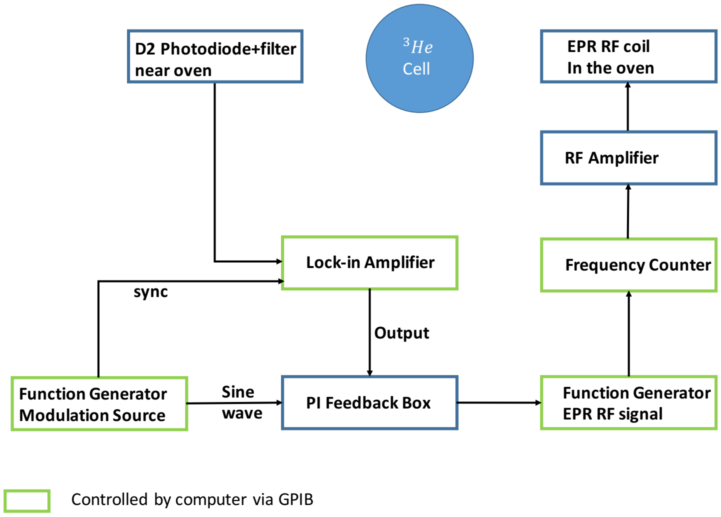

Figure 6-17: The electronics setup for EPR.

6.3.2.2 EPR Measurement

Fig. 6-17 shows the setup of EPR frequency modulation sweep system. The function generator (Model HP E4400B) generates a frequency-modulated RF signal. The modulation source comes from a constant 100 Hz sine wave and a DC output from a proportional integral (PI) box. The modulated RF signal is amplified by a RF amplifier (Model EI 3100L) first and sent to the EPR RF coil. Compared to the NMR RF coil which is used to produce the RF field for AFP in the whole cell region, the EPR RF coil has a size of around 4 inch in diameter and is mounted very close to the pumping chamber, to introduce the EPR transition in the pumping chamber only.

Once the alkali vapor is polarized by the diode laser, most of the Rb electrons are in the $F = 3$, $M_F = 3$ (or -3) state and cannot absorb the polarized light, and thus the 785 nm D_2 florescence ($5P_{3/2} \rightarrow 5S_{1/2}$) is weak or almost absent. For both Rb or K, the EPR transition will lower both the K and Rb polarization, and re-polarizing the Rb from $5S_{1/2}$ to $5P_{1/2}$ produces strong D_2 florescence from $5P_{3/2}$ to $5S_{1/2}$ because of the collisional mixing between $5P_{3/2}$ and $5P_{1/2}$, as shown in Fig. 6-18. The D_2 light is detected by a photodiode and measured by the lock-in amplifier (Model EGG 7265). A D_2 filter is placed before the photodiode to avoid the $D1$ light background. The lock-in amplifier output signal is approximately the derivative of the EPR florescence curve as a function of the RF frequency and is sent to the PI box input. The PI box provides a feedback to adjust the function generator's modulation frequency and help lock the EPR resonance by maintaining the lock-in signal at zero. Using this method, an EPR resonance can be reached when scanning the frequency. Fig. 6-19 shows a typical frequency scan spectrum to find EPR resonance for ^{39}K with $m_F = +2$ to $m_F = +1$. After the EPR resonance is found and locked, an NMR-AFP frequency sweep is performed to flip the ^{3}He spin to get the frequency shift $\Delta\nu_{EPR}$ as shown in previous Fig. 6-16.

The frequency shift $\Delta\nu_{EPR}$ in this particular measurement was $\Delta\nu_{EPR} = (34.78 \pm 0.06)$ kHz, which is calculated to give the polarization $P_{^3\mathrm{He}} = (30.3 \pm 0.4)\%$ using

Eq. 6.30.

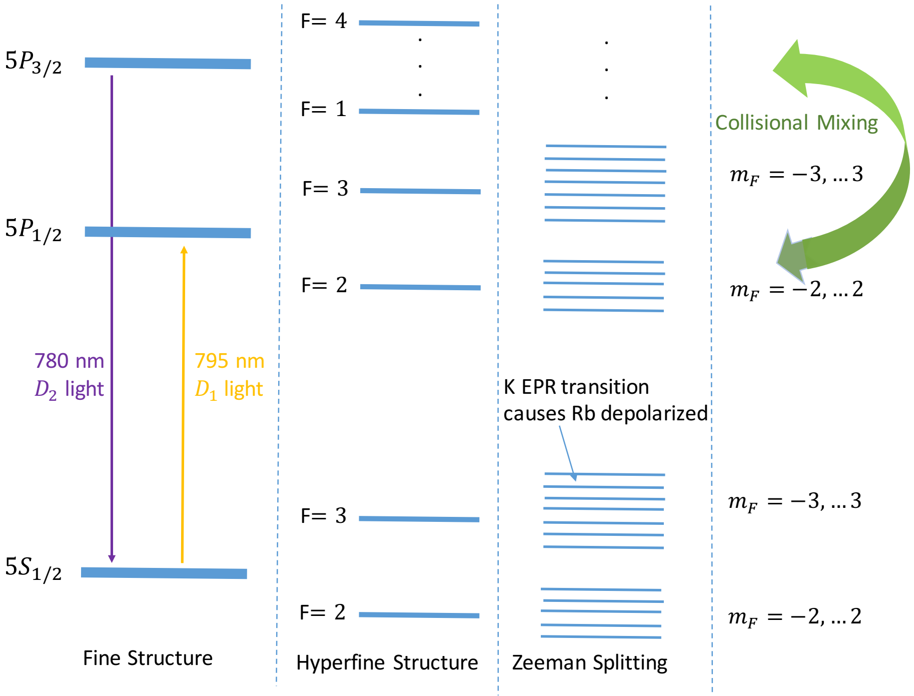

Figure 6-18: Optical pumping for ^{85}Rb during an EPR measurement for ^{39}K.

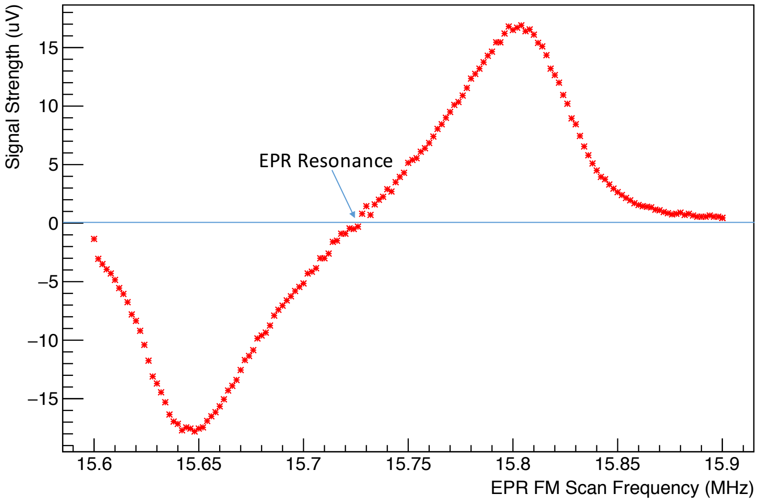

Figure 6-19: A typical frequency modulation scan to find the ^{39}K EPR resonance $m_F = +2$ to $m_F = +1$ with the PI box disabled.

6.3.3 Alkali Polarimetry

The NMR and EPR discussed in the Sec. 6.3.1 and Sec. 6.3.2 are polarimetry for ^{3}He. This section will discuss the polarimetry for the alkali vapor.

From Sec. 6.2.3, the maximum ^{3}He polarization is proportional to the alkali polarization as Eq. 6.10. The alkali polarization can be determined from EPR amplitude modulation sweeps. Compared to the EPR frequency modulation sweep mentioned in Sec. 6.3.2, the only difference is that the EPR RF signal generated by function generator (Model E4401B) is modulated with the amplitude input from the modulation sources. Fig. 6-20 shows the EPR spectrum from the amplitude modulation sweep: D_2 light relative intensity versus the frequency. In the plot, the highest peak corresponds to the transition $|F=2, m=2\rangle \leftrightarrow |F=2, m=1\rangle$ for ^{39}K.

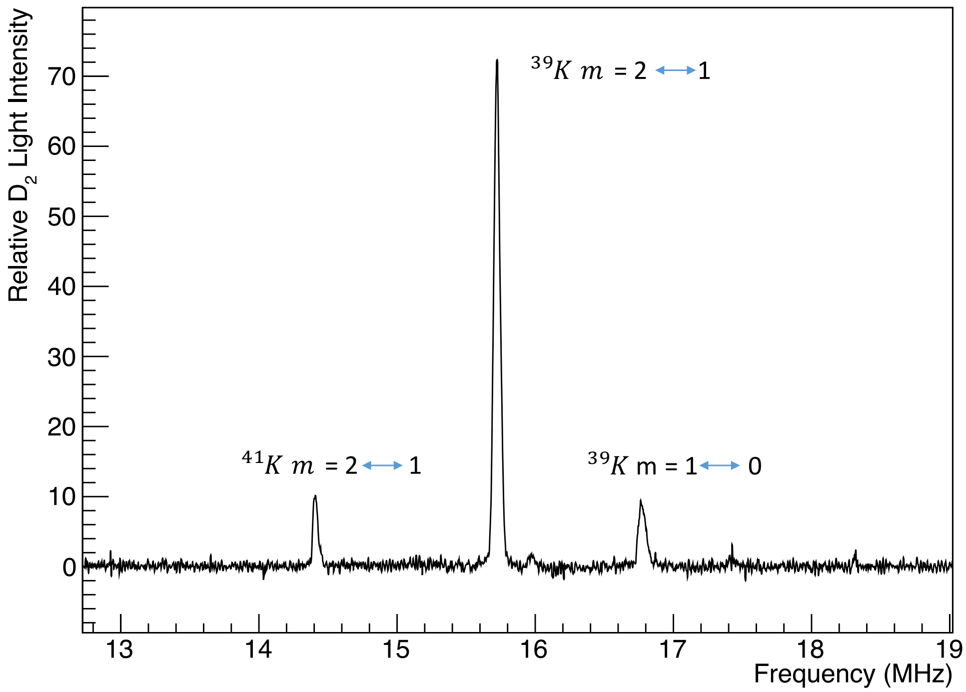

Figure 6-20: D2 light intensity versus the frequency from the EPR Amplitude modulation measurement.

According to[175, 176], the area $A_{F,m}$ under a particular line $|F, m\rangle \leftrightarrow |F, m-1\rangle$

in the EPR spectrum is proportional to the population difference between these two states $|F,m\rangle$ and $|F,m-1\rangle$:

$$A_{F,m} \propto f_I[A][\frac{H_{RF}}{2I+1}]^2[F(F+1)-m(m-1)](\rho_{F,m}-\rho_{F,m-1}), \tag{6.34}$$

where f_I is the natural fraction of the isotope, $[A]$ is the alkali number density, H_{RF} the RF magnetic field strength, and density $\rho_{F,m} \propto e^{\beta m}$ with $\beta = \frac{1+P_A}{1-P_A}$, with P_A the polarization of the alkali atoms.

In practice, the adjacent EPR transitions $|F,m\rangle \leftrightarrow |F,m-1\rangle$ and $|F,m-1\rangle \leftrightarrow |F,m-2\rangle$ can be well resolved, but not for twin transitions $|F,m\rangle \leftrightarrow |F,m-1\rangle$ with $F = I + 1/2$ and $|F^{'},m\rangle \leftrightarrow |F^{'},m-1\rangle$ with $F^{'} = I - 1/2$ since their difference is too small. Therefore, for the same alkali species, the ratio of areas of two successive peaks $m \leftrightarrow m-1$ and $m^{'} \leftrightarrow m^{'}-1$ is given by:

$$\begin{aligned} r &= \frac{A_{F,m}+A_{F^{'},m}}{A_{F,m^{'}}+A_{F^{'},m^{'}}} \\ &= \left[\frac{F(F+1)-m(m-1)+F^{'}(F^{'}+1)-m(m-1)}{F(F+1)-m^{'}(m^{'}-1)+F^{'}(F^{'}+1)-m^{'}(m^{'}-1)}\right]\beta(m-m^{'}). \end{aligned} \tag{6.35}$$

If choose $m^{'} = m-1$, the above Eq. 6.35 can be rewritten as

$$P_A = \frac{[F^2-(m-1)(m-2)]r-[F^2-m(m-1)]}{[F^2-(m-1)(m-2)]r+[F^2-m(m-1)]}. \tag{6.36}$$

For a nuclear spin $I = 3/2$ isotope like ^{39}K or ^{87}Rb under laser pumping, m=2, the ratio is

$$r = \frac{A_{2,2}}{A_{2,1}+A_{1,1}}, \tag{6.37}$$

and the the alkali polarization is

$$P_A = \frac{r-0.5}{r+0.5}. \tag{6.38}$$

For 6 GeV targets, the potassium polarization is close to 100% with three narrow-width diode lasers.

6.3.4 Two Chamber Polarization Model

Polarized ^{3}He cells at JLab usually consist two chambers with a small transfer tube connecting them, as shown in Fig. 6-8. The ^{3}He is polarized only in the pumping chamber and diffuses down to the target chamber. EPR can provide an absolute polarization measurement on the pumping chamber with high precision, however the target chamber is where the electron scattering happens, therefore a two chamber polarization model was developed to study the polarization dynamics and to obtain the polarization in the target chamber[177, 178]:

$$\begin{aligned} \frac{dP_p}{dt} &= \gamma_{SE}(P_A - P_p) - \Gamma_p P_p - d_p(P_p - P_t), && (6.39) \\ \frac{dP_t}{dt} &= -\Gamma_t P_t + d_t(P_p - P_t), && (6.40) \end{aligned}$$

where P_p (P_t) are the ^{3}He polarization in the pumping chamber (target chamber), P_A is the average alkali polarization, γ_{SE} is the spin-exchange rate per nucleus, Γ_p (Γ_t) is the ^{3}He spin relaxation rate per nucleus in the pumping chamber (target chamber), d_p (d_t) is the probability per unit time per nucleus that a nucleus will exit the pumping (target) chamber and enter the target (pumping) chamber. Substitute the Eq. 6.40 into Eq. 6.39, we obtain an homogeneous linear equation:

$$\frac{dP_t^2}{dt^2} + (d_t + \Gamma_t + d_p + \Gamma_p + \gamma_{SE})\frac{dP_t}{dt} + [d_p\Gamma_t + (\gamma_{SE} + \Gamma_p)(\Gamma_t + d_t)]P_t - d_t\gamma_{SE}P_A = 0. \qquad (6.41)$$

For an arbitrary initial condition:

$$\begin{aligned} P_p(t=0) &= X, && (6.42) \\ P_t(t=0) &= Y, && (6.43) \end{aligned}$$

and the equilibrium condition:

$$\begin{aligned}\frac{dP_p}{dt}(t=\infty) &= 0, &(6.44)\\ \frac{dP_t}{dt}(t=\infty) &= 0, &(6.45)\end{aligned}$$

the two chamber model can be solved analytically and the results are as follows:

$$\begin{aligned}P_p(t,X,Y) &= C_p e^{-\Gamma_f t} + (-P_p^\infty - C_p + X)e^{-\Gamma_s t} + P_p^\infty, &(6.46)\\ P_t(t,X,Y) &= C_t e^{-\Gamma_f t} + (-P_t^\infty - C_t + Y)e^{-\Gamma_s t} + P_t^\infty, &(6.47)\end{aligned}$$

where P_p^∞ (P_t^∞) is the maximum polarization in the pumping chamber (target chamber), Γ_f (Γ_s) is the fast (slow) time constant that governs the time evolution of the polarization, C_p (C_t) is the specific coefficient for the polarization in the pumping chamber (target chamber). They can be written as:

$$\Gamma_f = \frac{1}{2}[(d_p + \Gamma_p + d_t + \Gamma_t + \gamma_{SE}) + \sqrt{(d_p + \Gamma_p + \gamma_{SE} - d_t - \Gamma_t)^2 + 4d_pd_t}], \qquad (6.48)$$

$$\Gamma_s = \frac{1}{2}[(d_p + \Gamma_p + d_t + \Gamma_t + \gamma_{SE}) - \sqrt{(d_p + \Gamma_p + \gamma_{SE} - d_t - \Gamma_t)^2 + 4d_pd_t}], \qquad (6.49)$$

$$P_p^\infty = \frac{P_A\gamma_{SE}(d_t + \Gamma_t)}{(d_p + \Gamma_p + \gamma_{SE})(d_t + \Gamma_t) - d_pd_t}, \qquad (6.50)$$

$$P_t^\infty = \frac{d_t}{d_t + \Gamma_t}P_p^\infty, \qquad (6.51)$$

$$C_p = \frac{\Gamma_s P_p^\infty - \gamma_{SE}P_A + X(\gamma_{SE} + \Gamma_p + d_p - \Gamma_s) - Y d_p}{\Gamma_f - \Gamma_s}, \qquad (6.52)$$

$$C_t = C_p\frac{d_t}{\Gamma_t + d_t - \Gamma_f} = \frac{\Gamma_s P_t^\infty - X d_t + Y(\Gamma_t + d_t - \Gamma_s)}{\Gamma_f - \Gamma_s}. \qquad (6.53)$$

At the fast diffusion limit, d_p, $d_t \gg \gamma_{SE}$, Γ_t, Γ_p, one can get $\Gamma_f \approx d_p + d_t$, $\Gamma_s \approx 1/2\,[\Gamma_p + \Gamma_t + \gamma_{SE} - (d_p - d_t)/(d_p + d_t)(\Gamma_p + \gamma_{SE} - \Gamma_t)]$, and the polarization of both chambers can be expressed in a unified polarization evolution function as shown in Eq. 6.8 with $\Gamma_R = \Gamma_s$.

Assume the flux is constant and temperature varies linearly along the transfer tube, the diffusion rate d_p (d_t) can be computed as [159]

$$d_t = \frac{A_{tt}D_0}{V_t L_{tt}} \frac{n_0(2-m)(T_p - T_t)}{n_t T_0^{m-1}(T_p^{2-m} - T_t^{m-2})}, \tag{6.54}$$

$$d_p = \frac{n_t V_t d_t}{n_p V_p}, \tag{6.55}$$

where $D_0 = 2.789 \pm 0.007$ cm^2/s is the diffusion constant at $T_0 = 353.14$ K, $m = 1.705 \pm 0.003$ describes the temperature dependence of the diffusion constant, $n_0 = 0.7733$ amg is the density scale factor, A_{tt} (L_{tt}) is the cross section (length) of transfer tube, T_p (T_p) is the average pumping (target) chamber inner gas temperature, n_p (n_t) is the pumping chamber (target chamber) density and V_p (V_t) is the pumping chamber (target chamber) inner volume.

For the typical ^{3}He system during Transversity experiment[168], the diffusion rate is estimated as $d_t = 0.83$ h^{-1} with uncertainty $\frac{\delta d_t}{d_t} \approx 20\%$. This will contribute one of the largest systematic uncertainty (2-3)% in the target chamber polarization.

During a normal production run, the total relaxation rate Γ_t has 5 contributions:

$$\Gamma_t = \Gamma_{dip} + \Gamma_{wall} + \Gamma_{beam} + \Gamma_{AFP} + \Gamma_{\Delta B}. \tag{6.56}$$

where Γ_{dip} is related to ^{3}He-^{3}He dipolar interaction, Γ_{wall} is contributed from collisions between the ^{3}He nucleus and the cell glass wall, Γ_{beam} is the beam depolarization effect through ionization, Γ_{AFP} is from NMR-AFP sweep, and $\Gamma_{\Delta B}$ is the relaxation due to magnetic field gradient. During transversity experiment [168, 179], the pumping chamber polarization is around 60%, Γ_t is around 0.1 h^{-1}, d_t is around (0.6-0.8) h^{-1}, so the polarization gradient between target chamber and pumping chamber (Eq. 6.51):

$$\frac{P_t}{P_p} = (1 + \Gamma_t/d_t)^{-1} = (85 - 90)\%, \tag{6.57}$$

which means for $P_p \approx (50 - 60)\%$, the target chamber's absolute polarization is (5-10)% lower than the pumping chamber polarization.

6.4 Performance in the 6 GeV Era

By implementing both the narrow-width diode laser and the hybrid-pumping technique (Rb-K mixture), the spin up times for the JLab target were shortened from approximately 10 hours to 5 hours [168, 173], and the maximum polarization was increased from 40% (during A1n[76, 148] in 2001) to 60% (during Transversity[150, 151] in 2009), with a 15 μA electron beam on target[168, 173]. Without beam, the maximum ^{3}He polarization reached more than 70% (Cell Brady). At 15 μA, this target (40 cm long, 10 amg) used during Transversity, also set a world polarized luminosity record for polarized ^{3}He ($P_{^3\mathrm{He}} \times Luminosity \approx 1.0 \times 10^{36}/\mathrm{cm}^2/\mathrm{s}$). The Fig. 6-21 shows the figure-of-merit ($P^2_{^3\mathrm{He}} \times$ Current) evolution during the 6 GeV era.

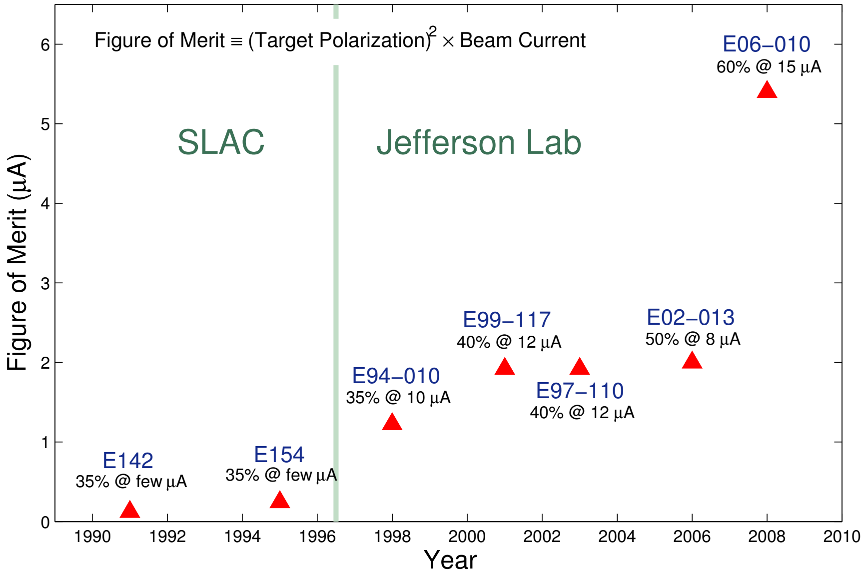

Figure 6-21: Figure-of-Merit history for high luminosity polarized ^{3}He targets used at SLAC and then the 6 GeV era of JLab[168].

For electron scattering experiments, the experiment performance depends directly on the target chamber polarization and its uncertainty. Table 6.1 shows systematic uncertainty for the target chamber polarization during the Transversity experiment[168]. There are several limitations for the target performance, described in this section.

Items		**Rel. Pol. Error**
Pumping Chamber	K-^{3}He EPR κ_0	2.7%
	Pumping chamber density	1.8%
	Pumping chamber temperature	0.5%
	Density fluctuation	0.4%
	Stat. error of NMR calib. constant	0.3%
Polarization Gradient	Diffusion rate	2.3%
	Target chamber intrinsic lifetime	2.0%
	Beam depolarization	1.6%
	Transfer tube depolarization	0.5%
	Spin flip loss	0.2%
Sum all		**4.9%**

Table 6.1: Systematic uncertainty budget for target polarization during the Transversity experiment[168].

6.4.1 Limitation of the 6 GeV Diffusion Cell

All 6 GeV experiments used the same cell design (Fig. 6-8) where the polarization propagates from the pumping to the target chamber purely by diffusion. We henceforth name such design "diffusion cell". From Sec. 6.3.4 and Table 6.1, the target chamber absolute polarization has some limitations due to the diffusion cell design:

- Target chamber absolute polarization is typically (5-10)% lower than the pumping chamber during the series of Transversity experiments due to the slow diffusion. This largely comes from the long transfer tube.

- One of the largest systematic uncertainty (2-3%) is due to the estimated uncertainty of diffusion rate $\frac{\delta d_t}{d_t} \approx 20\%$.

Some tests were performed to understand the diffusion rates [177, 178]. However, these measurements were done with initial polarization zero and without electron beam, which means the polarization gradient between pumping chamber and target chamber was not large. The larger the polarization gradient, the more significant the diffusion plays in the two chamber polarization dynamics, and thus the more accurate the diffusion rate studies is needed. A dedicated study on the diffusion rate was performed on cell Moss in EEL lab at JLab in 2012. The ^{3}He target was pumped to high polarization for both pumping chamber and target chamber first. A RF field was then applied to destroy the polarization in the target chamber completely while keeping the pumping chamber polarization as high as possible. Then both pumping chamber and target chamber polarization were recorded by NMR independently every 10 minutes, as shown in Fig. 6-22.

From Sec.6.3.4, the pumping chamber polarization $P_p(t, X, Y)$ and target chamber polarization $P_t(t, X, Y)$ can be described using Eq. 6.46 and Eq. 6.47 respectively. However, a modification is needed to account for the AFP loss from each NMR measurement. Denote the i-th measurement polarization as P_p^i (P_t^i), the AFP loss as $1 - \beta_p$ ($1 - \beta_t$) with $\beta_{p,t} \approx 1$, the measurement time interval as $\Delta t = t_{i+1} - t_i$, the (i+1)-th measurement can be described using Eq. 6.46- 6.47 with initial values $X = P_p^i \beta_p^2$ and $Y = P_t^i \beta_t^2$:

$$P_p^{i+1} = P_p(\Delta t, P_p^i \beta_p^2, P_t^i \beta_p^2) \tag{6.58}$$

$$P_t^{i+1} = P_t(\Delta t, P_p^i \beta_t^2, P_t^i \beta_t^2). \tag{6.59}$$

Fitting the measured NMR amplitudes using Eq. 6.58 and Eq. 6.59 leads to the parameters as shown in Table 6.2. For the cell Moss, the transfer tube cross section $A_{tt} = 0.71$ cm^2, the transfer tube length $L_{tt} = 9.4$ cm, the transfer tube volume $V_{tt} = 6.6$ cm^3, the target chamber volume $V_t = 74.0$ cm^3, the pumping chamber volume $V_t = 190.3$ cm^3 and the filled ^{3}He density $n_{^3He} = 7.96$ amg. The ^{3}He density in target chamber is related to the ratio of gas temperature in target chamber and pumping chamber, and is given by

$$n_t = \frac{n_{^3\mathrm{He}}}{1 + \frac{V_p}{V_{tot}}(\frac{T_t}{T_p} - 1)}, \tag{6.60}$$

$$\tag{6.61}$$

with $V_{tot} = V_t + V_p$. During the measurement, $T_p = 240.5$ °C and $T_t = 31.7$ °C, the calculated diffusion rate d_t from Eq. 6.55 is 0.79 h^{-1} which agrees with the fitted value (0.81 ± 0.02) h^{-1} within one σ.

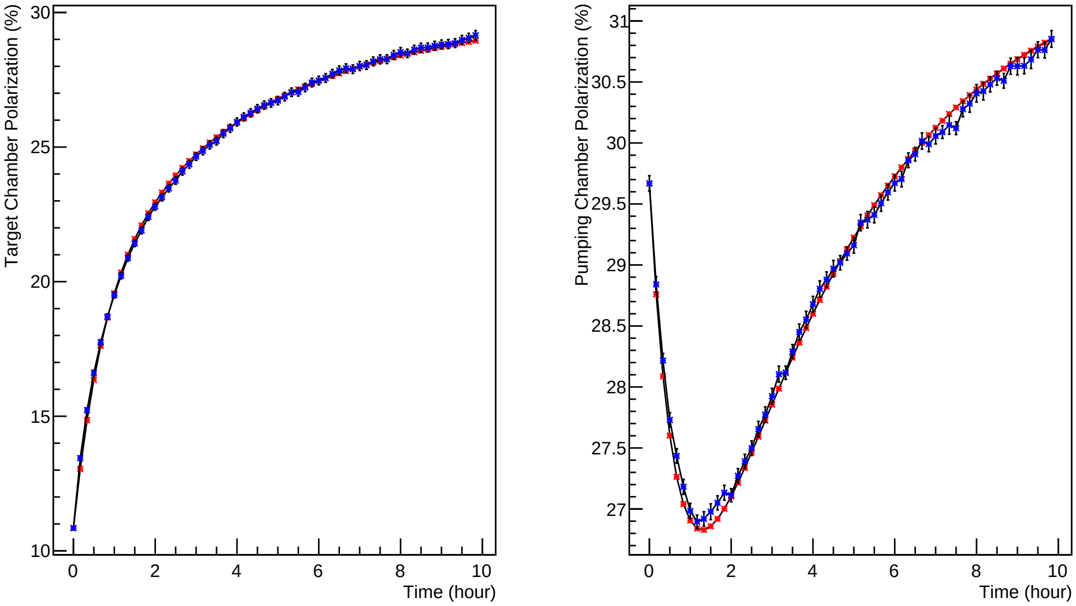

Figure 6-22: A test of the two chamber diffusion model performed in 2012 on cell Moss. The left shows the polarization evolution on the target chamber while the right shows for the pumping chamber. The red curves are from model predictions. The blue markers are the measured NMR amplitudes scaled by a fitted constant for the left plot, and a fixed EPR constant for the right.

Fitting Parameters	Fitting Results
Target Chamber diffusion rate d_t	(0.80 ± 0.02) h^{-1}
Target Chamber relaxation rate Γ_t	(0.04 ± 0.01) h^{-1}
Target chamber NMR calibration factor	1.05 ± 0.01
Target Chamber AFP loss β_t	0.22% fixed from AFP test
Pumping Chamber Diffusion rate d_p	(0.40 ± 0.05) h^{-1}
Pumping Chamber relaxation rate Γ_p	(0.06 ± 0.02) h^{-1}
Pumping chamber NMR calibration factor	1.36 fixed from EPR test
Pumping Chamber AFP loss β_p	0.85% fixed from AFP test
Alkali polarization P_A	$(94 \pm 3)\%$
spin-exchange rate γ_{SE}	(0.073 ± 0.006) h^{-1}

Table 6.2: Fitting results for the 2012 diffusion rate test.

6.4.2 Limitation of Polarimetry

As described in Sec. 6.3, two kinds of polarimetry, NMR and EPR were used to measure the polarization of the target. The relative uncertainty of the polarization was around 5% for hybrid cells (GEn and transversity series). One main aspect of this thesis work is to prepare the ^{3}He target for the 12 GeV era of JLab. From Sec. 6.3.2, Sec. 6.3.4 and Table 6.1, the target chamber polarization polarimetry has the following limitations:

- Existing measurements of the EPR calibration constant κ_0 were only performed at below 200°C, will contributes as one of the largest systematic uncertainty (2-3)% to EPR polarimetry.
- For high-beam current required by 12 GeV experiments, metal end-windows of target chamber are desirable. Therefore, NMR will not be suitable for measurements on the target chamber.

To satisfy the requirements of the approved experiments for the 12 GeV program at JLab, an upgrade of the polarized ^{3}He is essential, as will be discussed in the following sections.

6.5 Upgrade Plan for the ^{3}He Target at 12 GeV

For the 12 GeV program at JLab, there are already seven polarized ^{3}He target related experiments approved with high scientific ratings (three A's and four A-'s). Among the seven experiments, two experiments (with the SoLID spectrometer[180, 181]) demands the performance already achieved during the 6 GeV era, while the other five require a significant improvement and can be divided into two groups. The first group consists of three experiments (A_1^n-Hall A[182], d_2^n-Hall C[183] and SIDIS-SBS[184]) which requires a factor of 3-4 in the figure-of-merit, while the second group (A_1^n- Hall C[185] and GEN-II[186]) needs a further factor of 2, as shown in Table 6.4. A two-stage plan was developed to upgrade the polarized ^{3}He target to meet the requirements of these experiments[187]. Stage One aims to have a 40 cm long, 10 amg target with 30 μA electron beam current and reach an in-beam target polarization of 60%, a factor of 2–3 improvement in the figure of merit. In addition, the precision of the polarization measurement will be improved from 5% to 3%. This target will

Expt.	Density	Length	Pol.	Current	Pol. Luminosity	Pol. Rel. Err.
A_1^n-Hall A	10 amg	60 cm	65%	30 μA	$3 \times 10^{36}/\mathrm{cm}^2/\mathrm{s}$	3%
SIDIS-Hall A	10 amg	60 cm	65%	40 μA	$4 \times 10^{36}/\mathrm{cm}^2/\mathrm{s}$	3%
d_2^n-Hall C	10 amg	60 cm	55%	30 μA	$3 \times 10^{36}/\mathrm{cm}^2/\mathrm{s}$	3%
A_1^n-Hall C	10 amg	60 cm	60%	60 μA	$6 \times 10^{36}/\mathrm{cm}^2/\mathrm{s}$	3%
GENII-Hall A	10 amg	60 cm	65%	60 μA	$6 \times 10^{36}/\mathrm{cm}^2/\mathrm{s}$	3%
SIDIS E12-10-006	Achieved during 6 GeV era					
SIDIS E12-11-007	Achieved during 6 GeV era					

Table 6.3: Polarized ^{3}He Target needed by the approved 12 GeV experiments. As a comparison, the highest polarization luminosity (defined as $P_{^3\mathrm{He}} \times$ Current) during 6 GeV, achieved during the transversity experiment, was 1.0×10^{36} cm^{-2}s^{-1}.

satisfy the requirement of the first group of 12 GeV experiments to an acceptable level. Stage Two is to meet the needs of the second group of experiments: a 60 cm long, 10 amg target with a polarization reaching 65% with a 60 μA beam current. A metal end-window or metal target chamber cell with double-pumping-chamber design will be needed to handle the high beam current in this stage.

For the first stage, with the limited resources (engineering/design manpower and funding) available, the new target system will make full use of the existing 6 GeV setup and the upgrade steps are outlined as following:

- using convection flow to increase the ^{3}He transfer rate between two chambers.
- using a larger pumping chamber size: 3.5 inches in diameter, compared to the 3 inch during 6 GeV running. The volume will increase by 50%.
- developing a new polarimetry called pulsed NMR and calibrate it with EPR and water NMR.
- shielding the pumping chamber from radiation damage. The typical cell lifetime is around 4 weeks under the 6 GeV beam running condition. The pumping chamber gradually darkens due to radiation and ruptures under the high power laser pumping.
- measuring the EPR calibration constant κ_0 to a higher temperature that covers the hybrid cell operation temperature. These measurements will be performed

by JLab users (Prof. Cates's group at the University of Virginia and Prof. Averett's group at the College of William and Mary).

- using metal end-windows for the target chamber. This is optional for a 30μA beam, but is required for higher currents. This is currently also being studied by Prof. Cates's group at the University of Virginia.

6.6 Upgrade Progress

Fig. 6-23 shows the mechanical design of the target system for Stage One, which is very different from 6 GeV experiments. To have the target system ready, R&D efforts are ongoing to study the performance of the convection cell, a pulsed-NMR system, radiation shielding for high current beam and systematic uncertainties in target polarization measurements [188]. More details will be discussed in the following sections.

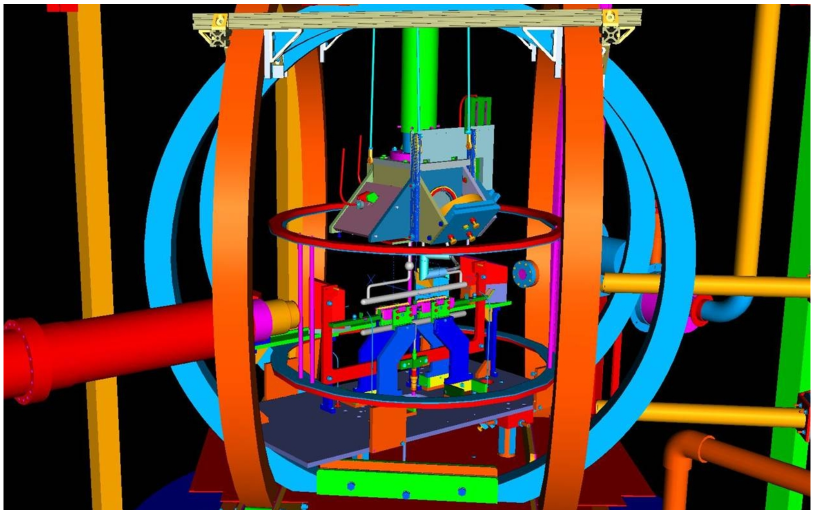

Figure 6-23: The polarized ^{3}He target mechanical design at JLab.

6.6.1 Convection System

A convection type cell was developed and tested at UVa [189]. The geometry of convection cell Protovec-I is shown in Fig. 6-24. The pumping chamber is a 3.5 inch diameter sphere located inside a 230 °C oven (where ^{3}He nuclei are polarized through spin exchange with a Rb-K mixture that is in turn polarized by 795 nm laser light). The target chamber is a 40 cm long tube. Compared with the previous diffusion cell shown in Fig. 6-8 and Fig. 6-9, the main difference is that it consists of a pair of short transfer tubes between the pumping chamber and the target chamber. A heating coil is placed on one of the transfer tube which cause the gas to flow due to convection. The convection design circulates gas between the pumping and target chambers much more rapidly than the previous design, which relied upon diffusion of the gas through a single tube connecting the chambers. In this section, I will describe a model for the polarization dynamics in the convection cell, and studies of the convection speed, AFP loss, spin up and down processes, and alkali polarization measurements for the convection cell.

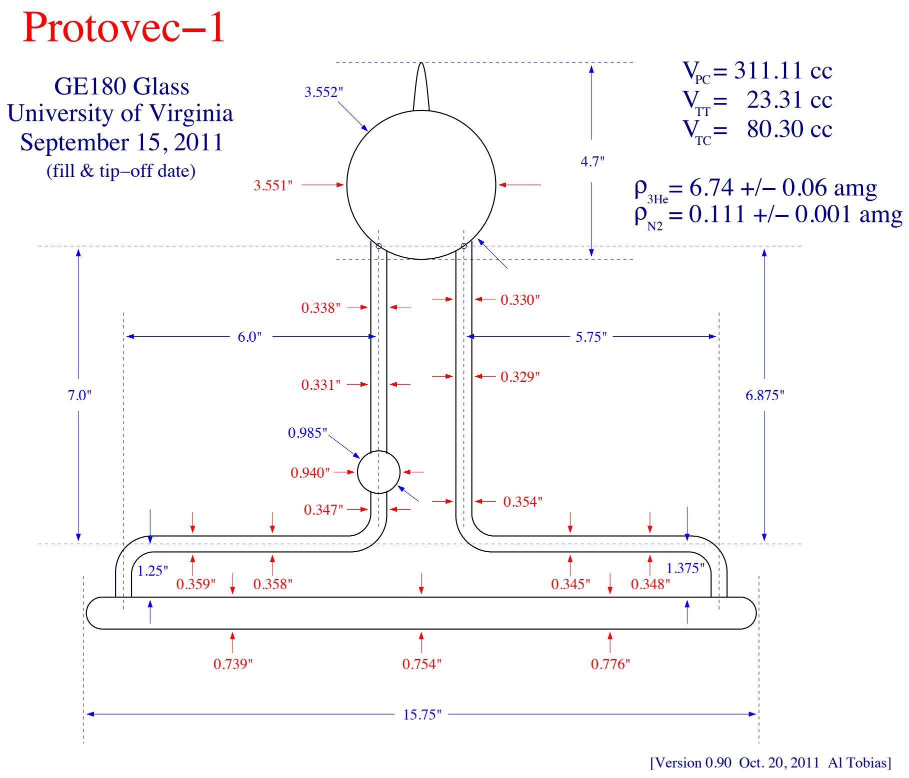

Figure 6-24: Geometry of Convection Cell Provotec-I.

6.6.1.1 Convection Model

A two chamber convection model was developed to study the polarization dynamics with convection. The polarization of the ^{3}He in the two chambers can be described by

$$\begin{aligned}\frac{dP_p}{dt} &= \gamma_{SE}(P_A - P_p) - \Gamma_p P_p - (d_p + G_p)(P_p - P_t), \qquad (6.62)\\ \frac{dP_t}{dt} &= -\Gamma_t P_t + (d_t + G_t)(P_p - P_t). \qquad (6.63)\end{aligned}$$

The above functions are very similar to the two chamber diffusion model discussed in Sec. 6.3.4, but with two additional terms G_p and G_t that are related to the convection. G_p (G_t) is the probability per unit time per nucleus that a nucleus exits the pumping (target) chamber and enters the target (pumping) chamber due to convection, and can be expressed as:

$$\begin{aligned}G_p &= \frac{vA_t}{V_t}\frac{n_t V_t}{n_p V_p} \approx \frac{v}{L}\frac{n_t V_t}{n_p V_p}, \qquad (6.64)\\ G_t &= \frac{vA_t}{V_t} \approx \frac{v}{L}. \qquad (6.65)\end{aligned}$$

Here v is the convection velocity of ^{3}He gas in the target chamber, L is the length of the target chamber, V_t (A_t) is the target chamber volume (cross section).

The polarization evolution in the two chambers are the same as Eq. 6.46 and Eq. 6.47 if substituting d_p (d_t) by G_p+d_p (G_t+d_t). From Eq. 6.57, the polarization gradient between the target chamber and the pumping chamber under a convection speed v is

$$\frac{P_t}{P_p} = \left(1 + \frac{\Gamma_t}{d_t + G_t}\right)^{-1}. \qquad (6.66)$$

Therefore, the additional term G_t reduces the polarization gradient between two chambers. Fig. 6-25 shows the calculated polarization gradient versus convection speed in the target chamber. For a typical convection speed around 6 cm/min, $G_t \gg$

d_t, and $\frac{P_t}{P_p} \approx 98\%$. So the ^{3}He polarization of the target chamber is almost the same as pumping chamber, and the systematic uncertainty of the target chamber polarization can be reduced. Many tests have been performed to demonstrate that the convection system works properly, to be described in the following sections.

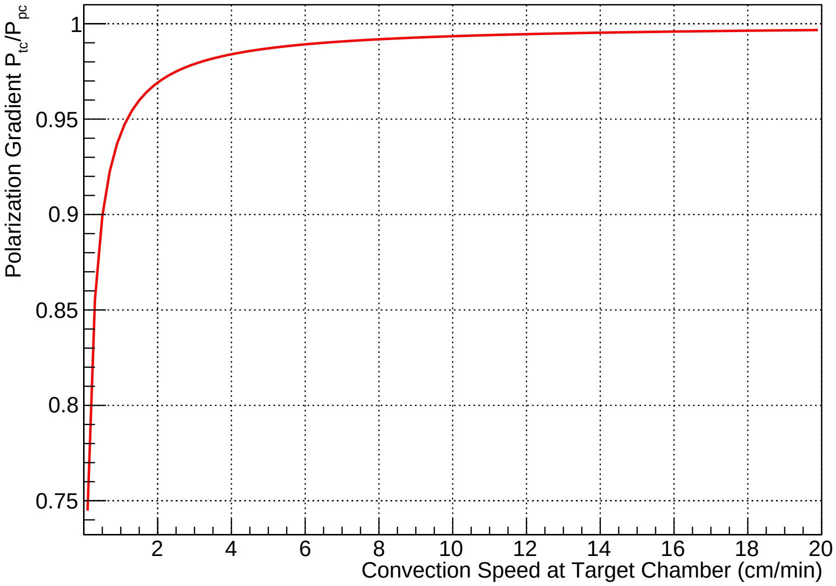

Figure 6-25: Polarization gradient versus convection speed in the target chamber calculated using Eq. 6.66. The target chamber relaxation rate is assumed to be 0.1 h^{-1}.

6.6.1.2 Convection Speed

From Fig. 6-25 convection speed is one of the key factor for the upgraded target system since the polarization gradient depends directly on it. Fig. 6-26 shows the setup for the convective flow measurement at JLab performed in 2013. A small heater on one of the two transfer tubes is used to establish a convective flow of gas between the pumping and target chambers, while a RF pulse from the Free-Induction-Decay (FID) coil is used to perturb the polarization of gas inside the 1.0 inch bulb on the other transfer tube. The polarization dynamics inside the target chamber are then monitored with two sets of pickup coils using NMR-AFP. The recorded NMR amplitudes are shown in Fig. 6-27. The convection speed can then be determined from the time difference between the two dips in the two sets of NMR amplitude curves and the distance between the two pickup coils. The convection speed was determined to be around 5.7 cm/min in the target chamber.

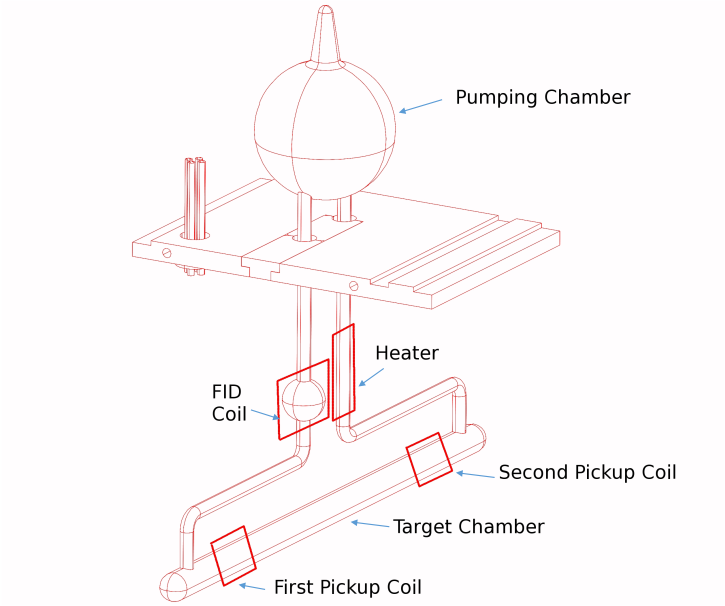

Figure 6-26: Set up for convection flow test.

6.6.1.3 AFP Loss

AFP loss refers to the polarization loss during one NMR scan. The NMR sweep speed is optimized to minimize the depolarization, typically less than 1% relative polarization is lost during each NMR measurement. For the convection design, the ^{3}He gas circulates in the cell and experiences a large gradient of the Helmholtz holding field in the whole cell region in a short time. In addition, the constant flow will cause more collisions between the cell wall and ^{3}He atoms. Both of these two processes can bring larger depolarization effects than diffusion only cells. AFP loss studies were used to characterize these effects by measuring the difference between subsequent up-sweep and down-sweep NMR amplitudes. These AFP measurements have been made with the convection heater on and off, and in both the target and pumping chambers.

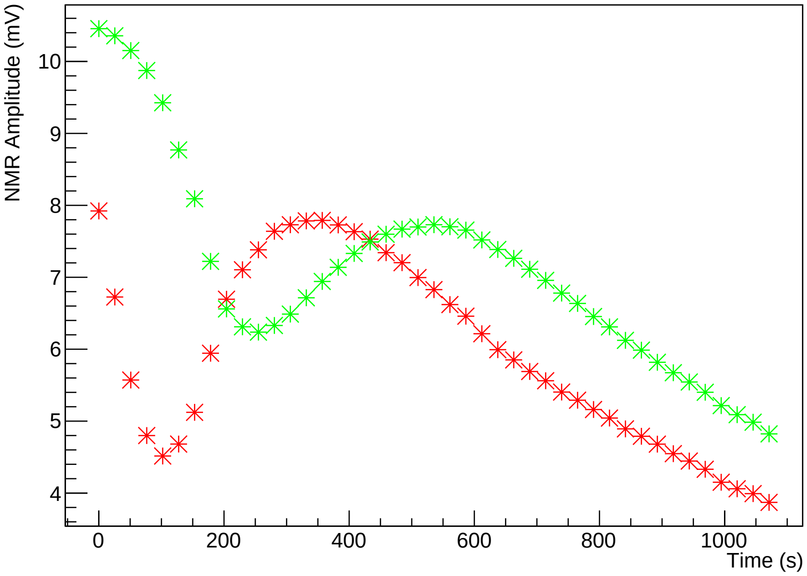

Figure 6-27: NMR signal amplitude versus time from the two pickup coils during the convection speed test, performed on cell Provotec-I at JLab in 2013. The red and green curves are the NMR amplitudes measured by the first pickup coil and the second pickup coil, respectively. Two pickup coils are 14.5 cm apart. The result indicates a gas flow velocity of 5.7 cm/min in the target chamber.

Results are show in Fig. 6-28 and Table 6.4. The total loss between AFP scans with convection on is slightly larger, but acceptable.

AFP loss per sweep	target chamber	pumping chamber
without convection	0.16%	0.72%
with convection	0.85%	0.87%

Table 6.4: AFP loss with convection on and off for both the pumping chamber and target chamber when the laser was off. The results were corrected for polarization loss due to spin relaxation. The absolute uncertainty for the AFP loss is about 0.05%.

6.6.1.4 Spin Up Test

The spin up test is to study how fast the ^{3}He gas can be pumped to the maximum polarization. At the typical convection speed 6 cm/min, G_{pc}, $G_{tc} \gg \gamma_{SE}$, Γ_{tc}, Γ_{pc}, the polarization of both chambers can be expressed in a unified time evolution function

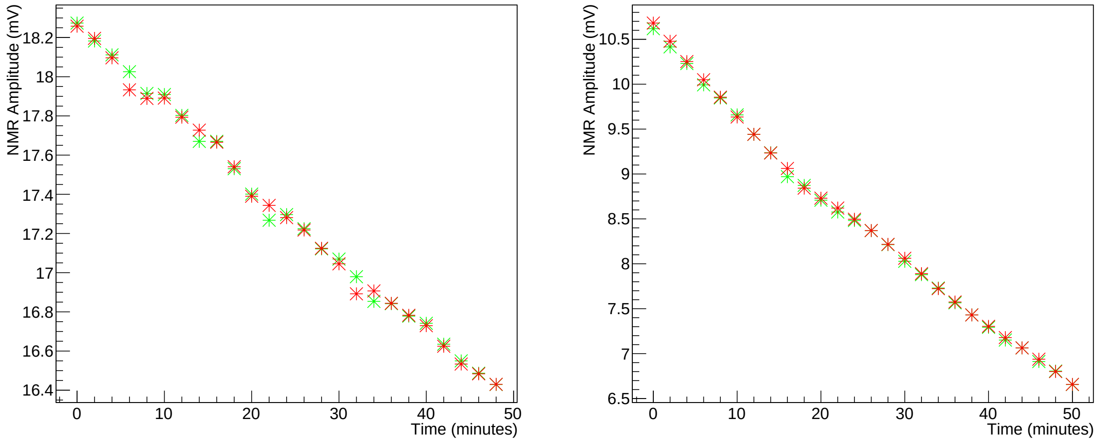

Figure 6-28: NMR amplitudes versus time (25 sweeps 2 minutes apart) for the target chamber during an AFP loss study, performed on cell Provotec-I at JLab in 2013. Red and green markers indicate the NMR sweep up and down amplitudes. The result with convection off (on) is shown in the left (right) plot, and numerical values are shown in Table 6.4.

as shown in Eq. 6.8. One can express it as:

$$P(t) \quad = \quad P^0 + (P^\infty - P^0)(1 - e^{-\frac{t}{\tau}}), \tag{6.67}$$

where P^∞ is the maximum polarization, P^0 is the initial polarization at $t = 0$.

A NMR field sweep consists of two scans: scan the field up though the resonance and scan back to the original field. Denoting the i-th measurement polarization as P^i_{up} for the up sweeps (P^i_{dn} for the down sweeps), the AFP loss as $1 - \beta$, the measurement time interval as $\Delta t = t_{i+1} - t_i$, the (i+1)-th measurement can be described:

$$P^{i+1}_{up} \quad = \quad P^i_{up}\beta^2 + (P^\infty - P^i_{up}\beta^2)(1 - e^{-\frac{\Delta t}{\tau}}), \tag{6.68}$$

$$P^{i+1}_{dn} \quad = \quad [P^i_{dn}\beta + (P^\infty - P^i_{dn}\beta)(1 - e^{-\frac{\Delta t}{\tau}})]\beta. \tag{6.69}$$

At $t = (n-1)\Delta t$, these functions can be solved analytically as

$$P^n_{up} \quad = \quad -\frac{P^\infty(1 - e^{-\frac{\Delta t}{\tau}})}{\beta^2 e^{-\frac{\Delta t}{\tau}} - 1} + \left[\frac{P^\infty(1 - e^{-\frac{\Delta t}{\tau}})}{\beta^2 e^{-\frac{\Delta t}{\tau}} - 1} + P^0\right](\beta^2 e^{-\frac{\Delta t}{\tau}})^{n-1} \tag{6.70}$$

$$P^n_{dn} \quad = \quad \beta P^n_{up}. \tag{6.71}$$

Fig. 6-29 shows the fitting for the pumping chamber (target chamber) spin up curve using Eq. 6.70 and Eq. 6.71 with a $\chi^2 \approx 1$. The spin up time constants for the pumping chamber is τ_{spinup}= (6.5 ± 0.1) hours and the target chamber is τ_{spinup}= (6.4 ± 0.1) hours.

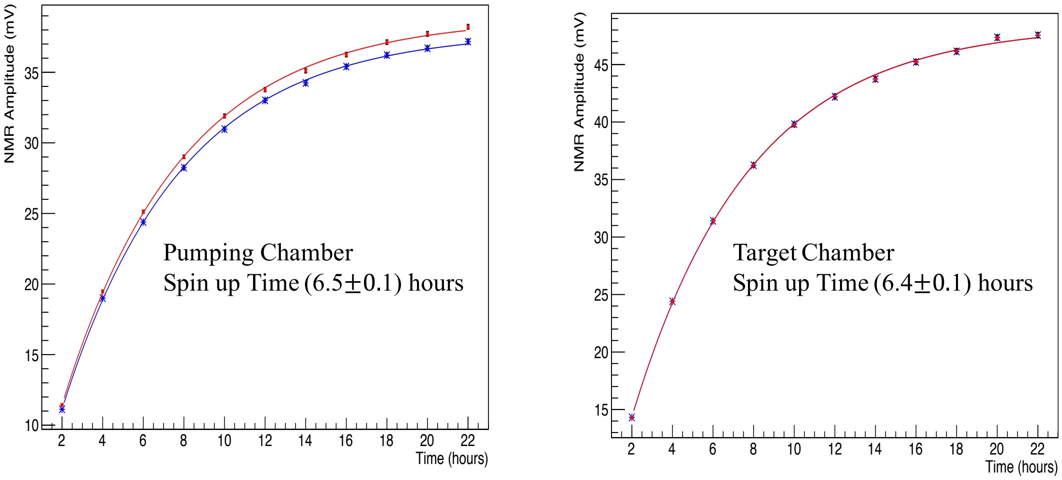

Figure 6-29: Spin up curves with convection on for the pumping chamber (left) and the target chamber (right) on cell Protovec-I at JLab in 2013. The two sets of data in each are for NMR up-sweep (red markers) and down-sweep (blue markers), and the curves are fits using Eq. 6.70 and Eq. 6.71 with β fixed from AFP study.

6.6.1.5 Spin Down Test

A spin down test studies how fast the ^{3}He depolarizes when lasers are off, and provides data on the spin relaxation rate Γ_t (Eq. 6.56). When the oven is cool and there is no electron beam, the relaxation depends largely on the wall relaxation. The wall relaxation rate depends on the procedure and the quality of the cell making and can vary significantly from cell to cell. A good cell should have a spin down time constant above 20 hours.

For cells with convection flow, more depolarization effects can occur, as discussed in Sec. 6.6.1.3. Therefore, it is essential to conduct a spin down measurement with the convection flow on and the oven off. Similar to the approach in Sec. 6.6.1.4, The polarization evolution P^n_{up} (P^n_{dn}) can be described as a function of the number of measurements n, the constant time interval $\Delta t = t_{i+1} - t_i$ and the AFP loss $1 - \beta$:

$$P^n_{up} = P^0(\beta^2 e^{-\frac{\Delta t}{\tau}})^{n-1}, \tag{6.72}$$

$$P^n_{dn} = P^n_{up}\beta. \tag{6.73}$$

Fig. 6-30 shows the fitting for the pumping chamber and target chamber spin down curves using Eq. 6.72 and Eq. 6.73. The averaged spin down time constant for the two chambers is $\tau_{spindown}$= (30.8 ± 0.3) h. And the constants are almost identical in the two chambers, and are long, indicates that this convection cell works properly.

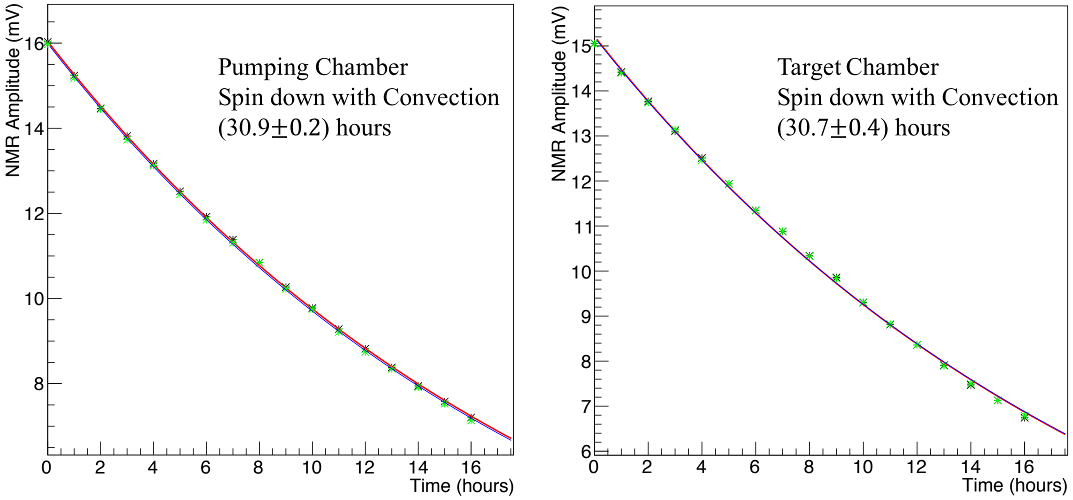

Figure 6-30: Spin down curve with convection on for the pumping chamber (left) and the target chamber (right) on cell Provotec-I at JLab in 2013. The two sets of data in each are for NMR up-sweep (black markers) and down-sweep (green markers), and the curves are fits using Eq. 6.72 and Eq. 6.73.

6.6.1.6 Alkali Polarization

From Sec. 6.3.3, EPR amplitude modulation sweep can be used to measure the alkali polarization. The alkali polarization P_A can be expressed as the ratio of areas under two peaks in the measured EPR spectrum, as shown in Eq. 6.37- 6.38. However, the EPR RF introduces an additional depolarization effect on the alkali[173]. The alkali polarization can be expressed as

$$P_A(\Gamma_{RF}) = \frac{\gamma_{pump}}{\gamma_{pump} + \Gamma_A + \Gamma_{RF}}, \tag{6.74}$$

where γ_{pump} is the optical pumping rate, Γ_A is total alkali relaxation rate in the absence of EPR RF, and Γ_{RF} is the EPR RF depolarization rate which is proportional to the RF power. We can write the alkali polarization as a function of the RF power P_{RF}:

$$\frac{1}{P_A} = \frac{\gamma_{pump} + \Gamma_A}{\gamma_{pump}} + \frac{\Gamma_{RF}}{\gamma_{pump}} = \frac{1}{P_0} + kP_{RF}, \tag{6.75}$$

with P_0 the alkali polarization without EPR RF perturbation.

Fig. 6-31 shows the the alkali polarization curve with different RF powers and two kinds of laser conditions. The Eq. 6.75 was fitted for both laser conditions with a $\chi^2 \approx 1$ achieved. The alkali polarization P_0 was $P^0_{^{39}\mathrm{K}}$= $(96.7 \pm 0.2)\%$ by using one Coherent and one QPC laser while $P^0_{^{39}\mathrm{K}}$= $(93 \pm 1\%)$ for only one Coherent laser. These results indicate a high alkali polarization was reached for the convection cell with a 3.5-inch diameter pumping chamber.

6.6.2 Pulsed NMR

Two kinds of polarimetry, NMR and EPR, were used to measure the polarization of ^{3}He targets during the 6 GeV era. However, the metal target chambers will be essential for future 12 GeV experiments with very high luminosity. This will present problems for NMR on the target chamber due to attenuation of the RF fields. A pulsed-NMR system is suitable for measurements on the transfer tube connecting the metal target chamber to the glass pumping chamber, was developed at UVa first and then modified and built in the JLab target lab.

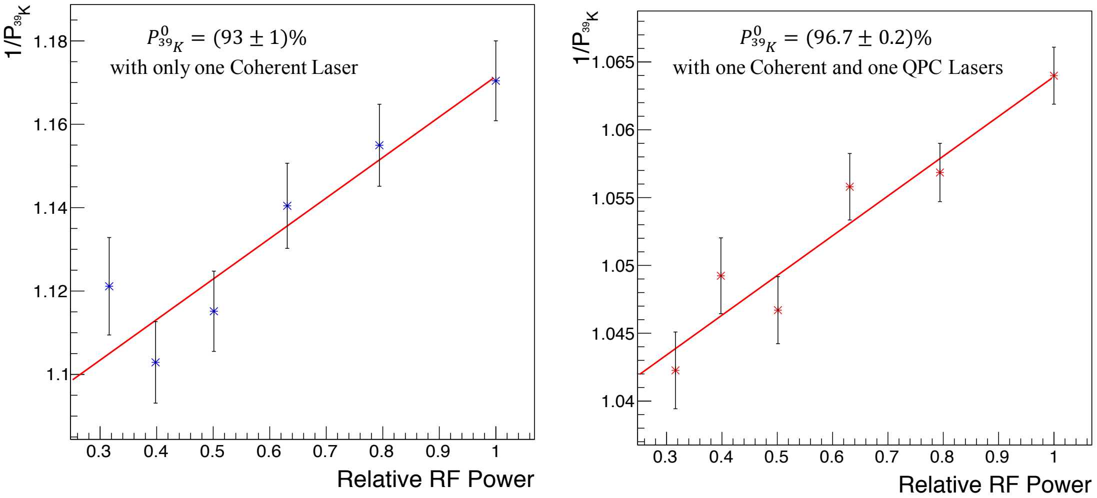

Figure 6-31: Alkali polarization versus the RF power, performed on cell Provotec-I at JLab in 2014. The left shows the polarization curve using one QPC and one Coherent lasers while the right for only one Coherent laser. Data points are fitted using Eq. 6.75 and the alkali polarization without EPR RF, P^0 is extracted and shown in each panel.

6.6.2.1 Pulsed NMR Principle

At the holding field $\vec{H} = H\hat{z}$, a RF pulse $\vec{H}_1$=$2H_1\cos(\omega t)\hat{x}$ tuned to the ^{3}He Larmor frequency, is sent to the FID coil shown in Fig. 6-26. At resonance in the rotating frame, the spin sees a constant field of

$$\vec{H}_{eff} = H_1\hat{x}, \tag{6.76}$$

which is orthogonal to its spin direction, as shown in Fig. 6-32. As a result, the ^{3}He magnetization vector tips away from the holding field through an angle θ_{tip} given by

$$\theta_{tip} = \frac{1}{2}\gamma H_1 t_{pulse}, , \tag{6.77}$$

where γ is the gyro-magnetic ratio and t_{pulse} is the RF pulse duration. At the conclusion of the pulse, the spin components $\vec{M}$ orthogonal to the holding field will experience free induction decay, described by the Bloch equations in the lab frame:

$$\frac{\partial M_x}{\partial t} = \gamma M_y H - \frac{M_x}{T_2}, \tag{6.78}$$

$$\frac{\partial M_y}{\partial t} = -\gamma M_x H - \frac{M_y}{T_2}, \tag{6.79}$$

$$\frac{\partial M_z}{\partial t} = -\frac{M_z - M_{eq}}{T_1}, \tag{6.80}$$

where T_2 (T_1) is the transverse (longitudinal) relaxation time and M_{eq} is the equilibrium magnetization at $t = \infty$. The solutions of the Bloch equations are[190]

$$M_x(t) = [M_x(0)\cos(\omega t) - M_y(0)\sin(\omega t)]e^{-\frac{t}{T_2}}, \tag{6.81}$$

$$M_y(t) = [M_x(0)\sin(\omega t) + M_y(0)\cos(\omega t)]e^{-\frac{t}{T_2}}, \tag{6.82}$$

$$M_z(t) = M_{eq} + [M_z(0) - M_{eq}]e^{-\frac{t}{T_1}}, \tag{6.83}$$

where $\omega = \gamma H$. The transverse magnetizations $M_{x,y} = M_z \sin(\theta_{tip})$ which generate the FID signal with amplitude S(t):

$$S(t) \propto \frac{dM_{x,y}(t)}{dt} = \omega M_z \sin(\theta_{tip}) \sin(\omega t + \phi_0) e^{-t/T_2}, \tag{6.84}$$

where ϕ_0 is related to how the pickup coil is oriented with respect to spin direction at the end of the RF pulse. This signal is used to evaluate the ^{3}He polarization after calibrating with either EPR or NMR.

6.6.2.2 Pulsed NMR Measurement

The JLab pulsed-NMR system setup is shown in Fig. 6-33. At the beginning, the gate generator (Model DS 345) sends out a TTL pulse with the timing window equals to t_{pulse}. The RF function generator (a) (Model DS 345) is triggered at the rising edge of the TTL pulse and output the RF pulse tuned at Larmor frequency (81 KHz) to the FID coil through the switch (a) (Model Mini-Circuits ZYSWA-2-50DR Coaxial Switch). The switches control the signal flow depends on whether the TTL signal voltage level is high or low. When the TTL signal is high, the switch (a) lets the

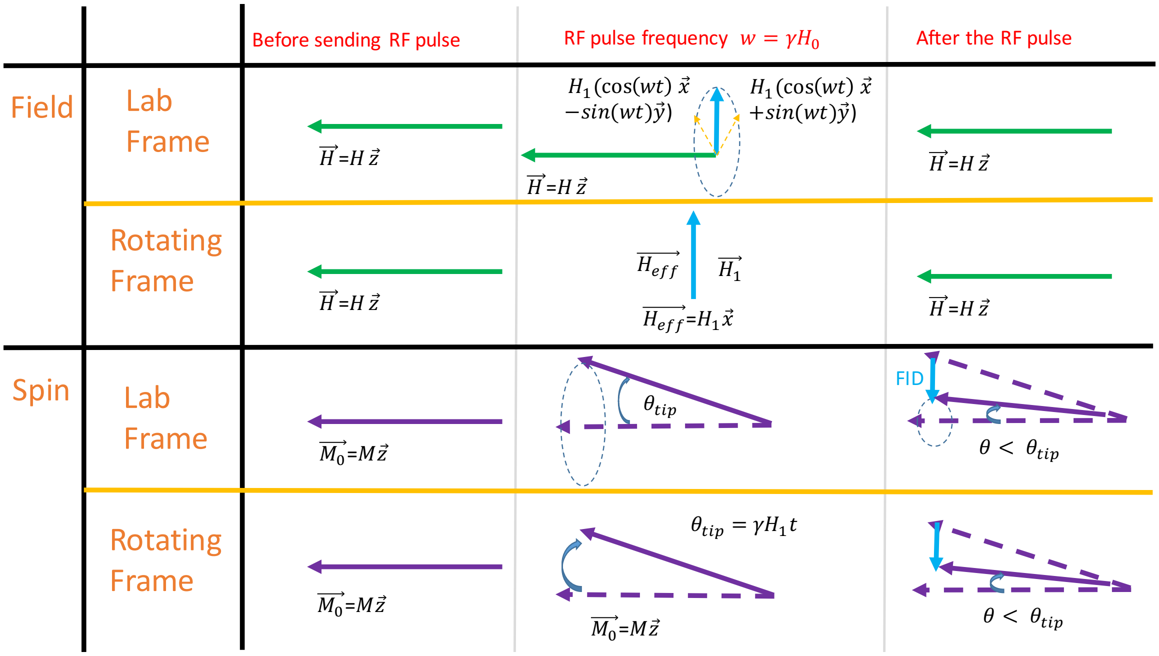

Figure 6-32: The field and magnetization change during the pulsed NMR measurement.

RF pulse pass through to the FID coil to tip away the ^{3}He spin while the switch (b) stops the RF going into the pre-amplifier (a) (Model SR560) to avoid damage; when the TTL signal is low, the switch (a) disconnects the FID coil from the RF function generator (a) to prevent noise while the switch (b) sends the FID signal from pulsed NMR coil to the pre-amplifier (a). The output from the pre-amplifier (a) is sent to a mixer (Model Mini-Circuits ZAD-8 Frequency Mixer) where the FID signal mixes with a signal from a reference RF generator (b) (Model DS345). The reference RF frequency is chosen to be the Larmor frequency $f_0 \pm \Delta f(\Delta f \simeq 200\text{Hz})$. Output from the mixer is sent into the preamplifier (b) to filter and boost the signal with frequency Δf. The oscilloscope is triggered by the falling edge of the TTL pulse and starts to record the output signal from the pre-amplifier (b). Fig. 6-34 shows a typical FID signal.

The pulsed-NMR results were cross-calibrated against NMR-AFP and EPR measurements made on all-glass target systems. Fig. 6-35 shows the ratio of amplitudes from pulsed NMR to NMR (both on target chamber) during a spin down measure-

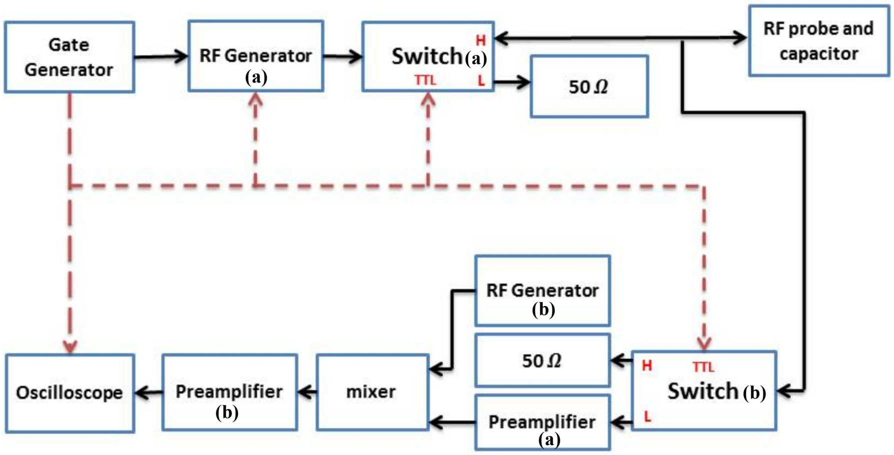

Figure 6-33: JLab pulsed-NMR system schematic.

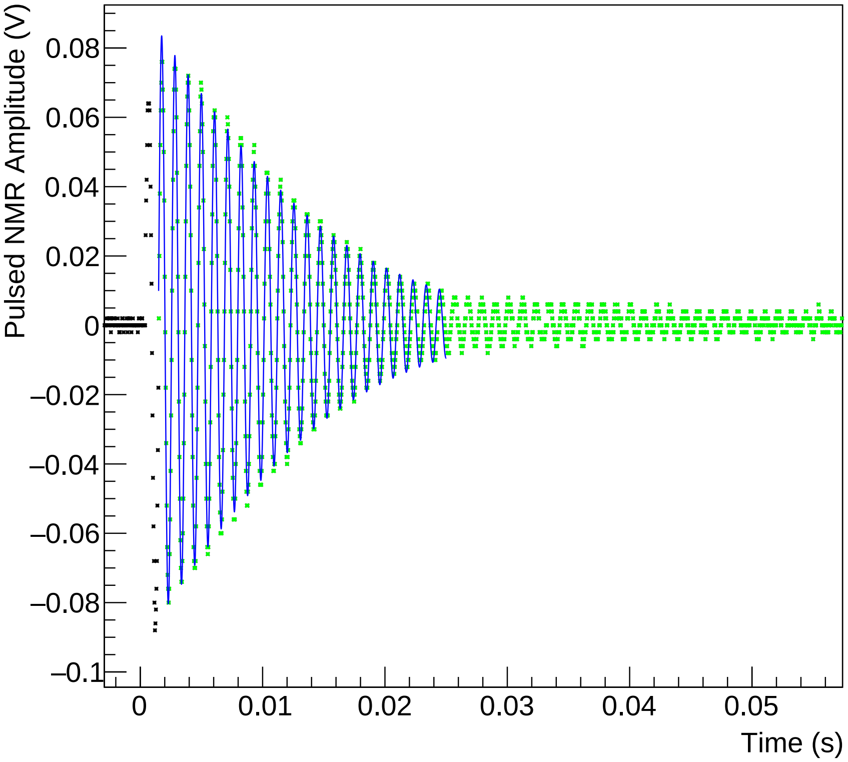

Figure 6-34: A typical FID signal. The blue curve are the fits using Eq. 6.84.

ment. The fitted ratio is 7.98 ± 0.07, which means the relative uncertainty of calibration constant is within 1%. Further systematic studies of the pulsed-NMR setup are currently underway.

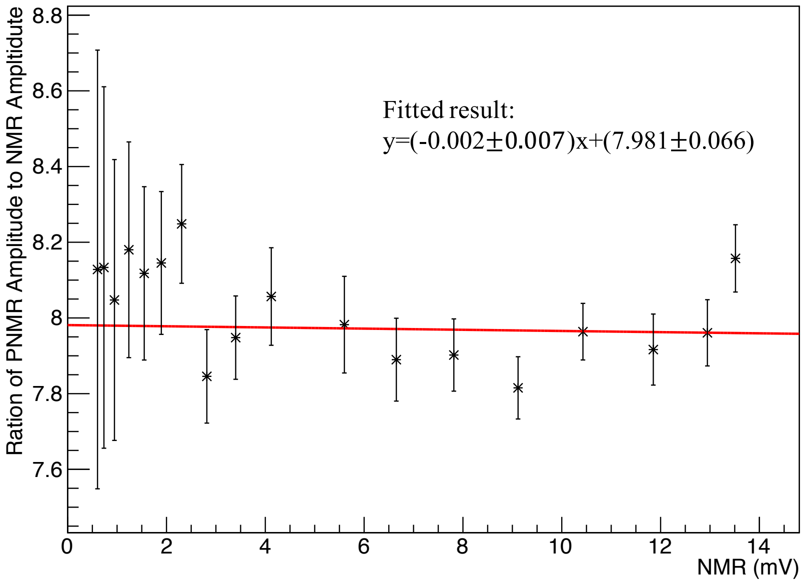

Figure 6-35: Ratio of Pulsed-NMR amplitude to NMR amplitude versus the NMR amplitude on cell Provotec-I at JLab in 2015. Both pNMR and NMR measured the polarization in target chamber.

6.6.3 Radiation Shielding

The polarized ^{3}He target is required to be able to handle at least 30 μA of electron beam for future 12 GeV experiments. A high beam current means more radiation damage to the pumping chamber, which will cause rupture of the cell. A radiation shielding study for the pumping chamber was performed using a Geant4 simulation. The polarized ^{3}He target setup is shown in Fig. 6-36.

The radiation study results are shown in Fig. 6-37. Doses corresponding to 350 hours of beam time were simulated for both the past Transversity experiment at 6 GeV [191, 192] and the future A_1^n-HallA[193] experiment at 12 GeV. For a convection

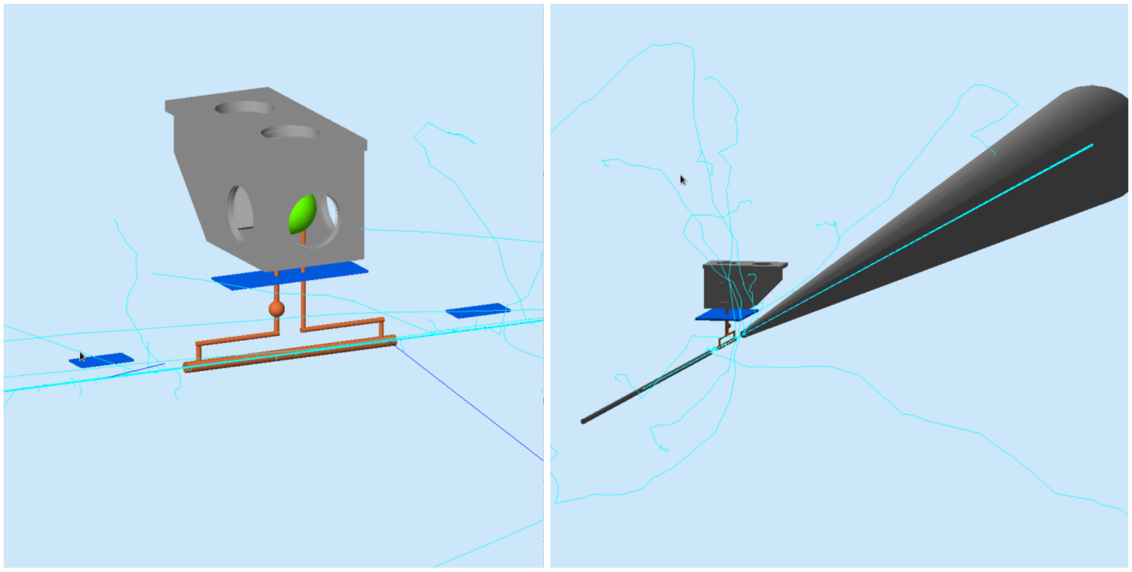

Figure 6-36: Simulation setup for radiation shielding study. The left plot shows the setup including the ^{3}He target, oven, collimators and a piece of shielding plate of lead, while the right plot shows the setup with the beam line.

cell with 25-cm long transfer tubes, the radiation damage is less than that of the diffusion cell utilized in the previous Transversity experiment.

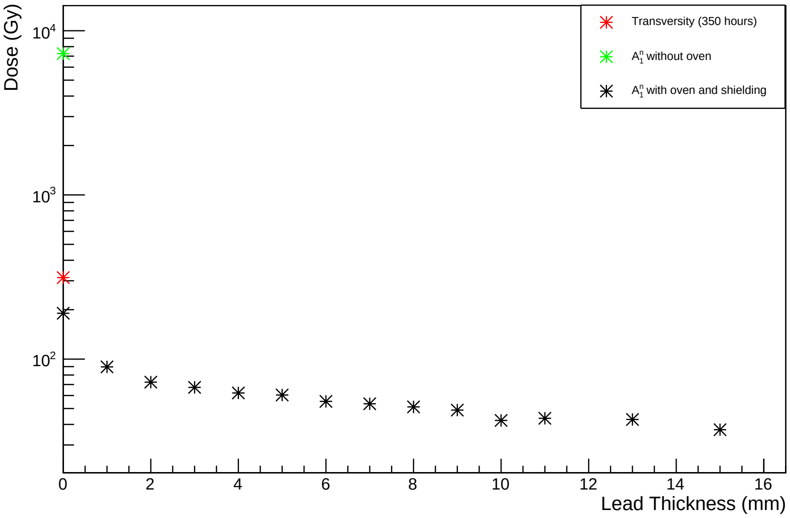

Figure 6-37: Dose on the pumping chamber due to radiation.

6.6.4 Masing effect

A high uniformity of the holding field is required to minimize the target depolarization. However, it was found that when the field gradient is reduced to less than $(10 - 15)$ mg/cm, masing effects[159] start when a particular polarization is reached, causing a significant drop in the ^{3}He polarization. The masing effect can be due to the nonlinear coupling between the ^{3}He spin and nearby coils. As the spins precess around the holding field, they introduce a small voltage in the nearby coils. This voltage will drive a current flow which induces a transverse RF field to tip the ^{3}He magnetization, then causes a larger induced current and in turn a larger transverse RF field. This effect was clearly observed with the FID coils in the target system, as shown in Fig. 6-38. The effect appeared (disappeared) with the connecting (disconnecting) of the FID coil whose Q value is tuned close to the Larmor frequency. To remove this masing effect, a pair of anti-Helmholtz was used to increase the field gradient. The anti-Helmholtz coils' axis was coincident with that of the holding field coils.

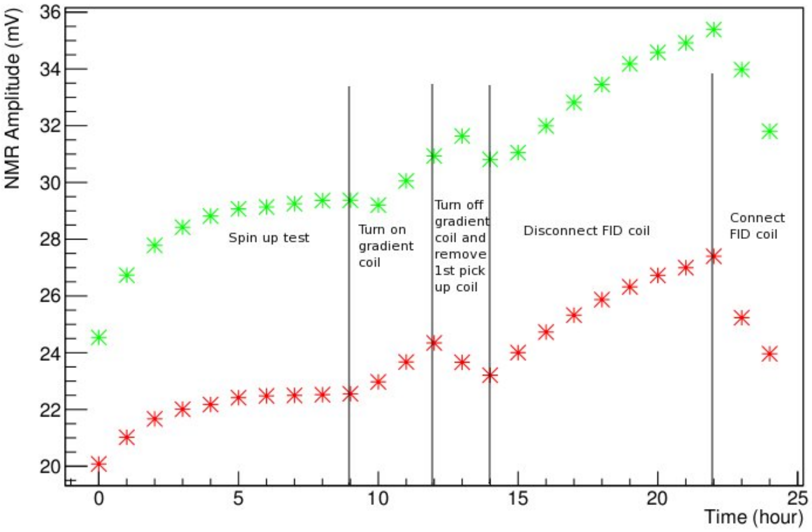

Figure 6-38: Masing effects for the ^{3}He system, test performed on cell Provotec-I in 2013.

6.7 Summary

The JLab polarized ^{3}He target had a world-record performance during the 6 GeV era. R&D activities are ongoing to upgrade the target for the 12 GeV program. Initial tests of the convection cells and the pulsed-NMR system have been made and proven successful. Full polarization tests and systematic studies are being studied further by two other UVa PhD students. The goal is to have the target system ready for the A_1^n experiment in Hall C in 2019.

Chapter 7

Polarized ^{3}He Performance in Tokamak Fuel Pellets

This chapter will discuss a possible application of polarized ^{3}He for future spin-polarized thermonuclear fusion. The work described here is to study the performance of polarized ^{3}He in inertial confinement fusion (ICF) polymer shells, including the polarization survival when ^{3}He gas permeates through the shell wall and the spin relaxation time T_1 after permeation. The purpose of such study is to prepare for a future demonstration experiment of spin-polarized fusion.

7.1 Introduction

Energy continues to be one of the leading problems the world is facing. Traditional fossil fuels have a limited supply and cause significant environmental issues. Renewable energy sources, such as solar and wind energy, have been developed fast in recent years and are commercially used at some occasions, but have their own limitations and are not suitable for large urban or industrial continuous use. Fission nuclear power plants, based on breaking a large nucleus into medium size ones, offer a great power but bring problems such as radioactive waste and occasionally even catastrophic Chernobyl or Fukushima Dai-ichi like accidents. An attractive approach to the energy problem is thermonuclear fusion, based on the union of two small nuclei to a larger one, which causes no air or radioactive pollution and no risk of uncontrolled energy release, holding the promise of a clean, sustainable, and powerful energy supply.

The following sections will introduce concepts of thermonuclear fusion, spin-polarized fusion and then present the performance study of polarized ^{3}He inside inertial confinement fusion (ICF) polymer shells (pellets).

7.2 Thermonuclear Fusion

7.2.1 Principles of Thermonuclear Fusion

Nuclear fusion is a reaction that combines light elements together to form heavier elements and often releases a large amount of energy because of the difference in the nuclear binding energy.

Nuclear binding energy is defined as the amount of energy necessary to break the nucleus apart into individual protons and neutrons. For a nucleus ${}^A_Z X$ with Z protons and $A - Z$ neutrons, the binding energy can be computed as:

$$BE_{nuclear} \quad = \quad \Delta mc^2 = \Big[Zm_p + (A-Z)m_n - M_X \Big] c^2. \tag{7.1}$$

where m_p is the proton mass, m_n is the neutron mass, and M_X is the nuclear mass of ${}^A_Z X$. Fig. 7-1 shows the binding energy per nucleon curve, BE/A. Such A-dependence of the nuclear binding energy can be interpreted using the liquid drop model, which describes the nucleus as a liquid drop due to its non-compressible feature, the limited range of the nuclear strong force ($\sim$ 1 fm), and including features such as Coulomb repulsion among protons. From Fig. 7-1, BE/A is clearly peaked at medium-A nuclei such as ^{56}Fe. For elements heavier than iron, such as uranium and plutonium, they release energy when fissioned into 2 or more smaller nuclei. While for elements lighter than iron, such as hydrogen and helium, they release energy when fused to a more stable nucleus. The energy released in fusion is about 3.5 MeV/nucleon, much higher than nuclear fission (1 MeV/nucleon) and fossil fuels (less than 10^{1-2} eV/nucleon).

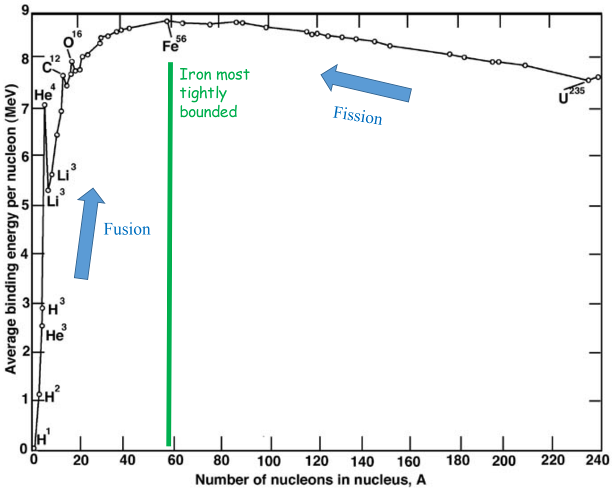

Figure 7-1: The binding energy per nucleon curve. Plot reproduced from[194].

To describe the energy released in nuclear reactions, we define the Q-value of a binary reaction $A + B \rightarrow C + D + \ldots$, as:

$$Q = (m_A + m_B - m_C - m_D - \ldots)c^2. \tag{7.2}$$

The following is a list of a few favorable nuclear fusion reactions for energy production:

$$\mathrm{D} + \mathrm{D} \rightarrow \mathrm{T} + p, \quad Q = 4.03 \text{ MeV} \tag{7.3}$$

$$\mathrm{D} + \mathrm{D} \rightarrow {}^{3}\mathrm{He} + n, \quad Q = 3.27 \text{ MeV} \tag{7.4}$$

$$\mathrm{D} + \mathrm{T} \rightarrow \alpha + n, \quad Q = 17.59 \text{ MeV} \tag{7.5}$$

$$\mathrm{D} + {}^{3}\mathrm{He} \rightarrow \alpha + p, \quad Q = 18.35 \text{ MeV} \tag{7.6}$$

$$\mathrm{T} + \mathrm{T} \rightarrow \alpha + 2\, n, \quad Q = 11.33 \text{ MeV} \tag{7.7}$$

$${}^{3}\mathrm{He} + {}^{3}\mathrm{He} \rightarrow \alpha + 2\, p, \quad Q = 12.86 \text{ MeV} \tag{7.8}$$

$$\mathrm{T} + {}^{3}\mathrm{He} \rightarrow \alpha + p + n, \quad Q = 12.1 \text{ MeV} \tag{7.9}$$

$$\mathrm{T} + {}^{3}\mathrm{He} \rightarrow \alpha + \mathrm{D}, \quad Q = 9.5 \text{ MeV} \tag{7.10}$$

$$p + {}^{6}\mathrm{Li} \rightarrow \alpha + {}^{3}\mathrm{He}, \quad Q = 4.02 \text{ MeV} \tag{7.11}$$

$$p + {}^{11}\mathrm{B} \rightarrow 3\, \alpha, \quad Q = 8.68 \text{ MeV} \tag{7.12}$$

where D stands for $^2_1$H (deuteron), H for $^3_1$H (triton), α for ^{4}He nucleus, and p (n) for the proton (neutron). The reaction D + T$\longrightarrow\alpha+n$ is the most favorable reaction for fusion reactors. This reaction holds several attractive features including large energy release, easily available fusion fuel, and a larger cross section over other reactions (especially at temperature around 10 keV).

7.2.2 Conditions of Thermonuclear Fusion

In the Standard Model of particle physics, the strong nuclear force, described by Quantum Chromodynamics (QCD), is one of the four fundamental forces of nature, with the others being gravity, the electromagnetic force, and the weak nuclear force. Strong nuclear force is the interaction between particles (quarks) that carry color charge. It is mediated by massless gluons and binds quarks together to form hadrons, including mesons ($q\bar{q}$) and baryons (qqq). Quarks, gluons and their dynamics are mostly confined within hadrons due to color-confinement. Outside of nucleons, the strong interaction appears as a residue force, remains outside nucleons which is what we commonly call the strong nuclear force. This strong nuclear force is responsible for the nuclear binding energy. According to H. Yukawa, the nucleon-nucleon force can be modeled as an exchange force mediated by massive mesons (Nobel Prize 1949)[195], and hence has a very short range. As shown in Fig. 7-2, the one pion exchange dominates the force in separation distance up to a few fm; and the closer range (1 fm< r <2 fm) receives significant contributions also from the exchange of multi-pions and heavy mesons (ρ, ω, and σ). The force beyond a few fm is zero. For distances below 1 fm, there is a very strong repulsive force possibly due to overlapping of the quark wavefunction within different nucleons. And some approximate QCD lattice simulations reproduced the empirical form of this potential recently[196, 197].

For nuclei x and y to fuse, they must be extremely close together in order for the attractive nuclear force to happen. However, there is also the repulsive Coulomb force preventing the positively charged nuclei to approach each other. In contrast to the nuclear force, the electric force falls off inversely as the square of the distance and does not diminish beyond a certain distance. The Coulomb barrier between the two

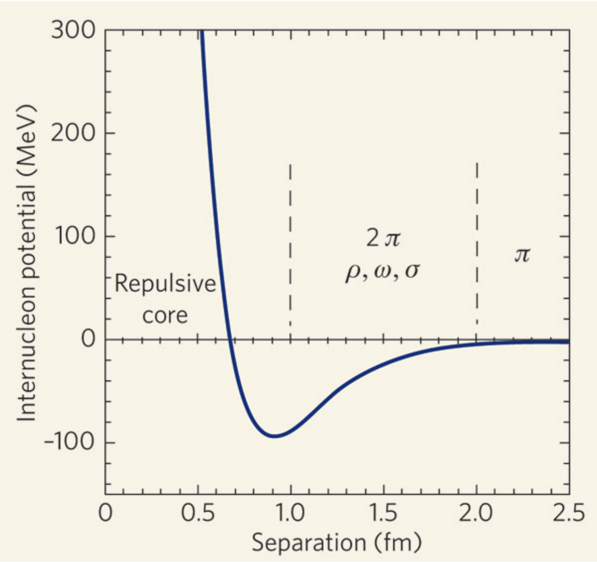

Figure 7-2: The nuclear force between nucleon and nucleon. Plot reproduced from [196].

reacting particles x and y separated at a distance d is

$$V_c = \frac{e^2 Z_x Z_y}{4\pi\epsilon_0(R_x + R_y + d)}, \tag{7.13}$$

where Z_x (Z_y) is the atomic number of x (y), ϵ_0 is the vacuum permittivity, R_x (R_y) is the radius of the nucleus and can be expressed as the function of A, the total number of nucleons:

$$R = 1.2A^{1/3}\text{ fm}. \tag{7.14}$$

For D-T fusion, Eq. 7.13 gives the calculated Coulomb barrier to be around 0.44 MeV at $d = 0$, and thus fusion could happen as long as the two nuclei are within ≈ 2 fm of each other, where the strong nuclear force can take over.

The barrier can be overcome in two ways in principle. The first way is through beam target scattering, but the cross section σ is too small to be useful. The second way is to heat the material so that the thermal energy of the nuclei can overcome the Coulomb barrier. Typically, this means the atoms are ionized and we deal with plasma. In some way this is also scattering, but the particles move back and forth, rather than beam-target scattering where beam particles scatter once or not at all, and are lost right away. For particles in a gas at temperature T, the probability of the thermal velocity between v and $v + dv$ can be described by the Maxwell-Boltzmann distribution:

$$p(v) \quad \propto \quad v^2 e^{-\frac{mv^2}{2kT}} \tag{7.15}$$

where k is the Boltzmann constant, m is the particle mass. The kinetic energy corresponding to the most probable speed is kT. In the case of D-T reaction, the energy requirement for $kT \geq V_c = 0.44\text{MeV}$ gives $T \approx 10^9$ K. In reality, fusion can happen at $T < 10^9$ K because of two mechanisms. One is that a significant population of particles is in the high energy tail of Eq. 7.15 with energy larger than kT. The other is due to quantum tunneling that the nuclei do not have to have energy $E > V_c$ to overcome the coulomb barrier completely.

The reaction cross section σ is a measure of the probability for fusion to happen and is a function of the relative velocity of the two reactant nuclei. Consider the velocity distribution, the average reaction rate (fusions per volume per time) is

$$f \quad = \quad n_x n_y \langle v\sigma \rangle, \tag{7.16}$$

where $\langle \sigma v \rangle$ is called reactivity and is expressed as

$$\langle \sigma v \rangle \quad = \quad \int p(v)\sigma(v) v dv. \tag{7.17}$$

Fig. 7-3 shows the average reaction rate for several commonly considered fusion reactions. Fusion reaction rates increase rapidly with the plasma temperature first and then gradually drop off. The D-T reaction rate peaks at a lower temperature around 70 keV ($\approx 8 \times 10^8$ K) and reaches a higher value compared with other reactions.

The energy released per unit of volume from fusion is

$$E_f \quad = \quad n_x n_y \langle v\sigma \rangle Q\tau, \tag{7.18}$$

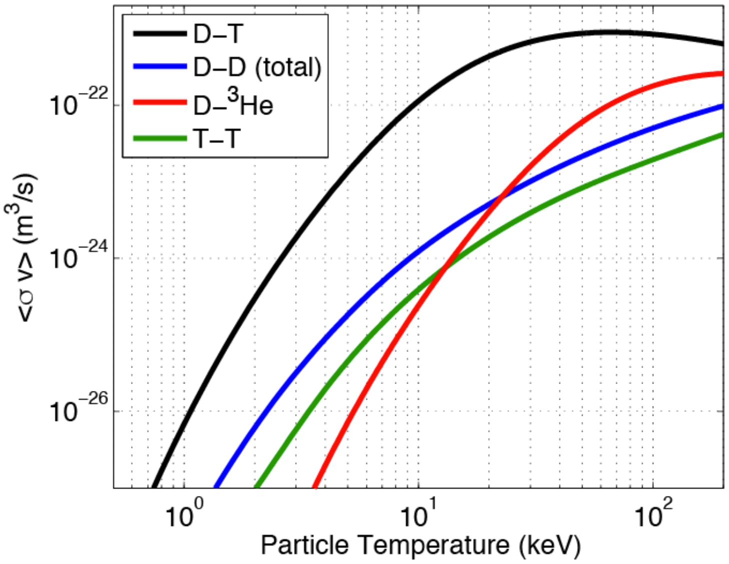

Figure 7-3: The fusion reaction rate versus temperature. Plot reproduced from [198].

where τ is the plasma confinement time. The thermal energy per unit of volume required for heating the plasma is

$$E_p = 3(n_x + n_y)kT = 3nkT, \tag{7.19}$$

where $n \equiv n_x + n_y$ is the total ion density.

The ignition point is defined as when the fusion power generated can maintain the plasma temperature without any external source of energy, at which point the fusion becomes self-sustaining. We consider fusion heating to be provided only from deposited energy in the plasma from charged particles. The ignition point can be achieved if the charged particle heating is enough to heat the plasma. Assuming equal ion density between the two species, i.e., $n_x = n_y = n/2$, Eq. 7.18 and Eq. 7.19 gives

$$n\tau > \frac{12kT}{\langle v\sigma\rangle Q_{ch}}, \tag{7.20}$$

where Q_{ch} is the energy carried by charged particle in the fusion final state. This is called the Lawson criterion for ignition.

For a D-T reactor, the fusion heating is from the deposited energy by α particles with Q_{ch}= 3.5 MeV. The right side $\frac{12kT}{\langle v\sigma\rangle Q_{ch}}$ minimizes near $kT = 25$ keV ($\approx 3\times 10^{8}$ K), so $n\tau$ needs to at least satisfy

$$n\tau \quad > \quad \left(\frac{12kT}{\langle v\sigma\rangle Q_{ch}}\right)_{min} \approx 1.5\times 10^{20}\frac{s}{m^3} \tag{7.21}$$

for the D-T interaction to be self-sustaining. The approaches and status of the thermonuclear fusion will be discussed in the following section.

7.2.3 Status of Thermonuclear Fusion

The Lawson criterion for ignition is achieved in stars and also by man-made hydrogen bombs on earth, as shown in Fig. 7-4. However, in a laboratory, it is an extremely challenging condition to satisfy for the controlled nuclear fusion. There are two main approaches being studied: magnetic confinement and inertial confinement. The first method uses strong magnetic fields to confine the hot plasma in a region thermally insulated from the surroundings, and is applied in facilities worldwide including the Joint European Torus (JET) and the Mega Amp Spherical Tokamak (MAST) in UK, the Tokamak Fusion Test Reactor (TFTR) and DIII-D National Fusion Facility (DIII-D) in the USA, the Japan Torus-60 (JT-60) in Japan, and the Experimental Advanced Superconducting Tokamak (EAST) in China. The second confinement method involves compressing a small pellet containing fusion fuel to extremely high densities using strong lasers or particle beams, and is used in the National Ignition Facility (NIF) in the USA and the Laser Mégajoule (LMJ) in France.

Despite decades of research, self-sustained energy production has not been reached in any of the fusion reactors built so far. The major industrialized nations of the world are currently engaging in an unprecedented effort to build the first prototype 500 MegaWatts Tokamak, the International Thermonuclear Experimental Reactor (ITER), with the goal of demonstrating the scientific feasibility of fusion power, as shown in Fig. 7-5. ITER is now under construction in Cadarache, France. Then,

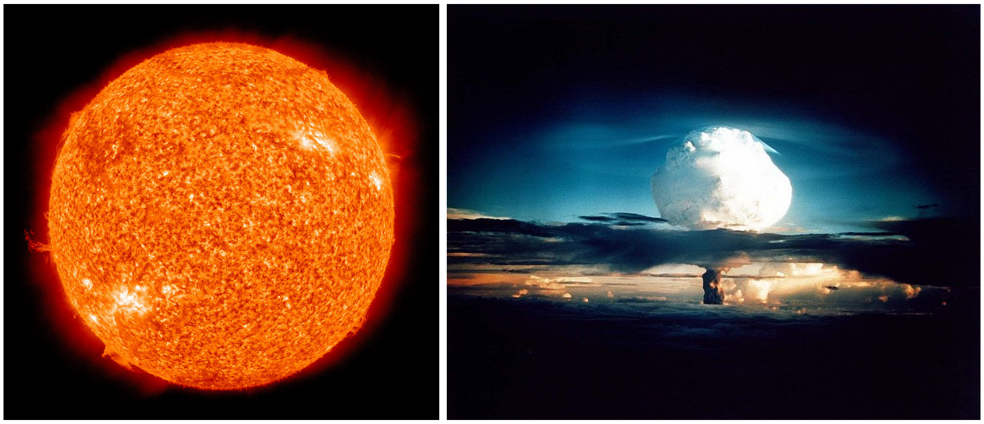

Figure 7-4: Nuclear fusion generates the power for the sun (left) and hydrogen bombs (right). Plot reproduced from [199].

the first demonstration power plant, DEMOnstration Power Station (DEMO), could start the construction shortly after the ITER full-power experiment (by year 2030) and start generating net electricity into the grid by 2050, according to the European Roadmap[200].

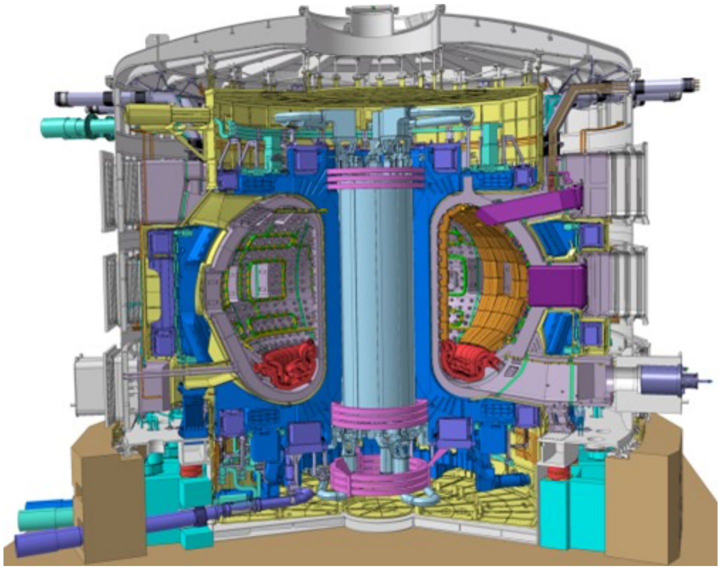

Figure 7-5: ITER Tokamak is currently being built in southern France in the framework of a collaboration between China, Europe, India, Japan, Korea, Russia and the USA. It will use superconducting coils. Its major radius R_0 is around 6.2 m, minor radius is 2.0 m, and its plasma volume is 820 m^3. The toroidal field at R_0 is 5.3 T. Plot reproduced from [200].

7.3 Spin Polarized Fusion

The idea of spin-polarized fusion was proposed as early as 1980s[19]. It was predicted that the fusion cross section between deuterium (D) and tritium (T) is boosted 50% when the fuel is fully polarized along the local magnetic field, the same principle also applies to its isospin-mirrored process, the D-^{3}He fusion. These two reactions are shown in Fig. 7-6.

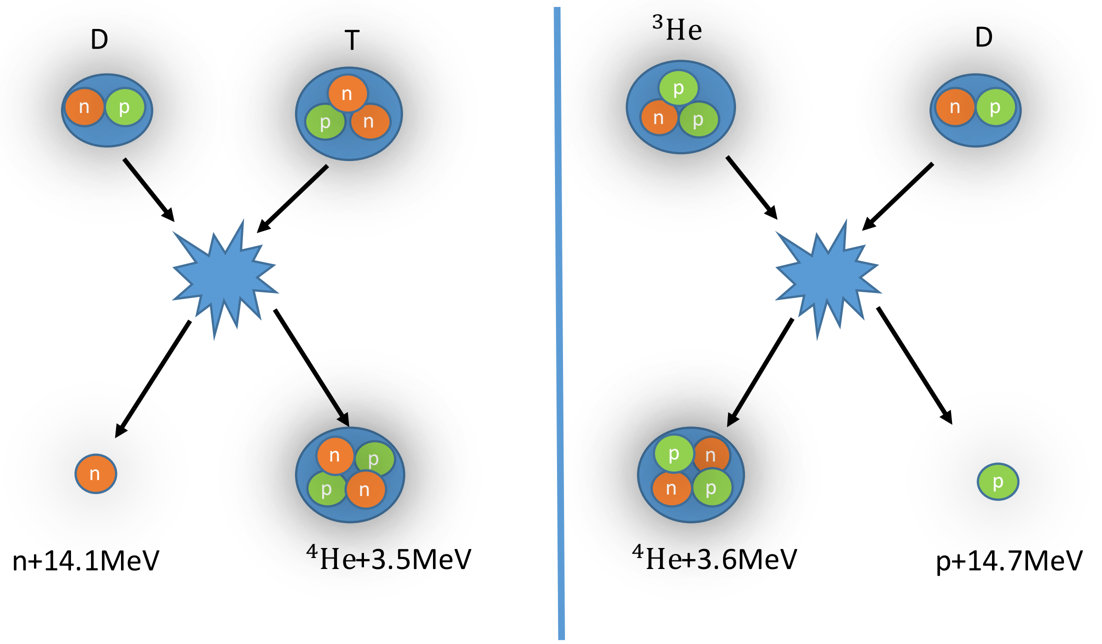

Figure 7-6: Fusion reactions D+T→α+n (left) and D+^{3}He→α+p (right). The released energy arises from the decrease in the total rest mass of particles. The resulting kinematic energy of each final state is shown.

7.3.1 Principles of Spin Polarized Fusion

At the low energy, the D-T reaction cross section arises primarily (about 99%) by forming an intermediate resonance state of ^{5}He, at 107 keV above the rest mass of the unbound D and T:

$$\mathrm{D} + \mathrm{T} \rightarrow^5 \mathrm{He}^* \rightarrow \alpha + n. \tag{7.22}$$

This excited state of ^{5}He has spin J=3/2 and even parity ($J^\pi = \frac{3}{2}^+$). If the reacting D-T system has a total angular momentum J=3/2 and even parity, the excited state can be formed with high probability and the fusion occurs; otherwise the reaction cannot happen in principle and in reality the probability is two orders smaller in magnitude. For the typical fusion reactors at the keV level, the reaction is dominated by the s-wave process, so the angular momentum must be supplied by the spin of D (spin 1/2) and T (spin 1) nuclei. There are six ways to combine the spin of D and T, and 2/3 of them form the J=3/2 state and 1/3 of them form the J=1/2 state, which implies that in an unpolarized plasma only 2/3 of nuclei can undergo fusion. Thus, compared with the unpolarized plasma, aligning all D and T ions' spins parallel to each other can enhance the fusion rate by 50%. In a Tokamak, this can be achieved by aligning both spins parallel to the toroidal field.

Assuming the field is along the z direction, the nuclear cross section for D+T$\longrightarrow\alpha$+n averaged over all possible spin orientations of D and T can be approximated as[18, 204]

$$\langle \frac{d\sigma(\theta)}{d\theta} v\rangle \quad = \quad \frac{1}{4\pi}\langle\sigma_0 v\rangle W(\theta). \tag{7.23}$$

Here $\frac{1}{4\pi}\langle\sigma_0 v\rangle$ is the isotropic rate observed in an unpolarized case and $W(\theta)$ is a purely angular function and can be expressed as

$$W(\theta) = 1 - \frac{1}{2}P_D^V P_T + \frac{1}{2}[\,3P_D^V P_T \sin^2\theta + \frac{1}{2}\ P_D^T(1 - 3\cos^2\theta)] \tag{7.24}$$

where $P_D^V = N_{+1} - N_{-1} \in [-1, 1]$ is the deuteron vector polarization, $P_D^T = N_{+1} + N_{-1} - 2N_0 \in [-2, 1]$ is the deuteron tensor polarization, $P_T = N_{+1/2} - N_{-1/2} \in [-1, 1]$ is the triton polarization, θ is the initial polar (pitch) angle of the charged fusion products with respect to the local magnetic field. For unpolarized plasma, $W(\theta) = 1$.

If the spin of D is parallel (↑↑)or anti-parallel (↑↓) to the spin of T along the magnetic field, $W(\theta)$ can be written as

$$\begin{aligned} W(\theta)_{\uparrow\uparrow} &= \frac{9}{4}\sin^2\theta, \quad \text{and} && (7.25) \\ W(\theta)_{\uparrow\downarrow} &= \frac{1}{4}(3+\cos^2\theta). && (7.26) \end{aligned}$$

From Eq. 7.25 and Eq. 7.26, an additional advantage of spin-polarized fusion is that the emitted α particles have a skew distribution in angle, which could be used to improve the confinement for α heating.

The total cross section could be obtained by integrating Eq. 7.24 over θ, the result can be written as a function of polarization vectors:

$$\langle \sigma v \rangle = \langle \sigma_0 v \rangle \left\{ 1 + \frac{1}{2}\vec{P}_D^V \cdot \vec{P}_T \right\}. \tag{7.27}$$

It is obvious that the reaction rate is increased by 50% if initial spins of D and T are aligned parallel to each other.

The increase in the reaction rate will increase the α particle production. For a large-scale Tokamak such as ITER which can contain all the α products, the increased α particle production can raise the temperature of the plasma core through collisional damping on electrons, which then further increase the reaction rate. These improvements can possibly lead to a higher fusion gain and achieve a more economical running condition.

Spin-polarized fusion requires that the polarization of the fuel persists in the tokamak long enough for fusion to occur. Many depolarization mechanisms, such as magnetic gradient and collisions, have been explored and polarization survival is expected theoretically[19]. However, polarization survival in an actual plasma environment has never been tested. A plan was developed to perform a direct measurement of the spin dependence of the D+^{3}He→α+p reaction in the plasma, see more details in the next section.

7.3.2 Spin-Polarized Fusion D-^{3}He in the Tokamak

The polarization survival test is a crucial step towards future spin-polarized fusion, but a direct test has not been carried out due to lack of technology to produce and handle polarized material. However, this situation has changed recently and a direct polarization survival test is now becoming practically possible.

The highly-polarized D (in the form of HD molecule) has been developed for nuclear and particle experiments[17, 201], and highly-polarized ^{3}He gas is routinely produced for both medical imaging applications and studies of nucleon spin structure[159, 173]. Polymer shells (pellets) have been extensively developed for the inertial confinement fusion (ICF) [202] and can be used to contain polarized material[18]. Cryogenic injection guns have been demonstrated to deliver ICF pellets of cryo-temperature into the Tokamak plasma core with high efficiency[203]. Therefore, the polarization survival can now be tested using D+^{3}He→α+p in the plasma. This reaction is an isospin-mirror reaction of D+T→α+n. Their intermediate states ^{5}He (from D-T) and ^{5}Li (from D-^{3}He) have nearly identical low-energy structures and the reaction processes involve identical spins and the same nuclear physics principles. The fully polarized D and ^{3}He fusion reaction rate can be increased (or decreased) 50% when they are aligned parallel (or anti-parallel) with respect to each other, just as for the D-T case. The lessons learned from polarized D-^{3}He fusion can be directly applied to spin-polarized D-T fusion.

An approach was developed to perform a direct test in the DIII-D tokamak in San Diego as follows[18, 204, 205]:

- Conduct R&D on polarized ^{3}He with existing University of Virginia facilities. The ^{3}He gas needs to be polarized in a glass cell first by using the spin-exchange optical pumping method discussed in Sec. 6.2.2 and then permeates into ICF pellets. Fig. 7-7 shows one particular ICF pellet made of Gas-Discharge-Polymer (GDP), sitting inside a 3mm inner diameter glass tube. The GDP pellet is made of $C_2(CH_3)H_2$, is about 1.8 mm in diameter and (for this particular shell) is 0.014 mm in wall thickness. A total of 12 shells were supplied by General Atomics

(GA)[202] for our study. The permeation time constant for ^{3}He to diffuse inside this pellet is around 240 s at 295 K, but increases rapidly with decreasing temperature, and reaches about 300 years at the liquid N$_2$ temperature (77 K) as shown on the right plot of Fig. 7-7. Therefore, the pellet can be sealed by cooling down with liquid N_2. Depending on how long the polarization remains within the pellet, a ^{3}He polarizer may need to be built locally at DIII-D.

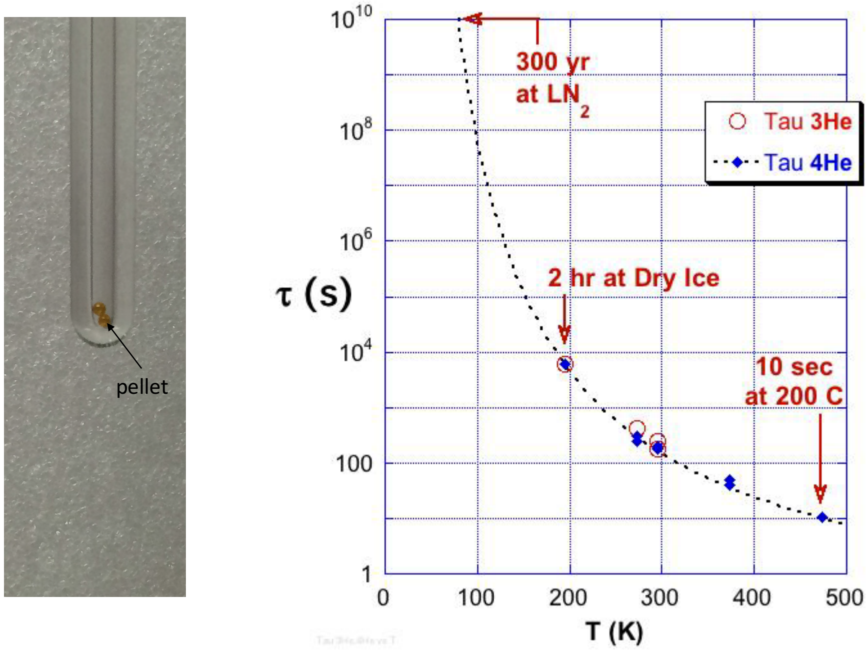

Figure 7-7: A GDP pellet (1.8 mm in diameter and 0.014 mm in wall thickness) inside a glass tube with 3 mm inner diameter (left) and the permeation time constant measured by the HDice group at JLab (right)[18, 204].

- Produce polarized deuterium with existing JLab HDice facility[17]. About 200-400 atm unpolarized HD will diffuse into a ICF pellet and then is cooled down to reach solid state. The D can be polarized to about 40% in the pellet using the polarizing technique of nuclear physics's HDice target[201]. These polarized HD pellets can be stored in a cryostat and shipped to DIII-D.

- Inject HD and ^{3}He pellets using the cryo-gun developed by Oak Ridge National Laboratory (ORNL) with alternating spin alignments into the high temperature plasma at DIII-D and then detect the proton yield difference.

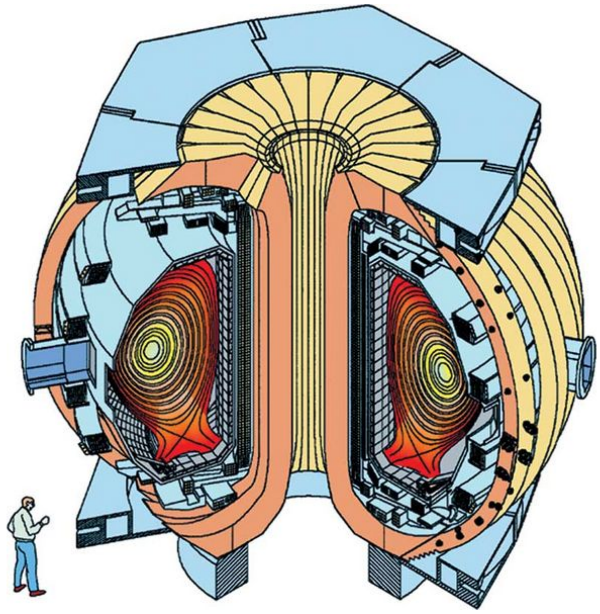

Figure 7-8: DIII-D tokamak in San Diego operated by GA[206]. Its a research-scale tokamak with room temperature coils. Its major radius R_0 is 1.67 m, minor radius is 0.67 m, plasma volume is 30 m^3. The toroidal field at R_0 is 2.1 T. Plot reproduced from [207].

Fig. 7-8 shows the structure of DIII-D. Assuming an anticipated polarization of 40% for D and 65% for ^{3}He, the expected proton yields from Eq. 7.28 for parallel and anti-parallel configurations are

$$\langle \sigma v \rangle_{\uparrow\uparrow} = 1.13 \langle \sigma_0 v \rangle, \tag{7.28}$$

$$\langle \sigma v \rangle_{\uparrow\downarrow} = 0.87 \langle \sigma_0 v \rangle, \tag{7.29}$$

so the proton yield ratio of anti-parallel to parallel spin alignment is

$$\frac{\langle \sigma v \rangle_{\uparrow\downarrow}}{\langle \sigma v \rangle_{\uparrow\uparrow}} = 0.77. \tag{7.30}$$

Considering the DIII-D acceptance efficiency, the predicted proton yield is shown in Fig. 7-12. The left plot shows the spatial distribution of the predicted fusion rate density for the D-^{3}He reaction assuming unpolarized fuels (scaled from $^2_1\text{D} -^2_1 \text{D}$

reaction with DIII-D Shot 96369). The right plot shows the predicted yields ratio along the inner wall of the DIII-D vacuum vessel. The predicted ratio holds a strong deviation from 1 for a large range of wall locations. A systematic study in [18, 204, 205] showed that 4 shots in each spin direction are needed to reach a 5σ significance if assuming a 8% systematic shot-to-shot variation. For reference, the typical neutron production rate varied less than 10% between shots for the past ${}^2_1\mathrm{D} -{}^2_1\mathrm{D}$ fusion experiments at ion temperature 8 keV in the DIII-D tokamak[205].

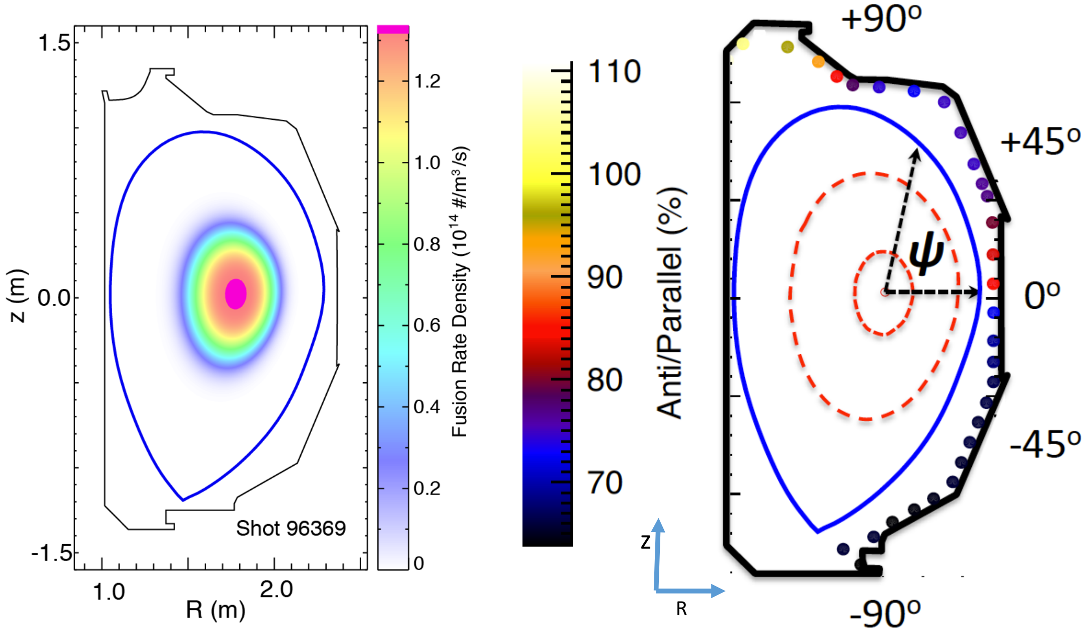

Figure 7-9: Predicted results for D-^{3}He reaction in DIII-D. The left plot shows the spatial distribution of the predicted proton rate density for the D-^{3}He reaction assuming unpolarized while the right shows the predicted ratio in the proton rate of anti-parallel to parallel along the inner wall of the DIII-D vacuum vessle. Plot reproduced from [18, 204, 205].

In this approach, one condition that must be satisfied is that the ^{3}He gas polarization must survive permeation of the GDP pellet wall and the polarization decay time must be sufficiently long enough to allow the pellet to be injected into the plasma. However, there exists no data on the ^{3}He performance in GDP pellets. The performance study of ^{3}He in the pellet is now actively pursued by a UVa-JLab team using MRI and the details are discussed below.

7.4 MRI Methods

The Medical Resonance Imaging (MRI) is based on a similar principle as the pulsed NMR polarimetry discussed in Sec. 6.6.2.2, but is much more sophisticated to achieve the multidimensional imaging[208].

7.4.1 Multidimensional Space Imaging

From Sec. 6.6.2.2, the FID signal S(t) for one voxel (or pixel) can be expressed as

$$S(t) = Ae^{i\omega_0 t}e^{-t/T_2}, \tag{7.31}$$

where $\omega_0 = 2\pi f_0$ is the Larmor frequency, T_2 is the transverse spin relaxation time constant, A is a constant factor accounts for the transverse magnetization after the RF pulse, the coil detection efficiency, and the system gain.

Now consider imaging in space and ignore the exponential time decay term first (the exponential time decay term will be discussed in Sec. 7.4.3). For the 1D case, with spin density $\rho(z)$ along the holding field direction $\hat{z}$ and assuming A is constant, the integrated signal is

$$S(t) = A\int_{-\infty}^{\infty} \rho(z)e^{i\omega_0 t}dz. \tag{7.32}$$

If a small linear gradient $G_z = dB_z/dz$ is applied along z direction after the RF pulse, the magnetic field experienced by nuclei at z is

$$B_z = B_0 + zG_z \tag{7.33}$$

and the corresponding precessional frequency is

$$\omega(z) = \gamma(B_0 + zG_z), \tag{7.34}$$

where γ is gyromagnetic ratio of the nuclear species (here means ^{3}He). Eq. 7.32 then becomes

$$S(t) = A \int_{-\infty}^{\infty} \rho(z) e^{i\omega_0 t + i\gamma G_z z t} dz, \tag{7.35}$$

where $\omega_0 = \gamma B_0$. Define $k_z \equiv \gamma G_z t/2\pi$, Eq. 7.35 can be rewritten as

$$S(t) = s(k_z) = A \int_{-\infty}^{\infty} \rho(z) e^{i2\pi(f_0 t + k_z z)} dz. \tag{7.36}$$

One can see that the signal $s(k_z)$ is the Fourier transform of $\rho(z)$. So the spin density $\rho(z)$ can be extracted with the reverse Fourier transform as

$$\begin{aligned} \rho(z) &= e^{-i2\pi f_0 t} \frac{1}{2\pi A} \int_{-\infty}^{\infty} s(k_z) e^{-i2\pi k_z z} dk_z \\ &\propto \frac{1}{2\pi} \int_{-\infty}^{\infty} s(k_z) e^{-i2\pi k_z z} dk_z \\ &= FFT^{-1}[s(k_z)]. \end{aligned} \tag{7.37}$$

Now consider the 3D case, the gradient

$$\vec{G} = \frac{dG_z}{dx}\hat{x} + \frac{dG_z}{dy}\hat{y} + \frac{dG_z}{dz}\hat{z} = G_x\hat{x} + G_y\hat{y} + G_z\hat{z} \tag{7.38}$$

is superimposed on the main magnetic field, and can point in any direction, causing the z component of the total magnetic field to vary linearly along that direction:

$$B(x, y, z) = B_0 + \vec{r} \cdot \vec{G} = B_0 + xG_x + yG_y + zG_z. \tag{7.39}$$

Then Eq.7.36 and Eq. 7.37 can be extended to 3D as

$$S(t) = s(\vec{k}) = A \int_{-\infty}^{\infty} \rho(\vec{r}) e^{i2\pi(f_0 t + \vec{k}\cdot\vec{r})} d\vec{r} \tag{7.40}$$

$$\rho(\vec{r}) \propto FFT^{-1}[s(\vec{k})]. \tag{7.41}$$

where $\vec{k} = \gamma\vec{G}t/2\pi$ defines the so-called “k-space" and $s(\vec{k})$ is usually referred as the “k-space data”.

In a general case, the applied gradient pulse $\vec{G}$ may be time dependent: $\vec{G}(t)$. Following the same procedure, the signal $S(t)$ and spin density $\rho(\vec{r})$ can be related as

$$\begin{aligned} S(t) = s(\vec{k}) &= A\int_{-\infty}^{\infty}\rho(\vec{r})e^{i2\pi f_0 t + i\gamma\int_0^t \vec{G}\cdot\vec{r}dt'}d\vec{r} \\ &= A\int_{-\infty}^{\infty}\rho(\vec{r})e^{i2\pi(f_0 t+\vec{k}\cdot\vec{r})}d\vec{r} \end{aligned} \tag{7.42}$$

$$\rho(\vec{r}) \propto FFT^{-1}[s(\vec{k})]. \tag{7.43}$$

with $\vec{k}$ the time integral of the applied gradient:

$$\vec{k} = \frac{\gamma}{2\pi}\int_0^t \vec{G}(t')dt'. \tag{7.44}$$

According to Eq. 7.42 and Eq. 7.43, the MRI measures the Fourier components of the image in the k-space by sampling the NMR signal in the presence of the gradient pulse $\vec{G}(t)$. The image of the spin distribution is recovered by taking the inverse Fourier transform of the k-space data.

To obtain k-space data in 1D, one can first apply a RF excitation, then apply 1D gradient $G_z(t)$ and sample the FID signal at the same time (typical sampling duration $\ll T_2$ to avoid the relaxation effect). For a 2D k-space ($k_z \times k_x$), one can apply multiple excitations by keeping gradient $G_z(t)$ the same but with different gradient $G_x(t)$ in the x direction thus producing discrete k_x-space data. This is similar for the 3D case. An image acquired by this technique is often referred as an projection image.

In practice, the discrete k-space data are recorded from the detectors, which form a vector for 1D imaging and a matrix for 2D or 3D cases. For the frequently used 2D space imaging, the image of spin distribution is reconstructed using discrete Fourier transform:

$$\rho(m\Delta x, n\Delta y) = \frac{1}{N_x N_y}\sum_{p=0}^{N_x-1}\sum_{q=0}^{N_y-1} s(p\Delta k_x, q\Delta k_y)e^{2\pi i\frac{mp}{N_x}}e^{2\pi i\frac{nq}{N_y}}. \tag{7.45}$$

where N_x (N_y) is the number of points sampled along the k_x (k_y) directions, Δx (Δy)

is the resolution of the reconstructed image which is related to the k-space range as

$$\Delta x = \frac{1}{N_x \Delta k_x} \tag{7.46}$$

$$\Delta y = \frac{1}{N_y \Delta k_y}. \tag{7.47}$$

7.4.2 Slice-selected Imaging

Slice-selected imaging acquires a series of 2D slices through the area of interest with well-defined orientation thickness[209]. The selective RF pulse is applied at a frequency ω_0 with bandwidth $\pm\Delta\omega$. Nuclei, whose resonance frequency is between $\omega_0 - \Delta\omega$ and $\omega_0 + \Delta\omega$, are tipped away from the holding field to generate the FID signal while nuclei outside of the frequency range are not affected. Fig. 7-10 shows the relationship between the frequency bandwidth of the pulse, the strength of the slice-select gradient, and the slice thickness of the image in the left plot. The slice thickness d is related to the frequency bandwidth and the slice-select gradient as

$$d = \frac{2\Delta\omega}{\gamma G_{slice}}, \tag{7.48}$$

if the RF pulse has a step frequency profile as shown in the right plot of Fig. 7-10.

The ideal pulse to achieve the frequency profile shown in Fig. 7-10 is an amplitude-modulated sine wave with base frequency ω_0, described by

$$x(t) \propto \frac{\sin \frac{\Delta\omega t}{2}}{\frac{\Delta\omega t}{2}} \sin(\omega_0 t). \tag{7.49}$$

However, this pulse would require an infinite number of side lobes (Fig. 7-11) and hence infinite transmission time to uniformly and exclusively excite the discrete band of frequencies. In practice, the pulse is "apodized" by limiting the number of side lobes. Typically, a Gaussian profile in frequency is generated to select the slice, which corresponds to a Gaussian profile in the thickness sampling.

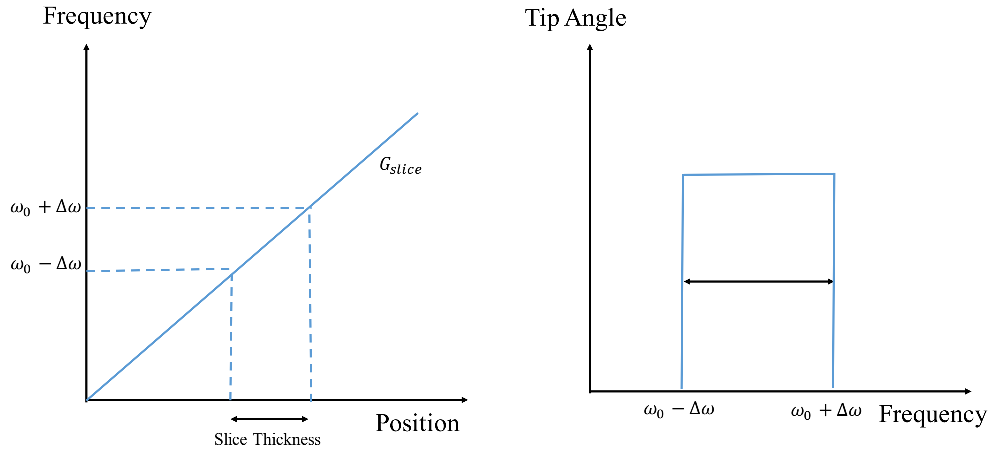

Figure 7-10: Slice selection imaging. The left plot shows the relationship between the frequency bandwidth of the pulse, the strength of the slice-select gradient slice, and the slice thickness of the image, while the right shows the corresponding frequency profile.

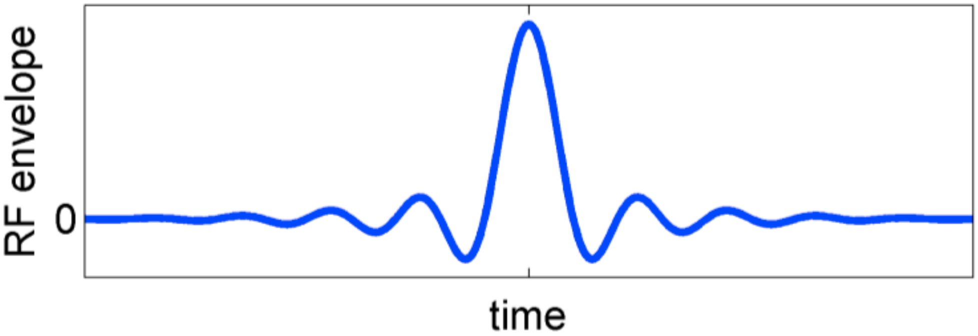

Figure 7-11: Ideal signal for slice selection in time domain[208].

7.4.3 Chemical Shifting Imaging

Chemical shift is the phenomenon that the same atomic nucleus differs slightly in resonance frequency when the nucleus is bound inside different molecules or by different molecular sites. The Chemical Shifting Imaging (CSI) provides mapping of chemical shifts by sampling the FID signal in the time dimension, in addition to the multi-dimensional space imaging through k-space. In practice, for each excitation, gradients are applied before readout to select particular resonance region to maximize the sensitivity for one chosen point in k-space, and then the gradient is turned off and the FID signal is sampled. This is basically a point-by-point scheme in k-space sampling. The CSI technique has several advantages: maximizing signal-to-noise ratio by taking full advantage of the long transverse spin relaxation time T_2, minimizing signal loss associated with gas diffusion during gradient application, and providing sensitivity to monitor the NMR frequency shift due to magnetic field disturbances. For a 2D CSI, the spectrum for one pixel can be described as

$$\rho(l\Delta f, m\Delta x, n\Delta y) = \frac{1}{N_t N_x N_y} \sum_{r=0}^{N_t-1} \sum_{p=0}^{N_x-1} \sum_{q=0}^{N_y-1} s(r\Delta t, p\Delta k_x, q\Delta k_y) e^{2\pi i \frac{lr}{N_t}} e^{2\pi i \frac{mp}{N_x}} e^{2\pi i \frac{nq}{N_y}}. \tag{7.50}$$

For one particular voxel located at $(m\Delta x, n\Delta y)$, the time dependence of the FID signal, $S(t) = Ae^{-t/T_2}e^{+i\omega_0 t}$, corresponds to a frequency spectrum and can be modeled with

$$\begin{aligned} G(\omega) &= \int_0^\infty S(t)e^{-i\omega t}dt = \int_0^\infty Ae^{-t/T_2}e^{+i\omega_0 t}e^{-i\omega t}dt = \int_0^\infty Ae^{-\frac{1}{T_2}t}e^{-i(\omega-\omega_0)t}dt \\ &= \frac{A}{\frac{1}{T_2} + i(\omega-\omega_0)} = \frac{A[\frac{1}{T_2} - i(\omega-\omega_0)]}{(\frac{1}{T_2})^2 + (\omega-\omega_0)^2}, \end{aligned} \tag{7.51}$$

if the whole FID signal is measured for $t = (0, \infty)$.

However, it is impossible to measure the entire FID signal to $t = \infty$. The FID signal S(t) is measured typically within a limited time $t \in [0, T]$. If one expresses the time window function $f(t)$ and FID signal $S(t)$ as

$$f(t) = \begin{cases} 1 & \text{if } t \in [0, T], \\ 0 & \text{if } t > T \text{ or } t < 0, \end{cases} \tag{7.52}$$

and

$$S(t) = \begin{cases} Ae^{-t/T_2}e^{i\omega_0 t} & \text{if } t \geq 0, \\ 0 & \text{if } t < 0, \end{cases} \tag{7.53}$$

the spectrum $\rho(m\Delta x, n\Delta y)$ can be described by the Fourier transform of the product $f(t) \times S(t)$:

$$\begin{aligned} H(\omega) &= \int_0^\infty f(t) \times S(t) e^{-i\omega t} dt = -A \frac{e^{-T[\frac{1}{T_2}+i(\omega-\omega_0)]} - 1}{\frac{1}{T_2} + i(\omega - \omega_0)} \\ &= \frac{A[\frac{1}{T_2} - i(\omega - \omega_0)]}{(\frac{1}{T_2})^2 + (\omega - \omega_0)^2} - A \frac{e^{-T/T_2}[\cos(\omega T - \omega_0 T) - i \sin(\omega T - \omega_0 T)]}{\frac{1}{T_2} + i(\omega - \omega_0)}. \end{aligned} \tag{7.54}$$

Here the first term is exactly the same as in Eq. 7.51 and the second term is the new part due to truncating the FID signal in time. Denote the second term as $N(\omega)$:

$$\begin{aligned} N(\omega) &= -A \frac{e^{-T/T_2}[\cos(\omega T - \omega_0 T) - i \sin(\omega T - \omega_0 T)]}{\frac{1}{T_2} + i(\omega - \omega_0)} \\ &= \frac{-Ae^{-T/T_2}[\frac{1}{T_2} \cos(\omega T - \omega_0 T) - (\omega - \omega_0) \sin(\omega T - \omega_0 T)]}{(\frac{1}{T_2})^2 + (\omega - \omega_0)^2} \\ &\quad + i \frac{Ae^{-T/T_2}[(\omega - \omega_0) \cos(\omega T - \omega_0 T) + \frac{1}{T_2} \sin(\omega T - \omega_0 T)]}{(\frac{1}{T_2})^2 + (\omega - \omega_0)^2}. \end{aligned} \tag{7.55}$$

The $N(\omega)$ term oscillates with a period of $\Delta f = 1/T$. In summary, when the FID signal is sampled in a limited time window $[0, T]$, the spectrum $\rho(m\Delta x, n\Delta y)$ can be expressed as

$$FFT[f(t) \times S(t)] = G(\omega) + N(\omega). \tag{7.56}$$

7.5 Test Setup at UVa

The polarization and permeation tests of ^{3}He into GDP pellets are performed at the radiology research facility (Snyder Building) at the School of Medicine of University of Virginia. A series of tests were done to study the ability to fill GDP pellets with pressurized polarized ^{3}He, using data acquired with a clinical 1.5-T magnetic resonance imaging (MRI) scanner.

7.5.1 Setup

Fig. 7-12 shows the setup for the UVa medical ^{3}He polarizer, very similar to the JLab polarized ^{3}He target setup discussed in Sec. 6.2.4, using hybrid spin-exchange optical pumping and narrow-width diode laser. This polarizer routinely produce ^{3}He up to 8 atm with a (60-70)% polarization. The polarized ^{3}He gas from the polarizer is dispensed into an L-shape tube (Fig. 7-15) with GDP pellets inside and transferred to the MRI setup for imaging, Fig. 7-13. The MRI scanner has a center field of 1.5 T and provides a relative polarization measurement of ^{3}He. An L-tube holder is used to help align the tube bottom with the free-induction-decay (FID) coil center and the isocenter of the MRI magnet system. The FID coil generates the RF field around the tube bottom and receives the ^{3}He FID signal after the RF pulse. The FID coil was designed to achieve a 0.5 mm resolution. The holder and FID coil were also able to accommodate an optional liquid nitrogen bath surrounding the end of the L-tube, as shown in the left of Fig. 7-14.

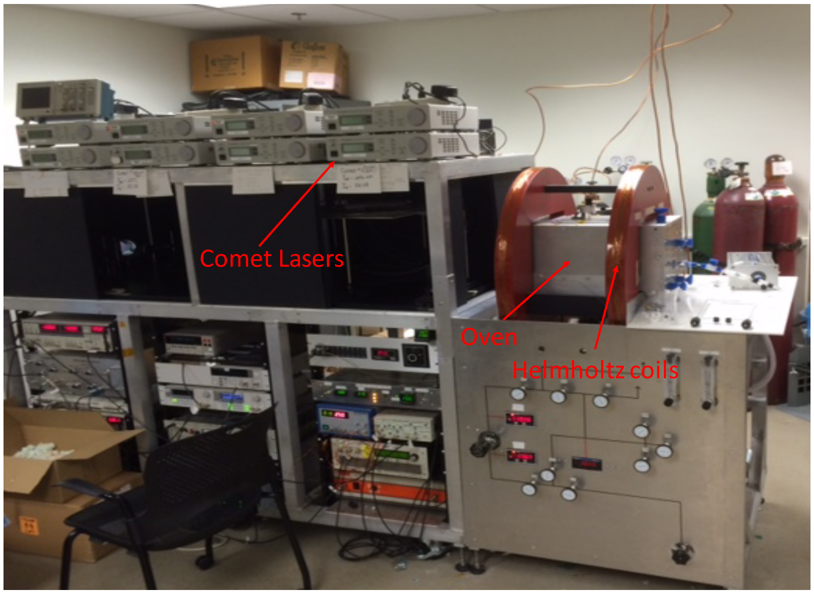

Figure 7-12: Polarizer setup at UVa.

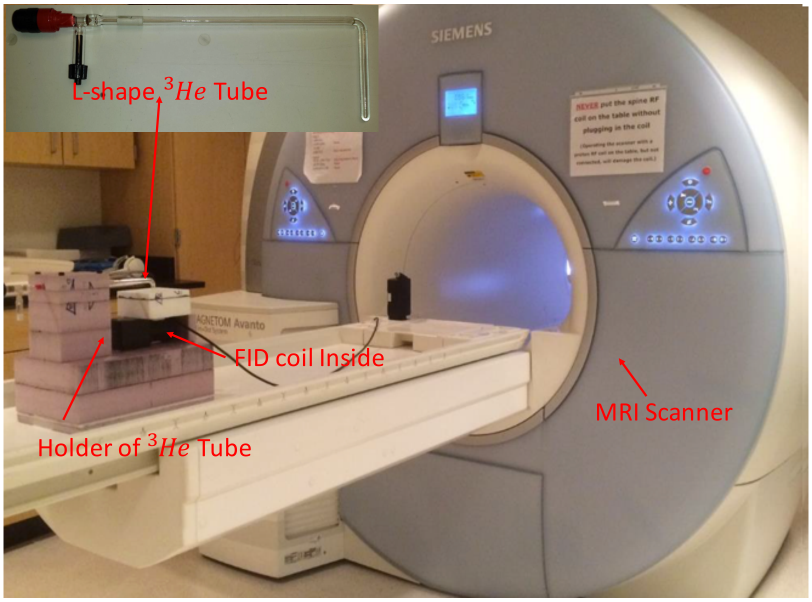

Figure 7-13: Setup for MRI scan on ^{3}He tube at UVa.

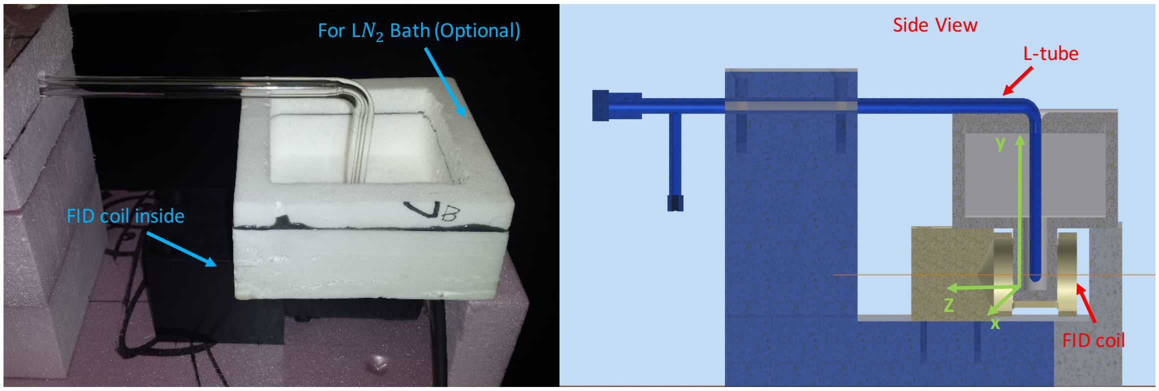

Figure 7-14: Styrofoam holder used to precisely position the L-tube (left) and the side view of holder with L-tube in (right).

7.5.2 L-Tubes and GDP Pellets

The L-tubes are made of Pyrex and blown by Mike Souza (Princeton University). There are a total of 11 L-tubes produced and categorized into two groups: 7 tubes with a round bottom and an inner diameter of 3mm (Tube A, B, C, D, E, F, G) and 4 tubes with a flat bottom and also an inner diameter of 3 mm (Tube H, I, X1, X2). As in nuclear physics targets (Sec. 6.2.4.1), the tube performance depends largely on the tube construction processes. Polarization lifetime (T_1) measurements were performed to screen the quality of tubes. Tubes with long T_1 were used for permeation tests, while those with short T_1 will be prepared as thermal calibration tubes. In a 1.5 T field, for the L-tubes of second group with the flat bottom, the frequency profile of FID signals in the pixel close to the tube bottom were found to be strongly distorted with multi-peaks due to the large amount of glass material. Therefore, most of ^3He tests were performed with L-tubes of the first group. Fig. 7-15 shows the schematic design for the L-tube of the first group. One can define a right-handed coordinates with $\hat{z}$ along the field direction, $\hat{x}$ horizontal, $\hat{y}$ vertical for the tube image illustration, as shown in Fig. 7-14 and 7-15. Table 7.1 shows the list of our GDP pellets provided by General Atomics.

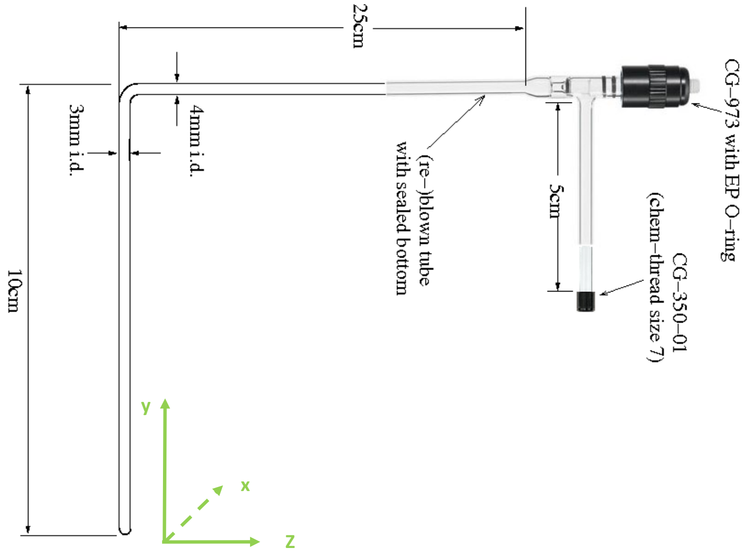

Figure 7-15: Schematic design of L-tubes with 3 mm inner diameter.

7.5.3 Imaging Analysis

For the 2D space imaging data, the analysis is very straightforward. Fig. 7-16 shows the 2D spin distribution $\rho(m\Delta x, n\Delta y)$ for an L-tube filled with polarized ^3He gas from the inverse FFT of the k-space data by employing Eq. 7.45 directly.

Hole No.	Capsule	$\sim$ O.D./Wall Thickness (μm)
1	10-23-1	1788/15
2	10-23-2	1788/15
3	10-23-3	1788/15
4	10-23-4	1788/15
5	empty	
6	11-27-1	1918/26.4
7	11-27-2	1918/26.4
8	11-27-3	1918/26.4
9	11-27-4	1918/26.4
10	empty	
11	11-33-1	1804/14
12	11-33-2	1804/14
13	11-33-3	1804/14
14	11-33-4	1804/14
15	empty	

Table 7.1: GDP pellets capsules provided by General Atomics[210].

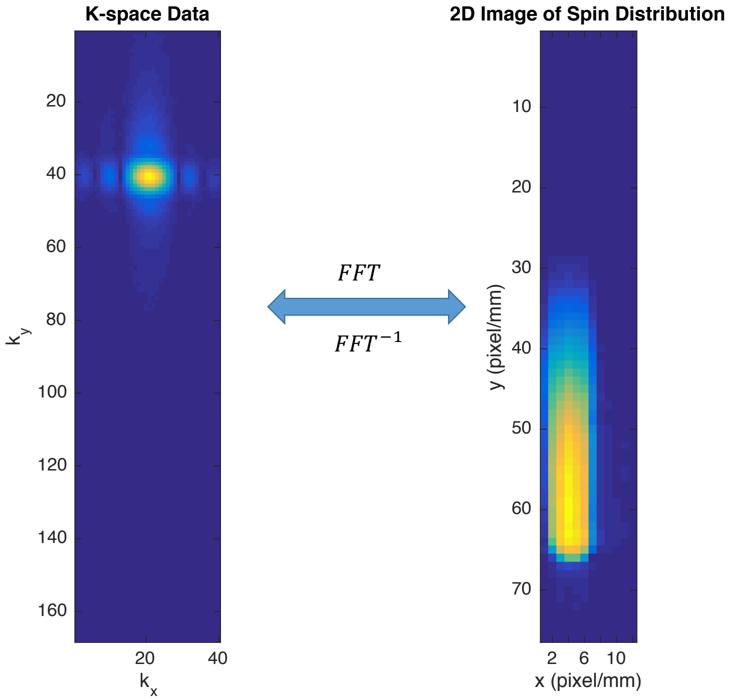

Figure 7-16: 2D space imaging for an L-tube (Tube E) filled with ^{3}He. The left plot shows the k-space data while the right shows the corresponding spin distribution in the 2D space, clearly showing the shape of the bottom of the L-tube.

However, the CSI imaging analysis is more complicated. The typical 2D CSI data are sampled with a fixed 96 ms data acquisition window ($T = 96$ ms in Eq. 7.52) with a 20 kHz sampling rate for each gradient application, as shown in Fig. 7-17. For each voxel, a direct FFT will get a resolution 10.4 Hz in the frequency domain, which is close to $1/T_2 \approx$ 10 Hz, as shown in Fig. 7-18. This resolution cannot show the peak structure clearly and make the peak fitting inaccurate.

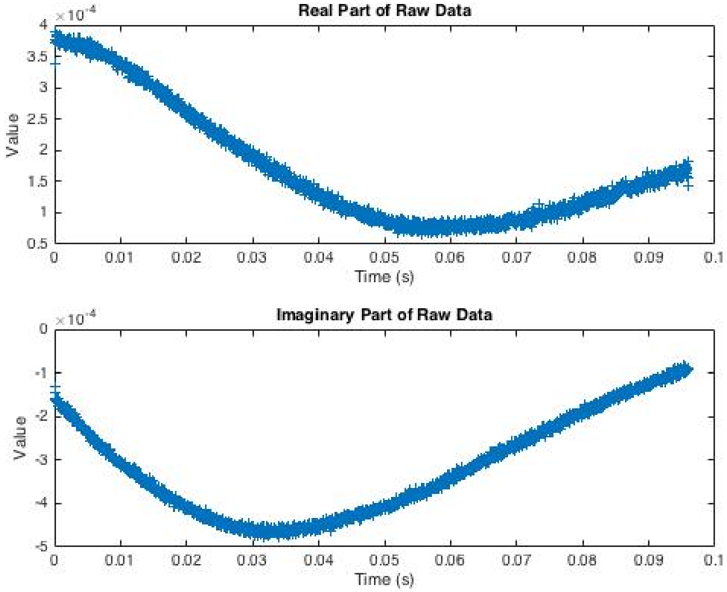

Figure 7-17: Raw CSI Data in time domain for one scan (pixel x=6, y=37 of tube E). The top plot shows the real part of the FID signal, while the bottom show the imaginary part.

A technique called zero paddling was used to increase the resolution in the frequency domain. The CSI data is paddled to 1s in Fig. 7-19, which gives a resolution of 1Hz. An oscillation appears after FFT as shown in Fig. 7-20. This is due to that the truncation of FID spectrum to 96 ms, which causes the $N(\omega)$ term in Eq. 7.55.

The 2D zero-paddled CSI data is then put into Eq. 7.50 to get the frequency spectrum for each voxel $\rho(l\Delta f, m\Delta x, n\Delta y)$. The spectrum is described well by Eq. 7.63 as shown in Fig. 7-21: The left most plot shows the 2D map for the fitted amplitude A, which relates to the spin distribution in the 2D spatial coordinates. The right top two plots show the fitting for the frequency spectrum in voxel (x=6, y=53) while the

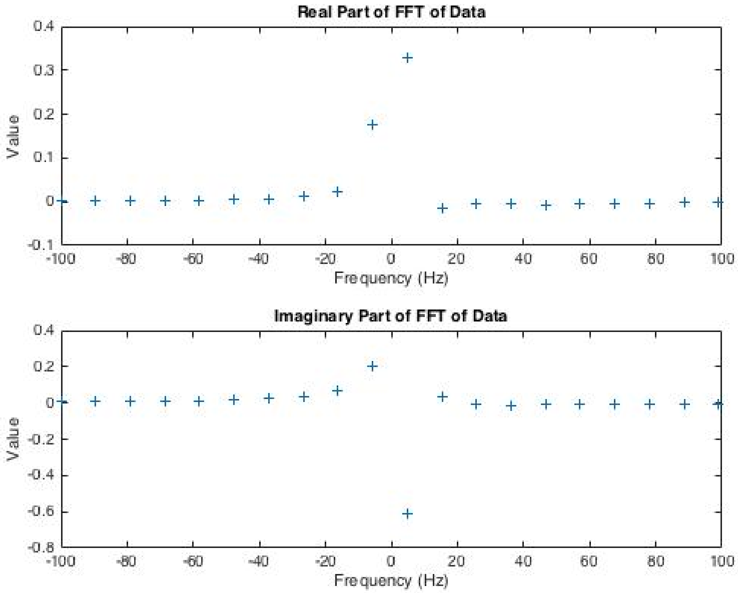

Figure 7-18: FFT of Raw CSI Data for one scan (pixel x=6, y=37 of tube E). The top plot shows the real part FFT, while the bottom show the imaginary part.

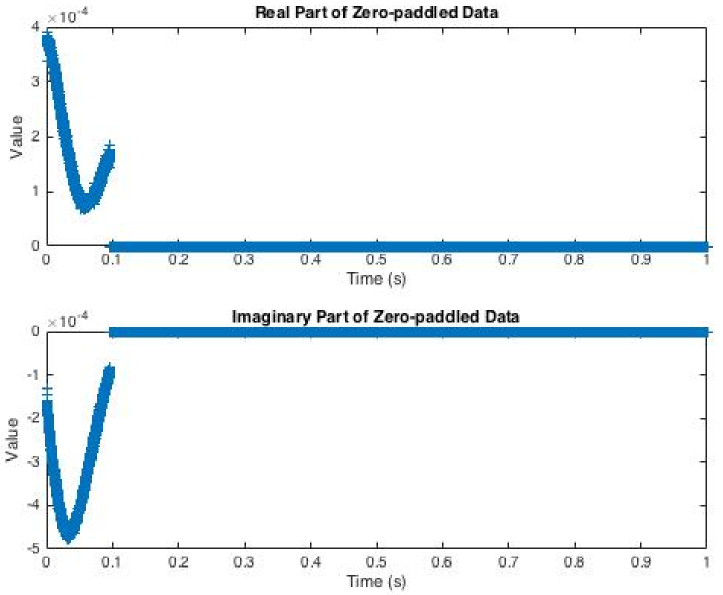

Figure 7-19: Zero-paddled CSI Data in time domain for one scan (pixel x=6, y=37 of tube E). The top plot shows the real part of FID signal, while the bottom show the imaginary part. The signal beyond the 0.96 ms sampling window is filled arbitrarily by zero's. This is called zero-paddling.

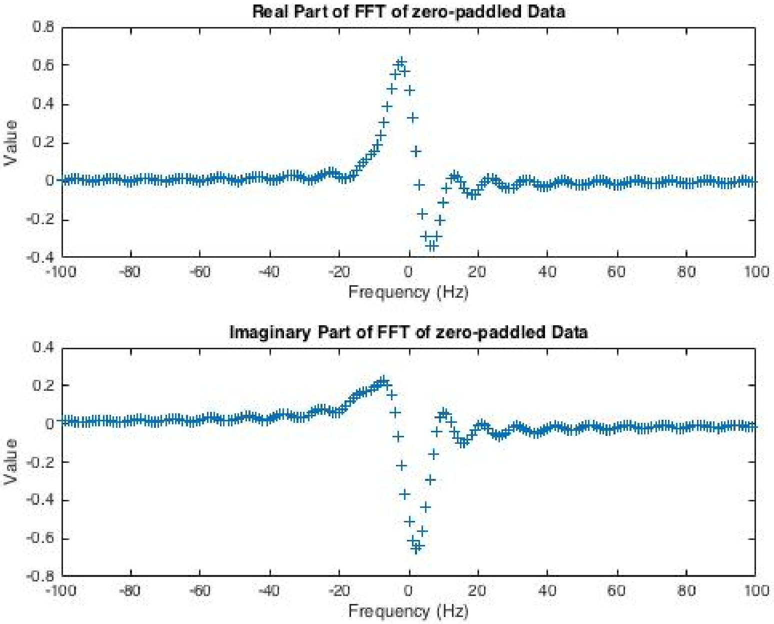

Figure 7-20: FFT of zero-paddled CSI Data for one scan (pixel x=6, y=37 of tube E). The top plot shows the real part FFT, while the bottom show the imaginary part.

right bottom two are for voxel (x=6, y=54).

Slice-selected data were analyzed similar to the CSI data, and are not detailed here.

7.6 Study of Polarized ^{3}He Performance in ICF Pellets

The polarization and permeation of ^{3}He in the GDP pellet are recorded dynamically by using MRI imaging techniques. The following tests were done to study the ^{3}He performance in the pellets.

7.6.1 Demonstration of ^{3}He Polarization Survival in the Pellet

The first step was to demonstrate the ^{3}He polarization can survive in the pellet after permeation.

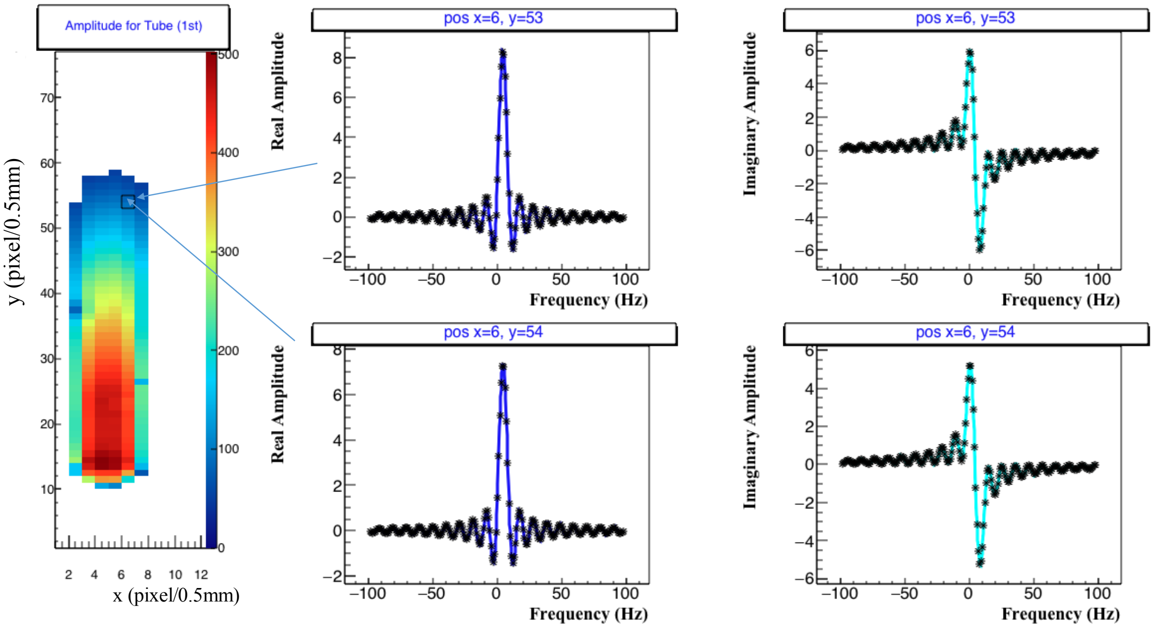

Figure 7-21: Fitting result for tube E filled with ^{3}He. The left most plot shows the fitted Amplitude A in the 2D spatial coordinates. The right top two plots shows the fitting (blue and cyan curves) for the frequency spectrum along with data (black markers) in voxel (x=6, y=53) while the right bottom two shows for the voxel (x=6, y=54).

The left plot of Fig. 7-22 shows two pellets sitting at the bottom of tube. To perform the measurement, the L-tube and pellets were evacuated to around 10 mTorr at the beginning. Then the L-tube was filled with polarized ^{3}He (pressure around 6 atm and polarization about 60%) from the polarizers and waited 15 mins (this is about 4 times the permeation time constant at room temperature) for ^{3}He to permeate into the pellet. The tube was then disconnected from the polarizer and put into the holder with a liquid nitrogen bath (shown in Fig. 7-14) and an MRI image was acquired. The ^{3}He tube and pellets were clearly visible in the middle plot of Fig. 7-22. From Sec. 7.3.2, the ^{3}He inside the pellet is sealed by the wall at this low temperature. Next, the ^{3}He outside of pellets was evacuated and another MRI image was acquired as shown in the right plot of Fig. 7-22. Only the pellets were visible this time, which means that although the absolute ^{3}He polarization was yet to be determined, the ^{3}He polarization did survive after permeation.

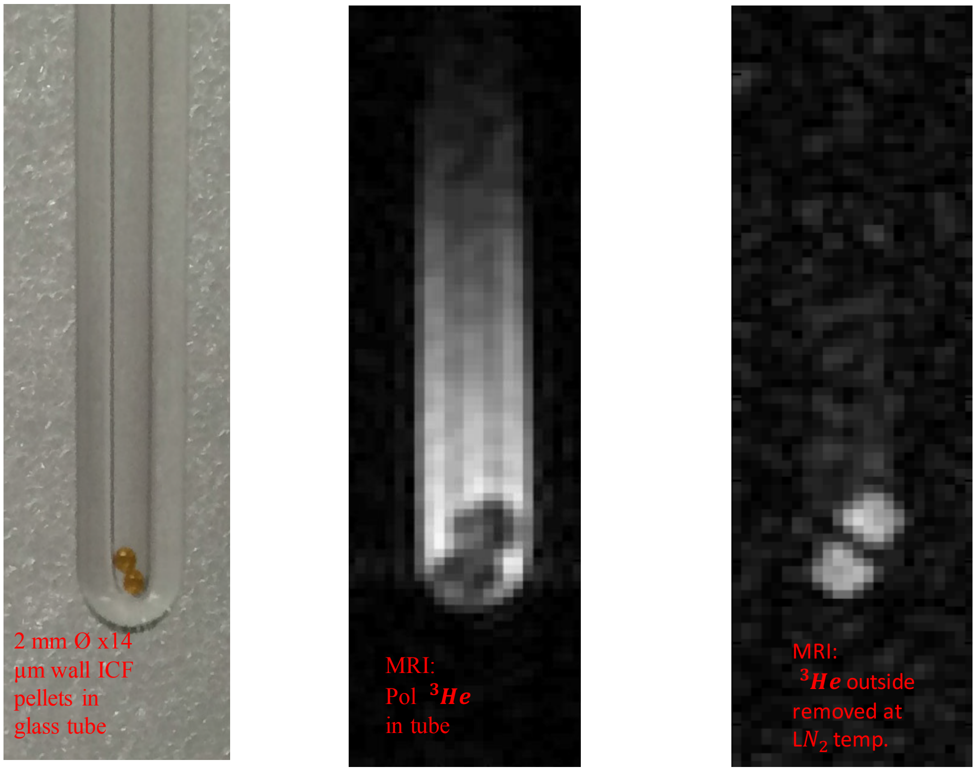

Figure 7-22: Demonstration of ^{3}He polarization survival in GDP pellets (Tube D, Pellets 10-23-3 and 10-23-4, on 10/24/2015). The left plot shows two pellets sitting at the bottom of tube, the middle plot shows one slice of the 3D image of the tube after ^{3}He permeation, and the right plot shows the same image after removing the ^{3}He outside of pellet at the liquid nitrogen temperature.

7.6.2 Measurement of ^{3}He Polarization Relaxation Time T_1 in ICF Pellets

The second step is to measure ^{3}He polarization relaxation time T_1 in the pellet at the liquid nitrogen temperature. For the purpose of testing in the Tokamak in the future, the ^{3}He polarization must not only survive during the permeation through pellet walls, but also need to have a sufficiently long relaxation time inside the pellet to allow enough time for the pellets to be injected into the plasma.

A similar approach as Sec. 7.6.1 was used. After the evacuation of the gas outside of the pellet at the liquid nitrogen temperature, a time sequence of images were acquired at t=0, 30 , 90, 210 min, as shown in Fig. 7-23. The signal strength, which is proportional to the ^{3}He polarization, decayed over time. The evolution of the polarization can be described by

$$P(t_i) \quad = \quad P_0 e^{-t_i/T_1}[1-(\cos\theta)^n]^{N_i}, \tag{7.57}$$

where P_0 is the initial polarization, e^{-t_i/T_1} is from spin relaxation and $[1-(\cos\theta)^n]^{N_i}$ is due to the depolarization caused by each RF excitation. Here θ is the tipping or flip angle, n is the number of excitations per image, N_i is the number of images acquired before t_i. The RF-corrected polarization is the raw polarization divided by the RF correction factor, which can be written as

$$\frac{P(t_i)}{[1-(\cos\theta)^n]^{N_i}} \quad = \quad P_0 e^{-t_i/T_1}. \tag{7.58}$$

During the measurement, $\theta = 1.6°$, $n = 40 \times 16$, N_i=0, 1, 2, 3. Fig. 7-24 shows the RF-corrected signal and the fitting using Eq. 7.58. The fitted T_1 is around 5 hours which indicates that the ^{3}He can survive long enough for the pellet to be transferred to a 77 K cryogenic injector and be rejected into a tokamak.

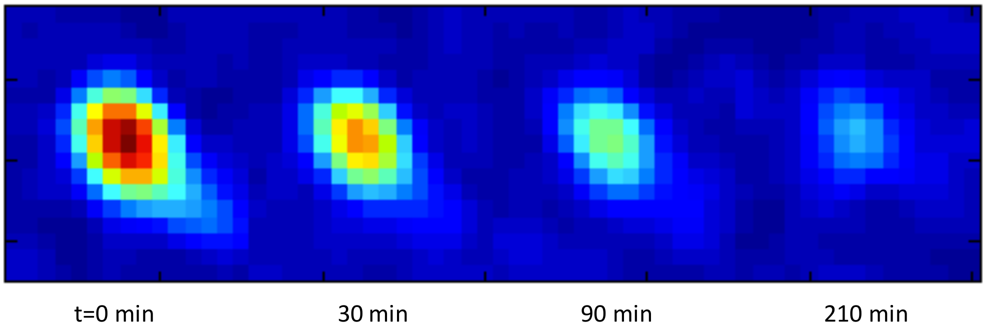

Figure 7-23: A time series of images acquired to measure the ^{3}He polarization relaxation in the pellets at the liquid nitrogen temperature (Tube D, Pellet 11-27-3, on 11/15/2015). The signal strength decreased over time.

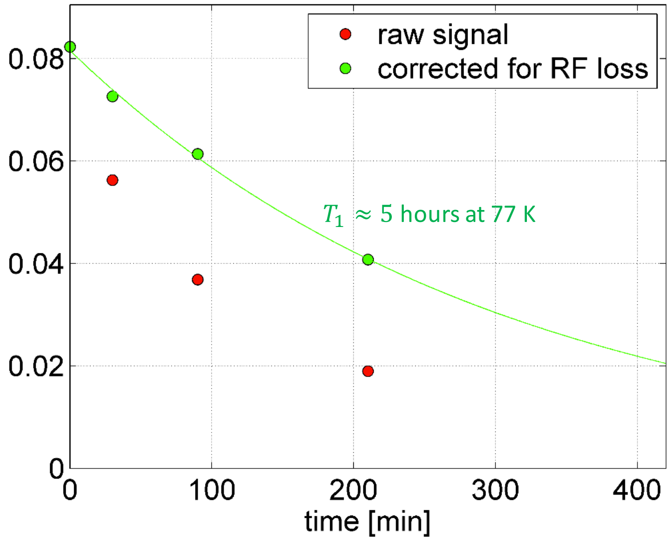

Figure 7-24: The ^{3}He signal versus time in the pellet (Tube D, Pellet 11-27-3, on 11/15/2015). The red points show the mean signal in the pellet while the green points the RF-corrected ones. The green curve is the fit using Eq. 7.58.

7.6.3 Measurement of the Flip Angle Map

This measurement is designed to measure the flip angle at each pixel or voxel, to characterize the depolarization effect for a RF excitation, which is a very important input for both T_1 measurements (as in Sec. 7.6.2) and for the permeation test discussed in the next section (Sec. 7.6.4). This test was conducted at room temperature.

From Eq. 7.57, if the time difference between images $\Delta t_i = t_i - t_{i-1}$ is small enough that $e^{-\Delta t_i/T_1} \approx 1$, the ^{3}He polarization evolution is given by

$$P(t_i) \quad = \quad P_0[1-(\cos\theta)^n]^{N_i}. \tag{7.59}$$

Therefore, a sequence of 2D projection images acquired within a very short time can be used to extract the flip angle. Eq. 7.59 can be rewritten as a linear function:

$$\begin{aligned} \log(P(t_i)) &= \log(P_0) + N_i[1-(\cos\theta)^n] \\ &= a + bN_i \end{aligned} \tag{7.60}$$

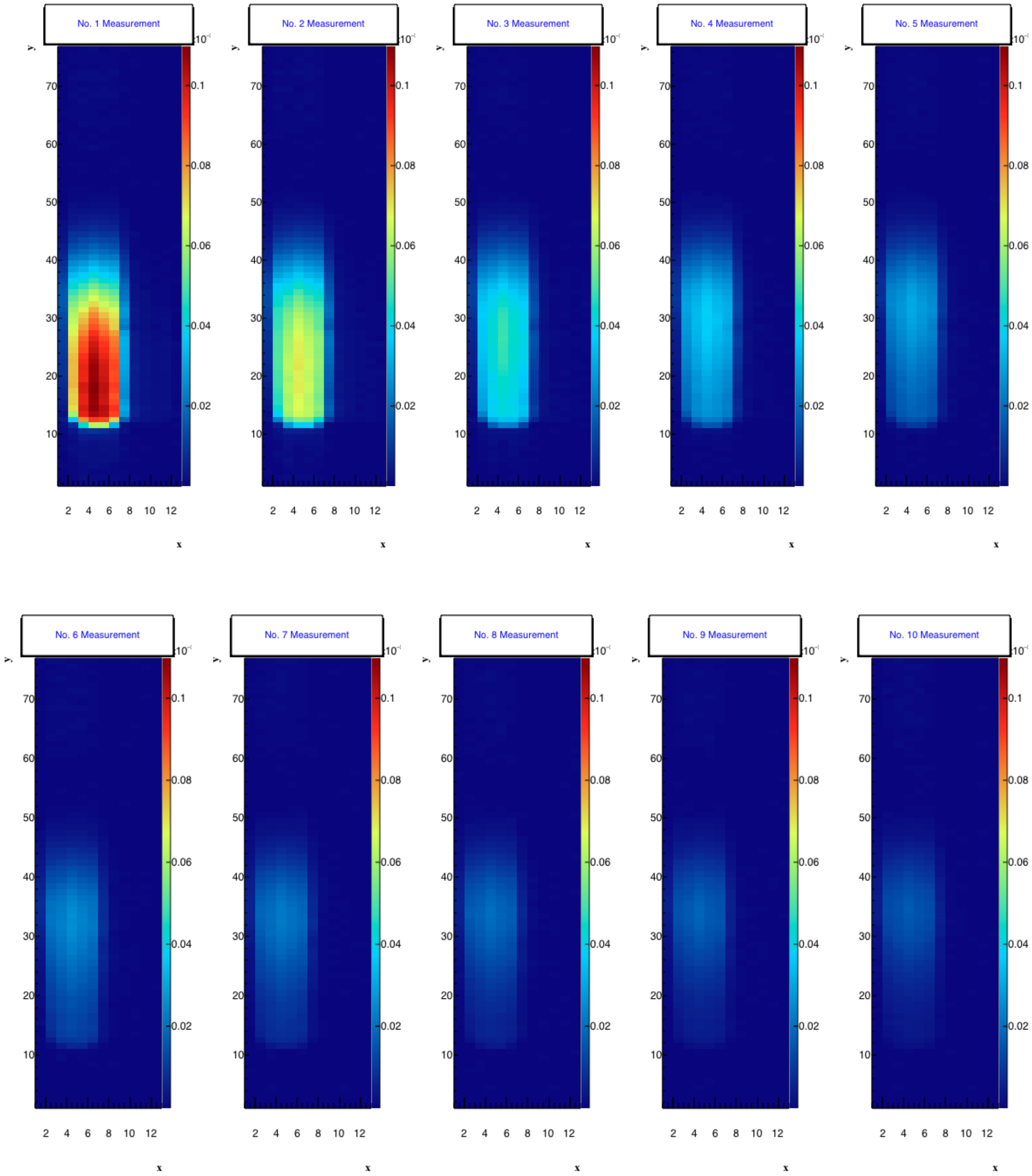

Figure 7-25: A sequence of 2D images acquired for flip angle measurement (Tube D, no glass bead, on 04/17/2016). The ten images were acquired every 0.32 s back-to-back (each consists of 40 RF excitations with repetition time 8 ms). The top shows the first 5 images in the same color scale from left to right while the bottoms shows the last 5 images. The unit is in pixel/0.5mm for both x and y direction.

where $a = \log(P_0)$ and $b = 1 - (\cos\theta)^n$. The left plot of Fig. 7-26 shows the raw signal versus measurement number for pixel (x=4, y=32) while the right plot of Fig. 7-26 shows the log scale. The log of signal deviated from the linear after the fourth point due to the fast diffusion. Only the first four points were fitted using Eq. 7.60 and the extracted flip angle is (6.00 ± 0.08) degrees for this pixel. Fig. 7-27 shows the obtained flip angle map.

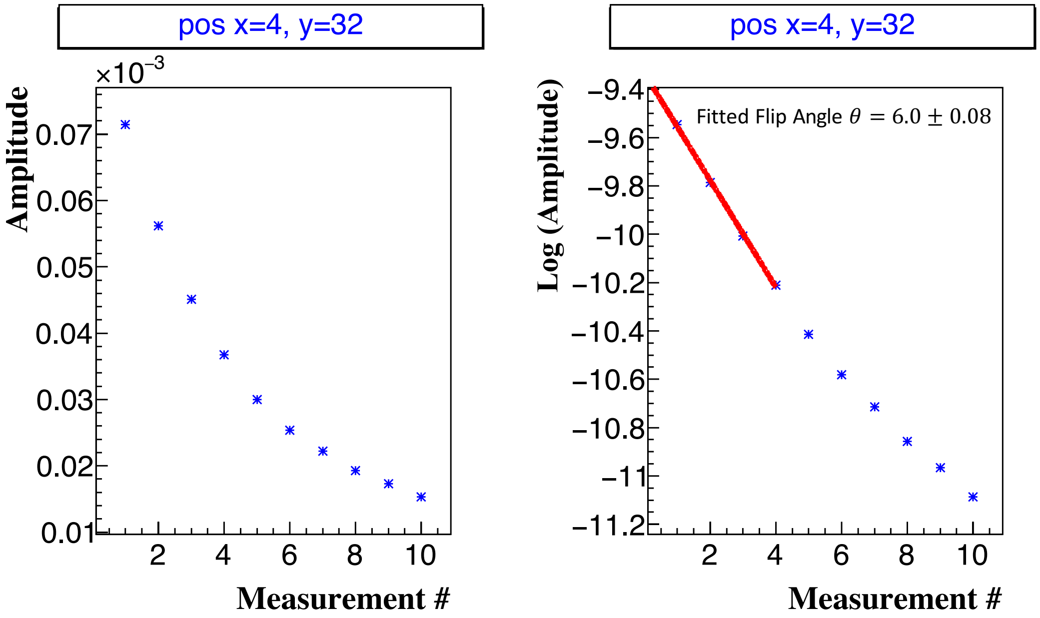

Figure 7-26: The signal versus measurement number for pixel (x=4, y=32) (Tube D, no glass bead, on 04/17/2016). The right plot shows the amplitude in log scale and fitted using the linear function of Eq. 7.60.

A more precise determination of the flip angle (than Eq. 7.60) can be done by including diffusion effect. A model was built to study both the diffusion and RF excitation simultaneously. Assuming no temperature gradient in the tube and dividing the tube into 0.5-mm sections in the vertical (y) direction, the polarization changes in ith-pixel due to the polarization gradient is given by[210]:

$$(\frac{dP_i(t)}{dt})_{\mathrm{diff}} = \frac{A_{i+1}D}{V_iL_{i+1}}(P_{i+1} - P_i) \tag{7.61}$$

where A_{i+1} and L_{i+1} are the cross-sectional area and the thickness ($L_{i+1} = 0.5$ mm) of the $i+1$-th section, V_i is the volume of the i-th section, and P_{i+1} (P_i) is the

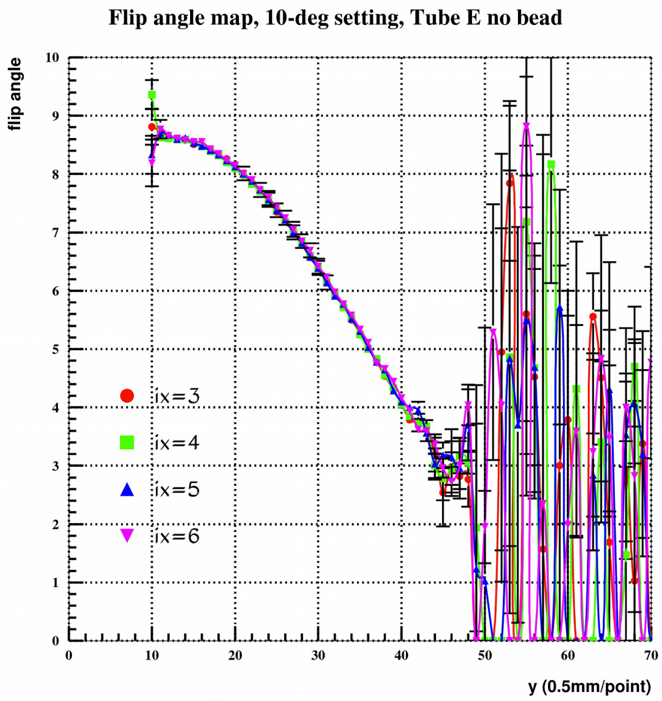

Figure 7-27: The fitted flip angle map (Tube D, no glass bead, on 04/17/2016) as a function of y for 4 x positions. $y = 10$ corresponds to the tube bottom (FID coil center), and $y = 50$ and beyond are outside the FID coil range.

polarization in the $i+1$-th (i-th) section.

The polarization dynamics during the measurement can be described by

$$P_i(t+\delta t) = \left\{ P_i(t)(1-\frac{\delta t}{T_1}) + \delta t \left[(\frac{dP_i(t)}{dt})_{\text{diff}} - (\frac{dP_{i-1}(t)}{dt})_{\text{diff}} \right] \right\} (1-\cos(\theta_i))^{N_i}, \tag{7.62}$$

where N_i is the number of excitations acquired between $[t, t+\delta t]$ (N_i can be 0). In addition, the FID coil can be approximated as two rectangular loops in the (y, z) plane, separated in x direction with well-defined field strength in the space. By fitting the raw signal with the Eq. 7.62 and the FID coil's magnetic field functions (the y-dependence of the RF field perpendicular to 1.5 T field), the diffusion constant can also be extracted. The fitted diffusion constant is $D = (0.135 \pm 0.001)$ cm^2/s for this measurement.

7.6.4 Measurement of the ^{3}He Polarization Survival during Permeation

Our last test, performed in Aug. 2016, was to quantify how large the polarization loss during permeation is. We used a 2-mm GDP shell with 26 μm wall thickness (Pellet 11-27-3) contained in tube F for this test. The test was done at room temperature.

From Sec. 7.3.2, permeation time constant τ were measured for all pellets of Table 7.1 and τ for pellet 11-27-3 is 374 s at room temperature. This is long enough such that several MRI scans can be acquired. Compared with the previous test, an ante-chamber was used to serve as a moveable container for the polarized ^{3}He so that the tube could be filled while inside the scanner rather than at the polarizer. Fig. 7-28 shows one L-tube connected with the ante-chamber. Before the measurement, the ante-chamber, L-tube and pellets were evacuated. Then polarized ^{3}He was only filled into the ante-chamber from the polarizer, with the valve closed between ante-chamber and the L-tube. The ante-chamber and the L-tube were carried to the scanner together. Several minutes were allowed to pass to make sure the polarization reaches equilibrium in the ante-chamber (to avoid the position-dependent depolarization effect when being moved into the strong field of the MRI scanner). The valve was then opened to allow the ^{3}He to fill the L-tube and the permeation began. At that instant (30 s after releasing the gas), a quick 2D image in $x-y$ plane was taken to determine the frequency for slice positioning in the $\hat{y}$ direction, see Fig. 7-29. The pellet was placed on top of a glass bead to prevent the pellet from touching the bottom of tube, where the large amount of glass at the concave bottom was found to cause a strong signal distortion. The polarization dynamics was recorded as a time series of slice-selected images. Each image took 10×10 RF excitations with a repetition time of around 100 ms. The flip angle of each excitation was set to around 1.5 degrees in the FID coil center, resulting in a $\approx 3.4\%$ relative polarization decrease per image due to RF excitations. Fig. 7-30 shows the time sequence MRI images of the cross-sectional slice at the pellet. For pixels located within the pellet, the signal strength increased at first as permeation contribution dominated and then decayed following the T_1 exponential curve, while the signal strength of pixels outside of pellet decayed with a different T_1.

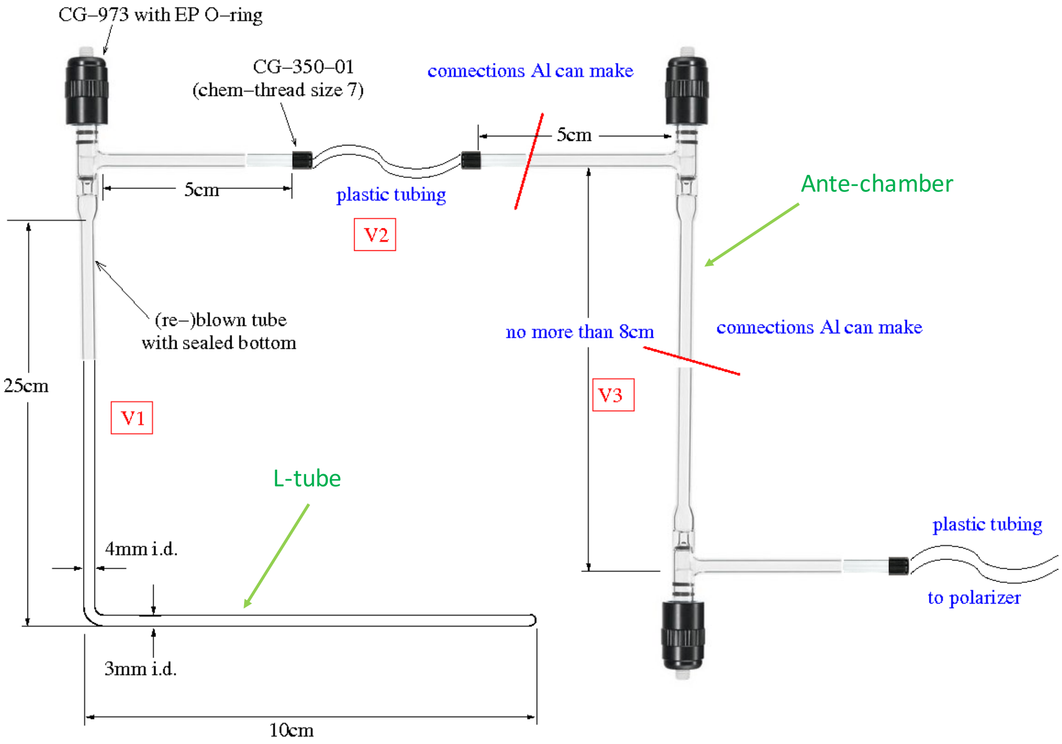

Figure 7-28: The L-tube connected with an ante-chamber.

A model was developed to describe the permeation and polarization dynamics inside and outside of pellets[210]:

$$A_i^{tube} = A_0 e^{-\frac{t_i}{T_1^{tube}}} \eta_i^{RF} \tag{7.63}$$

$$\begin{aligned} A_i^{pellet} &= A_{i-1}^{pellet} \left(\cos^{\frac{N_{i-1}}{2}} \theta_i\right) e^{-\frac{t_i - t_{i-1}}{T_1^{pellet}}} \left(\cos^{\frac{N_i}{2}} \theta_i\right) \\ &+ \frac{P_{in}}{P_{out}} A_0 \frac{e^{-\frac{t_{i-1}}{T_1^{tube}}} + e^{-\frac{t_i}{T_1^{tube}}}}{2} \frac{\eta_{i-1}^{RF} + \eta_i^{RF}}{2} (e^{-\frac{t_{i-1}}{\tau}} - e^{-\frac{t_i}{\tau}}) \cos^{\frac{N_i}{2}} \theta_i, \end{aligned} \tag{7.64}$$

where A_0 is the value representing the initial polarization in the tube, i is the number of measurement, T_1^{tube} (T_1^{pellet}) is the ^{3}He spin relaxation time constant outside (inside) of the pellet, θ_i is the flip angle, η_i^{RF} accounts for the RF loss and diffusion effect in

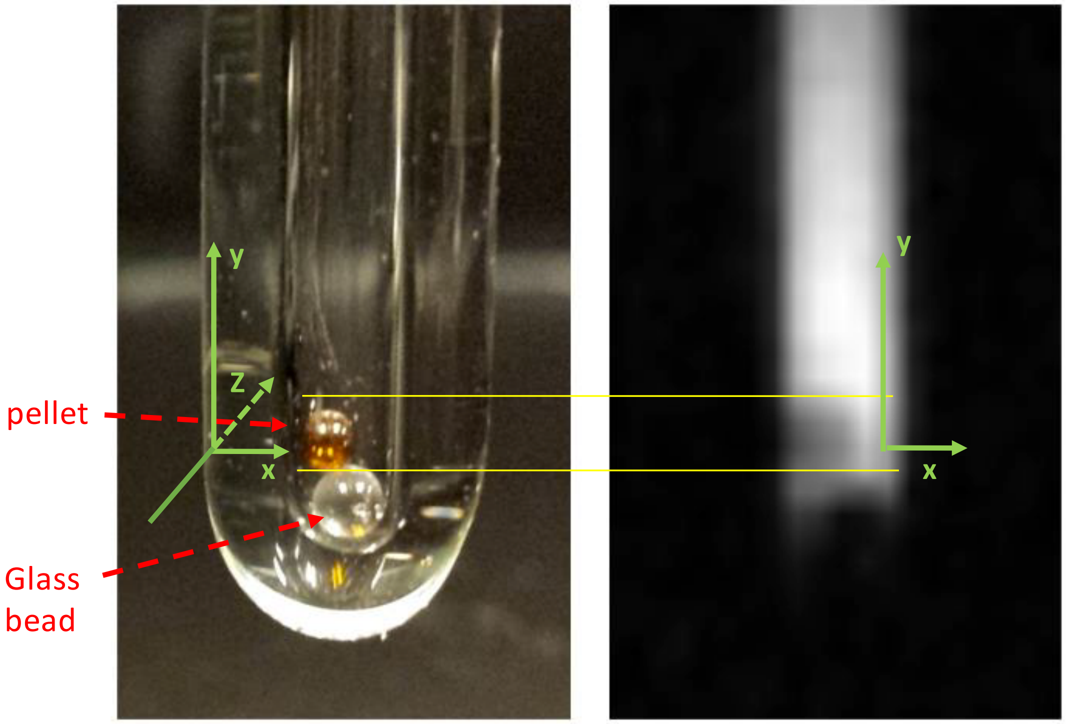

Figure 7-29: First step of the permeation test. A quick 2D image was measured for slice positioning when the permeation started.

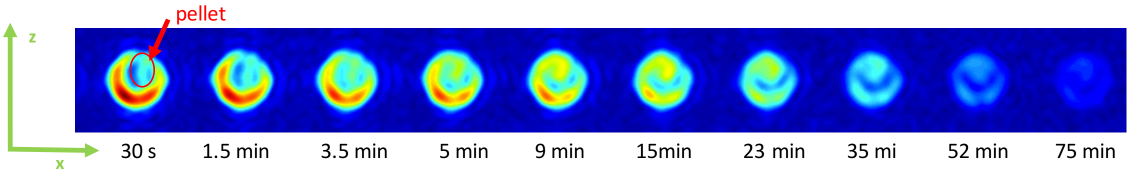

Figure 7-30: Test of ^{3}He polarization permeation through the pellet wall (Tube F, Pellet 11-27-3, 08/14/2016). A time sequence of slice-selection MRI images showing a cross-sectional slice through the 2 mm diameter spherical GDP pellet contained in the 3 mm ID glass tube during permeation of polarized ^{3}He.

the tube (discussed in Sec. 7.6.3), τ is the permeation time constant, and $\frac{P_{in}}{P_{out}}$ is the polarization retention after permeation into the pellet.

The values A_i^{pellet} and A_i^{tube} in Eq. 7.63 and Eq. 7.64 were further combined for each pixel using the slice thickness profile that accounts for different contributions from inside/outside the pellet volume, and were fit to the 2D slice-select CSI data to extract the permeation time, polarization loss during permeation and spin relaxation time constant T_1. Preliminary results are shown in Fig. 7-31 and Table 7.2. These indicated that about 2/3 of the polarization survived the permeation and the ^{3}He gas has a sufficiently long spin relaxation time inside the pellet at room temperature.

However, these results are still preliminary due to several reasons. One reason is

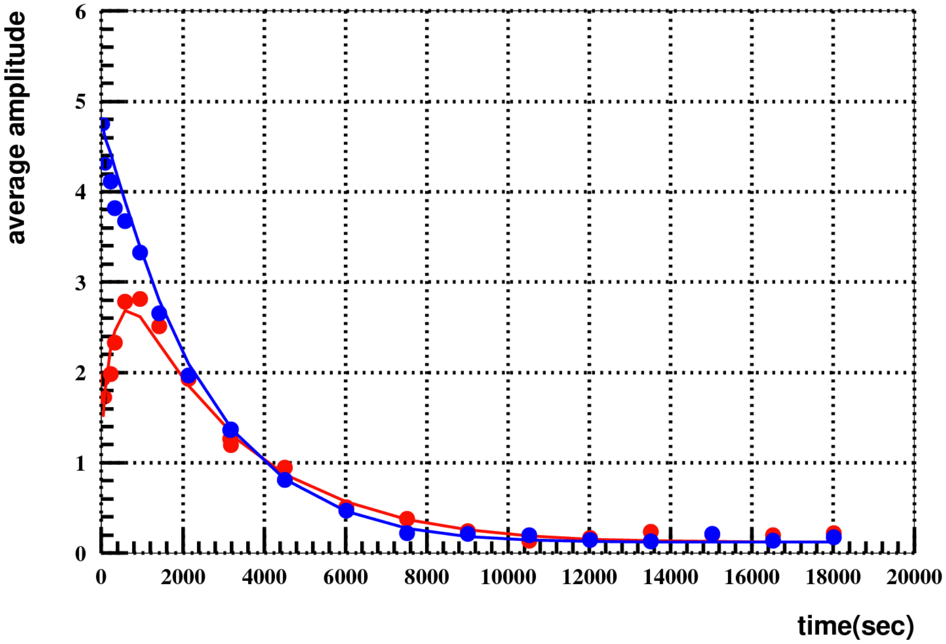

Figure 7-31: Fitting for the permeation test (Tube F, Pellet 11-27-3, 08/14/2016). The blue (red) points are the measured amplitude outside (inside) of pellet averaged over the relevant pixels, and the blue (red) curve is the fitting result using the model of Eq. 7.63 and Eq. 7.64. The fitting results are shown in Table 7.2.

Fitting Parameters	Fitting Results
Spin relaxation T_1^{pellet}	(67 ± 3) min
Spin relaxation T_1^{tube}	(41 ± 1) min
Permeation time constant τ	(387 ± 2) s
Fraction of polarization that survives permeation P_{in}/P_{out}	(67 ± 1) %

Table 7.2: The fitting results for the permeation test.

that the MRI signal itself can be affected by diffusion and this effect is different for pixels inside and outside the pellet. Such correction must be applied to MRI data. It can be simulated if the exact pressure polarization, and the diffusion constants are known for inside/outside pellet for each image. Another reason is that it was found the GDP pellet easily pick up static charge during pumping, and this static charge could significantly affect the ^{3}He polarization immediately around the pellet and can affect the fitting. Both effects are currently being investigated intensively.

7.6.5 Thermal-equilibrium Polarization Calibration using MRI

The MR imaging on the polarized ^{3}He is only a relative polarization measurement. This section describes the TE calibration which aims to quantify the absolute polarization in the tube or pellet.

The thermally polarized ^{3}He gas at room temperature and 1.5 T has a known polarization of about 4 ppm using Eq. 6.1. About 3 atm ^{3}He gas was filled in an L-tube with an identical shape as the permeation test but with a much short T_1 (these are often L-tubes produced with bad quality) and located in the same position on the MRI scanner to make a direct comparison. Since the thermal polarization is very small, a large flip angle ($\approx 80°$) was used and typically around 50-100 MRI images are acquired and averaged to increase the signal-to-noise ratio. However, a large flip angle means the TE polarization is almost completely lost after each excitation, and one must wait for a time $\gg T_1$ for the TE polarization to recover. Even for a tube with bad quality, the T_1 can be still around 10 min, thus a long time is needed to acquire one image (about 10 hours for one image of resolution 16×48). To minimize T_1, about 0.89 atm of O_2 was added into the tube to accelerate ^{3}He spin relaxation so that the thermal polarization could be recovered rapidly after each measurement. The expected T_1 for ^{3}He with O_2 presence is given by[211]

$$\frac{1}{T_1} = 0.45[O_2](\frac{299}{T})^{0.42} \text{ s}^{-1}/\text{amg}, \tag{7.65}$$

where $[O_2]$ is the oxygen density and T is the temperature of the gas. At an oxygen density $[O_2] = 0.89$ amg, the calculated $T_1 = 2.5$ s for ^{3}He. Each thermal-equilibrium image was acquired using 16×48 RF excitations with a repetition time of 5 s. For a measurement with a flip angle 80 degrees, about 89% of the thermal-equilibrium polarization is recovered during the 5 s repetition time.

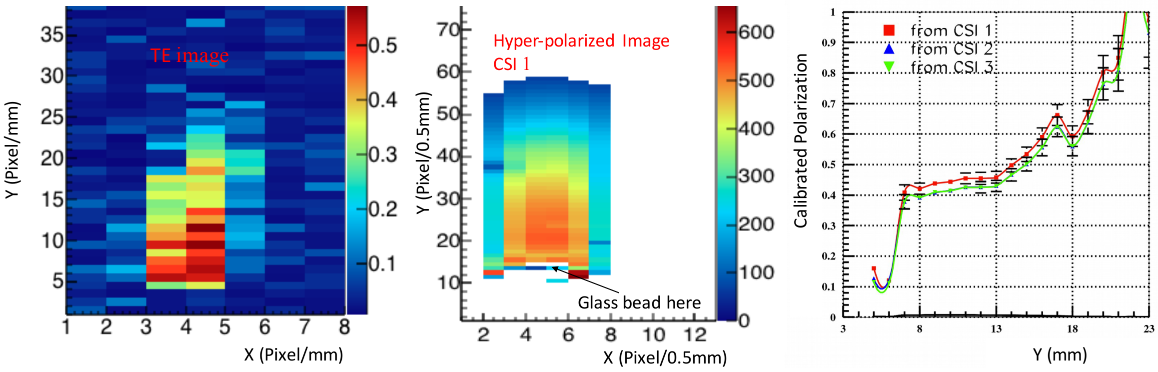

Figure 7-32: Absolute polarization calibration using CSI images. The left plot shows the TE ^{3}He CSI image at 300 K and 1.5 T (Tube A, on 07/04/2016), the middle plot shows the hyperpolarized ^{3}He CSI image of an L-tube with a glass bead at the bottom (Tube E, on 04/17/2016), and the right plot shows the calibrated polarization at $t = 0$ for three hyperpolarized ^{3}He CSI images acquired back-to-back. The presence of the glass bead is clearly evident at $y = (5 - 7)$ mm on the right. The region $y = (8, 13)$ mm has a polarization of $(42 \pm 2)\%$ from this test.

Fig. 7-32 shows the absolute polarization calibration for hyperpolarized ^{3}He CSI images. A total of 3 CSI measurements were performed back-to-back. The left plot shows the TE ^{3}He CSI image at 300 K and 1.5T, the middle plot shows the first hyperpolarized ^{3}He CSI image located at almost the same location in the MRI system (acquired with 12×76 excitations with repetition time of around 100 ms, flip angle setting 2 degrees). A glass bead was put at the bottom of the tube in the hyperpolarized case. The calibrated polarization at $t = 0$ is shown along the tube y direction in the right plot for all three measurements, corrected for the RF loss, diffusion effects, and T_1 loss. The agreement among the reconstructed polarization from the three CSI data indicates the T_1 loss and diffusion effect are accounted for correctly. The ^{3}He polarization was found to be around $(42 \pm 2)\%$ at the beginning of the test, within 5 mm of the tube bottom. The increase in the polarization for larger y ($y > 13$ mm) is believed to be due to systematic uncertainty in determining the flip angle map, as this region is near the edge of the FID coil.

7.7 Summary

Nuclear fusion has long been considered an ultimate solution for a clean, renewable, and powerful method of energy production. The use of spin-polarized fuel in a tokamak reactor would provide a significant boost to the fusion rate. The study of ^{3}He performance in polymer pellets is a crucial step towards realizing a direct polarization survival test by using the reaction D + $^3\text{He} \rightarrow \alpha +$ p in the DIII-D tokamak. The initial tests, described in Sec. 7.6, have demonstrated the ability to fill polarized ^{3}He into GDP pellets with high in-pellet polarization and sufficiently long spin relaxation time. Further tests are being carried out to maximize the in-pellet polarization and to improve the systematics uncertainties in the permeation test and the TE calibration. All these efforts are paving the way for a promising future of spin-polarized fusion.

Chapter 8

Conclusions

In this thesis, we discussed the development of spin physics and its application in parallel with the fundamental research. The JLab Hall A E08-027 experiment studied the proton spin structure (Chapters 2–5). The measured proton spin-dependent structure function g_2 at low momentum transfers can be used to study the quark-gluon interaction, and provide tests of predictions from effective field theory such as χPT in the non-perturbative region. The JLab polarized ^{3}He target upgrade, discussed in Chapter 6, is essential for the neutron spin structure study in the JLab 12 GeV program, which will provide complementary information to the flavor separation of nucleon structure. In Chapter 7, the polarization techniques are applied to study the polarized ^{3}He performance in ICF polymer pellets using data acquired with a clinical 1.5-T MRI scanner. The purpose of such study is to prepare for the first proof-of-principle, in-situ test of polarization survival and polarization dependence of D-^{3}He fusion in the DIII-D tokamak.

In summary, spin, a fundamental property of elementary particles like rest mass and charge, will continue to play an important role in modern physics. The development of spin physics will continue to drive a wide range of scientific and industrial applications, and offer more possibilities for our daily life.

Bibliography

[1] W. Gerlach and O. Stern, *Z. Phys.* **9**, 349 (1922).

[2] G.E. Uhlenbeck and S. Goudsmit, *Naturwissenchaften* **13**, 953 (1925); *Nature* **117**, 264 (1926).

[3] P.A.M. Dirac, *Proc. Roy. Soc. A* **117**, 610 (1928).

[4] I. Estermann and O. Stern, *Phys. Rev.* **45**, 761 (1934).

[5] I.I. Rabi *et al.*, *Phys. Rev.* **53**, 318 (1938).

[6] I.I. Rabi *et al.*, *Phys. Rev.* **55**, 526 (1939).

[7] T.D. Lee and C.N. Yang, *Phys. Rev.* **104**, 822 (1956).

[8] C.S. Wu *et al.*, *Phys. Rev.* **105**, 1413 (1957).

[9] M. J. Alguard *et al.*, *Phys. Rev. Lett.* **51**, 1135 (1983).

[10] J. Ashman *et al.*, *Phys. Lett. B* **206**, 364 (1988).

[11] S. Kuhn *et al.*, *Prog. Part. Nucl. Phys.* **63**, 1 (2009).

[12] M.G. Mayer, *Phys. Rev.* **74**, 235 (1948).

[13] `http://twist.phys.virginia.edu/documents.html`

[14] `http://galileo.phys.virginia.edu/research/groups/spinphysics/`

[15] M.S. Albert *et al.*, *Nature* **370**, 199 (1994).

[16] Y. Zheng *et al.*, *Nature* **537**, 652 (2016).

[17] C.D. Bass *et al.*, *Nucl. Inst Meth. Phys. Res. A* **737**, 107 (2014).

[18] A.M. Sandorfi, D. Pace, G.L. Jackson, L.R. Baylor, A. Deur, N. Eidietis, A. Hyatt, J. Liu, M. Lanctot, M.M. Lowry, G.W. Miller, S.P. Smith, H. St-John, X. Wei and X. Zheng, *Polarized fusion, its Implications and plans for Direct Measurements in a Tokamak*, (priv. comm; to be published).

[19] R.M. Kulsrud *et al.*, *Phys. Rev. Lett.* **49**, 1248 (1982).

[20] E. Rutherford, *Philosophical Magazine* **6**, 21 (1911).

[21] E. Rutherford, *Proceedings of the Royal Society A* **97**, 686 (1920).

[22] J. Chadwick, *Nature* **129**, 3252 (1932).

[23] M. Gell-Mann, *Physics Letters* **8**, 3 (1964).

[24] G. Zweig, *CERN Report No.*.8182/TH.401.

[25] M. Breidenbach *et al.*, *Phys. Rev. Lett.* **23**, 935 (1969).

[26] C. Amsler *et al.*, (Particle Data Group), *Phys. Lett. B* **667** (2008).

[27] M. Peskin and D. Schroeder, *An Introduction to Quantum Field Theory*, Westview (1995).

[28] A. W. Thomas and W. Weise, *The Structure of the Nucleon*, Wiley-Vch (2001).

[29] M. Anselmino *et al. Physics Reports*, **261**, 1 (1995).

[30] J. D. Bjorken and E. A. Paschos, *Phys. Rev.* **185**, 1975 (1969).

[31] M. N. Rosenbluth, *Phys. Rev.* **79**, 4 (1950).

[32] D. Drechsel, S. S. Kamalov, and L. Tiator, *Phys. Rev. D* **63**, 114010 (2001).

[33] L. N. Hand, *Phys. Rev.* **129**, 1834 (1963).

[34] R. P. Feynman, *Phys. Rev. Lett.* **23**, 1415 (1969).

[35] E. Leader and E. Predazzi, *An introduction to Gauge Theories and Modern Particle Physics*, Cambridge University Press, (1996).

[36] K.A. Olive *et al.*, Particle Data Group, *Chin. Phys. C* **38**, 090001 (2014).

[37] Y. L. Dokshitzer, *Sov. Phys. JETP* **46**, 641 (1977).

[38] V. N. Gribov and L. N. Lipatov, *Sov. J. Nucl. Phys.* **15**, 438 (1972).

[39] G. Altarelli and G. Parisi, *Nucl. Phys. B* **126**, 298 (1977).

[40] K. G. Wilson, *Phys. Rev.* **179**, 1499 (1969).

[41] A. V. Manohar, *arXiv:hep-ph/9204208*, (1992).

[42] R. L. Jaffe, *Comments. Nucl. Part. Phys.* **19**, 239 (1990).

[43] B. W. Filippone and X Ji, *arXiv:hep-ph/0101224*, (2001).

[44] W. Melnitchouk, R. Ent, and C. Keppel, *Phys. Rep.* **406**,127 (2005).

[45] V. Barone and P. G. Ratcliffe, *Transverse Spin Physics*, World Scientific, Singapore, (2003).

[46] S. Wandzura and F. Wilczek, *Phys. Lett. B* **72**, 195 (1977).

[47] F. R.Wesselmann *et al.*, RSS Collaboration, *Phys. Rev. Lett.* **98**, 132003 (2007).

[48] M. Amarian *et al.*, *Phys. Rev. Lett.* **92**, 022301 (2004).

[49] S. Weinberg, *Physica A* **96**, 327 (1979).

[50] W. Marciano and H. Pagels, *Phys. Rept.* **36**, 137 (1978).

[51] S. Scherer, *Adv. Nucl. Phys.* **27**, 277 (2003).

[52] V. Bernard, N. Kaiser, and U.-G. Meiner, *International Journal of Modern Physics E* **04**, 193 (1995).

[53] V. Bernard, N. Kaiser, and U. G. Meissner, *Phys. Rev. D* **48**, 3062 (1993).

[54] E. Jenkins and A. V. Manohar, *Phys. Lett. B* **255**, 558 (1991).

[55] E. Jenkins and A. V. Manohar, *Phys. Lett. B* **259**, 353 (1991).

[56] P. J. Ellis and H. B. Tan, *Phys. Rev. C* **57**, 3356 (1998).

[57] X. D. Ji, C. W. Kao, and J. Osborne, *Phys. Lett. B* **472**, 1 (2000).

[58] V. Bernard, T. R. Hemmert, and U. G. Meissner *Phys. Lett. B* **545**, 105 (2002).

[59] C. W. Kao, T. Spitzenberg, and M. Vanderhaeghen, *Phys. Rev. D* **67**, 016001 (2003).

[60] V. Bernard, T. R. Hemmert, and U. G. Meissner *Phys. Rev. D* **67**, 076008 (2003).

[61] H. Burkhardt and W. N. Cottingham, *Ann. Phys.* **563**, 453 (1970).

[62] R. L. Jaffe and X. Ji, *Phys. Rev. D* **43**, 724 (1991).

[63] J.-P. Chen, A. Deur, and Z.-E. Meziani, *Modern Physics Letters A* **20**, 2745 (2005).

[64] D. Drechsel, S. S. Kamalov, and L. Tiator *Phys. Rev. D* **63**, 114010 (2001).

[65] V. Nazaryan, C. E. Carlson, and K. A. Griffioen, *Phys. Rev. Lett.* **96**, 163001 (2006).

[66] S. G. Karshenboim, *Canadian Journal of Physics* **77**, 241 (1999).

[67] A. C. Zemach, *Phys. Rev.* **104**, 1771 (1956).

[68] D. Drechsel, O. Hanstein, S. S. Kamalov, and L. Tiator, *Nucl. Phys.* **A645**, 145–174 (1999).

[69] A. Camsonne, J. Chen, D. Crabb, and K. S. spokespersons, Jefferson Lab Experimental Proposal E08-027.

[70] P. L. Anthony *et al.*, *Phys. Rev. D* **54**, 6620 (1996).

[71] D. Adams *et al.*, *Phys. Rev. D* **56**, 5330 (1997).

[72] P. L. Anthony *et al.*, *Phys. Lett. B* **553**, 18 (2003).

[73] K. Abe *et al.*, *Phys. Rev. D* **58**, 112003 (1998).

[74] P. L. Anthony *et al.*, *Phys. Lett. B* **493**, 19 (2000).

[75] K. Kramer, *et al.*, *Phys. Rev. Lett.* **95**, 142002 (2005).

[76] X. Zheng *et al.*, *Phys. Rev. Lett.* **92**, 012004 (2004).

[77] K. Abe *et al.*, *Phys. Rev. Lett.* **78**, 5 (1997),

[78] M. Stratmann, *Z. Phys. C Part. Fields* **60**, 763 (1993).

[79] X. Song, *Phys. Rev. D* **54**, 1955 (1996).

[80] H. Weigel and L. Gamberg, *Nucl. Phys. A* **680**, 48 (2001).

[81] M. Wakamatsu, *Phys. Lett. B* 487, 118 (2000).

[82] JLab E97-110, Spokespersons, J. P. Chen, A. Deur and F. Garibaldi.

[83] P. Solvignon, *et al.*, *Phys. Rev. Lett.* **101**, 182502 (2008).

[84] M. Amarian *et al.*, *Phys. Rev. Lett.* **93**, 152301 (2004).

[85] V. Lensky, J. M. Alarcon, and V. Pascalutsa, *Phys. Rev. C* **90**, 055202 (2014).

[86] H. Dutz *et al.*, GDH Collaboration, *Phys. Rev. Lett.* **91**, 192001 (2003).

[87] Y. Prok *et al.*, CLAS Collaboration, *Phys. Lett. B* **672**, 12 (2009).

[88] V. Bernard, E. Epelbaum, H. Krebs, and U. G. Meissner, *Phys. Rev. D* **87**,054032 (2013).

[89] M. Battaglieri, A. Deur, R. D. Vita and M. Ripani (spokespersons), Jefferson Lab Experiment E03-006 (2003).

[90] C. Gu. *Helicity decoder for E08-027*, E08-027 Technical Note, Jefferson Lab (2014).

[91] C. K. Sinclair *et al.*, *Phys. Rev. Spec. Top. Accel. Beams* **10**, 023501 (2007).

[92] J. Alcorn *et al.*, *Nucl. Instrum. Meth. A* **522** (2004) 294-346.

[93] P. Zhu, *Beam Position Reconstruction for g2p Experiment in Hall A at Jefferson Lab*, E08-027 Technical Note, Jefferson Lab (2014).

[94] X. Zheng, *Ph.D. thesis*, Massachusetts Institute of Technology (2002).

[95] J. C. Denard, A. Saha, and G. Laveissiere, *in Proceedings of the 2001 Particle Accelerator Conference* (2001), p. 2326.

[96] J. Musson, *Functional Description of Algorithms Used in Digital Receivers*, Technical Note, Jefferson Lab (2012).

[97] M. Bevins, *in Proceedings of the 2005 Particle Accelerator Conference* (2005), p. 3819

[98] G2P ELog Entry 173, https://hallaweb.jlab.org/dvcslog/g2p/173.

[99] P. Zhu, *Beam Charge Measurement for g2p Experiment*, E08-027 Technical Note, Jefferson Lab (2015).

[100] P. Zhu *et al.*, *Nucl. Instrum. Meth. A* **808** 1 (2016).

[101] P. Piot, *Evaluation and Correction of Nonlinear Effects in FNPL Beam Position Monitors*, Technical Note, FNAL (2005).

[102] P. Zhu *Beam Position Reconstruction for g2p Experiment in Hall A at Jefferson Lab*, E08-027 Technical Note, Jefferson Lab (2014).

[103] C. Yan *et al.*, *Nucl. Instr. Meth. Phys. Res. A* **365**, 261 (1995).

[104] X. Zhan, *Ph.D. thesis*, Massachusetts Institute of Technology (2010).

[105] Møller Measurements for E08-027 (g2p) and E08-007, http://hallaweb.jlab.org/equipment/moller/e08-027.html.

[106] http://hallaweb.jlab.org/equipment/moller/.

[107] A. W. Overhauser, *Phys. Rev.* **92**, 411 (1953).

[108] C. D. Jeffries, *Phys. Rev.* **106**, 164 (1957).

[109] J. Maxawell, *Ph.D. thesis*, University of Virginia (2010).

[110] J. Pierce *et al.*, *Nucl. Instrum. Meth. A* **738**, 54 (2014).

[111] L.G. DeMarco, A.S. Brill, and D.G. Crabb. *J. Chem. Phys.* **108**, 4 (1998).

[112] D. G. Crabb and W. Meyer, *Annu. Rev. Nucl. Part. Sci.* **47**, 67 (1997).

[113] M. Goldman, *J. Magn. Reson.* **17**, 393 (1975).

[114] T. Badman, Proton Polarization Studies and Uncertainty Analysis for E08-027, E08-027 Technical Note, Jefferson Lab (2013).

[115] M. Cummings, *Ph.D. Thesis*, College of William and Mary, (2015).

[116] R. Zielinski, Determining the trigger efficiency for E08-027: update, g2p Technical Notes (2014).

[117] M. Cummings, *Efficiency Studies and PID Cut Optimization for E08-027*, E08-027 Technical Note, Jefferson Lab (2013).

[118] E. Longo and I. Sestili, *Nucl. Instrum. Meth.* **128**, 283 (1975).

[119] K. Fissum, *Nucl. Instr. Meth. Phys. Res. A* **474**, 108 (2001).

[120] T. Badman, *Dilution Analysis for E08-027*, E08-027 Technical Note, Jefferson Lab (2015).

[121] Y. Prok, Ph.D Thesis, University of Virginia, (2004).

[122] R. Fersch, Ph.D Thesis, The College of William and Mary, (2008).

[123] G. Chao, *Spectrometer Optics Study for E08-027*, E08-027 Technical Note, Jefferson Lab (2016).

[124] N. Liyanaga, *Optics calibration of the Hall A High Resolution Spectrometers using the New C++ Optimizer*, JLab-TN-02-012, (2002).

[125] M. Huang, *Ph.D. thesis*, Duke University (2016).

[126] P. E. Bosted *et al.*,*Phys. Rev. C* **78**, 015202 (2008).

[127] J. W. Lightbody and J. S. OConnell, *Computers in Physics* **2** (1988).

[128] S. Venkat, J. Arrington, G. A. Miller, and X. Zhan, *Phys. Rev. C* **83**, 015203 (2011).

[129] C. D. Jager, H. D. Vries, and C. D. Vries, *Atomic Data and Nuclear Data Tables* **14**, 479 (1974).

[130] K. C. Stansfield *et al.*, *Phys. Rev. C* **3**, 1448 (1971).

[131] L. S. Cardman *et al.*, *Phys. Lett. B* **91**, 203 (1970).

[132] W. Leo, *Techniques for Nuclear and Particle Physics Experiments*, Springer-verlag, (1987).

[133] Geant4 Physics Reference Manual (2016).

[134] K. Lassila-Perini, L. Urbán, *Energy loss in thin layers in GEANT*, *Nucl.Inst.Meth. A* **362**, 416 (1995).

[135] Y. S. Tsai, *Rev. Mod. Phys.* **46** 815 (1974).

[136] K. Nakamura *et al.*, (Particle Data Group), *J. Phys. G* **37**, 075021 (2010).

[137] E08-027 analysis wiki.

[138] Y. Qiang, *Ph.D. thesis*, Massachusetts Institute of Technology (2007).

[139] D. Drechsel, S. S. Kamalov, and L. Tiator, *Eur. Phys. J. A* **34**, 69 (2007).

[140] I. Akushevich *et al.*, *Comput. Phys. Commun.* **104**, 201 (1997).

[141] L. W. Mo and Y. S. Tsai, *Rev. Mod. Phys.* **41**, 205 (1969).

[142] A. Afanasev, I. Akushevich, and N. Merenkov, *Phys. Rev. D* **64**, 113009 (2001).

[143] J. L. Friar *et al.*, *Phys. Rev. C* **42**, 2310 (1990).

[144] M. Amarian *et al.*, *Phys. Rev. Lett.* **89**, 242301 (2002).

[145] Z. Meziani *et al.*, *Phys. Lett. B* **613**, 148 (2005).

[146] W. Xu *et al.*, *Phys. Rev. Lett.* **85**, 2900 (2000).

[147] F. Xiong *et al.* *Phys. Rev. Lett.* **87**, 242501 (2001).

[148] X. Zheng, *et al.*, *Phys. Rev. C* **70**, 065207 (2004).

[149] S. Riordan *et al.*, *Phys. Rev. Lett.* **105**, 262302 (2010).

[150] X. Qian *et al.*, *Phys. Rev. Lett.* **107**, 072003 (2011).

[151] J. Huang *et al.*, *Phys. Rev. Lett.* **108**, 052001 (2012).

[152] JLab E07-013, Spokespersons, T. Averett, T. Holmstrom and X. Jiang.

[153] JLab E06-014, Spokespersons, S. Choi, X. Jiang, Z.-E. Meziani, B. Sawatzky.

[154] JLab E05-015, Spokespersons, T. Averett, J. P. Chen and X. Jiang.

[155] JLab E05-102, Spokespersons, S. Gilad, *et al.*.

[156] JLab E08-005, Spokespersons, T. Averett, *et al.*.

[157] F. Colegrove *et al.*, *Phys. Rev.* **132**, 2561 (1963).

[158] T. E. Chupp *et al.*, *Phys. Rev. C* **36**, 2244 (1987).

[159] M. V. Romalis, *Laser polarized He-3 target used for a precision measurement of the neutron spin structure*, Princeton University (1997).

[160] M. V. Romalis, *et al.*, *Phys. Rev. A* **56**, 4569 (1997).

[161] Kelly A. Kluttz and Todd D. Averett, *Phys. Rev. A* **87**, 032516 (2013).

[162] T. G. Walker *et al.*, *Phys. Rev. A* **40**, 4959 (1989).

[163] B. Chann *et al.*, *Phys. Rev. A* **66**, 032703 (2002)

[164] A. Ben-Amar Baranga, *et al.*, *Phys. Rev. Lett.* **80**, 2801 (1998).

[165] E. Babcock *et al.*, *Ph.D. thesis*, University of Wisconsin (2005).

[166] W. C. Chen *et al.*, *Phys. Rev. A* **75**, 013416 (2007).

[167] Y. Qiang, *AIP Conf.Proc.* **1182**, 864 (2009).

[168] Y. Zhang, *PhD thesis*, Lanzhou University (2011).

[169] Jianming Jin, *Electromagnetic analysis and design in magnetic resonance imaging*, CRC press, 1999.

[170] G. Breit and I. I. Rabi, *Phys. Rev.* **38**, 2082 (1931).

[171] E. Arimondo, M. Inguscio, and P. Violino *Rev. Mod. Phys.* **49**, 31 (1977).

[172] M. V. Romalis and G. D. Cates *Phys. Rev. A* **58**, 3004 (1998).

[173] Jaideep Singh, *Ph.D. thesis*, University of Virginia (2010).

[174] E. Babcock, *et al.*, *Phys. Rev. A* **71**, 013414 (2005).

[175] B. Chann *et al.*, *Phys. Rev. A* **66**, 032703(2002).

[176] A. B.-A. Baranga *et al.*, *Phys. Rev. A* **58**, 2282 (1998).

[177] Q. Ye *et al.*, *Eur. Phys. J. A* **44**, 55 (2010).

[178] P. Dolph et al., *Phys. Rev. C* **84**, 065201 (2011).

[179] Y. Zhang, *PhD thesis*, Rugsters University (2013).

[180] JLab E12-10-006, Spokespersons, J.P.Chen, *et al.*.

[181] JLab E12-11-007, Spokespersons, J.P.Chen *et al.*.

[182] JLab E12-06-122, Spokespersons, T. Averett *et al.*.

[183] JLab E12-06-121, Spokespersons, T. Averett *et al.*.

[184] JLab E12-09-018, Spokespersons, G. Cates *et al.*.

[185] JLab E12-06-110, Spokespersons, G. Cates *et al.*.

[186] JLab E12-09-016, Spokespersons, G. Cates *et al.*.

[187] Hall A Annual Report (2012).

[188] JLab polarized ^{3}He target lab wiki.

[189] P.A.M. Dolph *et al.*, *Phys. Rev. C* **84**, 065201 (2010).

[190] F. Bloch, *Physical Review* **70**, 460-473 (1946)

[191] X. Qian *et al.*, *Phys. Rev. Lett.* **107**, 072003 (2011).

[192] J. Huang *et al.*, *Phys. Rev. Lett.* **108**, 052001 (2012).

[193] JLab E12-06-122, Spokespersons, T. Averett, *et al.*.

[194] NASA website.

[195] H. Yukawa, *Proc. Phys. Math. Soc. Japan.* **17** 48 (1935).

[196] Frank Wilczek, *Nature* **445**, 156-157 (2017).

[197] N. Ishii *et al.*, *Phys.Rev.Lett.* **99** 022001 (2007).

[198] Z.S. Hartwig *et al.*, PSFC MIT (2012)

[199] Open source from wikipedia.

[200] F. Romanelli *et al.*, Fusion Electricity-EFDA (Nov. 2012)

[201] M.M. Lowry *et al.*, *Nucl. Inst Meth. Phys. Res. A* **815**, 31 (2016).

[202] A. Nikroo *et al.*, *Fus. Sci. Tech.* **41**, 214 (2002)

[203] L.R. Baylor *et al.*, *Nucl. Fusion* **47**, 1598 (2007)

[204] A.M. Sandorfi *et al.*, *Springer Proc. Phys.* **187**, 115 (2016).

[205] D.C. Pace *et al.*, *J. Fus. Energy* **35**, 54 (2016).

[206] N.H. Brooks *et al.*, *Journal of Nuclear Materials*, **145-147** 770-774 (1987).

[207] DIII-D website: `https://fusion.gat.com/global/DIII-D`.

[208] G.W. Miller, A. Deur, J. Liu, M.M. Lowry, A.M. Sandorfi, K. Wei, X. Wei, and X. Zheng, *Performance of Laser-Polarized ^{3}He in Tokamak Fuel Pellets*, (priv. comm; to be published).

[209] A. Webb, *Introduction to Biomedical Imaging*, IEEE press, 2003.

[210] JLab/UVa polarized fusion discussion wiki.

[211] B.Saam *et al.*, *Phys. Rev. A* **52**, 862 (1995).